Analysis and Optimisation of Thermal Energy Storage

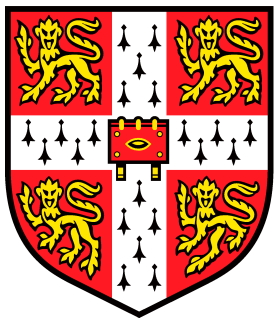

Joshua McTigue

St. Catharine's College

Cambridge University Engineering Department

September 29, 2016

A dissertation submitted for the degree of Doctor of Philosophy

Declaration

This dissertation is the result of my own work and includes nothing which is the outcome of work done in collaboration except as declared in the Preface and specified in the text.

It is not substantially the same as any that I have submitted, or, is being concurrently submitted for a degree or diploma or other qualification at the University of Cambridge or any other University or similar institution except as declared in the Preface and specified in the text. I further state that no substantial part of my dissertation has already been submitted, or, is being concurrently submitted for any such degree, diploma or other qualification at the University of Cambridge or any other University of similar institution except as declared in the Preface and specified in the text.

The following does not exceed 65 000 words or 150 figures as set out by the Department of Engineering degree committee. This thesis contains 56 661 words and 84 figures.

Abstract

The focus of this project is the storage of thermal energy in packed beds for bulk electricity storage applications. Packed beds are composed of pebbles through which a heat transfer fluid passes, and a thermodynamic model of the heat transfer processes within the store is described. The packed beds are investigated using second law analysis which reveals trade-offs between several heat transfer processes and the importance of various design parameters. Parametric studies of the reservoir behaviour informs the design process and leads to a set of design guidelines. Two innovative design features are proposed and investigated. These features are segmented packed beds and radial-flow packed beds respectively.

Thermal reservoirs are an integral component in a storage system known as Pumped Thermal Energy Storage (PTES). To charge, PTES uses a heat pump to create a difference in internal energy between two thermal stores; one hot and one cold. The cycle reverses during discharge with PTES operating as a heat engine. The heat pumps/engines require compression and expansion devices, for which simple models are described and are integrated with the packed bed models. The PTES system behaviour is investigated with parametric studies, and alternative design configurations are explored.

A multi-objective genetic algorithm is used to undertake thermo-economic optimisations of packed-bed thermal reservoirs and PTES systems. The algorithm generates a set of optimal designs that illustrate the trade-off between capital cost and round-trip efficiency. Segmentation is found to be particularly beneficial in cold stores, and can add up to 1% to the round-trip efficiency of a PTES system. On the basis of the assumptions made, PTES can achieve efficiencies and energy densities comparable with other bulk electricity storage systems. However, the round-trip efficiency is very sensitive to the efficiency of the compression–expansion system. For designs that utilised bespoke reciprocating compressors and expanders, PTES might be expected to achieve electricity-to-electricity efficiencies of 64%. However, using compression and expansion efficiencies typical of off-the-shelf devices the round-trip efficiency is around 45%.

Contents

List of Figures

List of Tables

Journal papers resulting from this thesis

"Analysis and optimisation of segmented packed-bed thermal reservoirs for electricity storage applications"
A. J. White, **J. D. McTigue**, C. N. Markides
Manuscript accepted by the IMechE Journal of Power and Engineering

"Segmented packed beds for improved thermal energy storage performance"
J. D. McTigue, A. J. White
Manuscript accepted by IET Renewable Power Generation, June 2016

"Parametric studies and optimisation of pumped thermal electricity storage"
J. D. McTigue, A. J. White, C. N. Markides
Applied Energy, vol. 137, pp. 800–811, Sept. 2015

"Wave propagation and thermodynamic losses in packed-bed thermal reservoirs for energy storage"
A. J. White, **J. D. McTigue**, C. N. Markides
Applied Energy, vol. 130, pp. 648–657, 2014

Conference proceedings resulting from this thesis

Presentations

"A comparison of radial-flow and axial-flow packed beds for thermal energy storage"
International Conference on Applied Energy (ICAE 2016), 8–11/10/2016, Beijing, China

"Analysis of radial-flow packed beds for thermal energy storage"
UK Thermal Energy Storage (UKTES) Conference, 8–9/06/2016, London, UK

"Segmented packed beds for improved thermal energy storage performance"
FETE (Fluids, Energy and Turbomachinery Expo, Department of Engineering Division A Graduate Conference), 16/07/2015, Imperial War Museum, Duxford, UK

"Segmented packed beds for improved thermal energy storage performance."
Offshore Energy and Storage (OSES) Conference, 1–3/07/2015, Edinburgh, UK

"A parametric study of losses in packed-bed reservoirs for electrical energy storage."
13th UK Heat Transfer Conference, 2-3/09/2013, London, UK

Posters

"Optimisation of Pumped Thermal Energy Storage."
P. Farres-Antunez, C. Willich, **J. D. McTigue**, A. J. White
SolarStor, London UK, 14/04/2016

"Operational management and electrical grid integration of Pumped Thermal Electricity Storage"
C. Bordin, A. Ibrahim, **J. D. McTigue**, C. Dent, B. Kazemtabrizi, A. J. White
UK Energy Storage Conference, Birmingham, UK

"The role of energy storage in future energy systems"
UK Energy Research Centre International Summer School, 5-10/07/2015, Cambridge, UK

"Thermo-economic optimisation of a thermal energy storage system"
9th International Renewable Energy Storage (IRES) Conference, 9-11/03/2015, Dusseldorf, Germany

Funding

I gratefully acknowledge the following organisations for their financial support:

The UK Engineering and Physical Sciences Research Council (EPSRC) for providing a Doctoral Training Grant

St. Catharine's College, University of Cambridge for providing travel grants.

Cambridge University Engineering Department for providing travel grants.

The Energy Storage Research Network (ESRN) for providing a travel grant.

Isentropic Ltd. who provided a maintenance bursary.

Acknowledgements

I'm grateful to my supervisor, Alex White, for his guidance and help throughout this interesting and rewarding project. I have also appreciated the useful discussions and enjoyable conferences that I've shared with Alex and the rest of the group.

I am very thankful to my parents and to the Docherty clan for their generous and unerring support and hospitality. And to Fiona Docherty, I am more grateful than I could express here. I am also thankful to all those people who have made life in Cambridge a wonderful and memorable experience. In particular, (and in chronological order) I thank BR, MB, CS, FS, GM, RG, BL, LP, SS, AC, FD, AR, SS, SW, RS, SH.

I would also like to convey my thanks to the staff and academics at St. Catharine's College, Cambridge, and Cambridge University Engineering Department, who have been a pleasure to know and have provided invaluable assistance to me throughout my time in Cambridge.

Finally, I acknowledge the people and organisations who have used their time and resources to develop open-source software. Without the use of the following programs and databases, this project would have been very different: Unix, Linux, GNU Project (specifically Gnuplot, gfortran, GIMP, GNU Emacs), GSView, LaTeX, TeXstudio, Open office, xfig, Coolprops, Mendeley Desktop, Notepad++, CES Edupack

We are like tenant farmers chopping down the fence around our house for fuel when we should be using Nature's inexhaustible sources of energy sun, wind and tide. . . . I'd put my money on the sun and solar energy. What a source of power! I hope we don't have to wait until oil and coal run out before we tackle that.

Thomas Edison

Humanity had been strong, energetic, and intelligent, and had used all its abundant vitality to alter the conditions under which it lived. And now came the reaction of the altered conditions.

"The Time Traveller", H. G. Wells

Chapter 1

Introduction

1.1 Context: current and future trends in energy supply

Since the late 20th century there has been a surge in the deployment of renewable energy technologies (see figure 1.1) driven by concerns about anthropogenic climate change, the health impacts of particulate pollution, and diminishing fossil fuel reserves. Although climate change is a natural process, recent human activities have contributed to changes in the global climate. Carbon dioxide levels have increased from 284 ppm in 1832 to 397 ppm in 2013 [9] and ice cores have determined that the CO_2 levels in 2005 (379 ppm) exceed the natural range for the past 650 000 years (180 - 300 ppm) [10]. These increases are primarily due to the burning of fossil fuels and changing land use. Scientific consensus suggests that climate change could severely impact a large proportion of the world's population through a number of mechanisms including an increased rate of severe weather patterns and risks to the security of supply of food, water and energy [11–14].

A number of policies have been developed in response to the above risks. In 1997 the Kyoto Protocol set internationally binding emissions reduction targets for participating industrialised countries. The UK's target is to reduce greenhouse gas (GHG) emissions to 8% below 1990 levels in the period 2008-2012 [21]. The Doha Amendment to the Kyoto Protocol extended this value to 18% below 1990 levels in the period 2013-2020 [22]. The 2008 Climate Change Act committed the UK to reducing GHG emissions by 80% by 2050 [23], and the UK had achieved a 35% reduction by 2014 [24].

The 2009 EU Renewable Directive aims to increase the renewable energy share to 15% of the final energy consumption by 2020 for EU member states. Whilst there has been good progress so far, it is predicted that many countries may not meet these targets unless further changes to policy are made [25]. In 2015, 7.0% of the UK's energy consumption came from renewable sources (up from 5.2% in 2011) [15]. To meet the Renewable Directive target, the UK will have to increase renewable energy deployment from around 64 TWh to approximately 230 TWh (for heat, transport and electricity) [16, 26]. Figure 1.1 shows predicted capacities of several renewable sources in 2020 and illustrates the large investment that the UK is preparing to make into renewable energy. By implementing these changes, it is forecast that around 30% of UK electricity will come from renewable sources [16].

There is much discussion about how to tackle these pressing issues and a variety of views

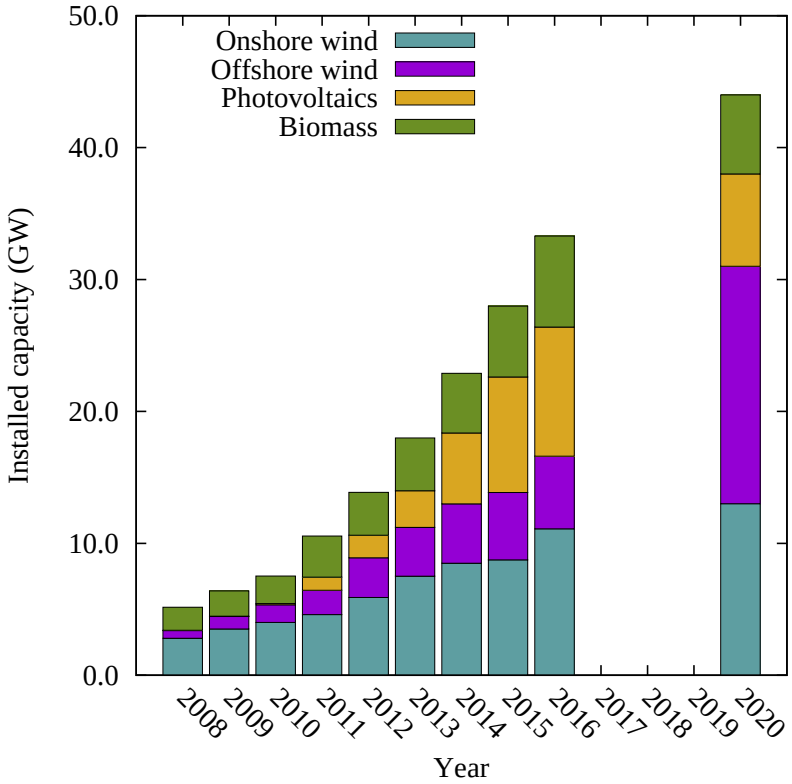

Figure 1.1: Installed capacity of various renewable energy sources in the UK. Data from 2008–2014 from Department for Energy and Climate Change (DECC) DUKES 2015 report [15, 16]. 2015 values are from DECC Energy trends reports [17]. 2016 values are estimated based on installed capacity plus capacity under construction, data for which can be found from various sources, including DECC [18–20]. Values at 2020 are predicted capacities taken from [15] and are subject to uncertainty (for instance the value for solar photovoltaics could vary between 7 and 20 GW)

on technologies, economics and politics have been presented [27–34]. However, it is clear that regardless of the route taken, the UK will become increasingly dependent on renewable sources, especially onshore and offshore wind and solar power. The intermittent nature of renewable technologies creates problems for the electrical grid such as congestion, frequency and voltage control, and balancing of supply and demand. Several solutions exist, as discussed in section 1.3, and this thesis focusses on energy storage. As well as facilitating the deployment of renewable technologies, energy storage provides a number of further benefits to the electrical grid. The next section provides some historical context and applications of energy storage, before the intermittency problem is discussed in more detail. This thesis is concerned with a particular energy storage technology, known here as

Pumped Thermal Energy Storage (PTES), which utilises packed-bed thermal reservoirs as the energy stores. Several prominent energy storage technologies are summarised before PTES is described in detail.

1.2 Background and applications of energy storage

Technology based on the accumulation of energy has a long history. 30 000 years ago, rocks were employed as thermal stores and were used to cook food and boil water, thereby leading to more nutritious and digestible meals [35]. Somewhat more recently, the Romans developed a mining method known as *hushing* where powerful torrents of water were released from reservoirs with capacities of over 10 million litres in order to reveal mineral veins [36].

The development of the electrical grid in the 19th and 20th centuries provided opportunities for bulk electricity storage. At the beginning of the 20th century generating stations were shut down at night, leaving the residual loads to be supplied by lead-acid accumulators [37]. While electrical batteries that power portable devices are currently a ubiquitous technology, bulk electricity storage has not been widely deployed leading to a system where electricity is, for the most part, consumed as it is produced. Generating plants must be capable of satisfying demand that varies on daily and seasonal timescales, with maximum demand that may only last for a few hours each year [38]. Chen et al. [39] suggests that the resulting plants are inefficient, over-designed and expensive.

There is a wide array of energy storage technologies which have a diverse range of applications [39]. These can be categorised roughly according to the time scales at which they discharge and the applications they are therefore suitable for.

Milliseconds – Seconds

Energy storage can combat random short-term fluctuations and improve power quality and reliability by providing voltage and frequency control [39, 40]. Appropriate technologies typically have high power ratings and low energy capacity, for example capacitors, batteries, fly wheels and superconducting magnetic energy storage [39].

Seconds – Minutes

Energy storage can provide continuity of service by allowing ride through of momentary shortages. Appropriate technologies may overlap with the above category, since a fast response is required, although a larger energy storage capacity is beneficial. Batteries and fuel cells are perhaps the most suitable since they have fast response (less than a second) and appropriate discharge durations [39].

Hours – Days

Energy storage can be used in 'peak shaving': unexpected surges in demand are matched by using energy that was stored during a period of surplus supply. This may be done on a large scale by storing energy generated at off-peak times in order to supply it during periods of higher demand, and is known as load levelling. Load levelling also allows for arbitrage of the electricity price. Another application is to integrate energy storage with intermittent renewable energy generators to help match fluctuating demand and supply.

Appropriate technologies have large energy storage capacities. Chen et al. [39] suggests that for large scale management (e.g. applications greater than 100 MW) Pumped Hydro (PHES) and Compressed Air Energy Storage (CAES) are most suitable, whilst thermal energy storage, large scale batteries, fuel cells and solar fuels are more suitable for smaller capacities of 10 – 100 MW. It has been suggested that increasing proportions of renewable energy will move the energy mix away from large scale generating plants, towards smaller scale more widely distributed plants [40]. Therefore a distributed network of medium scale energy storage may be an appropriate way of integrating with distributed supply.

Storage can decouple energy supply from demand, and thereby provide benefits to all aspects of electricity generation, transmission and supply. For instance, energy storage could be used to ease electrical grid congestion; installing storage may be more affordable than upgrading the grid [41]. Ref. [41] suggests that other benefits include providing back up and the ability to shift load to off-peak hours for both home users and commercial and industrial use.

Strbac et al. [1] carried out a detailed analysis of a number of mechanisms by which stor-

age can provide value. For instance, energy storage could be used to offset investment in additional generation plants, investment in the transmission network and interconnection, and reduce the need for distribution network reinforcement. As energy systems continue to develop and evolve, other applications for energy storage systems may emerge.

Strbac's analysis suggested that energy storage provides greatest value when there is a high proportion of renewable energy technologies. Furthermore, he suggested that only a few hours of storage are necessary to reduce peak demand and capture significant value. Surprisingly, Strbac's analysis suggested that the value of storage was quite insensitive to the efficiency of the storage system: for instance, the value of storage only increased by 10% when the efficiency was increased from 50% to 90%. However, it was also noted that the round-trip efficiency became much more important in applications which required large storage capacity.

A recent report by the National Infrastructure Commission [42], a UK government backed organisation, recognised the benefits that storage could provide and recommended regulatory change to encourage investment in storage. In response, the UK government has committed £50 million towards "innovation in energy storage, demand-side response and other smart technologies" [43].

The above discussion demonstrates there are a range of applications for energy storage systems, and that energy storage could provide value in a number of ways. Each of these applications has different requirements in terms of, for instance, power and energy capacity, storage duration, depth of discharge, and frequency of charge-discharge. Since different technologies will be more or less suited to different applications, it is likely that a portfolio of diverse technologies will be necessary.

1.3 Solutions to the intermittency of renewable power; how much energy storage is required?

Renewable energy sources are intermittent, and electricity demand fluctuates throughout the day. Figure 1.2 illustrates the variability in wind power and electricity demand in the United Kingdom for the week at the beginning of January and July 2013. Electricity de-

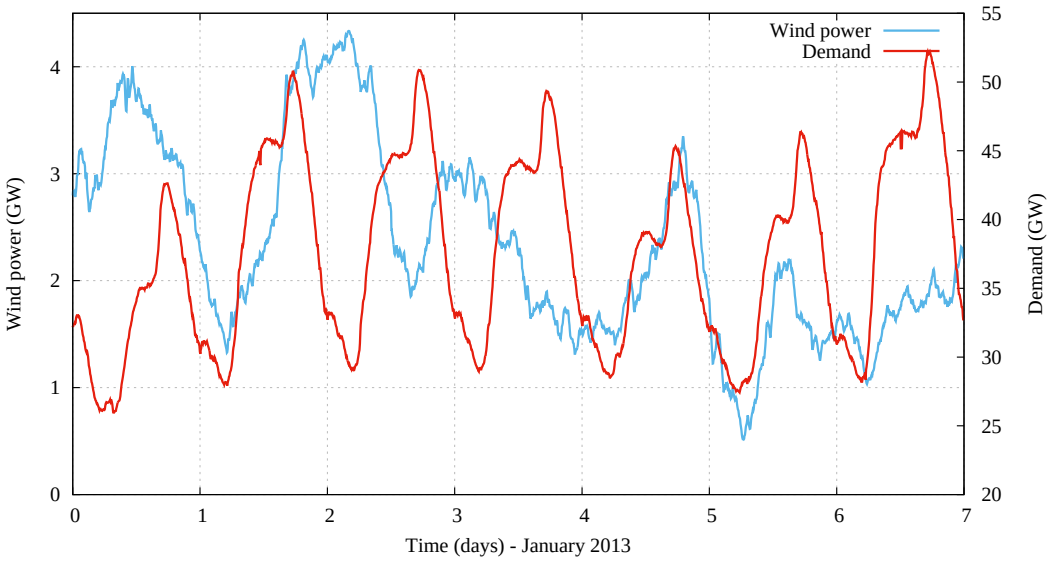

(a)

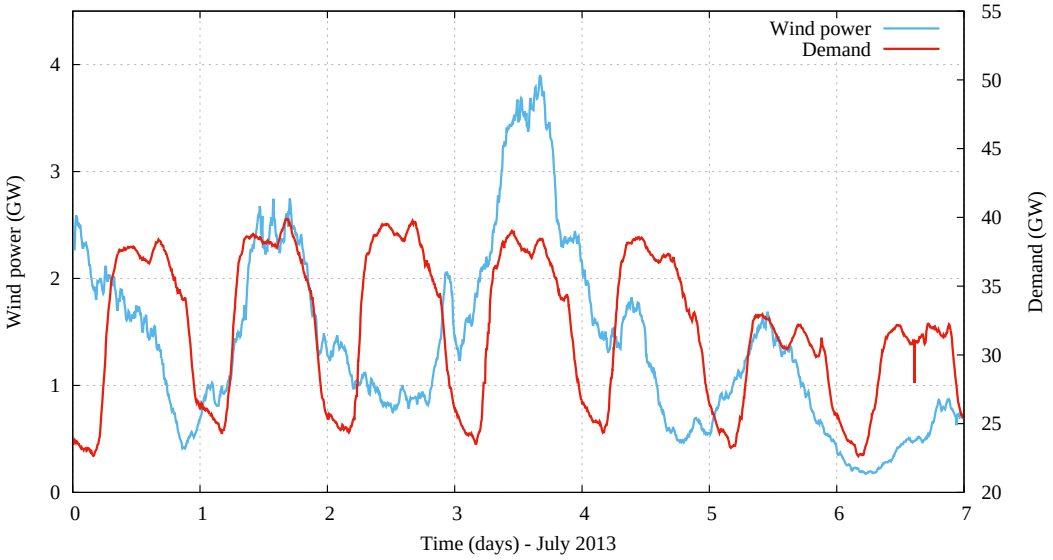

(b)

Figure 1.2: Instantaneous wind generation (left axis) and electricity demand (right axis) in the United Kingdom during the first week in **(a)** January 2013 and **(b)** July 2013. Data from Gridwatch [44].

mand clearly follows a diurnal pattern and peaks at around 55 GW in the winter and 40 GW in the summer. Wind power follows seasonal patterns, with the average wind power output being greater in the winter than the summer. Variability in the weather (which includes a degree of randomness) leads to variations in the supply of electricity which can include lulls lasting hours to days [28]. Consequently, demand and supply of renewable electricity are unmatched, which leads to difficulties in scenarios with large proportions of renewable energy. At shorter time scales, intermittency may cause problems with frequency control as demand and supply can change very quickly.

There are a number of solutions to these problems. One suggestion is that increasing the land area over which wind is installed will average out the variability [45–47]. Figure 1.3 shows the normalised wind power output in the first week of January 2013 for three countries: Ireland, the UK and Denmark. The curves show the sum of wind generation across each country and the output is clearly still intermittent. In addition, wind generation follows a similar pattern in each country: the UK lags behind Ireland by a few hours (as the prevailing wind is from the south-west), and Denmark lags this by another few hours[1]. Combining the wind output of these countries would reduce the intermittency to an extent, but variability would still exist. This solution would require greater interconnection and collaboration between countries on a continent-wide scale (which may provoke concern over energy security). However, interconnection is thought to have a number of advantages and there are plans to expand interconnection between the UK and Europe from the current 4 GW to around 10–11 GW [42].

A second option is demand side response, whereby energy consumers use energy in a more flexible manner to accommodate the current supply of energy. For instance, the national grid may ask large industrial consumers to switch off equipment in periods of low supply and high demand. Smaller, more distributed options involve controlling when household systems such as washing machines and dishwashers are switched on and off, requiring a degree of flexibility from the user. Electric car batteries have also been suggested as a tool for a demand-side management system [28].

Other options include maintaining peaking power plants, developing more flexible generation plants and over-sizing renewable energy capacity, all of which may not be economi-

[1]Denmark's data looks a little different as it is reported hourly, whereas Irish data was reported every 15 minutes, and UK data every 5 minutes.

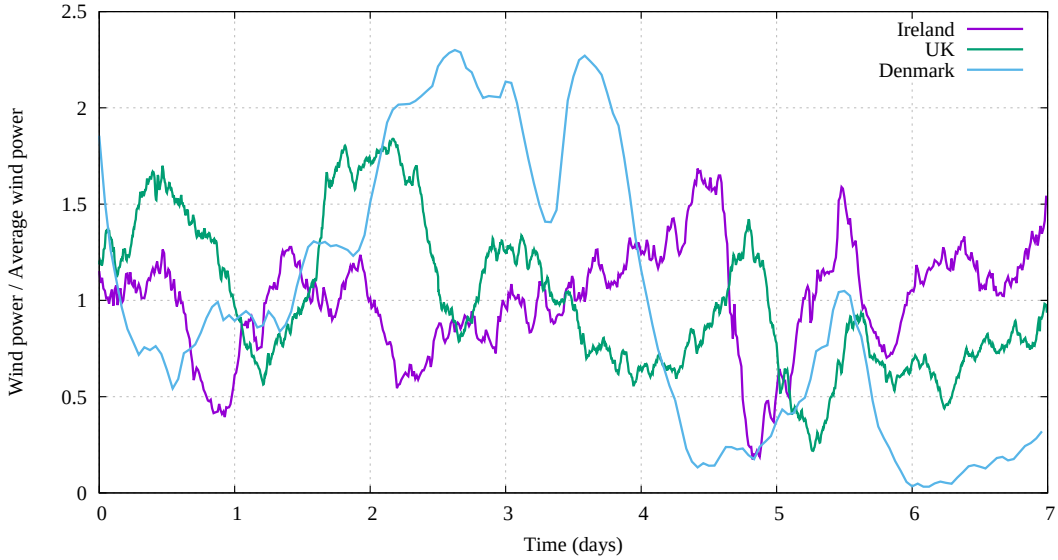

Figure 1.3: Instantaneous wind generation during the first week of January 2013 in three European countries. Wind power is normalised by the average wind power in that country for that week. Sources: Ireland (EirGrid Group) [48], UK (Gridwatch) [44] and Denmark (Energinet.dk) [49].

cally feasible.

Another solution to the 'intermittency problem' is bulk electricity storage, where surplus electricity is stored until a later period when electricity demand increases above power generation. A wide array of storage technologies has been proposed and an overview is given in the next section.

Estimating the energy storage capacity that would address the intermittency problem depends on a number of uncertain factors, such as the proportion of renewables, the influence of other schemes (interconnection and demand side management), and economic considerations. Nevertheless, several authors have made estimates based on simplified scenarios. For instance, MacKay [28] calculated the storage capacity required if storage were to compensate for a lull in wind power that lasted for five days. For an installed wind capacity of 33 GW[2] delivering 10 GW on average, Mackay proposed a storage capacity of 1200 GWh. This amounts to a storage capacity of 36 GWh for every GW of installed wind capacity, which can deliver power at 30% of installed capacity. This is an overestimate, since during the five day lull the wind output is not zero, and energy could be obtained from

[2] 33 GW of installed wind is in line with the UK targets for 2020, see figure 1.1.

other sources. In addition, the storage would be under-utilised as five-day lulls are fairly infrequent.

Carbajales-Dale et al. [50, 51] carried out the same analysis and provided mathematical expressions for the required energy storage capacity. Their analysis therefore provides the same result to MacKay for the example of a five-day lull.

Another simple estimate of required energy storage capacity is presented here. Wind generation data for 2015 was collected [44] and the average wind output was found to be 2.7 GW for a total installed capacity of around 13 GW[3]. Like the above analyses, it was assumed that wind output would be kept constant at the average value of 2.7 GW. Any time that the wind output dropped below this average value was classified as a lull. The lull continued until the power increased above the average value. Lulls that occurred within four hours of one another were counted as one lull (as there probably would not have been sufficient time to recharge the storage). Figure 1.4 demonstrates that the majority of the lulls ($>$50%) are less than 20 hours, and over 75% of the lulls are less than 50 hours long. The histogram indicates that lulls lasting for over 5 days do occasionally occur, although it probably would not be economical to build energy storage to provide for all possible scenarios although a solution is required. The storage required to account for 75% of the lulls at the average wind output would require $2.7 \times 50 = 135$ GWh, which corresponds to a rule of thumb of 15 GWh of storage per GW of installed wind capacity. Scaling this up to MacKay's scenario with 33 GW of installed wind suggests a storage energy capacity of 340 GWh, which is ten times the current UK storage capacity. Note, it is possible that the storage requirement may not scale linearly with the installed capacity of renewables, and that these values may underestimate the required storage.

These analyses are somewhat approximate as many of the factors are arbitrary, and a number of complex factors that may significantly affect the problem have been neglected. For instance, buffering wind to provide a constant output is not realistic: supply needs to be variable in order to be able to match demand. These studies also consider only one application of energy storage and do not include other intermittent energy sources such as solar power. However, the above analyses give some indication as to the storage energy capacity

[3]This suggests quite a low capacity factor of 21%. However, wind data is only available for metered farms, and many smaller farms are not metered. Assuming a capacity factor of 30% suggests that the installed capacity of metered farms is around 9 GW

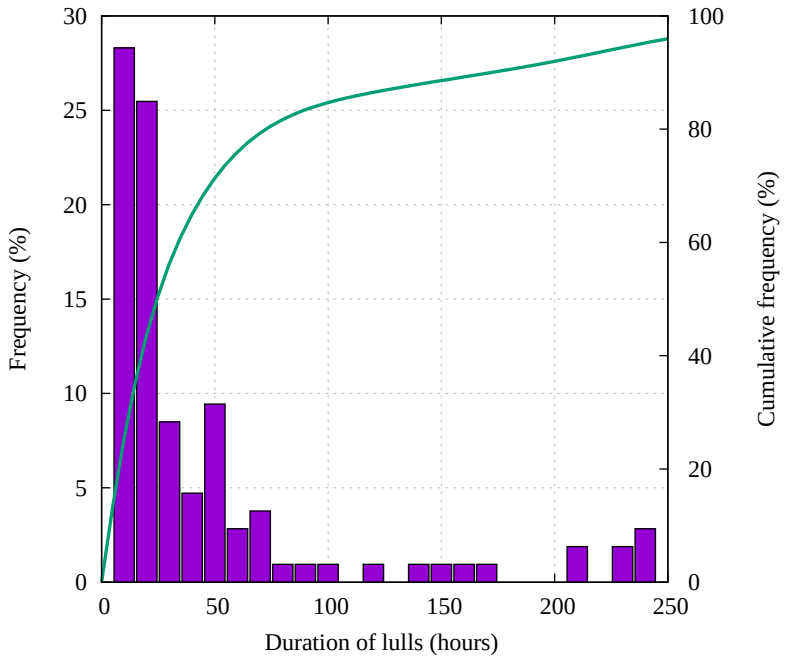

Figure 1.4: Distribution of the duration of lulls in wind power in the UK for 2015. Lulls are considered to be any time wind power fell below the average wind power that year (2.67 GW). If lulls occur within four hours of one another, they are considered to be the same lull.

that may be required, and suggest that the required energy capacity is not insignificant. For instance, the UK currently has around 30 GWh of storage installed (predominantly as pumped hydro) whereas the above estimates suggested an order of magnitude more may be required if intermittency is to be addressed in 2020. It is also interesting to note that all the UK's pumped hydro plants (which provide 26.7 GWh) were opened between 1963 and 1984, which indicates the low levels of investment in storage in the past three decades.

Other authors have undertaken different types of analyses, and frequently focus on the economic aspects of storage. Grünewald et al. [52] took into account energy prices to calculate the net present value of several storage technologies under scenerios with different proportions of renewable energy. For one case with 60 GW of renewables (42 GW wind and 18 GW solar) and a mean demand of 36 GW, Grünewald found that the optimal energy capacity of a Compressed Air Energy Storage (CAES) system was 69 GW h. Another analysis [53] considered de-carbonisation of the US electricity grid, and how the cost of storage (per kW and per KWh) would affect storage capacity. Ref. [53] found that the optimal energy capacity of the cheapest storage systems modelled (100 $/kW and 5 $/kWh)

would store two days worth of average electricity demand. In 2015 the average UK demand was 33 GW suggesting that complete de-carbonisation would require 1580 GWh storage.

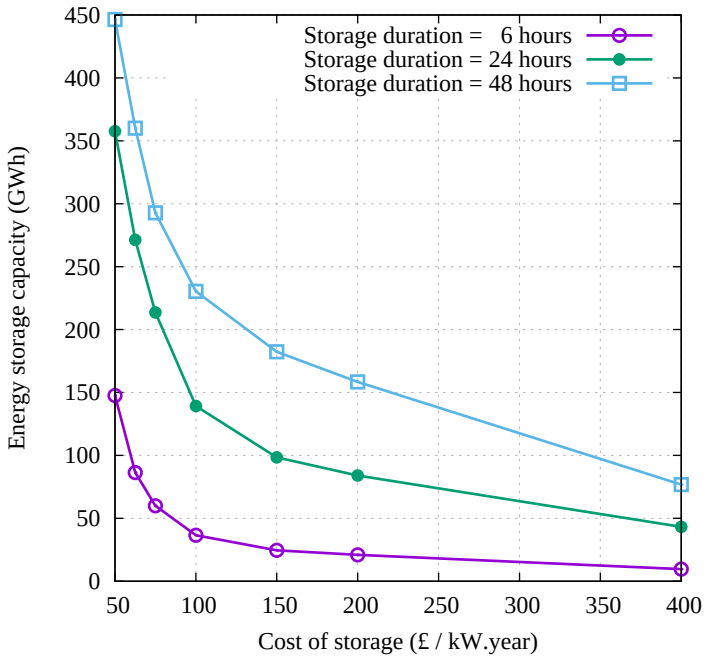

Figure 1.5: Optimal energy storage capacity as calculated by Strbac [1] for various storage costs and duration of storage.

Strbac et al. [1] carried out a detailed investigation into the benefit of energy storage to the electrical grid. The analysis considered the economic value that storage would provide in future scenarios. They used the DECC 2050 Pathways as a guide for future energy mixes, and particularly focussed on a pathway known as *Grassroots* where, of a generation capacity of 190 GW, approximately 75 GW were renewable (of which 70 GW were wind power) in 2030. Strbac developed a system model incorporating generation, transmission and distribution systems. The model aims to satisfy the short-term supply and demand balance in an economically optimal way by considering long term investment decisions. Strbac investigated the optimal storage capacity for various costs of storage and durations of storage. Unsurprisingly, Strbac noted that cheaper storage corresponded to larger optimal storage capacities. Some of these results are reproduced in figure 1.5. Further analysis by Strbac suggested that only a few hours of storage were sufficient to reduce peak demand. For storage durations beyond six hours, the marginal value of storage decreased sharply. By considering the six hours storage duration curve in figure 1.5 for optimistic storage costs

of 75–150 / kW·year suggests storage capacities of 25–60 GW h.

A wide range of energy storage capacities have been predicted, and there are a number of methods for analysing the problem. These studies have many different assumptions, and calculate storage energy capacity for different objectives and scenarios. Thus it is hard to compare the results, in which a large degree of variation exists. While there may not be much agreement on the required quantity of storage, the above authors all identified that storage would provide value in a number of ways.

1.4 Prominent energy storage types

Chen et al. [39] provides a review of a large number of prominent energy storage technologies, and compares their technical and economic characteristics. Technologies are typically categorised into broad groups, such as mechanical, electrical, chemical and thermal storage. These categories are then further divided and sub-divided due to the breadth and diversity of technologies that exist. Mechanical storage technologies include fly-wheels, Compressed Air Energy Storage, and pumped hydro; electrical storage includes capacitors, supercapacitors and magnetic storage; chemical storage includes fuel cells, conventional battery technologies (such as lead-acid, lithium-ion) and flow cells (such as zinc-bromine and vanadium redox); thermal storage may include cryogenic storage, sensible heat storage or latent heat storage such as phase change materials. In some cases technologies from one category may be integrated with those of another category, for instance thermal stores can be incorporated in CAES technology. The range of storage systems makes a comprehensive review beyond the scope of this thesis and the reader is directed to Chen's review for further details. However, a brief discussion of Pumped Hydro Energy Storage (PHES), Compressed Air Energy Storage (CAES) and thermal energy storage systems is now provided in order to provide context, background and comparison for the technology that is the focus of this work: Pumped Thermal Energy Storage (PTES).

Metrics are required to provide a comparison between different storage schemes, and a number of these factors have been developed. The energy density ρ_E and power density ρ_P are important performance metrics for energy storage systems and give an indication of the scale and economic feasibility of the system; capital cost per unit energy storage ($ / kWh)

and per unit power capacity ($ / kW) vary approximately inversely with ρ_E and ρ_P. The precise definition of energy and power density varies from author to author and depends on the technology. Densities may be volumetric or gravimetric, depending on whether the energy stored is divided by the volume of the system or its weight, respectively. In this thesis, densities are volumetric, and ρ_E is defined as the stored *available* energy divided by the volume of the storage media. (Energy densities which incorporate the full footprint of the plant will necessarily be lower than this measure, but this measure is not used here due to uncertainty over the plant size.)

The round-trip of energy storage systems is defined as the ratio of net work output during discharge to the net work input during charge, such that

$$\chi = \frac{\text{Net work output}}{\text{Net work input}} = \frac{W^{\text{net}}_{\text{dis}}}{W^{\text{net}}_{\text{chg}}} \tag{1.1}$$

1.4.1 PHES

Pumped Hydro Energy Storage (PHES) is the most widely implemented energy storage technology [39] for electricity, with over 129 GW installed at more than 200 sites globally [54]. PHES operates using two water reservoirs at different elevations and energy is stored in the gravitational potential of water. The quantity of energy stored is proportional to the height difference and volume of the reservoirs. The available energy density ρ_E is given by

$$\rho_E = \rho g \Delta H \tag{1.2}$$

Where ρ is the density of water, g is the acceleration due to gravity, and ΔH is the height difference between the upper and lower reservoirs. The largest PHES scheme in the UK is Dinorwig power station in Gwynedd, Wales which has ΔH of roughly 500 m [28]. The three other PHES schemes in Wales have height differences of 170–350 m. Dinorwig's energy density is roughly 1.4 kWh m^{-3}, while Chen et al. [39] suggests PHES schemes have energy densities in the range 0.5–1.5 kWh m^{-3}. A comparison with other technologies is shown in table 1.1 on page 21.

PHES is a proven technology with a high efficiency, fast response and long storage time.

For instance, Dinorwig power station has an efficiency of 74–75% and can attain full load in less than two minutes from standstill, and less than 20 seconds if spinning [55]. Furthermore, it has a low risk investment with a low levelised cost of energy[4] [39, 41]. It has numerous drawbacks, however, including limited suitable sites, long construction time, high capital cost and low energy density. Moreover, there is a significant environmental impact associated with clearing and flooding a large area, and the moving of large quantities of earth to build the dam [56].

Various alternatives to the standard design have been proposed with the aim of reducing the geographical limitations of PHES. Underground pumped hydro uses an underground reservoir which exchanges water with a surface reservoir [57]. Since the two reservoirs can be vertically aligned, frictional losses are reduced. Excavating the lower reservoir includes several challenges, such as finding geologically suitable sites, technical requirements and cost [58]. Disused mine shafts and underground caverns may provide suitable locations, which would then lead underground pumped hydro to having similar geographical constraints to CAES.

1.4.2 CAES, I-CAES and AA-CAES

Compressed Air Energy Storage has garnered much interest due to its low capital costs, high energy densities and efficiencies. There are currently two CAES plants in operation, although several more are planned or under construction [39]. These existing plants are known as Diabatic CAES since they are similar to conventional gas turbines, except that the compression and expansion stages are decoupled. After compression, the high pressure gas is stored in a large underground cavern. Energy is discharged by taking the compressed air, heating it and expanding it through a high pressure turbine. Fuel is then added to the exhaust, which combusted and passed through a low pressure turbine.

The first Diabatic CAES plant was installed at Huntorf, Germany in 1978. The storage comprises two salt domes with a volume of 300 000 m^3 which operated at a maximum pressure of 100 bar. The plant takes eight hours to charge and can discharge at 290 MW for two hours. The second operational CAES system is the McIntosh plant in Alabama, USA

[4]The levelised cost of energy is the price of energy from a certain source that will allow that venture to break even over its lifetime.

and has a cavern of 500 000 m^3 which operates at 75 bar. The McIntosh plant can produce 110 MW for 26 hours and uses a recuperator to reuse heat from the gas turbine exhaust in order to reduce fuel consumption [39, 59].

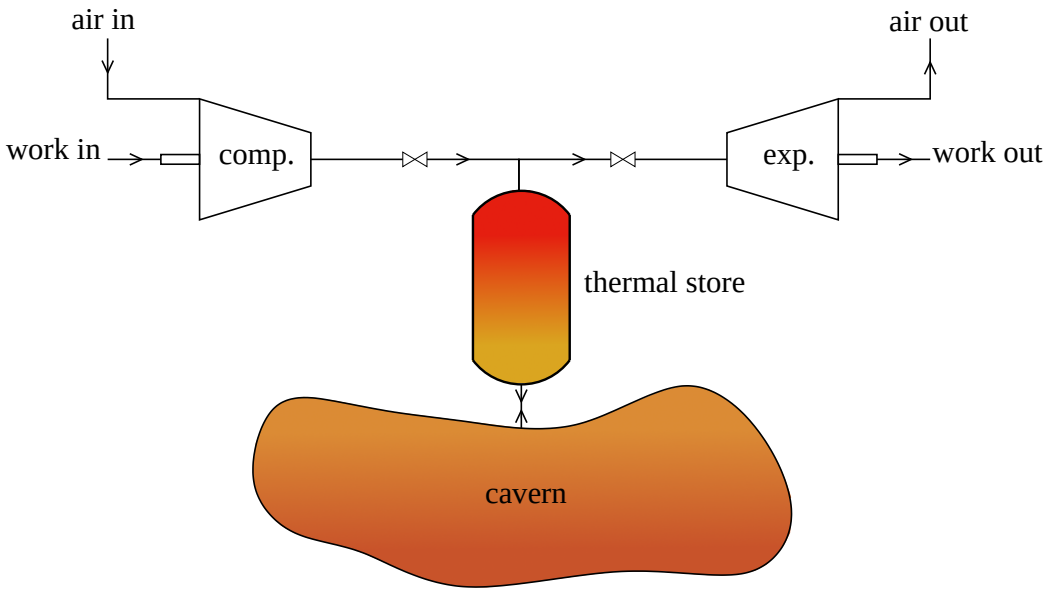

Figure 1.6: Schematic of an AA-CAES system

The available energy density for a constant volume container is given by [60]

$$\rho_E = p\left\{\ln\left(\frac{p}{p_0}\right) - \left(1 - \frac{p_0}{p}\right)\right\} \tag{1.3}$$

where p_0 is ambient pressure and p is the charged pressure which is typically 40–80 bar [39], leading to energy densities of around 7.5 kWh m^{-3}. However, in practice, CAES systems tend not to be discharged to p_0 and energy densities are therefore lower than this.

CAES round-trip efficiency can be improved with isothermal compression and expansion, and such systems are known as Isothermal CAES (I-CAES). Thermal energy is continuously removed during compression, and continuously added during expansion [61]. The gas is therefore kept at ambient temperature. Isothermal compression and expansion are difficult to achieve, although Grazzini and Milazzo [61] point out that some schemes have been proposed.

A more practicable approach involves a number of compression and expansion stages, be-

tween each of which heat can be removed or added. As the number of stages increases, the process gets closer to being isothermal, although with increasing cost. Such a system is known as Advanced Adiabatic Compressed Energy Storage (AA-CAES), illustrated in figure 1.6. Furthermore, AA-CAES avoids the need for fossil fuels by storing the thermal energy generated by compression and returning it to the gas before the expansion [62]. In a multi-stage AA-CAES system, it is conceivable that different storage materials could be used at each stage, depending on what is most appropriate. For instance, a packed bed could be used after the first stage of compression where pressures are reasonably low, leading to lower cost pressure vessels. At later stages, heat could be transferred to water or molten salts with a heat exchanger.

The main advantage of CAES systems is that they are based on well established technologies, have a low capital cost, and AA-CAES plants are predicted to achieve efficiencies of 60-80% [59]. The performance of these systems is mainly governed by the efficiency of the turbo-machinery [61], however, the thermal energy store may also have significant impact. For instance, Pickard et al. [63] suggests that low heat exchanger effectiveness could limit the quantity of energy stored in the thermal store, therefore leading to lower round-trip efficiencies (around 50%). Of course, these estimates depend on the exact type of thermal store employed and the manner in which heat is transferred to these stores (i.e. directly or via several heat exchangers which serve to intercool the compression process [61, 62]). CAES and AA-CAES have geographical limitations and are constrained by the location of suitable caverns. CAES is likely to have a lower environmental impact than PHES [64].

1.4.3 Thermal energy storage

Thermal energy storage has applications in cooling and refrigeration [39], solar power plants [65], solar cooking [66] and seasonal energy storage [67]. It can be divided into two categories: latent and sensible heat. Latent heat systems store energy by changing the phase of the material. This has several advantages, such as high energy densities and the ability to provide heat at a constant temperature. However, problems include a change in volume associated with the phase change, pinch point constraints and identifying suitable materials [68].

A simple example of a latent heat system is the conversion of water to ice for cooling purposes although there are a wide range of other materials (paraffins, waxes etc.) that can be used. Cryogens (that is, liquefied gases) such as air, nitrogen, or hydrogen are also used as thermal stores [69]. Cryogens have the advantage of high exergy densities (table 1.1) and Li et al. [69] notes that the second law of thermodynamics indicates that a cold reservoir is a "higher quality" energy source than a hot store. In addition, cryogens can be readily stored and transported.

Liquid-vapour transition PCMs require a large volume for the gas storage (unless air is used) and generally solid–liquid transitions are preferred [70]. There are a wide range of such materials, although finding a material that satisfies the necessary requirements (such as chemical and thermal stability, phase change at the appropriate temperature etc.) is challenging [70]. Moreover, PCMs can be expensive. There have been many attempts to improve the properties of phase change materials, such as increasing the thermal conductivity by encapsulating the material in graphite or some other material [70].

Sensible thermal energy

Sensible heat systems store energy by virtue of the change of temperature of a material[5]. One example from the UK in the 1970s is the storage heater: a domestic heating system where a material (brick or clay) was heated during the night on low-cost tariffs. This heat was then delivered through the day when it was required [71]. Sensible heat technologies are relatively cheap and simple to manufacture although they have a lower energy density than latent heat systems.

Water is a popular choice for sensible heat storage, due to its high specific heat capacity and density, chemical inertness and the fact it can be used as both a heat transfer fluid and a storage medium. Water is limited to a certain temperature range unless it is pressurised, therefore for high temperature operation solids (or liquids with a low vapour pressure) are generally preferred. Heat resistant oils are available that can operate in a broader range of temperatures without pressurisation than water. These oils tend to have lower specific heat capacities than water [72]. Other suitable liquids include molten salts, which have a

[5]Note that availability can be stored by cooling a material, since there is still the potential to extract work with the use of a heat engine.

wide range of operating temperatures (despite having high freezing points) and are non-toxic, non-flammable and are widely used in solar plants [70]. Rocks are a good alternative to liquids since they are cheap, readily available and can operate at high temperatures. However, the effect of high temperatures on the mechanical performance of solid stores should be considered; the compressive strength of concrete reduces by about 20% at 400°C, for example [73].

Comprehensive reviews of thermal energy storage materials and technologies can be found in [68, 70, 73]. Thermal energy storage systems may be comprised solely of the storage medium as is the case in some heating applications, or as part of a wider system. Systems which contain a thermal energy store include AA-CAES (as above) and PTES (below).

The available energy density for a thermal store operating between states 1 (charged) and 2 (discharged) is given by

$$\rho_E = \rho_s \left[h_1 - h_2 - T_0 (s_1 - s_2) \right] \tag{1.4}$$

Where ρ_s is the density of the storage material, h is its specific enthalpy, s is its specific entropy, and T_0 is the dead state (or environment) temperature. For a sensible thermal energy store consisting of a packed bed of solid pebbles this expression becomes

$$\rho_E = (1 - \varepsilon)\, \rho_s \left[\int_{T_1}^{T_2} c_s(T) dT - T_0 \int_{T_1}^{T_2} c_s(T) \frac{dT}{T} \right] \tag{1.5}$$

where c_s is the specific heat capacity which is a function of temperature, $(1 - \varepsilon)$ is the fraction of volume taken up by the storage, T_1 is the discharged temperature and T_2 is the charged temperature. The energy density of several materials is given in table 1.1.

A number of innovative design features for solid thermal stores have been suggested. Zanganeh et al. [2] developed a conical store to reduce the effect of thermal ratcheting. Daschner et al. [74] suggested that pressure losses could be reduced by using packed beds where the gas flowed radially rather than axially. Refs. [75–77] investigated incorporating phase change materials into packed beds. Ref. [77] found that PCMs increased the energy density, although the thermal front would de-stratify more rapidly. One disadvantage of solid stores is that the exit temperature changes as the thermal front approaches the end of the store. Generally this energy has to be rejected in heat exchangers, although it could be

used in waste heat applications or domestic heating systems. Utilising the waste heat in this way is complicated by the fact the outlet temperature varies as the thermal front progresses out of the reservoir. Placing PCMs at the end of the reservoirs was also seen to stabilise the outlet temperature.

Crandall and Thatcher [78] developed another design feature called segmentation as a way to maintain thermal stratification in packed beds for solar air heating systems. Segmented stores were being developed by Isentropic Ltd. for PTES systems [79] and are discussed in detail in section 3.3. White et al. [80] showed that by reducing pressure losses, segmentation allowed smaller particles to be used, thereby reducing thermal losses and leading to larger efficiencies. Furthermore, segmentation reduces conductive losses during the storage phase as described by McTigue and White [81].

Storage system	χ (%)	ρ_E (kWh m^{-3})	ρ_P (kW m^{-3})
Hot water[a]	-	10–100	-
Hot gravel[b]	-	130	-
Cold gravel[b]	-	60	-
Cryogen (nitrogen)[c]	-	170	-
Cryogen (hydrogen)[c]	-	236	-
PHES[d]	70–85	0.5–1.5	5000
CAES[d]	70–80	3–6	330[e]
CAES - Huntorf[f]	42	1.9	-
CAES - McIntosh[f]	54	5.7	-
PTES[g]	50–70	100	260

Table 1.1: Comparison of energy and power densities and efficiencies of several prominent energy storage systems and media.

[a] For hot water $\rho_E = \rho_{H_2O}\left[h_1 - h_2 - T_0(s_1 - s_2)\right]$ c.f. equation 1.5. Properties are calculated with CoolProps [82] for water between 15°C and the saturation temperature at 1 bar (lower bound) and 100 bar (upper bound).
[b] Gravel is taken to be magnetite with $\rho_s = 5175$ kg m^{-3}, $\varepsilon = 0.4$ and $\bar{c}_s = 800$ kJ/kgK. For hot gravel $T_1 = 500$°C and for cold gravel $T_1 = -150$°C.
[c] Values taken from Li et al. [69] for the thermal exergy density of the cryogen. This value does not include the *chemical* exergy which is due to the compositional difference between the chemical and the reference environment (air at standard conditions). Nitrogen's chemical exergy is very low whilst that of hydrogen is very large ($\sim$2300 kWh m^{-3}). It is not included as the cryogens are assumed to be part of a closed cycle.
[d] χ and ρ_E for PHES and CAES are estimates from Chen et al. [39] (energy densities show good agreement with equations 1.2 and 1.3) ρ_P are taken from White et al. [83].
[e] White et al. [83] uses the power density of a low specification gas turbine to provide an approximate comparison with other storage technologies
[f] This data is for operational diabatic CAES plants and data has been taken from [39, 59].
[g] PTES data is from equations 1.7 and 1.8 and the efficiency is from [84].
For comparison, the energy density of this thesis is roughly 3 kWh m^{-3}, based on a calorific value of 13.5 MJ kg^{-1} and a density of 800 kg m^{-3}

1.5 Pumped Thermal Energy Storage

This thesis is concerned primarily with a thermal energy storage system based on heat pumps/engines. A number of variants exist and perhaps the most widely used name is Pumped Heat Energy Storage (PHES) [5, 85, 86]. Other names include Electrothermal Energy Storage (ETES) [87], Thermo-electrical energy storage (TEES) [88], Compressed Heat Energy Storage (CHEST) [89] or Stockage d'Électricité par Pompage Thermique (SEPT) [90, 91]. Liquid Air Energy Storage (LAES) [69, 92–95] can also be included in this class of thermal energy storage technologies. Stamatiou noted that the abundance of names led to difficulties with identifying relevant work before introducing a further variant known as the Dual Energy Storage and Converter (DESC) [96]. Following the group based in Cambridge, and to avoid confusion with pumped hydro (PHES), this thesis uses the nomenclature Pumped Thermal Energy Storage (PTES) [60, 80, 81, 83, 84, 97].

The concept that unifies these variants is energy storage by means of 'reversible' heat pumps and engines. In this context, reversible means that the direction of gas flow through the heat pump is reversed to begin operation as a heat engine. PTES systems typically utilise two thermal stores (one hot and one cold) although this is not necessarily the case. The modern study of PTES systems has concentrated on two main variants, which are heat pumps/engines based on either the Joule-Brayton cycle or the Rankine cycle, as illustrated in figure 1.8. During charge the system operates as a heat pump, and uses electrical energy to move heat from a cooler region to a hotter region, thereby storing available energy, as in figure 1.7. The *T*–*s* diagrams are traversed anti-clockwise during charge, with compression occurring from 1–2 and expansion from 3–4. The flow reverses direction during discharge and operates as a heat engine to generate electricity.

PTES systems have comparable energy densities, power densities, and efficiencies to other large scale energy storage technologies as illustrated in table 1.1 on p. 21. It is also considered to have a number of advantages over these systems. For instance, unlike PHES or CAES, it is not constrained geographically. Unlike batteries, the energy and power capacities are decoupled and can be varied independently by varying the size of the thermal stores and the size of the compression–expansion system (or mass flow rate), respectively. Furthermore, PTES systems are likely to have a low impact on the environment as the storage

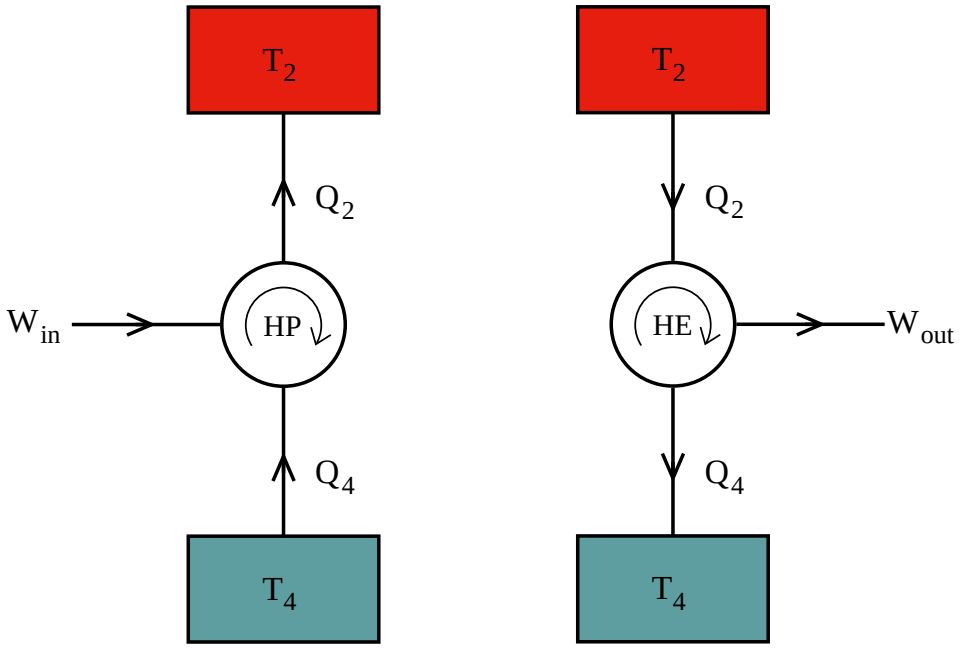

Figure 1.7: (Left) PTES during charge acting as a heat pump. (Right) PTES during discharge acting as a heat engine.

materials are relatively abundant, inert and non-toxic. Finally, it is anticipated that PTES systems will be relatively affordable, since the system could be constructed from off-the-shelf components. However, PTES requires four compression-expansion processes and is therefore sensitive to the performance of these devices.

This section proceeds by providing a historical background to the development of PTES-type systems. The basic theory of PTES systems is then developed with the results being generally applicable to all its variants. The modern development of these systems is then categorised into those based on the Joule-Brayton cycle and those based on the Rankine cycle and an overview of the academic and industrial work that has been undertaken is presented.

Historical background

The concept of using a heat pump/engine to store energy has been re-invented a number of times. Marguerre published perhaps the first example of a Rankine cycle based system in 1924 [98]. This system used a steam turbine and compressor, and stored energy in steam

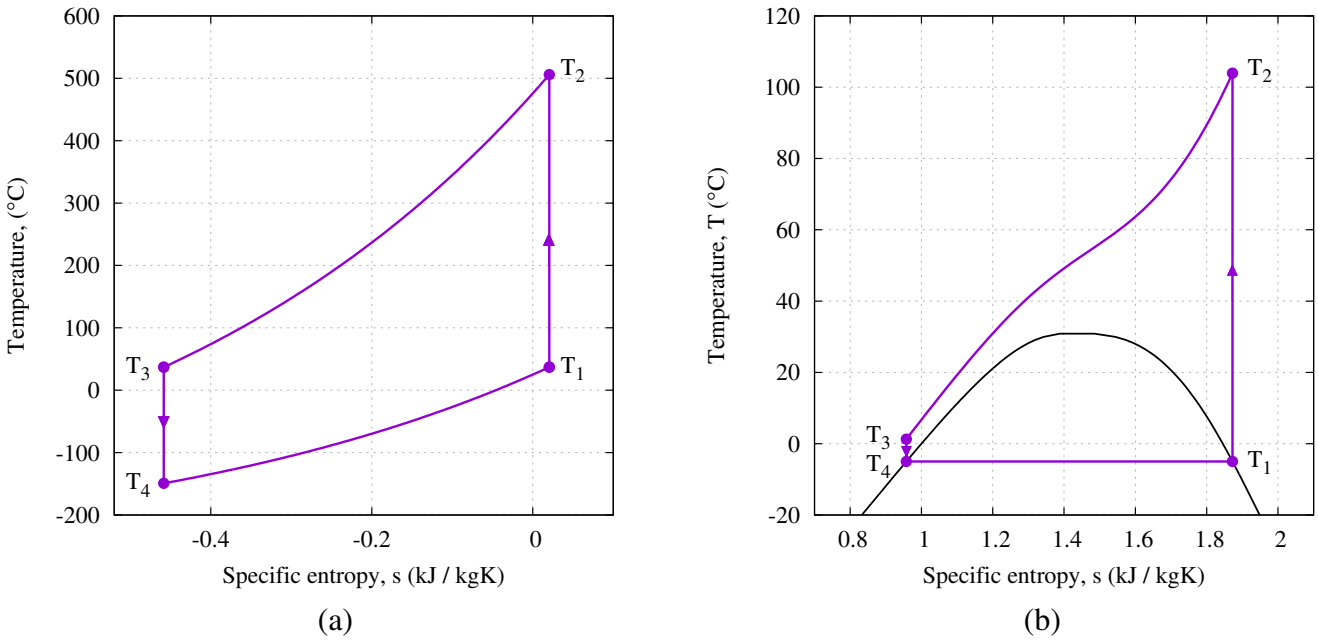

Figure 1.8: Ideal *T*–*s* diagram for PHES systems during charge for systems based on **(a)** the Joule-Brayton cycle and **(b)** a transcritical CO_2 Rankine cycle.

accumulators. During charge, low pressure steam from the low pressure accumulator was drawn into the compressor and its temperature increased. The high pressure steam was then condensed in the high pressure steam accumulator. In discharge, the high pressure steam was drawn from the high pressure accumulator and used to power the steam turbine, before being condensed in the low pressure accumulator [99]. Descriptions of Marguerre's system in English can be found in two patents filed in the 1930s [100, 101].

In 1972 Babcock [102] patented a system that utilised superheated steam drawn from a nuclear power plant. This steam was compressed and stored in an accumulator composed of ceramic refractory material at a temperature of around 450°C and pressure of 200 bar. In 1978 Cahn [103, 104] developed a similar system also based on the use of steam. He envisioned a system that was independent of the power plant and could use waste heat [104]. In Cahn's system energy was transferred to the hot and cold stores in heat exchangers. The cold store consisted of water that was cycled between approximately 40°C and 99°C. The hot store was described as a 'low vapour pressure thermal energy retention material', which Cahn specified to be some kind of hydrocarbon oil. When charged the hot store would have

a temperature of 230–320°C, and when discharged it would be 65–150°C. Each store therefore consisted of two tanks, with the storage media passing from one tank to the other via the heat exchanger. Cahn mentioned that this had the advantage over a solid store such as the Babcock design, since there are no thermal fronts and conductive losses would therefore not occur.

Another early heat pump system was described by Smith in 1977 [92]. During charge, air is compressed and subsequently cooled and liquefied. The energy extracted during cooling is stored in a regenerator or packed bed and the resulting cryogen is stored in a tank. Discharge of the system uses an open super-critical Rankine cycle; the liquid air is compressed and reheated in the regenerator before being expanded through a turbine to produce work. The resulting cool air is stored in a cool store which is used in the liquefaction process during charge. This system was the precursor of Liquid Air Energy Systems (LAES) described by Ameel et al. [94] and Morgan et al. [95] and developed by Highview Power [93]. While these systems are broadly similar, there are a number of differences, such as the liquefaction process (Linde cycle or Claude cycle), the compression–expansion processes (isothermal or adiabatic), the number of compression/expansion stages, and the details of how energy is recovered in the regenerator. The prototype recently developed by Highview Power achieved efficiencies of just 8%, but Morgan et al. [95] attributed this low value to the small scale of the plant and the fact that the regenerator was not used to its full extent (i.e. not all the energy produced during expansion was stored). Morgan identified that pinch point constraints in the Highview design restricted the maximum round-trip efficiency to 36%. However, it was noted that optimisation of the system (particularly the regenerator and expansion processes) should enable efficiencies above 50%. Therefore, LAES could achieve similar efficiencies to other PTES systems, and shares the advantages of using well established technologies, abundant storage media, and geographical flexibility. Unlike PTES systems, LAES is not a cyclic process and it consequently has fewer compressions and expansions than PTES.

Recent research has focussed on PTES systems based on Rankine cycles and Joule-Brayton cycles. Isentropic Ltd. began construction of a Joule-Brayton cycle based prototype in 2015, and ABB expressed interest in constructing a Rankine cycle based system, and a number of papers have been published on both systems. Before carrying out a literature review of this work, the basic thermodynamic theory of these PTES systems is set out.

1.5.1 Energy and power densities

Simple expressions for the energy and power density are obtained by considering a fully reversible PTES system, as represented by the *T–s* diagram in figure 1.8. Compression and expansion are isentropic and heat addition and rejection are isobaric.

The energy density is defined as the available energy stored per unit volume of storage medium. The stored availability is the difference between the stored enthalpies of the two reservoirs, such that

$$\rho_E = \frac{(H_2 - H_3) - (H_1 - H_4)}{V^H + V^C} \tag{1.6}$$

Where H is the enthalpy, V is the volume of the store, and superscripts H and C refer to the hot and cold store respectively. The above equation is written in such a way that it can be applied to systems that may have different storage materials for the hot and cold store, and includes enthalpy changes associated with phase change. A simplified expression was developed by White et al. [83] for a system with the same solid packing material in both reservoirs. The enthalpies therefore become $\Delta H = \rho_s V c_s (1-\varepsilon)\Delta T$, where ρ_s is the solid density, V is the volume of the reservoir, c_s is the specific heat capacity of the solid (which varies with the temperature of the store), and ε is the void fraction. By noting that charging the stores in the same amount of time introduces the constraint that $(\rho_s c_s V)^H = (\rho_s c_s V)^C$ (see [60] and equation 2.5 for the nominal charging time of a thermal reservoir) where superscripts H, C indicate the hot and cold store. The energy density then becomes

$$\rho_E = \rho_s(1-\varepsilon)\left(\frac{c_s^H c_s^C}{c_s^H + c_s^C}\right)[(T_2 - T_3) - (T_1 - T_4)] \tag{1.7}$$

A more accurate estimation could include the volume required for insulation and containment, or even the full footprint of the plant. However, as a first estimation the above expression is satisfactory and useful.

The power density is defined here as the power capacity divided by the volumetric flow rate of working fluid. Other definitions include normalising by the volume required by the compression and expansion devices or considering the maximum exergetic flux per unit

power capacity [84]. However, the above definition again leads to a simple expression:

$$\rho_P = \rho_{g,1} c_p \left[(T_2 - T_1) - (T_3 - T_4) \right] \tag{1.8}$$

where $\rho_{g,1}$ is the fluid density at point 1 on figure 1.8, and c_p is the specific isobaric heat capacity for the working fluid. White et al. [83] further manipulated equations 1.7 and 1.8 to reveal how these factors depend on PTES design for Joule–Brayton type systems. By introducing the compressor/expander temperature ratio $\tau = T_2/T_1 = T_3/T_4$ and the work ratio $R = T_1/T_4 = T_2/T_3$ which is approximately the ratio of compression work to expansion work during charge, the above equations become

$$\rho_E = 1/2 \rho_s c_s T_1 (\tau - 1) \left(1 - \frac{1}{R} \right) \tag{1.9}$$

$$\rho_P = \frac{\gamma}{\gamma - 1} p_1 (\tau - 1) \left(1 - \frac{1}{R} \right) \tag{1.10}$$

where T_1 and p_1 are the temperature and pressure at point 1 and γ is the ratio of specific heats. These expressions indicate that the energy and power densities may be increased by using larger temperature ratios τ, and therefore larger pressure ratios. Increasing the work ratio R leads to larger energy and power densities, and this can be achieved by increasing T_1 or decreasing T_3. Furthermore, the power density is increased by raising the system pressure p_1. White et al. [83] additionally point out the importance of the isentropic index on the power density, noting that $\gamma/(\gamma - 1)$ takes a value of 5/2 for monatomic gases and 7/2 for diatomic gases.

Table 1.1 provides a comparison of these ideal energy and power densities with other established energy storage systems, and indicates that PTES has competitive values.

1.5.2 Round-trip efficiency

The round-trip efficiency of energy storage systems is defined as the ratio of electricity output during discharge to electricity input during charge. For PTES systems a thermodynamic round-trip efficiency is used, which neglects the efficiency of the electrical machines. This metric is defined as the ratio of net work output during discharge to the net work input

during charge, such that

$$\chi = \frac{\text{Net work output}}{\text{Net work input}} = \frac{W_{\text{dis}}^{\text{net}}}{W_{\text{chg}}^{\text{net}}} \tag{1.11}$$

For an ideal PTES cycle with reversible compression and expansion stages evaluation of the round-trip efficiency is trivial and is given by the COP of a heat pump multiplied by the Carnot efficiency of a heat engine.

$$\chi = \left(\frac{1}{1-\frac{T_4}{T_2}}\right) \times \left(1-\frac{T_4}{T_2}\right) = 1 \tag{1.12}$$

Where T_2 is the maximum temperature of the hot store, and T_4 is the minimum temperature in the cold store. Thus, the round-trip efficiency of PTES is limited only by irreversibilities within the cycle. Several approximations to the efficiency have emerged in the literature, and these take the form of either classical cycle calculations [83, 90] or endo-reversible thermodynamics [85, 87].

The endo-reversible approach assumes that irreversibilities are the result of heat transfer between the thermal reservoirs and the thermodynamic cycles (i.e. heat pump or heat engine) that interact with them. By assuming that a finite temperature difference ΔT exists between the thermal reservoirs and the cycles, Mercangöz et al. [87] developed the following expression:

$$\chi = \left(\frac{T_2 - T_4 - 2\Delta T}{T_2 - \Delta T}\right) \times \left(\frac{T_2 + \Delta T}{T_2 - T_4 + 2\Delta T}\right) \tag{1.13}$$

Thess [85] used a similar methodology to develop an alternative expression, which he then further manipulated to remove the variable ΔT. Thess's expression has been widely cited, however Guo et al. [105] noted that a mistake had been made, and found the correct expression to be:

$$\chi = \frac{(T_2/T_4)^{1/2} - 1/2}{(T_2/T_4)^{1/2} + 1/2} \tag{1.14}$$

(This expression has the same form as Thess's equation, which slightly over-predicts the efficiency). This analysis involved maximising the power output of the heat engine which is an unrealistic assumption as PTES is unlikely to be operated in this way. The heat pump is not treated in an equivalent way since the heat pump power cannot be optimised. Furthermore, as shown on figure 1.9(a), this expression predicts an efficiency of 33% when

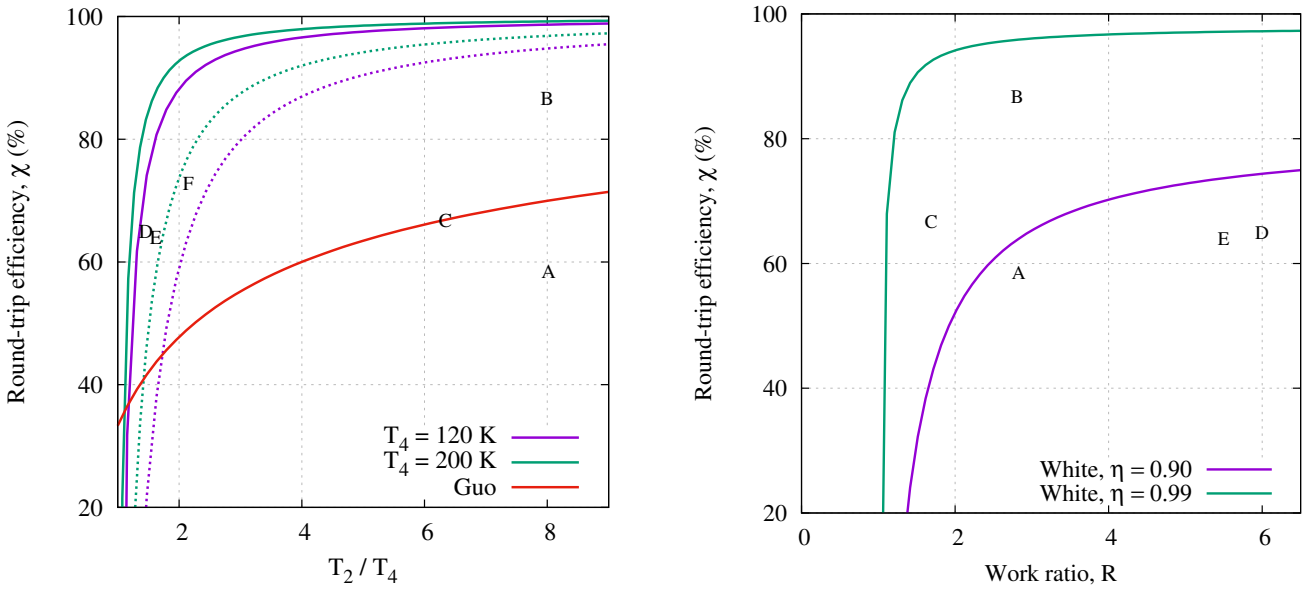

Figure 1.9: Variation in PTES round-trip efficiency with operating temperatures and work ratio. Data points are from numerical evaluations of PTES systems: A. McTigue et al. [84] with $\eta = 0.90$; B. McTigue et al. [84] with $\eta = 0.99$; C. Desrues et al. [90]; D. Mercangöz et al. [87]; E. Morandin et al. [88]; F. Steinmann [89]. **(a)** PTES round-trip efficiency calculated using endoreversible thermodynamics. Purple and green lines are calculated using equation 1.13. Solid lines have $\Delta T = 5$ K, dotted lines have $\Delta T = 20$ K. Guo's expression is from equation 1.14. **(b)** PTES round-trip efficiency calculated using classical cycle analysis from equation 1.15.

$T_2/T_4 = 1$. At such a condition the power input and output are zero, and any irreversibilities should lead to a negative efficiency. As a result, equation 1.14 is not applicable at $T_2/T_4 = 1$, and may in fact be unreliable at a larger range of values.

Mercangöz's and Guo's expressions are plotted in figure 1.9(a) against T_2/T_4. It is clear that the efficiency is maximised by increasing the hot reservoir storage temperature, and decreasing the cold store storage temperature. Equation 1.13 implies that the finite temperature difference should be minimised, which could be achieved by increasing the area for heat transfer, or reducing the rate of heat transfer. Equation 1.13 allows the impact of the low temperature store at a fixed T_2/T_4 to be studied. Figure 1.9(a) illustrates that increasing T_4 at fixed T_2/T_4 leads to higher efficiencies.

Classical cycle analysis allows the irreversibility of the compression and expansion devices

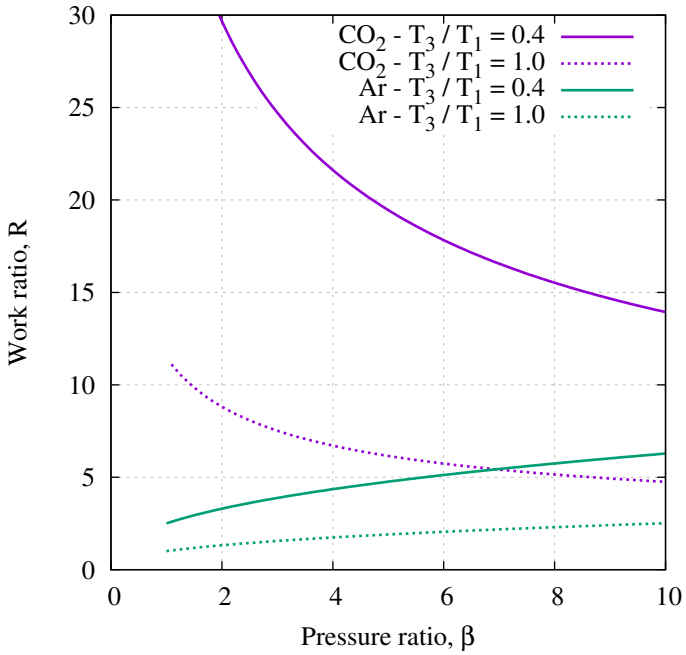

Figure 1.10: Variation of work ratio R with pressure ratio and T_3/T_1. Results are shown for Rankine cycles with carbon dioxide as the working fluid, and for Joule-Brayton cycles with argon as the working fluid. Working fluid data taken from CoolProps [82].

to be considered and includes the influence of the parameters T_1 and T_3. White et al. [83] developed an approximate expression for the efficiency based on the irreversibility in the compressors and expanders and assuming ideal heat transfer in the thermal reservoirs. By scaling the ideal compression work by $1/\eta_s$ and the ideal expansion work by η_s, where η_s is the isentropic efficiency, they obtained

$$\chi \approx \frac{R\eta_s^2 - 1}{R - \eta_s^2} \tag{1.15}$$

The work ratio R was introduced above as the ratio of compression work to expansion work during charge. This expression was also independently developed by Kim et al. [106] shortly after. As depicted in figure 1.9(b), equation 1.15 implies that the efficiency is a monotonically increasing function of R; a larger work ratio ensures that losses will have a less significant effect on the net work of the system. For Joule-Brayton cycles, the work ratio is given by $R = \tau T_1/T_3$ and can be increased by a) increasing the temperature ratio (and hence pressure ratio) b) increasing T_1 c) decreasing T_3 as shown in figure 1.10. For

Rankine cycle based PTES systems, equation 1.15 is also true, although the expression for R is no longer so simple due to the phase change between point 4 and 1. In this case, the work ratio is given by

$$R = \frac{c_p T_1}{p_4/\rho_4} \frac{\beta^{\frac{\gamma-1}{\gamma}} - 1}{\beta - 1} \tag{1.16}$$

where c_p is the isobaric specific heat capacity of the gas, p_4 and ρ_4 are the liquid pressure and density at point 4, and β is the pressure ratio. It is less clear how to maximise the work ratio from this expression, and instead some results are shown on figure 1.10 with carbon dioxide as the working fluid. For these calculations, the pressure at point 4 is fixed at the saturation pressure at -5°C. The pressure ratio is varied and the properties are calculated around the Rankine cycle (assuming isentropic compression/expansion) from which the work ratio may be evaluated. A trade-off now occurs in Rankine cycles: reducing the pressure ratio increases the work ratio, albeit at the expense of the energy and power density. In addition, the results show that the ratio T_3/T_1 should be minimised, although this may not be practicable: Rankine based cycles typically use ice as the cold storage medium, and to match the temperature profiles of the ice and working fluid T_1 and T_3 should ideally be almost equal. However, it is conceivable that the cold storage could be made up of more than one thermal reservoir. For instance, if T_1 is greater than the saturation temperature at that pressure (denoted say by T_1'), then a sensible heat reservoir could store the energy between T_1 and T_1', while ice storage operates between points $1'$ and 3.

PTES systems require two compressions, and two expansions for one complete charge-discharge cycle. Consequently, the isentropic efficiency has a significant impact on the round-trip efficiency as shown in figure 1.9(b). White et al. developed a more detailed analysis based on the polytropic efficiency and found that the round-trip efficiency was most sensitive to the polytropic efficiency at low temperature ratios τ (and therefore pressure ratios, β) and that reducing T_3/T_1 reduced the sensitivity [83]. Numerical results by McTigue et al. [84] indicated that for the Isentropic Ltd. design with a value of $\tau = 2.5$ the efficiency would drop around 2 percentage points for every percentage drop in polytropic efficiency.

While the equations above are simplifications of the true behaviour of PTES systems, together these two approaches provide a useful insight and are a first step in design optimisation. More accurate estimations of the round-trip efficiency, energy density and power

density require numerical simulation which is discussed in the following sections.

1.5.3 The Joule-Brayton cycle PTES

In this scheme, the charging phase consists of heat pumping by a reverse Joule-Brayton cycle which establishes a temperature difference between two thermal stores. Energy is recovered by reversing the cycle into heat engine mode (forward Joule-Brayton cycle), and returning heat from the hot to the cold store. Two independent patents seem to have emerged almost simultaneously in 2008–2009 for similar schemes which are referred to here as the Saipem approach [107] and the Isentropic approach [108], after the companies that filed the patents. A further scheme was patented much earlier in 1979 by Weissenbach of Messerschmitt-Bölkow-Blohm (MBB) [109]. *T–s* diagrams of the *ideal* Isentropic and Saipem schemes are shown in figure 1.11. These variants will be described briefly before discussing the Joule-Brayton PTES system in more detail.

MBB system

Weissenbach's system is an open cycle using atmospheric air as the working fluid. As such the 'cold' store consists of a regenerator at atmospheric temperature and pressure. The hot store was specified to be around 800–900°C, with thermal energy stored in ceramic balls contained in steel tubes. Little further information is available to the knowledge of the author, so it is unclear what temperatures T_2 and T_3 were and therefore what the pressure ratio was. Weissenbach anticipated efficiencies in the region of 65–75%.

Saipem system

The Saipem scheme was the first to suggest using argon as the working fluid, due to its high ratio of heat capacities. The scheme therefore uses a closed cycle. The thermal stores consisted of porous refractory material, or clay with a high content of magnesia, alumina and lime. This material was formed into bricks and perforated with cylindrical holes for the working fluid to pass through. Compression and expansion was undertaken with turbomachinery meaning that two compressors and two expanders are required (one for charging

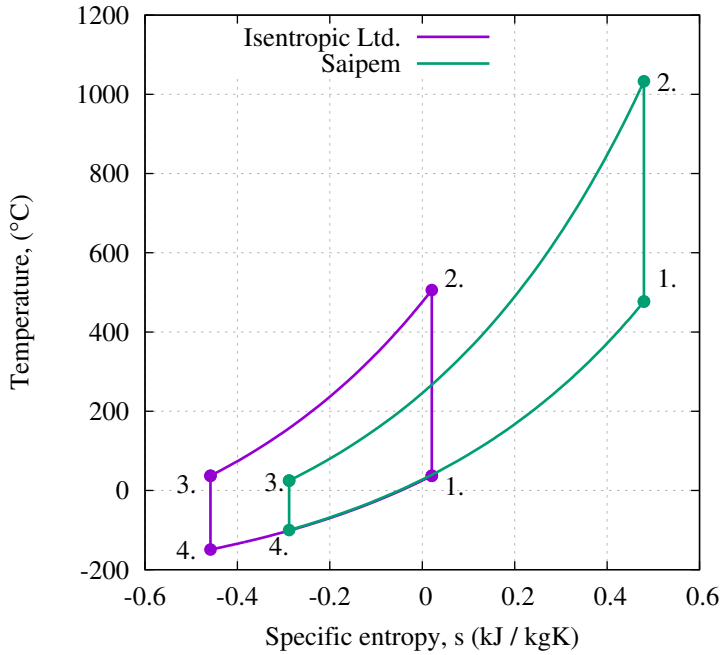

Figure 1.11: *T–s* diagrams for Joule-Brayton cycle based PHES systems proposed by Isentropic Ltd. and SAIPEM

and one for discharging).

The *T–s* diagram for a typical Saipem scheme is shown in figure 1.11, and further details are given in table 1.2. The original design uses a low pressure ratio of around 4, but achieves a high work ratio by increasing the value of T_1 to around 480°C and fixing T_3 to ambient temperature. The low pressure ratio should reduce the cost of the system, although the use of four turbo-machines would be expensive.

The Saipem scheme has been modelled in the literature by Desrues et al. [90, 91] and Ni and Caram [86]. Desrues et al. [91] modelled the heat transfer processes within the thermal stores with a finite volume scheme, and included axial conductivity and pressure losses. The turbomachines were modelled using polytropic efficiencies of around 90%, although off-design behaviour was also modelled by developing characteristics from commercial data as described in Desrues' PhD thesis [91]. On the other hand, Ni and Caram modelled the turbomachines with polytropic efficiencies. For the thermal reservoirs, they used a technique known as exponential matrix solutions to solve the governing thermal reservoir energy equations (which are known as the Schumann equations and are described in

section 2.3). The authors suggested that this has the advantage of quickly obtaining the converged steady state solution. However, numerical experimentation has indicated that this scheme is slower than the numerical schemes that are described in section 2.4. In addition, the variation of physical properties with temperature cannot be included and Ni's analysis did not include conduction or heat leakage as it was based on the Schumann model.

Isentropic system

The Isentropic system[6] also utilises a closed cycle with argon as the working fluid. Compression and expansion is achieved with reciprocating piston engines. By changing the valve timings, a reciprocating compressor can also work as an expander. Consequently, only two devices are required: one on the 'hot' side between points 1 and 2 to carry out compression during charge, and expansion during discharge; and another on the 'cold' side to expand during charging and compress during discharge. Isentropic efficiencies of reciprocating devices may be in the range of 75-85% [110], but much of the loss is due to valve pressure losses. By developing bespoke reciprocating devices with a new valve system [5], Isentropic Ltd. aimed to reduce these losses significantly and (perhaps optimistically) quoted isentropic efficiencies of 95-99%. Modelling of reciprocating devices is discussed in more detail in section 4.2.

The original patent suggested that the thermal stores would consist of particles or fibres randomly packed to allow gas to flow through. These particles would be metallic or possibly a mineral or ceramic. Subsequent work [97] suggested that iron oxides such as magnetite (Fe_3O_4) or hematite (Fe_2O_3) would be suitable materials, as they have reasonably high specific heat capacities, a wide temperature range of operation, and are relatively cheap and abundant. Investigations typically assume these particles are uniformly sized and spherical, although this is unlikely to be the case in practise.

The *T*–*s* diagram for a typical Isentropic scheme is shown in figure 1.11, and further details are given in table 1.2. The original design uses a pressure ratio of around 12, and has $T_3/T_1 \approx 1$ meaning that the Isentropic scheme has a lower work ratio than the Saipem scheme. Achieving high round-trip efficiencies therefore depends heavily upon developing

[6]Note that Isentropic is capitalised to emphasise this scheme is named after the company Isentropic Ltd., and does not imply that any process in the system is isentropic.

reciprocating devices with high isentropic efficiencies.

The majority of the literature on the Isentropic scheme originated at Cambridge University, and has focussed predominantly on the design of the packed-bed thermal reservoirs and simple cycle modelling. These papers include a semi-analytical packed bed model based on Schumann's equations (therefore neglecting conduction and heat leakage) and defined a number of exergetic loss coefficients and the effect of certain design parameters upon them [60]. The impact of the variation of specific heat capacity with temperature was investigated in detail [97]. An early paper by White et al. [83] that focussed on the Isentropic scheme developed equation 1.15 and explored the sensitivity of the efficiency to various uncertain parameters. This paper suggested the importance of the reciprocating device isentropic efficiency as well as the irreversible heat transfer that occurs in these devices. This analysis was extended by McTigue et al. [84] who integrated the packed bed model with compression-expansion devices that were modelled by polytropic efficiencies, pressure loss factors and heat leakage factors. They undertook a parametric study of the main parameters and used a genetic algorithm to optimise the design. The optimisation converged on solutions similar to the Isentropic design, and some results are shown in table 1.2. The top temperature T_2 was constrained to be less than 600°C by material limits. If this constraint is relaxed, then it is possible that the optimiser would have converged on Saipem-like designs. Again, this study highlighted the importance of the compression-expansion efficiency. Ref. [84] also described the importance of the charging frequency or utilisation (the duration of the charging/discharging phases) in controlling the trade-off between efficiency and energy density: high utilisations leads to high energy densities but low efficiencies also observed by Ni and Caram [86]. It was also noted that the optimal discharging pressure ratio was slightly less than the charging pressure ratio.

More recent papers have again focussed on the thermal reservoir model, which was updated to include axial conduction and heat leakage, behaviour during storage phases, and to model segmentation of the packed beds [80, 81]. In these works, the packed beds were considered in isolation, but were sized for bulk electricity storage. It was found that segmentation (i.e., dividing the bed into layers) could improve performance in both hot and cold stores, although only the cold store benefit was significant enough to suggest that it would be a worthwhile investment. These results are also applicable to other thermal energy storage systems which utilise hot or cold packed beds.

	Saipem [107]	Isentropic [5]	Desrues [90]	McTigue 1. [84]	McTigue 2. [84]
Polytropic efficiency	0.90	0.90	0.90	0.90	0.99
Pressure ratio	2–4	12.0	4.6	10.9	7.6
T_1 (°C)	400–1000	45	477	35	117
T_2 (°C)	1000–1500	500	995	600	598
T_3 (°C)	10–50	45	25	35	37
T_4 (°C)	-80 – -20	-166	-73	-164	-134
Work ratio, R	$\sim$4	2.4	4.2	2.8	2.8
Efficiency*, χ (%)	70	61	71	64	96
Efficiency$^+$, χ (%)	$>$60	-	67	59	87
Energy density, ρ_E (MJ m^{-3})	-	-	100	65	94

Table 1.2: Operating conditions for Joule-Brayton based PHES systems suggested by patents and literature. * refers to efficiency calculated with equation 1.15, and $^+$ refers to the efficiency calculated in the source. McTigue 1. and 2. refer to optimised results where the points with highest efficiency have been selected for the given polytropic efficiency.

1.5.4 The Rankine cycle based PTES

The first PTES systems that were described by Maguerre and Cahn were based on Rankine cycles. Modern research has taken place predominantly in Switzerland with input from the company ABB.

Mercangöz et al. [87] described a transcritical CO_2 cycle which used water as the hot store and ice slurry as the cold store. Most of the subsequent research has developed this type of cycle. Mercangöz et al. emphasised the importance of matching the temperatures of the cycle working fluid and the storage fluid. For instance, the water storage is a sensible heat store, thus its temperature increases as energy is transferred to it. Irreversibilities due to heat transfer can be minimised by reducing the temperature difference between the working fluid and the storage material. If the working fluid changes phase (condenses) it would do so at a constant temperature, leading to large temperature differences and, consequently, exergetic losses. During charge, the CO_2 is therefore compressed to a super-critical state, before following a trans-critical path as it releases its energy - i.e. the fluid remains above the critical point as illustrated on figure 1.8(b). The temperatures of the working fluid and the storage media are therefore 'matched' for the high pressure part of

the cycle. However, as figure 1.8(b) shows, the CO_2 must undergo a phase change in the low pressure part of the cycle. Matching the temperatures of the working fluid and storage therefore requires a storage medium that also undergoes a phase change, and ice slurry is the suggested medium.

The requirement to match temperatures therefore places constraints upon the Rankine-cycle system that do not exist for the Joule–Brayton system. Materials with suitable thermodynamic properties are required. Matching the CO_2 and ice slurry temperatures requires the CO_2 to be at high pressure: around 32 bar on the low pressure side and 140 bar on the high pressure side. The high pressures add to the cost, but the cycle benefits from not needing to pressurise the thermal stores. In addition, hot water has a high heat capacity but a narrow temperature range of operation unless it is pressurised. Mercangöz and subsequent researchers therefore employ several hot water tanks that operate over different temperature ranges. In addition, there is the possibility of using molten salts or heat transfer oils for the appropriate temperature ranges.

The use of liquid pumps or expanders means that the Rankine-cycle system can achieve higher work ratios than the Joule-Brayton cycle based system. Mercangöz et al. [87] optimised a 50 MW system and achieved a work ratio of roughly 6 and an efficiency of 65%, as shown in figure 1.9. Morandin et al. [111] developed the work by Mercangöz et al. and described a modelling method based on pinch analysis. An optimisation study gave an efficiency of 60% at a work ratio of 5. Morandin also undertook a more detailed thermo-economic optimisation of the Rankine-cycle system [88]. The study optimised the system topology (i.e. the number of storage tanks and their layout). Morandin also investigated intercooling between the discharging expanders in this study.

Another Rankine-cycle system developed by Steinmann [89] is known as CHEST: Compressed Heat Energy Storage. The basic CHEST configuration system uses steam as the working fluid, and the atmosphere as the cold store. The hot store comprises both sensible heat and latent storage, which enables the temperature of the storage media to match the temperature of the condensing steam. Steinmann also considered “cascaded cycles”: a low pressure ammonia cycle is used as it has lower volumetric flow rates compared to water. The hot store of the ammonia cycle then acts as the cold reservoir for the high pressure steam cycle. In a simplified analysis, Steinmann estimated the round-trip efficiency to be

72.8%. The analysis did not include pressure losses or heat leakage losses in any of the compressors, expanders, pipes or storage systems. Analysis in section 4.4.1 indicates that inclusion of these factors (at least in the compression-expansion system) may be expected to cause a further loss in efficiency of several percentage points.

Figure 1.9 compares the results of more detailed studies on PTES systems against the simplified expressions for efficiency that were derived in section 1.5.2. A direct comparison between different PTES configurations is challenging as authors typically make different assumptions in the modelling process.

1.6 Aims of the project

This thesis focusses on the Joule-Brayton cycle variant of Pumped Thermal Energy Storage (PTES). The ultimate objective of the project is to develop a detailed thermo-economic model of the full system, and to use optimisation techniques to determine optimum designs. Ideally these methods should be combined with other approaches such as experiments and computational fluid dynamics in order to validate the results. However, these technologies are at an early stage of development. Consequently, thermodynamic models are a useful tool which can be used to quickly investigate the potential performance of energy systems. The models will help to develop an understanding of the system behaviour, generate design guidelines, and also suggest promising designs or areas for further work.

The bulk of the thesis concentrates on thermodynamic modelling of the system and its subcomponents. Of particular interest are the packed-bed thermal reservoirs to which thermal energy is transferred and stored. A number of heat transfer processes occur within the packed beds. In chapter 2 the packed bed theory is discussed with the aim of characterising the most significant phenomena, and developing a robust thermodynamic model. Having developed a thermodynamic model, individual processes that cause a reduction in efficiency (or 'loss generating mechanisms') are quantified.

The objective of chapter 3 is to take the theory developed in chapter 2 and improve the understanding of the behaviour and performance of packed-bed thermal reservoirs for bulk electricity storage. This is achieved by undertaking parametric studies of a number of de-

sign variables to uncover their influence on the various loss generating mechanisms. These studies inform design, and two innovative design features are investigated. The first is segmentation of the packed beds, and the second is radial-flow packed beds. A rigorous investigation of these design features is undertaken using the theoretical framework developed in chapter 2 and in such a way that the investigations are consistent and allow comparison between different features.

The aim of chapter 4 is to develop a thermodynamic model of the PTES system. This involves developing models of the compression and expansion system and the heat exchangers, and integrating them with the thermal reservoir model. Like the preceding chapters, a framework is established that allows the various processes that reduce the efficiency to be accounted for. Having developed a model of the PTES system, its behaviour is investigated with parametric studies. By doing so, and by considering alternative modes of operation, an understanding of the system can be developed that is necessary for design optimisation.

Realistically, the system design cannot be optimised by considering only technical factors. The 'best' design may not be the most efficient, but may be the one that is most affordable or most flexible. Holistic design optimisation therefore requires the consideration of several, possibly conflicting objectives. Since externalities can be uncertain or difficult to quantify chapter 5 begins by developing a simplified economic model of the PTES system. The aim is to keep the model relatively simple whilst capturing the key parameters that impact on the cost of the system.

The objective of chapter 5 is to find optimum system designs for thermal energy storage. Optimisation theory is discussed and an appropriate multi-objective optimisation algorithm is described. The optimisation scheme is applied with the aim of finding a range of optimal solutions: some designs will have better thermodynamic performance, some will have better economic performance, and others will be a compromise between these objectives. Optimisation of hot and cold packed-bed thermal reservoirs is first undertaken. This is carried out on a range of different scenarios with the aim of testing some of the designs developed in earlier chapters. The overall PTES system is then optimised, and several alternative configurations are tested. Conclusions and a discussion of areas for future research are given in chapter 6.

Contribution of the author

At the beginning of this project, a thermal reservoir model had already been developed by Alex White of Cambridge University. The author extended this model to include other heat transfer processes, such as heat leakage and conduction, and to model other behaviour, such as that of segmented stores. The thermal reservoir codes were then integrated with models of compressors, expanders and heat exchangers and thereby developed a model of PTES. The author undertook a number of investigations using these models, such as parametric studies and thermo-economic optimisation. For the latter, the author programmed a multi-objective optimisation algorithm, and developed simple cost models of the storage systems. Much of the work presented in this thesis is either an extension of earlier published work [84, 97], or work that is currently being published [80, 81], and has also contributed to a number of conference proceedings, see page xv.

Chapter 2

Modelling of packed-bed thermal reservoirs

2.1 Introduction

Packed-bed thermal reservoirs are an integral component of the Pumped Thermal Energy Storage (PTES) system described in chapter 1, and are also used in other storage systems. Investigating the performance of PTES requires accurate modelling of the heat transfer processes in the packed beds. This chapter begins with a discussion of the assumptions that underlie the thermodynamic theory of packed-bed thermal reservoirs. These assumptions lead to a set of governing energy equations known as the Schumann model which are described in section 2.3.

A numerical scheme based on that developed by White et al. [80] is used to solve the governing equations. As part of this project, several modifications and extensions have been made, such as including axial conduction, modelling of segmented stores, and integrating the numerical scheme into a model of PTES. For comparison, the equations are also solved with a widely used, but less efficient, numerical scheme: the predictor-corrector (or Adams-Bashforth-Moulton) method. These schemes are validated against the existing analytical solution to the Schumann equations.

Capturing the packed bed characteristics allows assessment and comparison of packed bed designs and is therefore a key requirement of the thermodynamic model. In section 2.5 a Second Law approach to packed bed analysis is presented and various entropy generating processes are discussed in detail. These loss-generating mechanisms are quantified by so-called 'loss coefficients' as defined by White [60]. Solid and gas properties that affect the loss coefficients are discussed. By simplifying the expressions for the loss coefficients, the influence of the packed bed design on performance is revealed. Together this approach provides a basis for the more detailed analysis that is presented in chapter 3

2.2 Description of packed bed reservoirs

Packed-bed thermal reservoirs typically contain a solid storage material composed of spheres, irregularly shaped pebbles or gravel, or some other internal structure (such as a concrete matrix) through which the heat transfer fluid passes. The packing is encased in one or more

layers of insulation and a steel containment vessel which may be pressurised (as is the case for the hot store in PTES). PTES pressure vessels are cylindrical (with closed ends), but some packed beds that have been investigated are conical [2] or other shapes.

During charge, the heat transfer fluid (which is argon in PTES) enters the packed bed at temperature T_1 and, having transferred its energy to the packing material, exits the packed bed at temperature T_2. The flow reverses direction during discharge. A schematic diagram for a hot store is shown in figure 2.1. The packing material has a length L and a diameter D, although the store itself will be larger than this due to the insulation and steel containment. The particles have a diameter of d_p and occupy a fraction of the store equal to $(1 - \varepsilon)V$, where ε is known as the void fraction.

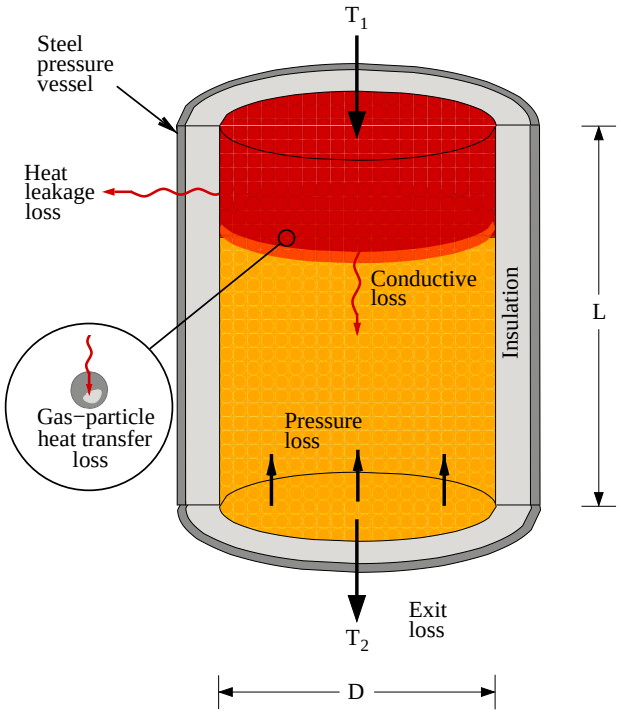

Figure 2.1: Schematic layout of a packed bed. The hot thermal reservoir is orientated vertically during charge. Gas enters at T_1 and exits at T_2. Several entropy generating mechanisms are illustrated and are discussed in section 2.5.

2.3 Heat transfer in packed bed reservoirs

Main concepts and thermal fronts

A number of different models exist for describing heat transfer in packed beds and are discussed comprehensively in [112, 113]. Figure 2.2 illustrates the main heat transfer processes that occur in an infinitesimal control volume for a hot reservoir, in which it is assumed that the flow is one-dimensional, and that the particles have a uniform temperature. Gas flows from top to bottom to avoid buoyancy issues. Convective heat transfer between the gas and solid results in a temperature change across the packed bed. This region is known as the 'thermal front' or 'thermal wave'.

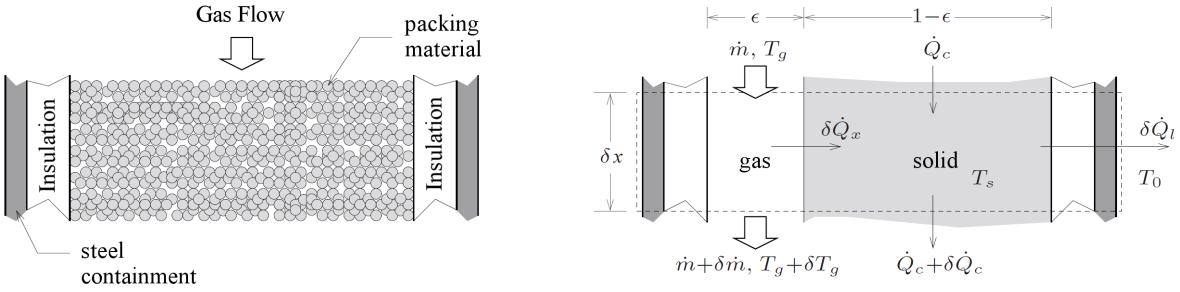

(a) Basic structure (b) Equivalent control volume

Figure 2.2: Schematic view of the packed bed structure and the equivalent control volume which displays heat transfer processes: where Q_x, Q_l and Q_c are gas-solid heat transfer, heat leakage through the walls and conduction along the bed, respectively.

The velocity of the thermal front V_f can be found by assuming the front remains perfectly abrupt (i.e. a step change from T_1 to T_2) as shown in figure 2.3. Applying the first law to the thermal front yields

$$\frac{dE_s}{dt} = \dot{m}c_p(T_1 - T_2) \tag{2.1}$$

$$(1-\varepsilon)\rho_s\bar{c}_s A(T_1 - T_2)\frac{dx}{dt} = \rho_g u_s c_p A(T_1 - T_2) \tag{2.2}$$

Where $u_s = \dot{m}/\rho_g A$ is the superficial (or open tube) gas velocity, c_p is the gas specific heat capacity, $\bar{c}_s$ is the average solid heat capacity and ρ_s and ρ_g are the solid and gas densities.

The thermal front velocity $V_f = dx/dt$ is therefore

$$V_f = \frac{\rho_g c_p}{(1-\varepsilon)\rho_s \bar{c}_s} u_s \tag{2.3}$$

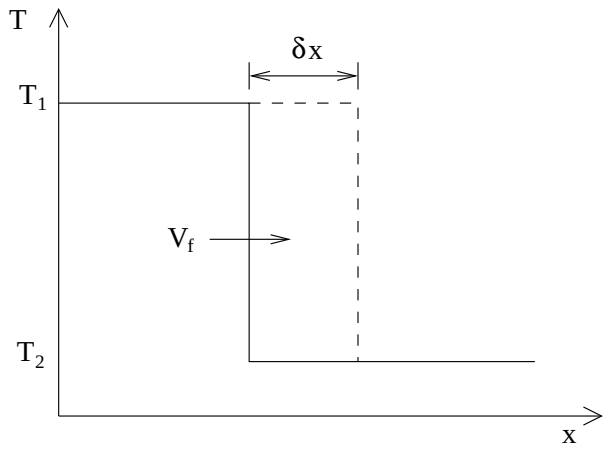

Figure 2.3: Schematic of an ideal thermal front between temperatures T_1 and T_2 travelling at velocity V_f (see equation 2.3)

The solid heat capacity c_s is a function of temperature (see figure 2.10 on page 61), and thereby influences the shape of the thermal front as cold regions travel more rapidly that hot regions. The nominal thermal front velocity in equation 2.3 is defined in terms of the average solid heat capacity over the temperature range of interest $\bar{c}_s$ which is given by

$$\bar{c}_s = \frac{E_{s,1} - E_{s,2}}{T_1 - T_2} \tag{2.4}$$

where $E_s = \int_{T_{\text{ref}}}^{T} c_s dT + E_{\text{ref}}$ is the energy of the solid. An abrupt thermal front would require there to be no thermal resistance between the gas and solid, so in practice, the front tends to vary between T_1 and T_2 with a finite gradient that changes. However, V_f can still be interpreted as the *nominal* speed of the front, and the nominal charging time is then given by

$$t_N = \frac{L}{V_f} = \frac{M_s \bar{c}_s}{\dot{m} c_p} \tag{2.5}$$

where L is the reservoir length, and M_s is the mass of the solid packing material.

Other considerations

Thermal gradients within particles are generally ignored, since the internal thermal resistance of particles is small for the pebble sizes considered here. Thus the Biot number is effectively zero and heat transfer to and from the solid is limited by the thermal resistance at the surface. For instance, the average Biot number is 0.07 in a hot store and 0.05 in a cold store [60].

In certain cases, radial variations in temperature and velocity can be significant. For instance, Beasley and Clark [114] demonstrated the different thermal fronts that occur along the wall and the centreline of a packed bed, as reproduced in figure 2.4(a). Radial effects are predominantly due to two factors: heat leakage from the walls of the store, and variations in the packing density. According to [4] there are damped oscillations in the void fraction ε with radius: at the wall ε increases to 1 and then decreases to around 0.3–0.4 (depending on the packing structure) as distance from the wall increases. The lower frictional resistance at the wall results in a 'by-pass' flow [114]. Van Antwerpen et al. [4] collected several correlations for the void fraction variation, and shows that the oscillations are fully damped after around five particle diameters, as shown in figure 2.4(b).

The radial variations shown in figure 2.4(a) are particularly pronounced because the store was not insulated leading to more heat leakage than a typical insulated thermal store. Furthermore, the ratio of bed diameter to particle diameter was $D/d_p \approx 30$ meaning that roughly 56% of the bed area was affected by variations in the packing density and therefore the velocity. These factors are less significant in the packed beds that are studied in this work. For instance, the stores are well insulated to prevent energy loss which reduces radial temperature variations. Moreover, thermal stores typically have much larger volumes than those on which experiments are performed. The lower surface-area-to-volume ratios will also reduce heat leakage.

Furthermore, the large stores investigated in the present study have values of D/d_p of the order of 1000. As a result, the area of the bed that is affected by void fraction variations is typically around 1–2%. Meier et al. [116] suggest that radial non-uniformities can be neglected for $D/d_p > 40$.

Consequently, radial effects are not considered and a set of one-dimensional governing

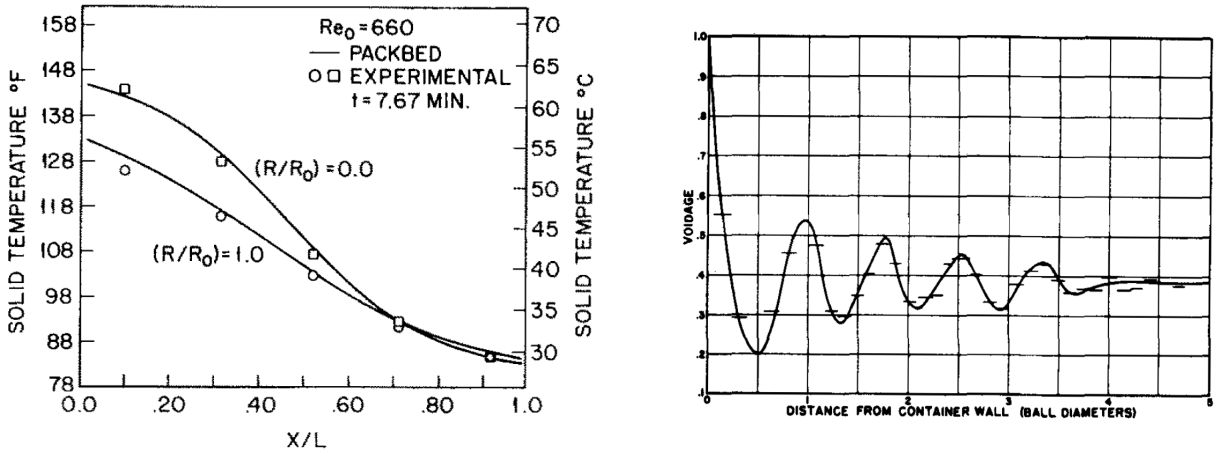

(a) (b)

Figure 2.4: (a) Experimental and numerical results showing thermal fronts in a packed bed during charge. The curves show the fronts at two radial positions: on the centreline ($R/R_0 = 0.0$) and along the wall ($R/R_0 = 1.0$). Figure from Beasley and Clark [114]. **(b)** Experimental results showing the variation in void fraction with distance from the wall for uniform spheres in a packed bed with $D/d_p = \infty$. Figure from Benenati and Brosilow [115].

equations is developed. Furthermore, it is assumed that the particle heat transfer characteristics can be represented by an average equivalent diameter – i.e. the particles are spherical and uniformly sized. Numerous studies of this type have been presented in the literature but only a few have been experimentally validated. Figure 2.5 provides two examples and demonstrates that one-dimensional models can provide a good fit to experimental data. However, in most cases (including the two shown) only the centreline temperatures are measured so it is unclear if what the radial effects may be. In particular, heat leakage is apparent in the thermal profiles of figure 2.5(b) which suggests that a two-dimensional model may have been more appropriate.

To the best of the authors knowledge there have been no experimental studies into the significance of radial variations in insulated stores with very high D/d_p. Such a study would clarify when it is appropriate to use one-dimensional models and when two-dimensional models are necessary. However, under these conditions it is likely that radial effects will be reduced. One-dimensional models therefore provide a comparatively efficient and straightforward way to gain an understanding of the major parameters that affect packed bed behaviour.

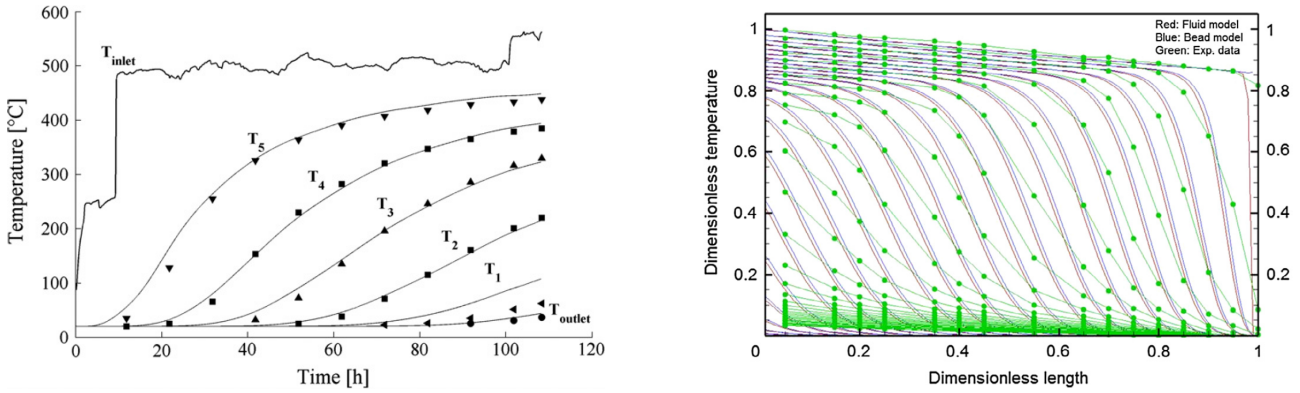

(a) (b)

Figure 2.5: Comparison of theoretical models and experimental results showing thermal fronts in packed beds. Theoretical models both use one dimensional energy equations similar to those developed in section 2.3. **(a)** Figure from Zanganeh et al. [2]. **(b)** Figure from Anderson et al. [3]

Models typically have a temperature for the solid T_s and a temperature for the gas T_g. However, 'single-phase' models use a single temperature [113]. In deriving the single-phase model, Ref. [117] showed that it was not necessary to assume the gas and solid temperatures were equivalent, but only that their second derivatives were equal. Anderson et al. [3] also developed a one-phase model coupled with the Navier-Stokes equation in order to investigate energy storage applications. This model showed reasonable agreement to experimental results. However 'single-phase' methods are not sufficiently detailed for evaluation of energy storage systems, since the gas-solid temperature difference is required to calculate the availability destruction due to heat transfer across the finite temperature difference, as detailed in section 2.5.1. A 'two-phase', one dimensional model is now described in detail.

Governing equations

The governing equations may be derived by considering the energy flows in the control volume of figure 2.2. The convective heat transfer rate between gas and solid is given by

$$\delta\dot{Q}_x = (1-\varepsilon)AS_v h(T_g - T_s)\delta x \tag{2.6}$$

where A is the cross-sectional area, h is the heat transfer coefficient, and S_v is the particle surface-to-volume ratio. The heat flux due to conduction into the control volume is

$$\dot{Q}_c^{\text{in}} = -k_{\text{eff}} A \frac{\partial T_s}{\partial x} \tag{2.7}$$

where k_{eff} is the effective conductivity, which takes into account various physical processes as discussed in more detail in section 2.5.3. The heat flux out of the control volume due to conduction is given by

$$\dot{Q}_c^{\text{out}} = -k_{\text{eff}} A \frac{\partial T_s}{\partial x} - \frac{\partial}{\partial x}\left(k_{\text{eff}} A \frac{\partial T_s}{\partial x}\right)\delta x \tag{2.8}$$

The heat flux resulting from heat leaking through the wall of the packed bed is

$$\delta \dot{Q}_L = U_w A_w (T_s - T_0)\delta x \tag{2.9}$$

where U_w is the overall heat transfer coefficient, A_w is the surface area of the wall, and T_0 is the ambient temperature.

The gas and solid equations are then given by applying the unsteady energy equation to the gas and the First Law to the solid:

$$\varepsilon \frac{\partial}{\partial t}\left(\rho_g e_g\right) + \frac{\partial}{\partial x}\left(G h_g\right) = (1-\varepsilon) S_v h (T_s - T_g) \tag{2.10}$$

$$\rho_s c_s (1-\varepsilon)\frac{\partial T_s}{\partial t} = S_v h (1-\varepsilon)(T_g - T_s) + k_{\text{eff}} \frac{\partial^2 T_s}{\partial x^2} - \frac{U_w A_w}{A}(T_s - T_0) \tag{2.11}$$

Where $G = \dot{m}/A$. The continuity and momentum equations are given by

$$\varepsilon \frac{\partial \rho_g}{\partial t} + \frac{\partial G}{\partial x} = 0 \tag{2.12}$$

$$\frac{\partial G}{\partial t} + \frac{\partial}{\partial z}\left(\frac{G^2}{\rho_g} + \varepsilon^2 (p - \rho_g g x)\right) = -\varepsilon(1-\varepsilon)\tau_s S_v \tag{2.13}$$

where τ_s is the effective shear stress on the particle. These equations are coupled, and the numerical scheme should take this into account. A numerical scheme along these lines would require small time-steps and be computationally expensive. However, numerical

experimentation has shown that gas unsteady terms are usually small and that the energy and momentum equations are effectively 'one-way coupled' since the mass flow rate is approximately constant. (For example, the main cause of density change in the reservoir is due to the progression of the thermal front, which moves slowly).

This may be illustrated by considering the fractional change of mass across an ideal thermal front. The thermal front is vertical as illustrated in figure 2.3 travelling a distance of δx. The change in mass of the control volume is

$$\Delta m = (\rho_2 - \rho_1) A \delta x = \frac{p}{R}\left(\frac{1}{T_2} - \frac{1}{T_1}\right) A \delta x \tag{2.14}$$

The mass that enters the control volume is $\dot{m}_1 \delta t$ where δt is the time taken for the front to move δx which is given by

$$\delta t = \frac{\delta x}{V_f} \tag{2.15}$$

Therefore the fractional change in mass is

$$\frac{\Delta m}{m_{\text{in}}} = \frac{1}{(1-\varepsilon)\rho_s c_s} \frac{p c_p}{R}\left(\frac{T_1 - T_2}{T_1 T_2}\right) \tag{2.16}$$

For a nominal hot reservoir operating between 500°C and 25°C at 10 bar with argon, the fractional change in mass is around 0.2% suggesting that the mass flow rate is approximately constant.

Employing these simplifications, and using $h_g = e_g + p/\rho_g = c_p T_g$ and introducing the Stanton number $\text{St} = h/c_p G$ allows the energy equations to be written as

$$\frac{\partial T_g}{\partial x} = \frac{T_s - T_g}{\ell} + \mathcal{C} \tag{2.17}$$

$$\frac{\partial T_s}{\partial t} = \frac{T_g - T_s}{\tau} + \alpha \frac{\partial^2 T_s}{\partial x^2} - \beta(T_s - T_0) \tag{2.18}$$

where the length scale (ℓ), time scale (τ), diffusivity (α) and other factors are given by

$$\ell = \frac{1}{(1-\varepsilon) S_v \text{St}} \tag{2.19}$$

$$\tau = \frac{\rho_s c_s}{c_p G S_v \text{St}} \tag{2.20}$$

$$\alpha = \frac{k_{\text{eff}}}{\rho_s c_s (1-\varepsilon)} \tag{2.21}$$

$$\beta = \frac{U_w A_w}{\rho_s c_s (1-\varepsilon) A} \tag{2.22}$$

$$\mathcal{C} = \frac{\varepsilon \rho_g}{G} \frac{\partial}{\partial t} \left(\frac{p}{\rho_g c_p} - T_g \right) \tag{2.23}$$

This formulation of the energy equations is often known as the Schumann model [118], or a Schumann-style model. The quantity $\mathcal{C}$ is a small correction to the steady-flow energy equation to account for the unsteady accumulation of energy within the control volume.

For the special case where $\alpha = 0$, $\beta = 0$, ℓ and τ are constant, and pressure losses are ignored, an analytical solution can be developed by non-dimensionalising and transforming equations 2.17 and 2.18 in the following way [112]:

$$\frac{\partial \theta_g}{\partial \xi} = \theta_s - \theta_g \tag{2.24}$$

$$\frac{\partial \theta_s}{\partial \eta} = \theta_g - \theta_s \tag{2.25}$$

Where $\theta_{g,s} = (T_{g,s} - T_2)/\Delta T$, $\Delta T = T_1 - T_2$, and ξ and η are dimensionless length and time variables given by

$$\xi = \frac{x}{\ell}; \qquad \eta = \frac{t}{\tau} - \frac{\varepsilon x}{u_s \tau} \tag{2.26}$$

The dependence of η on x arises from the unsteady accumulation of internal energy within the gas. For the application considered here (argon flowing through a rock bed), this term can be ignored, due to the low heat capacity of gas per unit volume compared with that of the solid. The analytical solution was first presented by Anzelius in 1926 [119] and is given by

$$\theta_g - \theta_s = \exp\left[-(\xi + \eta) I_0 \left(2\sqrt{\xi \eta} \right) \right] \tag{2.27}$$

Where I_0 is the zero-th order modified Bessel function of the first kind. Full equations for T_s and T_g of a similar form are presented in [118] but these expressions require evaluation of an infinite sum of Bessel functions making calculation of the analytical solution cumbersome. In addition, the analytical result assumes that thermal constants are independent of temperature, whereas this is not a necessary requirement for numerical approaches. Furthermore, this solution does not include heat leakage, axial conduction, or pressure losses.

As a result, numerical solutions generally prove to be a comparatively straightforward, flexible and efficient alternative, and the analytical solution may be used for validation.

2.4 Numerical solutions of the energy equations

The Schumann-style model presented above can be solved with a variety of numerical schemes, several of which will be described and validated now. Firstly, a correlation for the Stanton number is required. There is significant variation in the available experimental data as a result of difficulties in obtaining reliable measurements of heat transfer coefficients in packed beds. For the range of Reynolds numbers of interest, the following correlation was developed by Wakao et al. [120]

$$\mathrm{St} = \frac{2}{\mathrm{RePr}} + \frac{1.1}{\mathrm{Re}^{2/5}\mathrm{Pr}^{2/3}} \tag{2.28}$$

where $\mathrm{Re} = \rho_g u_s d_p / \mu_g$ is the Reynolds number based on the particle size. The most straightforward approach to solving the gas and solid equations 2.17 and 2.18 is by explicit finite differences as used by Zanganeh et al. [2]. The stability of this method can be improved substantially by using a predictor-corrector method, also known as Adams-Bashforth-Moulton. The equations are solved explicitly in the predictor step, and the result is then refined in the corrector step which typically uses an implicit formulation of the equations [121]. Firstly, equations 2.17 and 2.18 are re-formulated with the time differential on the left-hand side

$$\begin{aligned} \frac{\partial T_g}{\partial t} &= \frac{G}{\varepsilon\rho}\left(\frac{T_s - T_g}{\ell} - \frac{\partial T_g}{\partial x}\right) + \frac{1}{\rho c_p}\frac{\partial p}{\partial t} \\ &= \mathcal{A} \end{aligned} \tag{2.29}$$

$$\begin{aligned} \frac{\partial T_s}{\partial t} &= \frac{T_g - T_s}{\tau} + \alpha\frac{\partial^2 T_s}{\partial x^2} - \beta(T_s - T_0) \\ &= \mathcal{B} \end{aligned} \tag{2.30}$$

The stencil for the predictor-corrector scheme is shown in figure 2.6. Information is known at all nodes at time $(n-1)$. An initial guess for the temperatures $\hat{T}_{g,s}$ at time n and node

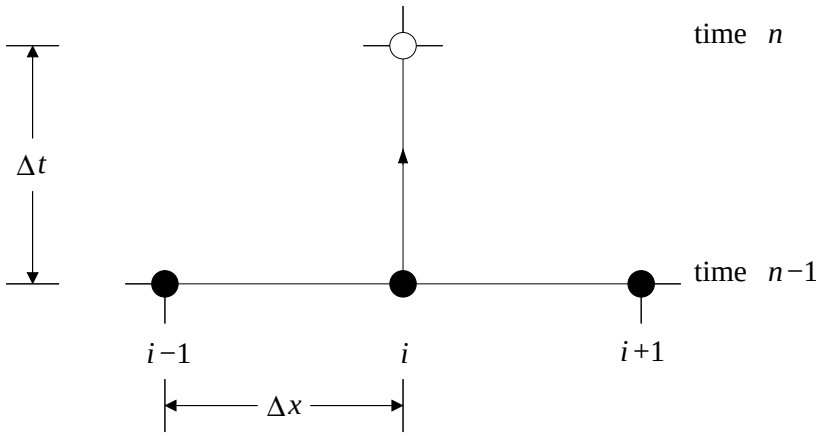

Figure 2.6: A stencil of the computational grid for the predictor-corrector numerical scheme. Information is known at all filled nodes, and unknown at the open nodes.

i is found in the predictor step by solving the equations using central differences and the explicit Euler method such that

$$\begin{aligned}\frac{\hat{T}_{g,i}^{n}-T_{g,i}^{n-1}}{\Delta t} &= \frac{G_i^n}{\varepsilon\rho_i^n}\left(\frac{T_{s,i}^{n-1}-T_{g,i}^{n-1}}{\ell_i^{n-1}}-\frac{T_{g,i+1}^{n-1}-T_{g,i-1}^{n-1}}{2\Delta x}\right)+\frac{1}{\rho_i^{n-1}c_p}\left(\frac{\hat{p}_i^n-p_i^{n-1}}{\Delta t}\right)\\ &= \mathcal{A}_i^{n-1} \qquad (2.31)\end{aligned}$$

$$\begin{aligned}\frac{\hat{T}_{s,i}^{n}-T_{s,i}^{n-1}}{\Delta t} &= \frac{T_{g,i}^{n-1}-T_{s,i}^{n-1}}{\tau_i^n}+\alpha\left(\frac{T_{s,i+1}^{n-1}-2T_{s,i}^{n-1}+T_{s,i-1}^{n-1}}{\Delta x^2}\right)-\beta\left(T_{s,i}^{n-1}-T_0\right)\\ &= \mathcal{B}_i^{n-1} \qquad (2.32)\end{aligned}$$

In the corrector step, the initial guesses are corrected by re-evaluating $\hat{\mathcal{A}}^n$ and $\hat{\mathcal{B}}^n$ using the predicted values of $\hat{T}_{s,g}^n$. The updated gas and solid temperatures at time n are then given by

$$\frac{T_{g,i}^{n}-T_{g,i}^{n-1}}{\Delta t} = \frac{1}{2}\left(\mathcal{A}_i^{n-1}+\hat{\mathcal{A}}_i^{n}\right) \qquad (2.33)$$

$$\frac{T_{s,i}^{n}-T_{s,i}^{n-1}}{\Delta t} = \frac{1}{2}\left(\mathcal{B}_i^{n-1}+\hat{\mathcal{B}}_i^{n}\right) \qquad (2.34)$$

In this method, other variable parameters such as p^n, G^n and ℓ^n can be updated after the predictor step. Strictly, the mass flow rate per unit area G^n should be calculated in a similar manner using a predictor-corrector scheme. However, G only varies slightly as a result of the change in mass of stored gas brought about by the progression of the thermal front. The pressure is calculated from Ergun's equation (equation 2.53) from which the gas density can be updated from $\rho_g = p/RT_g$. Finally, the mass flow rate per unit area is found from the continuity equation:

$$G_i^n = G_{i-1}^n + \varepsilon \frac{\Delta x}{\Delta t} \left(\rho_{g,i}^{n-1} - \rho_{g,i}^n \right) \tag{2.35}$$

The predictor-corrector method is verified against the analytical solution for single blow operation of a charging hot packed bed in figure 2.7 from which it is clear there is good agreement between the solutions. In accordance with the derivation of the analytical solution, there are no pressure losses, conduction, or heat leakage, and factors such as ℓ are kept constant. Even in this simplified scenario, extremely small time-steps are required; in this case $\Delta t/\tau \leq 0.5 \times 10^{-3}$ in order match the analytical results as well as obtain converged estimates for the thermal loss. Grid steps can be somewhat larger at $\Delta x/\ell \leq 0.5$. As a result, the predictor-corrector method runs slowly and developing an alternative scheme is worthwhile.

An alternative method devised by White et al. [80] achieves stable results with larger grid and time-steps. This semi-implicit method is similar to that in [60] and [97], although it is extended to include conduction and heat leakage. Similar integration schemes are presented in Willmott [112].

The Schumann-style gas and solid equations are marched forward in space and time, respectively, along the paths indicated in figure 2.8. All derivatives are represented semi-implicitly (with the exception of the conduction term in the solid equation) such that quantities in the derivatives take on their average value along the path of integration. The equations are therefore

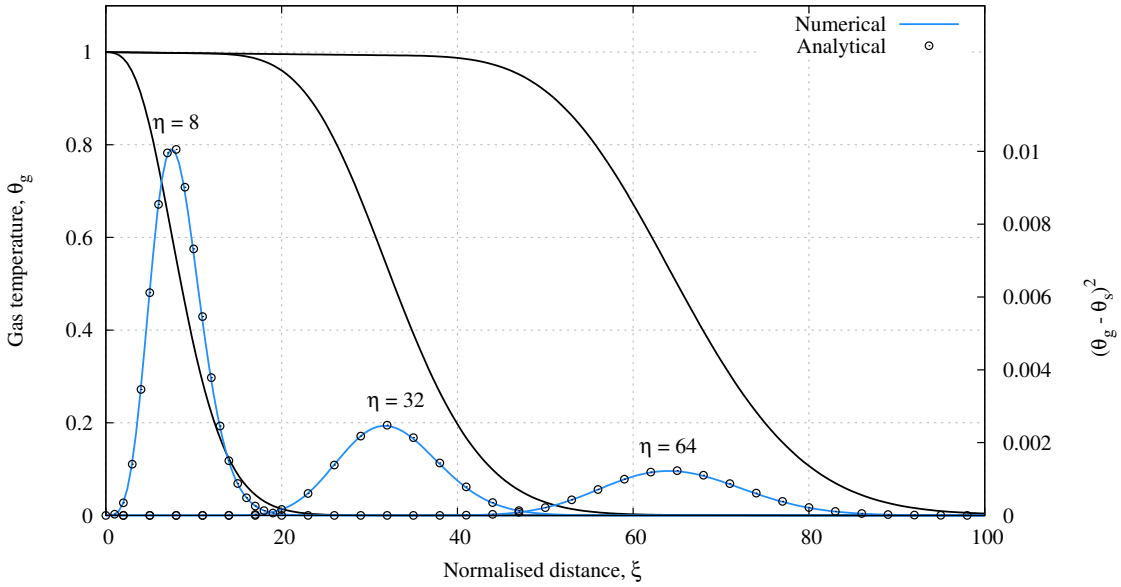

Figure 2.7: Temperature profiles generated using the predictor-corrector scheme at three different times. $(\theta_g - \theta_s)^2$ are plotted on the right-hand axis, and are verified against the analytical solution of equation 2.27

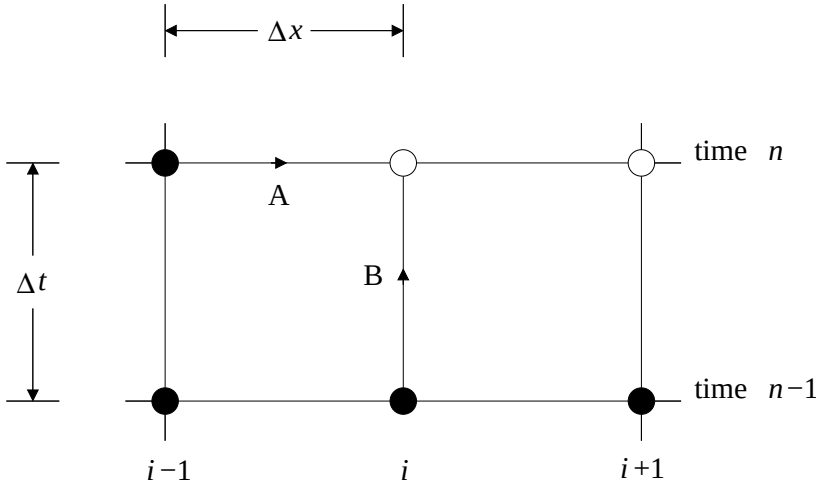

Figure 2.8: A stencil of the computational grid for the semi-implicit method. Properties are known at nodes that are filled, and unknown at open points. The two energy equations are integrated along paths A and B to obtain T_s and T_g at node (i, n)

$$\frac{T^n_{g,i} - T^n_{g,i-1}}{\Delta x} = \frac{\bar{T}^A_s - \bar{T}^A_g}{\ell} + \mathcal{C} \tag{2.36}$$

$$\frac{T^n_{s,i} - T^{n-1}_{s,i}}{\Delta t} = \frac{\bar{T}^B_g - \bar{T}^B_s}{\tau} + \alpha \frac{T^{n-1}_{s,i+1} - 2T^{n-1}_{s,i} + T^{n-1}_{s,i-1}}{\Delta x^2} - \beta\left(\bar{T}^B_s - T_0\right) \tag{2.37}$$

where superscripts A and B represent that the quantity is evaluated at its average value along that path (see figure 2.8)

$$\bar{T}^A = \frac{1}{2}\left(T^n_{i-1} + T^n_i\right) \tag{2.38}$$

$$\bar{T}^B = \frac{1}{2}\left(T^n_i + T^{n-1}_i\right) \tag{2.39}$$

The unsteady gas accumulation term is accounted for by $\mathcal{C}$ which is small and may be evaluated with sufficient accuracy at the upstream location $(i-1)$. Expanding these expressions and rearranging, allows the resulting pair of equations to be represented in matrix form as

$$\begin{bmatrix} (1+\phi) & -\phi \\ -\psi_1 & (1+\psi_1+\psi_2) \end{bmatrix} \begin{Bmatrix} T^n_{g,i} \\ T^n_{s,i} \end{Bmatrix} = \begin{Bmatrix} K_1 \\ K_2 \end{Bmatrix} \tag{2.40}$$

where

$$K_1 = (1-\phi)T^n_{g,i-1} + \phi T^n_{s,i-1} + \mathcal{C}^n_{i-1}\Delta x \tag{2.41}$$

$$K_2 = (1-\psi_1-\psi_2-2\psi_3)T^{n-1}_{s,i} + \psi_3\left(T^{n-1}_{s,i+1} + T^{n-1}_{s,i-1}\right) + \psi_1 T^{n-1}_{g,i} + 2\psi_2 T_0 \tag{2.42}$$

and

$$\phi = \frac{\Delta x}{2\ell}$$

$$\psi_1 = \frac{\Delta t}{2\tau}; \quad \psi_2 = \frac{\beta \Delta t}{2}; \quad \psi_3 = \frac{\alpha \Delta t}{\Delta x^2}$$

The gas and solid temperatures at node (i, n) can then be found by inverting this 2 x 2 matrix at each node. The pressure, density and mass flow rate per unit area are then updated as in the predictor-corrector method. The semi-implicit scheme is compared with

the predictor-corrector method in figure 2.9 for a hot reservoir which includes conduction, heat leakage and pressure losses. (The semi-implicit scheme was also verified against the analytical solution for the most simplified scenario as in figure 2.9). It is possible to take much larger time-steps than the predictor-corrector scheme, and for convergence of the thermal losses $\Delta t/\tau, \Delta x/\ell \leq 1/2$ is sufficient. These results demonstrate that the numerical results are consistant with the theory, although validation against experimental results is also required. (Note, these equations are commonly used in the literature and can produce comparable results to experimental data, as shown in figure 2.5 on page 48).

A further stability constraint is $\alpha \Delta t/\Delta x^2 \leq 1/2$ which arises from the explicit coding of the conduction term. The conduction terms can be represented implicitly by separating the solid equation into two separate steps. In the first step, $\psi_2 = \psi_3 = 0$ are substituted into the above equations to obtain the gas and solid temperatures. In the second step, the solid temperature is updated such that

$$\frac{\partial T_s}{\partial t} = \alpha \frac{\partial^2 T_s}{\partial x^2} - \beta(T_s - T_0) \tag{2.43}$$

This is simply the one-dimensional heat diffusion equation which can be solved implicitly using the Crank-Nicolson method [121]. This method was tested and has very similar performance to the full semi-implicit method described above. A comparison of the CPU times taken by each algorithm for the case described above is given in table 2.1.

	Predictor-corrector	Semi-implicit	
		$\Delta t/\tau = 0.1$	$\Delta t/\tau = 0.4$
CPU times (s)	128	2.4	0.40

Table 2.1: Comparison of CPU times for one cycle for each numerical scheme. Calculations were undertaken on a typical laptop (Intel i5 -2430M, 2.40 GHz, 6 GB RAM)

A wide range of other techniques have been developed in the literature. Beasley and Clark [114] describes a range of approaches that have been used, as well as developing a two-dimensional solver in which the energy equations were formulated such that the conductive terms were included in the gas energy equation. The solid equation could then be discretised implicitly and substituted into the finite-difference form of the gas equation. The resulting set of equations could be solved using matrix decomposition approaches for banded matrices. This method was deemed to be quite stable, although small time-steps

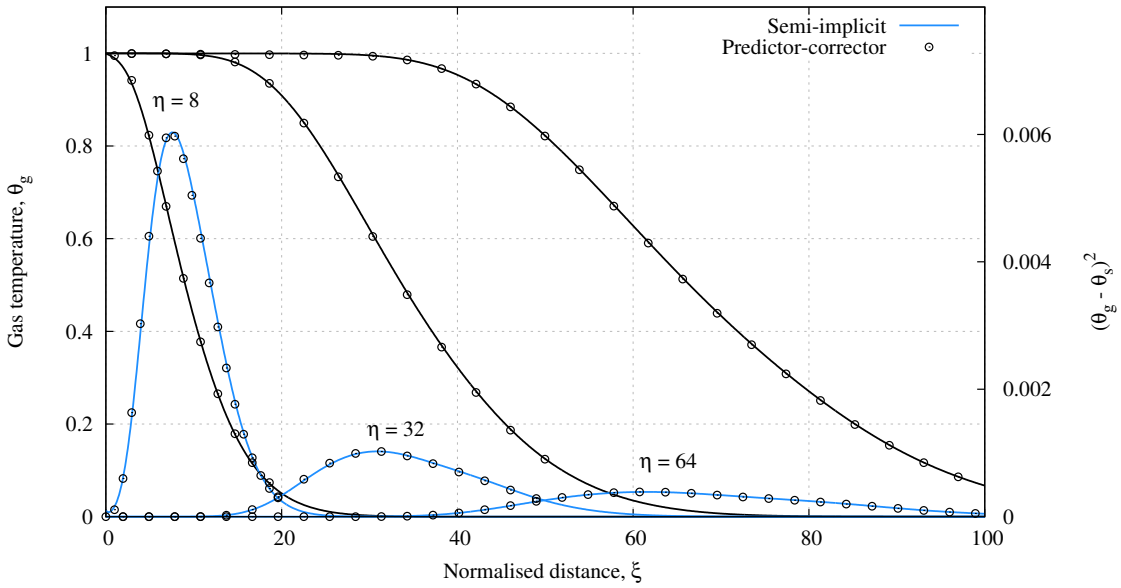

Figure 2.9: Temperature profiles generated using the semi-implicit scheme at three different times. $(\theta_g - \theta_s)^2$ are plotted on the right-hand axis, and are verified against the predictor-corrector method. Conduction ($k_{\text{eff}} = 2$ W/mK), heat leakage ($U_w = 0.15$ W m^{-2}K^{-1}) and pressure losses are included.

were required in order to achieve convergence. Another approach by Ni and Caram [86] develops a closed form matrix solution to the steady-state cyclic operation problem. However, this method requires at least as much computational expense as typical numerical schemes, and is not easily extendible to treat the temperature-dependent properties described in [97].

2.5 Availability destruction in packed beds

Various physical processes lead to a reduction in the available energy stored in the reservoir. Each loss mechanism may be affected in different ways by the packed bed design parameters. Accurate modelling therefore provides a way to understand the impact of each variable on performance, and aid the design of optimal systems. In this section the main mechanisms that cause a reduction in availability are described.

For the reservoir alone (i.e. excluding the power conversion machinery) the round-trip storage efficiency χ may be defined as the *available* energy recovered from the reservoir during discharge as a fraction of that which enters during charge. A loss coefficient ζ may

be derived for each of the mechanisms that causes a loss in availability. Each of these loss coefficients is defined as the fraction of the inlet available energy that is lost such that $\zeta = B_{\text{lost}}/B_{\text{in}}$ and

$$\chi = \frac{B_{\text{out}}}{B_{\text{in}}} = 1 - \sum \zeta \tag{2.44}$$

where B is the total amount of available energy added and B_{in} is given by

$$B_{\text{in}} = \dot{m} c_p t_{\text{chg}} \left[(T_1 - T_2 - T_0 \ln \left(\frac{T_1}{T_2} \right) \right] = \dot{m} c_p t_{\text{chg}} \beta \tag{2.45}$$

where t_{chg} is the charging duration.

Note that in the present work the term *availability* or *available energy* is used. The specific availability function is defined as $b = h - T_0 s$, and as such only changes in availability are meaningful. Exergy is a commonly used quantity and is the difference between the actual value of b and b_0, which is the availability at a point where the fluid has zero potential to do work. This point is called the dead state and is typically at atmospheric pressure and temperature. As such, the specific exergy may be defined as $\xi = (b - b_o) = (h - T_0 s) - (h_0 - T_0 s_0)$, and it can be seen that $\Delta b = \Delta \xi$. In this work, availability or exergy could be used interchangeably. However, the use of availability is more natural because the thermal stores operate between T_1 and T_2 and are not necessarily discharged to the dead state.

2.5.1 Thermal losses

Availability losses are caused by the irreversible heat transfer that occurs across the finite temperature difference between gas and solid. Following [60, 97] this loss is referred to here as the "thermal loss". The instantaneous entropy generation rate is given by,

$$\dot{S}_{\text{irr}} = \int \left(\frac{1}{T_s} - \frac{1}{T_g} \right) d\dot{Q} \tag{2.46}$$

and $d\dot{Q} = hAS_v(1 - \varepsilon)(T_g - T_s)dx$. By incorporating the definition of ℓ, equation 2.46 becomes

$$\dot{S}_{\text{irr}} = \dot{m} c_p \int_0^{\lambda} \frac{(T_g - T_s)^2}{T_g T_s} \frac{dx}{\ell} \tag{2.47}$$

where λ is the length of the thermal front. (Equation 2.47 could equally be integrated over the length of the packed bed L, since $T_g - T_s = 0$ outside of the thermal front). The thermal loss coefficient ζ_t is found by integrating equation 2.47 over the duration of operation t and normalising by the net flux of inlet availability B_{in}

$$\zeta_t = \frac{T_0}{\beta t_{\text{chg}}} \int_0^{t_{\text{chg}}} \int_0^{\lambda} \frac{(T_g - T_s)^2}{T_g T_s} \frac{dx}{\ell} dt \tag{2.48}$$

By approximating the thermal fronts as linear profiles of length λ the effect of various design parameters on ζ_t may be revealed. Ignoring the small contribution of $\mathcal{C}$ in equation 2.17 the thermal gradient may be estimated as

$$\frac{\partial T_g}{\partial x} \approx \frac{\Delta T}{\lambda} = \frac{T_s - T_g}{\ell} \tag{2.49}$$

where $\Delta T = T_1 - T_2$. Substituting this into the expression for ζ_t and integrating along the linear profile gives the simplified expression

$$\zeta_t \approx \frac{T_0}{\beta} \left(\frac{\Delta T^2}{T_1 T_2} \right) \frac{\ell}{\lambda} \tag{2.50}$$

Minimising thermal losses clearly requires a long thermal front and small value of ℓ which may be achieved by increasing the Stanton number or reducing the particle size. As will be seen, this conflicts with minimising pressure losses and a compromise must be sought.

Factors affecting thermal losses

Various factors affect the length of the thermal front, including the time which the packed bed charges and discharges for during cyclic operation (discussed in more detail in chapter 3) and the dependence of specific heat capacity c_s on temperature. The heat capacity per unit volume tends to increase with temperature as illustrated for various materials in figure 2.10. Since the thermal front speed varies inversely with c_s (equation 2.3), cold regions of the front travel more quickly than hot regions. As a result, the thermal fronts change shape. For instance, during charge thermal fronts in a hot reservoir will become less steep, whereas those cold reservoirs become steeper, as shown in figure 2.11(a). As the

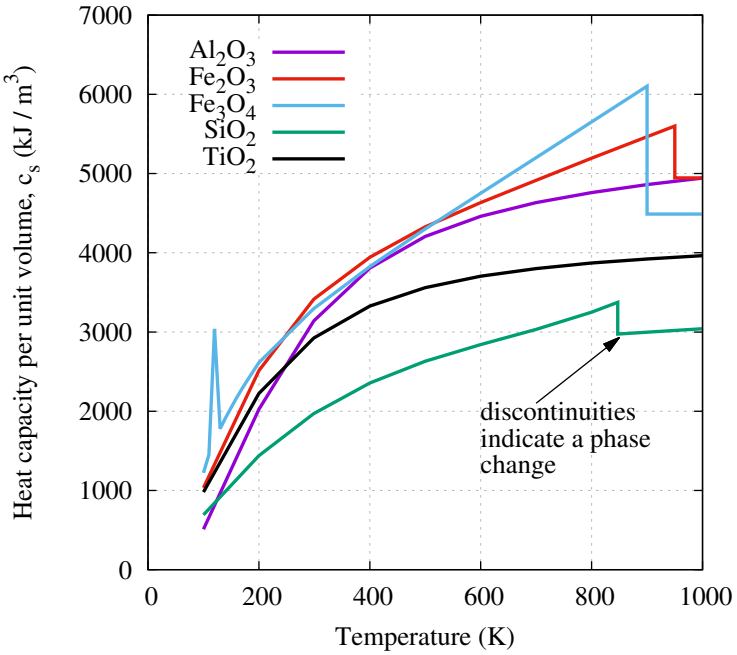

Figure 2.10: Heat capacity per unit volume for various materials [97]

cold thermal front travels along the reservoir, its length λ decreases, and thermal losses thus increase. Eventually, the losses reach a constant value and White et al. [97] explains that this is the result of the wave catch-up effect being balanced by the dissipative effects caused by irreversible heat transfer, as shown in figure 2.11(a). The sudden change in properties across the thermal front, as well as the losses becoming independent of the detailed dissipative processes (i.e. ℓ) means that the front can be thought of as a thermal "shock-wave". The shape of the thermal front also remains constant.

Realistic operation of the thermal stores will probably involve regular charging and discharging phases. During discharge, any effects of wave steepening in the cold store will be reversed and thermal shock-waves are unlikely to form during such cyclic operation. However, as figure 2.11(b) illustrates, thermal fronts still steepen during charge compared to the case where c_s is constant. The average thermal gradients that occur for constant and variable c_s are actually approximately equal. However, for variable c_s the fluctuation of these gradients between charge and discharge generates larger losses because ζ_t varies

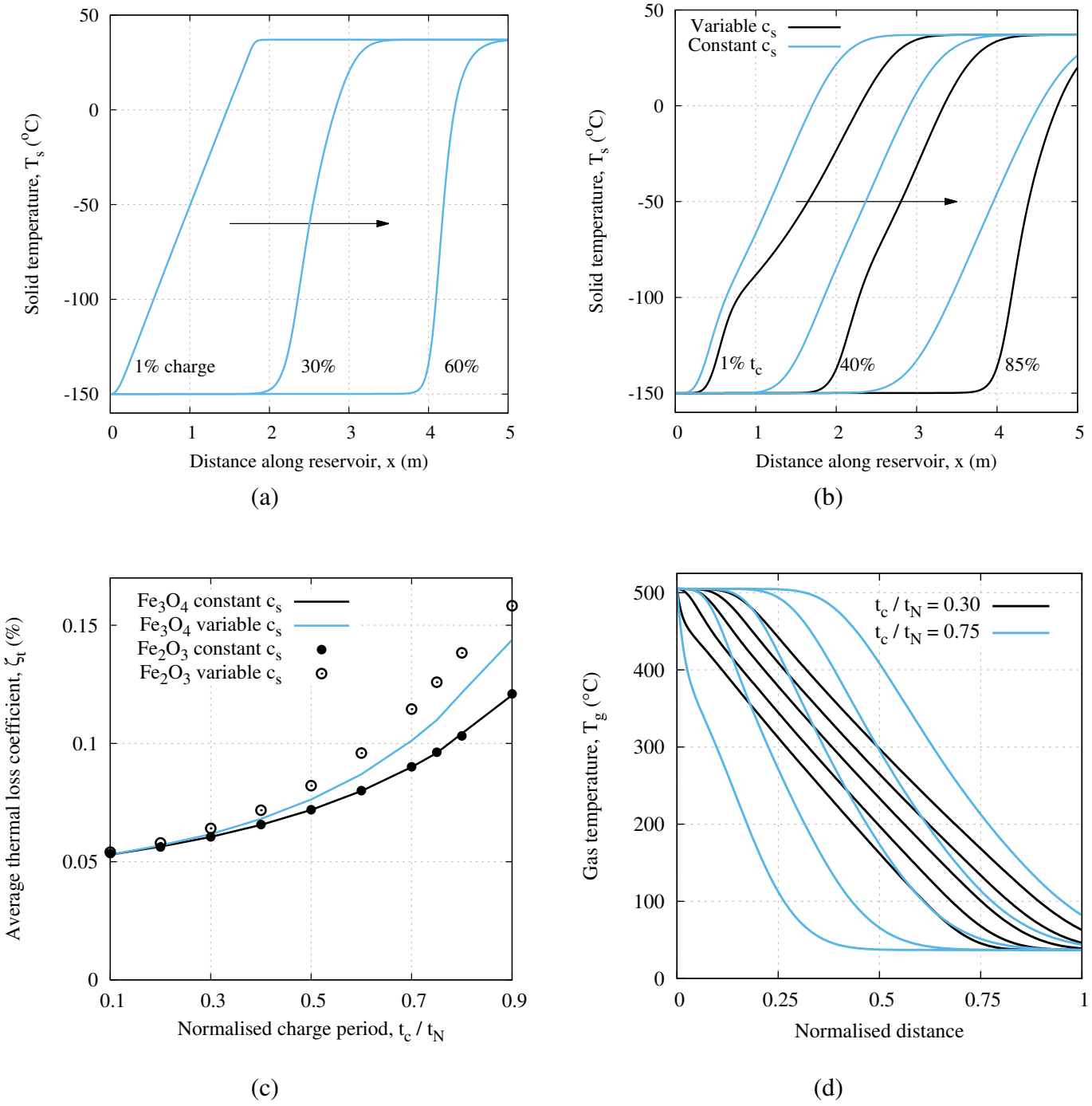

Figure 2.11: Effect of variable c_s on thermal front formation in cold stores **(a)** Temperature profiles in a cold store during the charging phase. Variable c_s causes wave catch-up and shock wave formation. **(b)** Temperature profiles in a cold store under cyclic operation. Profiles are shown at 1%, 40% and 85% through the charge phase. **(c)** Thermal losses for 20 mm diameter particles in a cold reservoir undergoing cyclic operation. **(d)** Effect of cycle period t_c/t_N on thermal front shape in a hot store.

inversely with the front length λ. For instance, the thermal loss is given by

$$\zeta_t \approx \frac{T_0}{\beta t_{\text{chg}}} \left(\frac{\Delta T^2}{T_1 T_2} \right) \ell \int_0^{t_{\text{chg}}} \frac{1}{\lambda} dt \tag{2.51}$$

If the average front length $\bar{\lambda}$ is substituted into this rather than the fluctuating front length (which is a function of time $\lambda = \lambda(t)$) then it is the case that

$$\int_0^{t_{\text{chg}}} \frac{1}{\lambda(t)} dt > \frac{t_{\text{chg}}}{\bar{\lambda}} \tag{2.52}$$

This result is demonstrated in Appendix A. As a result, the fluctuation of the thermal front shape due to variable c_s leads to slightly greater thermal losses than when c_s is constant. Furthermore, larger fractional changes in c_s (given by $\Delta c_s / \bar{c}_s$) will lead to greater losses [97]. This is supported by figure 2.11(c) which shows thermal losses in a cold reservoir during cyclic operation for two materials (hematite and magnetite) which have different fractional changes in c_s. It is notable that ζ_t for magnetite and hematite with constant c_s are almost identical since the average heat capacity for these materials is similar. However, when c_s was allowed to vary losses were greater for hematite as this material has a higher fractional change in c_s.

As a result, thermal losses can be reduced by selecting materials and operating temperatures that minimise the fractional change in heat capacity $\Delta c_s / \bar{c}_s$ where $\bar{c}_s$ is the average heat capacity over the temperature range of interest [97].

Figure 2.11(c) shows that thermal losses increase as the length of the cycle period t_c / t_N is increased. This is due to the steeper gradients that are formed during longer cycles, as shown in figure 2.11(d). During cyclic operation, the thermal fronts are the same from one cycle to another, and the loss in available energy is the same for every cycle. In order for the reservoir to return to its initial condition at the end of each charge-discharge cycle, the total flux of entropy out of the reservoir must equal the entropy generation within the reservoir. To achieve this, 'information' must be propagated from one end of the packed bed to the other in the time of one charge cycle. For short cycle periods, the thermal front will only travel a small fraction of the reservoir length (roughly given by $V_f t_c / L$). Therefore, the thermal fronts are longer and less steep so that entropy can be 'flushed' out of the packed bed, resulting in lower thermal losses.

2.5.2 Pressure losses

The momentum flux is approximately constant along the reservoir, so the pressure drop is computed in a manner analogous to that for fully-developed pipe flow. The pressure gradient is given by [60],

$$\frac{\partial p}{\partial x} = -\frac{S_v(1-\varepsilon)G^2 C_f}{2\varepsilon^3 \rho_g} \tag{2.53}$$

Where C_f is the friction coefficient which depends on the Reynolds number and is given here by the Carman correlation [122]

$$C_f = \frac{10}{\mathrm{Re}_m} + \frac{8}{10\mathrm{Re}_m^{\frac{1}{10}}} \tag{2.54}$$

Re_m is the "modified" Reynolds number given by $\mathrm{Re}_m = \rho_g u_s/(1-\varepsilon)S_v\mu_g$. The instantaneous entropy generation rate due to the pressure drop is

$$\dot{S}_{\text{irr}} = -\dot{m}R\ln\left(\frac{P_{\text{out}}}{P_{\text{in}}}\right) \tag{2.55}$$

Equation 2.53 is integrated along the length of the reservoir to give the overall pressure drop which is then converted to an entropy increase and hence a loss coefficient,

$$\zeta_p = \frac{T_o}{\dot{m}c_p\beta t_{\text{chg}}}\int_0^{t_{\text{chg}}} \dot{S}_{\text{irr}}dt = \frac{T_o}{\beta t_{\text{chg}}}\frac{\gamma-1}{\gamma}\int_0^{t_{\text{chg}}} \ln\left(\frac{P_{\text{out}}}{P_{\text{in}}}\right)dt \tag{2.56}$$

Pressure losses are typically larger in the cold reservoir compared to hot reservoirs since fractional pressure changes are more significant, and gas densities are relatively low. Minimisation of pressure losses requires a reduction in frictional effects which is achieved by increasing particle size and reducing the length of the reservoir, which is directly at odds with minimising thermal losses. This conflict motivated the concept of segmented stores, whereby gas is diverted around areas of the packed bed where no heat exchange is taking place in order to reduce frictional effects. Segmented stores are discussed in more detail in section 3.3.

2.5.3 Conductive losses

Entropy generation due to axial conduction

The dissipative nature of conduction causes a loss in availability. This loss is generated during the charging and discharging phases but is also significant during storage periods since spreading of the thermal front results in a loss of available energy. The instantaneous entropy generation due to axial conduction is found by considering the first and second laws applied to a control volume, as in figure 2.12.

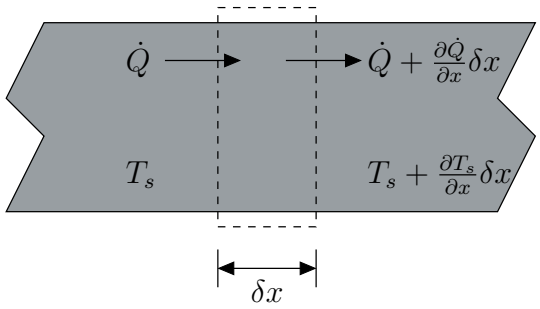

Figure 2.12: Control volume for heat conduction along a packed bed

Applying the first law of thermodynamics to the elemental control volume yields

$$c_s \delta M_s \frac{\partial T_s}{\partial t} = -\frac{\partial \dot{Q}}{\partial x}\delta x \tag{2.57}$$

where c_s and δM_s are the specific heat capacity and mass of solid within the element. The rate of entropy generation due to irreversibility is found by applying the second law to give

$$\begin{aligned} \Delta \dot{S}_{\text{irr}} &= \frac{\partial}{\partial t}\left(\delta S_{CV}\right) - \sum\left(\frac{\dot{Q}}{T_s}\right) \\ &= \frac{\partial}{\partial t}\left(\delta S_{CV}\right) + \frac{\partial}{\partial x}\left(\frac{\dot{Q}}{T_s}\right)\delta x \\ &= c_s \delta M_s \frac{1}{T_s}\frac{\partial T_s}{\partial t} + \frac{1}{T_s}\frac{\partial \dot{Q}}{\partial x}\delta x - \frac{\dot{Q}}{T_s^2}\frac{\partial T_s}{\partial x}\delta x \end{aligned} \tag{2.58}$$

where δS_{CV} is the entropy of elemental mass δM_s. Substituting in equation 2.57 eliminates

the first two terms on the right-hand-side. Fourier's law of conduction is

$$\dot{Q} = -k^x_{\text{eff}} A \frac{\partial T_s}{\partial x} \tag{2.59}$$

The instantaneous entropy generation rate is then given by

$$\dot{S}_{\text{irr}} = \int_0^L k^x_{\text{eff}} A \left(\frac{1}{T_s} \frac{\partial T_s}{\partial x} \right)^2 dx \tag{2.60}$$

where k^x_{eff} is the effective conductivity in the axial direction, the value of which will be discussed in section 2.5.3. The loss coefficient due to conduction ζ_c is defined in a similar way to equation 2.48. The expression for ζ_c can also be simplified so that it is comparable to the thermal loss ζ_t by assuming that the gas and solid temperature gradients are approximately equal and using a simplified version of equation 2.17 to give

$$\frac{\partial T_s}{\partial x} \approx \frac{\partial T_g}{\partial x} \approx \frac{T_s - T_g}{\ell} \tag{2.61}$$

This simplification assumes that conduction will not significantly affect thermal front shapes. Substituting this expression into equation 2.60 produces

$$\dot{S}_{\text{irr}} = \int_0^L k^x_{\text{eff}} A \left(\frac{T_s - T_g}{\ell T_s} \right)^2 dx \tag{2.62}$$

By comparing this expression to the instantaneous entropy generation caused by temperature differences in equation 2.47, and by assuming $T_s^2 \approx T_s T_g$ in the denominator, the ratio of the two entropy generation rates simplifies to

$$\frac{\zeta_c}{\zeta_t} = \frac{k^x_{\text{eff}}}{c_p G \ell} \tag{2.63}$$

This equation is most appropriate for low values of k^x_{eff} and figure 2.17(d) on p. 74 illustrates its accuracy compared to the full expression above.

Evaluation of the effective axial conductivity k^x_{eff}

The effective axial conductivity is subject to much uncertainty and a large number of papers have been published on the subject. There are a several mechanisms that contribute to the effective conductivity and Yagi and Kunii [123] divided these into two groups:

Heat transfer processes that are independent of the fluid flow:

1. Thermal conduction through the bulk of the solid particles
2. Thermal conduction through the contact surfaces of the particles
3. Radiative heat transfer between the faces of two particles
4. Radiative heat transfer between neighbouring voids

Heat transfer processes that are dependent on the fluid flow:

1. Thermal conduction through the fluid film near the contact surface of the particles
2. Convection between the solid and fluid
3. Heat transfer by lateral mixing of the fluid (turbulent transport in eddies)

Many empirical and numerical correlations have been developed, and several reviews exist [4, 124]. These correlations are typically empirical and require estimation of several unknown parameters. For instance, several models require details of the number of points of contact (the coordination number). This can be estimated for idealised packings with uniformly sized spherical particles, but it is unlikely to be reliable for more realistic packed beds. Various other correlations, which incorporate factors such as surface roughness and contact area, have been developed more recently (see for example, [4]). However, these models contain additional parameters that are difficult to obtain experimentally. Furthermore, experimental results from which the correlations are developed are often very specific to certain types and shapes of materials, and the results may not be generally applicable.

Balakrishnan and Pei [124] suggests that the difficulty of obtaining a general correlation is due to the interaction of the major modes of heat transfer; gas-to-particle heat transfer convection and effective conduction through the bed. This may be illustrated by combining equations 2.18 and 2.17 (with $\beta = \mathcal{C} = 0$) which gives an expression for the progress of

the thermal front:

$$\frac{\partial T_s}{\partial t} + V_f \frac{\partial T_g}{\partial x} = \frac{\alpha \ell}{\tau} \frac{\partial^2 T_s}{\partial x^2} \tag{2.64}$$

where $V_f = \ell/\tau$ is the thermal wave speed, as defined in equation 2.3. Substituting $T_g = T_s + (T_g - T_s)$ into this equation, and then replacing $(T_g - T_s)$ using equation 2.17 produces

$$\frac{\partial T_s}{\partial t} + V_f \frac{\partial T_s}{\partial x} = \frac{\ell}{\tau} \frac{\partial}{\partial x} \left(\ell \frac{\partial T_g}{\partial x} \right) + \alpha \frac{\partial^2 T_s}{\partial x^2} \tag{2.65}$$

The gas-solid equation above shows wave propagation at speed V_f combined with a dissipative process [97] (on the right-hand-side). Therefore, both axial conduction and gas-particle heat transfer manifest themselves as diffusion of the thermal front. When $\alpha = 0$ the effective diffusivity is

$$\mathcal{D} = \frac{\ell^2}{\tau} = \frac{V_f}{\mathrm{St}(1-\varepsilon)S_v} \tag{2.66}$$

This equation is consistent with the analysis in section 2.5.1 and equation 2.50 and in particular it suggests that thermal losses associated with irreversible heat transfer can be minimised by reducing ℓ. In the case of finite thermal conductivity k^x_{eff} there is an additional dissipative term due to axial conduction. The relative importance of the two sources of dissipation is given by the ratio $\alpha\tau/\ell^2 = k^x_{\text{eff}}/(c_p G \ell)$, which is the ratio between conductive and thermal losses as shown above. Thus equation 2.65 suggests that there are two main sources of dissipation due to the two different heat transfer processes.

The combination of dissipative processes makes designing experiments that quantify the individual effects a challenging task. In the following section, several correlations are compared with the aim of establishing the correct order of magnitude for the effective conductivity.

Thermal conductivities of magnetite (Fe_3O_4) and hematite (Fe_2O_3)

Lis and Kellard [125] report that experimental data on magnetite conductivity range between 0.5 W/mK and 8 W/mK for experiments carried out at the same temperature. They found the following correlation for thin oxide films ($\sim$0.1 mm thick) in terms of porosity

P (expressed as a percentage) in the temperature range 35–80°C

$$k_{\text{mag}} = 1.24 \pm 0.18 - 9.15 \times 10^{-3} P \tag{2.67}$$

For a single crystal of magnetite, Slack [126] measured thermal conductivities in the range of 5–7 W/mK at 300K, and noted that the conductivity was independent of temperature in the range 119–300K. In addition, Slack noted that the orientation of the crystal affected the conductivity.

Mølgaard [127] carried out experiments on a range of magnetite and hematite samples across a range of temperatures. Regression analysis gave the following correlations for thermal conductivity in terms of temperature T:

$$k_{\text{mag}} = 4.23 - 1.37 \times 10^{-3} T \tag{2.68}$$

$$k_{\text{hem}} = 8.39 - 6.63 \times 10^{-3} T \tag{2.69}$$

These different measurements indicate that there is considerable uncertainty for the conductivity of the solid material, even without considering other factors that contribute to the effective conductivity.

Correlations for effective conductivities

Many well established models for effective conductivity were developed for packed beds with stagnant fluids, presumably since it is more straightforward to obtain correlations without having to consider turbulent transport of heat. These results are applicable for the storage phases (i.e. between charge and discharge) which are discussed in more detail in section 2.5.6.

Upper and lower estimates of the effective thermal conductivity can be found by placing the solid and fluid in series or in parallel, as in [128]. The series arrangement has successive layers of solid and gas which are perpendicular to the flow direction, as illustrated in

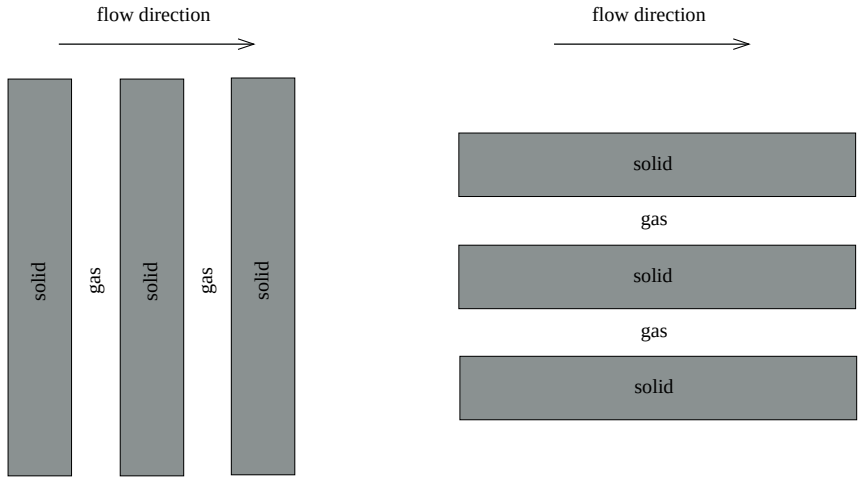

a) minimum conductivity b) maximum conductivity

Figure 2.13: Packing arrangements giving maximum and minimum axial heat conduction

figure 2.13 and gives the minimum conductivity,

$$\frac{k_{\text{eff}}^{\min}}{k_f} = \frac{1}{\varepsilon + (1-\varepsilon)k_f/k_s} \tag{2.70}$$

The parallel arrangement has successive layers of solid and gas parallel to the flow direction and gives an upper bound on the thermal conductivity:

$$\frac{k_{\text{eff}}^{\max}}{k_f} = \varepsilon + (1-\varepsilon)\frac{k_s}{k_f} \tag{2.71}$$

where $k_{f/s}$ is the fluid/solid thermal conductivity and ε is the void fraction. Using $k_{Ar} = 17 \times 10^{-3}$ W/mK, $k_{\text{mag}} = 4.23$ W/mK (from Mølgaard's correlation above), and $\varepsilon = 0.40$ this suggests that the effective conductivity will lie in the range of 0.042 W/mK $< k_{\text{eff}} <$ 2.54 W/mK.

A number of more complex models for effective conductivities are reviewed in [4]. These typically also consider factors such as the contact number – i.e., the number of other particles in contact with the particle in question. Kunii and Smith [129] developed correlations with and without radiation including parameters that describe the packing density and the contact number, but not the contact area. On the basis of data from Prasad et al. [130] Ref. [4] shows that the correlation without radiation fits experimental data well provided

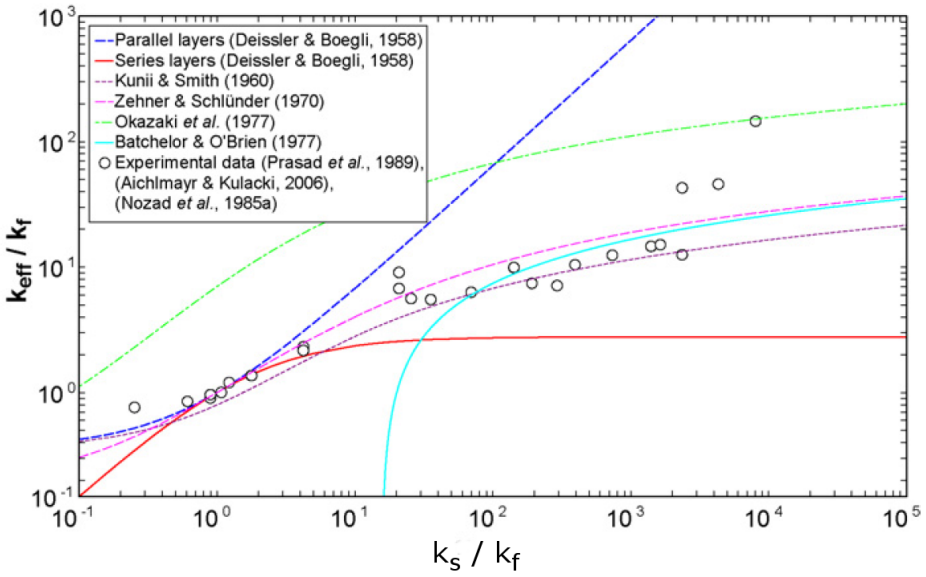

Figure 2.14: Comparison of experiments and theoretical correlations for the effective conductivity. Figure taken from van Antwerpen et al. [4]. Experimental data is from Prasad et al. [130]. The correlation developed by Kunii and Smith [129] is shown, as are the results using the minimum and maximum effective conductivity of equations 2.70 and 2.71 which were developed by Deissler and Boegli [128].

that $k_s/k_f < 10^3$, as shown in figure 2.14. Above this value, additional factors such as the contact area become important. (For the particular case given above with argon and magnetite $k_s/k_f \sim 250$). These experiments were carried out over quite a limited temperature range of 50 K.

Impact of radiation on effective conductivity

Zanganeh et al. [2] argues that radiation makes an important contribution to the effective conductivity, especially at high temperatures. Using Kunii and Smith's correlation, Zanganeh suggests that at around 900 K, radiation could contribute to 70% of the value of k_{eff}, giving k_{eff} a value of $\sim$2.0 W/mK. (For this analysis, Zanganeh used concrete as the solid medium, and air as the fluid). However, the inclusion of radiation in Ref. [2] only has a slight impact on the thermal front shapes.

A simplified model of radiation can be developed to estimate the dependence of the effective conductivity on various parameters. Particles are assumed to be arranged in layers,

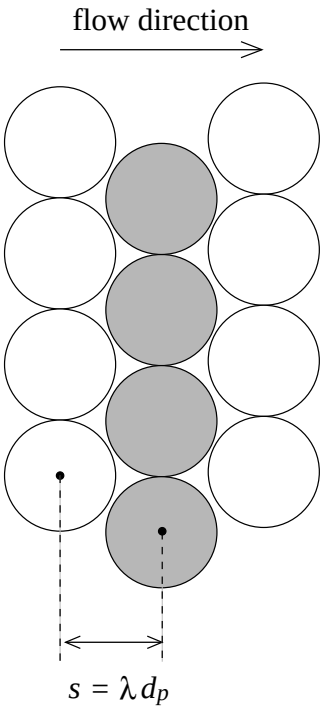

Figure 2.15: Idealised depiction of successive layers of spherical particles in a packed bed

and radiation occurs between the surfaces of one layer and the next, as illustrated in figure 2.15. The surfaces are uneven due to the curvature of the particles, but it is assumed that the surfaces are flat. The centres of successive layers are a distance $s = \lambda d_p$ apart, where λ is approximately unity. (For example, for close packed spheres of a uniform size, $\lambda = \sqrt{2/3}$). The heat transfer is modelled as a resistor network as shown in figure 2.16. With a view factor of $F = 1$ the rate of heat transfer $\dot{Q}$ is

$$\dot{Q} = \frac{\varepsilon \sigma A \left(T_1^4 - T_2^4\right)}{2 - \varepsilon} \tag{2.72}$$

Assuming that

$$T_2 \approx T_1 + \lambda d_p \frac{\partial T_1}{\partial x} \tag{2.73}$$

and comparing the resulting heat transfer rate to Fourier's law of conduction leads to an effective conductivity due to radiation of

$$k_{\text{eff}} \approx 4 \sigma \lambda d_p T_1^3 \tag{2.74}$$

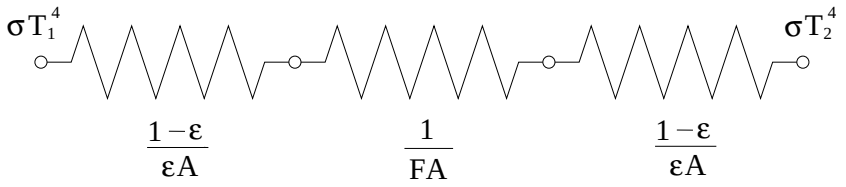

Figure 2.16: Electrical analogy for radiative heat transfer between successive layers of particles

where it has been assumed that the emissivity is one. If $\varepsilon < 1$ then k_{eff} is reduced slightly, but the correction can be absorbed into λ which is treated as an empirical factor. Equation 2.74 shows that larger particles increase the effective conductivity. k_{eff} also depends strongly on the temperature.

Figure 2.17(a) illustrates the correlations described using magnetite and argon. Radiation has a significant effect on the value of the effective conductivity, especially for high temperatures and large particles and this is consistent with [2,129]. Particle size is unlikely to have much of an effect on the effective conductivity in cold stores, where radiative effects are small. Hot stores may also see reasonably low values of k_{eff} despite the high temperatures, because particle sizes will be small due to the low pressure losses. The simplified model of equation 2.74 is shown for $d_p = 10$ mm and under-predicts k_{eff} compared to Kunii's expression. However, equation 2.74 does show the correct trends.

Impact of gas flow on effective conductivity

During charging and discharging phases, the turbulent transport of heat can have a significant effect on the effective conductivity, although quantifying this is difficult as explained above. Ref. [124] describes how the effective conductivity due to mixing of fluid could be represented as

$$\frac{k_{\text{eff,t}}}{k_f} = c\text{RePr} \tag{2.75}$$

where c is an empirical factor depending on the packing geometry, Re is the Reynolds number and Pr is the Prandtl number. Yagi and Kunii [123] argued that the physical processes that influenced k_{eff} for stagnant fluid and flowing fluid were independent of one another,

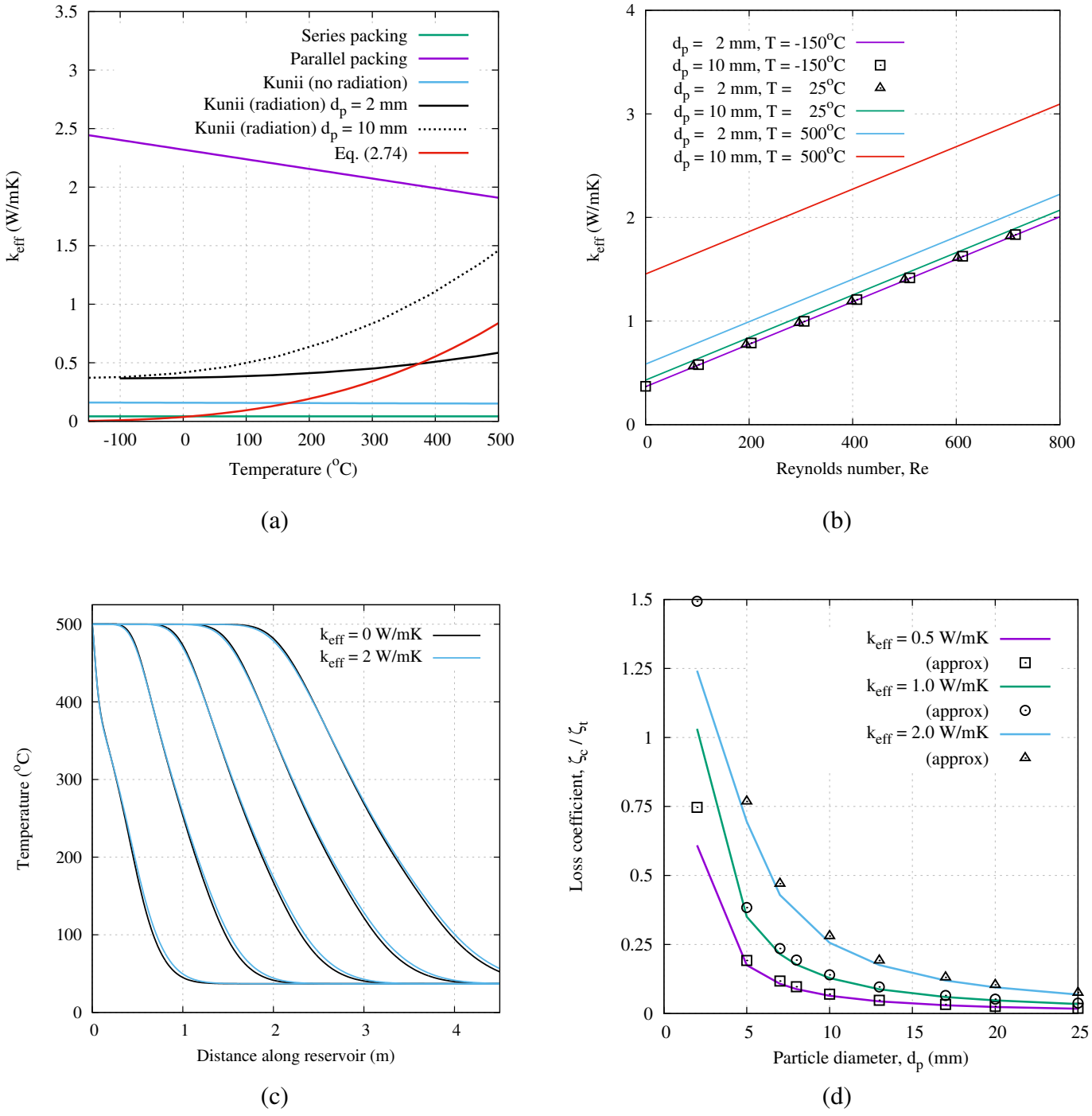

Figure 2.17: Correlations for axial effective conductivity k_{eff}^{x} and its impact on thermal front shape and availability losses in hot stores. **(a)** Correlations for effective conductivity k_{eff} in a stagnant fluid. Calculations for equation 2.74 are undertaken with $d_p = 10$ mm and $\lambda = 0.8$. **(b)** Correlations for effective conductivity k_{eff} in a flowing fluid. **(c)** Effect of conductivity on thermal front shapes in a hot reservoir with $d_p = 5$mm. **(d)** Conductive loss coefficient normalised by thermal loss coefficient for a hot reservoir (nominal design). Approximate values are given by equation 2.63.

and that a general correlation could therefore be given by

$$\frac{k_{\text{eff}}}{k_f} = \frac{k^o_{\text{eff}}}{k_f} + c\text{RePr} \tag{2.76}$$

where k^o_{eff} is the effective conductivity with stagnant fluid as given by Kunii and Smith [129]. Clearly, the presence of fluid flow increases the effective conductivity and this is shown in figure 2.17(b). For typical thermal reservoir designs, the Reynolds number varies between 10–200 for hot stores, and 50–500 for cold stores, depending on particle diameter and geometry. While these correlations are somewhat uncertain, they give approximate values that are useful for understanding the significance that axial conductivity may have in packed beds. On the basis of the above references, values of k_{eff} in the range of 0.5–1.5 W/mK seem realistic. The effective conductivity changes along the length of the bed since it depends on temperature. However, for realistic packed bed designs (where hot stores have small particles less than 2 mm and cold stores operate at low temperatures), these variations are small. Furthermore, the effective conductivities are sufficiently low to have an almost negligible impact on the thermal front shape (figure 2.17(c)). Given the uncertainty, it seems satisfactory to use an average value of k_{eff} rather than recalculating it at every time-step at each axial node along the reservoir.

Impact of conduction on losses

Figure 2.17(c) shows that axial conductivity does not have a significant effect on thermal front shape in a hot reservoir even when quite a large value of k_{eff} is chosen. Loss coefficients are shown for a range of particle diameters in figure 2.17(d). The conductive losses are shown as a fraction of thermal losses ζ_t and numerical results are compared to the simplified expression in equation 2.63. The figure shows good agreement between the numerical and approximate solutions, particularly for large d_p and low k_{eff} i.e. the cases when $T_g \approx T_s$ and conductivity does not significantly effect thermal profiles.

As would be expected from equation 2.62, conductive losses increase almost linearly with effective conductivity. In addition, figure 2.17(d) illustrates that ζ_c drops rapidly with particle diameter, since larger particles form thermal fronts with less steep gradients (i.e. $\partial T_s/\partial x$ is reduced). Figure 2.17(d) shows that conductive losses have a similar order of

magnitude to thermal losses, especially for small particles when thermal losses are lowest. Consequently, axial conduction is an important process to include in modelling of packed beds for thermal energy storage. Thermal losses were also seen to decrease by a small amount as the effective conductivity was increased, as conduction acts to spread out the thermal fronts. However, these effects were hardly significant, as conduction only has a small impact on the thermal gradient.

While conductive losses are not insignificant during charging and discharging phases, they will probably have the greatest impact during storage periods, although the extent of the losses will depend on the duration of storage and geometry of the system.

2.5.4 Heat leakage

The rate of available energy loss due to heat leakage is given by multiplying the rate of heat loss by the efficiency with which it could have been converted to work via a reversible heat engine, see figure 2.18. Thus,

$$\dot{W}_L = \int \left(1 - \frac{T_0}{T_s}\right) d\dot{Q}_L \qquad (2.77)$$

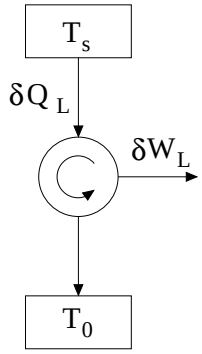

Figure 2.18: Reversible heat engine

Heat leakage may occur from the side walls and from the top or bottom of the store. For side wall leakage $d\dot{Q}_{L,w} = \pi D U_w (T_s - T_0) dx$, whilst heat transfer from an end wall is $\dot{Q}_{L,t} = \frac{\pi D^2}{4} U_t (T_s - T_0)$ where U is an overall heat transfer coefficient. (Note that this expression assumes flat end walls. It is likely that the end walls will in fact be a domed shape, meaning that the heat transfer area would be greater than $\pi D^2/4$). As with other loss coefficients, these lost work terms are multiplied by T_0 and integrated over time, noting that leakage losses occur during charge, discharge and storage phases, and normalised by the inlet available energy input during charge. Therefore,

$$\zeta_{L,w} = \frac{\pi D}{\dot{m} c_p t_{\text{chg}} \beta} \int_0^{t_{\text{chg}}} \int_0^L U_w \frac{(T_s - T_0)^2}{T_g} dx dt \qquad (2.78)$$

$$\zeta_{L,t} = \frac{\pi D^2}{4\dot{m} c_p t_{\text{chg}} \beta} \int_0^{t_{\text{chg}}} U_t \frac{(T_s - T_0)^2}{T_g} dt \tag{2.79}$$

To a first approximation, the overall heat transfer process can be estimated by considering a simple lumped heat capacity model for the packing and calculating the fractional energy loss per second, giving

$$\frac{dE_s}{dt} = -U_L A_L (T_s - T_0) = -\frac{U_L A_L}{M_s \bar{c}_s} E_s = -\frac{E_s}{\tau_L} \tag{2.80}$$

where E_s is the energy stored in the solid, U_L is the overall heat transfer coefficient, A_L is the surface area at the packing-insulation interface, and $\tau_L = M_s \bar{c}_s / U_L A_L$ is the heat leakage time constant. For instance, setting τ_L to 200 days corresponds to an internal energy loss rate of approximately 0.5% per day. (The fractional available energy loss will be somewhat higher, depending on T_s). Nominal designs for hot and cold stores are developed in chapter 3 and quantified in table 3.2. For the hot nominal design, with $L/D = 1$, $A_L = 8\pi R^2$ (including hemispherical ends), and setting $\tau = 200$ days, then the overall heat transfer coefficient is approximately

$$U_L = \frac{\rho_s \bar{c}_s R}{4\tau_L} \approx 0.13 \text{Wm}^{-2}\text{K}^{-1} \tag{2.81}$$

However, the lumped capacity model is only valid if the temperature distributions are radially uniform. White et al. [80] shows that, as would be expected, low Biot numbers are required in order to obtain uniform temperature profiles[1]. For an infinite cylinder the Biot number is given by $\text{Bi} = U_L R / k_{\text{eff}}$ where k_{eff} is the effective conductivity of packing. The requirement of a low Biot number thus places an upper limit on the overall heat transfer coefficient U_L: for a nominal design with $\text{Bi} = 0.01$ then $U_L \approx 0.11$ W m^{-2}K^{-1}.

The overall heat transfer coefficient U_L can also be calculated by considering the various thermal resistances between the solid particles and the atmosphere as described below.

[1]Radial temperature variations could be permitted, although it is not possible to asses the full impact that this would have on radial performance without undertaking two-dimensional calculations.

Thermal resistance of casing

Each material in the casing will contribute to the thermal resistance depending on its thickness and thermal conductivity. The insulation thickness t_I has the greatest influence, and should be set so as to reduce the overall heat transfer coefficient to a sufficiently low number, such as that described above. In addition, the insulation thickness may have to be increased further so that the steel temperature does not rise excessively (to prevent creep). The thermal conductivities of insulating materials vary by a factor of over 10, but a typical value for glass foam (a cheap and widely used insulator) is $k_i \approx 0.05$ $\mathrm{Wm^{-1}K^{-1}}$ [131].

The steel thickness t_s can be estimated from substituting the longitudinal σ_l and hoop σ_h stresses of a thin walled cylinder into the von Mises yield criterion, which is given by

$$(\sigma_h - \sigma_l)^2 + \sigma_h^2 + \sigma_l^2 = 2Y^2 \tag{2.82}$$

where Y is the yield stress of steel ($Y \approx 200$ MPa). The steel thickness is therefore given by,

$$t_s = \frac{\Sigma\sqrt{3}\Delta P r_I}{2Y} = \bar{\sigma} r_I \tag{2.83}$$

where Σ is a safety factor, r_I is the outer radius of the insulation, and $\Delta P = P_{in} + \rho_s g L - P_0$ is the pressure difference across the casing walls (including the hydrostatic pressure due to the packing material's weight). For designs that are typical for the present application, the steel thickness is roughly 10–20 mm for a hot store. Combining the high thermal conductivity the steel casing $k_s \approx 25$ $\mathrm{Wm^{-1}K^{-1}}$ [131] with the low thickness means that steel only makes a small contribution to the total thermal resistance.

Wall convective heat transfer coefficient

There are numerous correlations for the convective heat transfer coefficient at the packing-insulation interface h_w and a summary is presented by Ref. [132]. Evaluation of h_w is not straightforward due to radial variations in temperature, and the increased flow rate that may occur at the walls as a result of reduced particle packing density. Yagi and Wakao [133] developed a correlation which assumes that the temperature does not vary in the radial direction. Li and Finlayson [134] extended the analysis to consider radial temperature

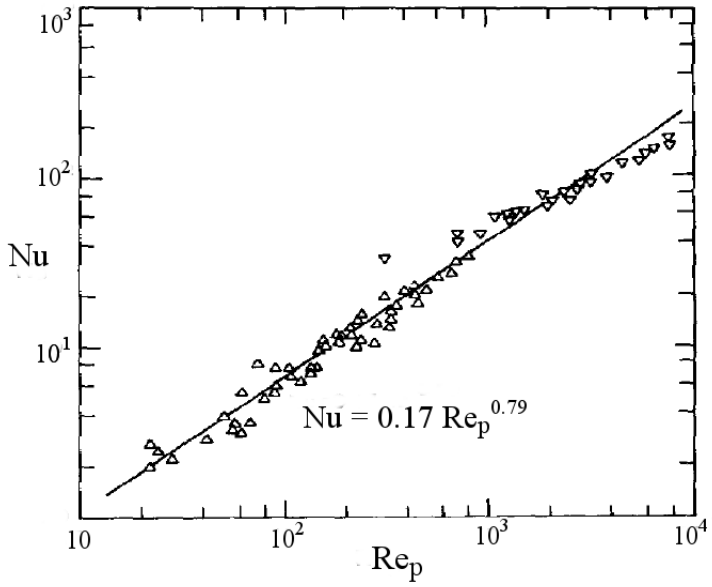

Figure 2.19: Comparison of experimental results and the correlation for the wall heat transfer coefficient developed by Li and Finlayson [134] in equation 2.84. Figure is taken from [134].

variations and an abrupt temperature change at the wall. This study also incorporated data from a range of sources (including Yagi) and developed the following correlation which fits experimental data well, as shown in figure 2.19.

$$\mathrm{Nu}_w = 0.17\mathrm{Re}_p^{0.79}; \qquad 20 \leq \mathrm{Re}_p \leq 7600 \tag{2.84}$$

where Nu_w is the Nusselt number at the wall and Re_p is the Reynolds number based on the particle diameter. Li and Finlayson found that this correlation fitted the data better than another widely used correlation developed by Beek [135]. Note that this correlation is not suitable for storage periods, since, as Ref. [136] points out, the correlation implies that $\mathrm{Nu}_w = 0$ when $\mathrm{Re}_p = 0$. Equation 2.84 yields a wall heat transfer coefficient in the region of $h_w \approx 14$ W m^{-2}K^{-1} for a hot store, and $h_w \approx 25$ W m^{-2}K^{-1} for a cold store, for nominal designs with average Reynolds numbers. The large value of h_w suggests that it may be reasonable to neglect these terms.

External convective heat transfer coefficient

Free convection on the outer surface of the reservoir can lead to the formation of a vertical plume that grows with increasing height. Again, various correlations exist for the external convective heat transfer coefficient h_x and are discussed in [137] and [138]. Ref. [138] compares various correlations for flat plates and isothermal cylinders, and flat plate correlations provide a good approximation for aspect ratios close to or less than 1 (which is likely in thermal stores). A common flat plate correlation was developed by Churchill and Chu [139] and is given by

$$\mathrm{Nu}_x = 0.68 + \frac{0.67(\mathrm{GrPr})^{0.25}}{\left\{1 + \left(\frac{0.492}{\mathrm{Pr}}\right)^{\frac{9}{16}}\right\}^{\frac{4}{9}}} \tag{2.85}$$

where Gr is the Grashoff number, which for ideal gases is given by

$$\mathrm{Gr} = \frac{g\beta(T_x - T_0)L^3}{\nu^2} \approx \frac{g(T_x - T_0)L^3}{\bar{T}\nu^2} \tag{2.86}$$

where $\bar{T} = 1/2(T_x + T_0)$. As the stores charge and discharge the surface temperature changes with position and time and consequently a steady-state plume is not formed. One approximation is to take $L = R$ which corresponds to a half charged reservoir. For lower states of charge, the effective height over which buoyancy driven flow can develop is reduced and leads to lower Grashoff and Nusselt numbers. However, convective currents are then likely to be dominated by heat transfer at the top surface of the vessel. The surface temperature is required to calculate Gr so that knowledge of the thermal resistance of the casing is required before T_x can be calculated iteratively. A constraint is placed on the maximum surface temperature and the insulation thickness is recalculated if this value is exceeded. For a maximum value of $|T_x - T_0| = 50$ K, the external heat transfer coefficient is approximately $h_x \approx 2.75$ W m^{-2}K^{-1} for a nominal hot reservoir.

Overall heat transfer coefficient – illustrative example

Each of the above processes contributes to the overall thermal resistance. The relative magnitude of these processes may be compared by considering an illustrative example

with a hot packed bed radius of $R = 2.5$ m and insulation thickness of $t_I = 0.5$ m. The overall heat transfer coefficient for the side walls is given by

$$\frac{1}{U_w} = \frac{1}{h_w} + \frac{R\ln(1+t_I/R)}{k_I} + \frac{R\ln(1+\bar{\sigma})}{k_s} + \frac{R+t_I(1+\bar{\sigma})}{Rh_x}$$

$$\frac{1}{U_w} = \underset{\text{Internal convection}}{0.07} + \underset{\text{Insulation}}{9.12} + \underset{\text{Steel}}{0.001} + \underset{\text{External convection}}{0.44}$$

Each term has been estimated by using the approximate values developed above. The thermal resistance due to the insulation clearly dominates, and the other factors may be neglected.

The analysis on page 77 suggested a value for the overall heat transfer coefficient of $U_L = 0.11$ W m^{-2}K^{-1}. The insulation thickness may be calculated by only considering the insulation term in the above equation, yielding

$$t_I = R\left[\exp\left(\frac{k_I}{RU_w}\right) - 1\right] \approx 0.5 \text{ m} \tag{2.87}$$

(In fact, this value slightly over-estimates the required insulation thickness.) The surface temperature are then calculated by the inclusion of the h_x term and, as discussed above, if this exceeds the desired surface temperature, the insulation thickness is increased accordingly (although the surface temperature is rarely found to exceed 50°C. In this instance it is 45°C for the hot store).

Strictly speaking, for accurate evaluation of heat leakage and the associated availability loss, the overall heat transfer coefficient should be re-calculated at every x position and time-step in order to take into account variations in h_w and h_x. However, since the vast majority of thermal resistance is provided by the insulation, this is unnecessary and has a negligible effect on the results. It is more efficient and straightforward to assume that U_w remains at a constant value determined by either the heat leakage time constant τ, the Biot number constraints, or the steel surface temperature requirement; whichever provides the lowest value of U_w.

2.5.5 Exit losses

Exit losses ζ_x occur as the thermal fronts approach each end of the reservoir, as shown by the 85% charged curve in figure 2.11(b). When the 'nose' of the thermal front emerges from the reservoir at a temperature greater (or less) than ambient temperature a loss in available energy is incurred. These exit losses serve to 'flush' entropy out of the reservoir. Since irreversible processes occur internally in the reservoir, for the reservoir to reach a cyclic state then the entropy of the system must be reduced and thus exit losses cannot be avoided. Consequently, exit losses are closely related to thermal losses ζ_t.

The loss coefficient is defined as the excess availability energy leaving the store above that which occurs if the gas exited at the design temperature and pressure. For instance, during the charge of a hot reservoir the gas initially leaves the reservoir at temperature T_2 and an exit loss occurs when the exit temperature $T_x > T_2$. Thus, the loss coefficient is

$$\zeta_x = \frac{1}{B_{\text{in}}} \int_0^{t_{\text{chg}}} \left\{ \dot{B}(T_x, p_1) - \dot{B}(T_2, p_1) \right\} dt \tag{2.88}$$

Note, that the availability fluxes are calculated using the reservoir inlet pressure, because pressure losses have already been accounted for in the pressure loss coefficient.

In principle, the available energy in the exit flow could be recovered and utilised. There are many uses for excess industrial heat [140, 141], and a commonly discussed application is domestic heating. As such, it is unclear whether exit losses should be included in definitions of the round-trip efficiency. Whilst exit losses are a loss of availability from the reservoir, it is conceivable that it should not be counted as a loss if that energy is used elsewhere. Furthermore, for reservoirs that are part of a thermodynamic cycle such as PTES, this energy could be recovered in other parts of the cycle.

2.5.6 Storage losses

Storage losses ζ_s are the availability losses that are incurred during storage periods and are comparable to self-discharge of batteries. Axial conduction causes thermal gradients to decay. In the case where there is no heat leakage (perfectly insulated store) and the total energy within the store remains constant, the degradation of the thermal gradients

results in a loss of availability. Furthermore, heat leakage reduces the energy content of the reservoir and contributes to the storage loss. While insulation thickness and effective conductivity are important parameters, it is obvious that storage losses depend heavily on the duration of storage. Innovative reservoir design (such as segmenting the stores) can reduce these effects significantly, but cannot eradicate them completely. Thermal stores are consequently more appropriate for storage durations of hours to weeks rather than months.

The storage loss is calculated as the difference in availability within the reservoir between the beginning and end of storage

$$\begin{aligned} \zeta_s &= \frac{\rho_s A(1-\varepsilon)}{\dot{m} c_p \beta t_{\text{chg}}} \int_0^L c_s \left(T_b - T_e - T_0 \ln\left(\frac{T_b}{T_e}\right)\right) dx \\ &\approx \frac{1}{V_f \beta t_{\text{chg}}} \int_0^L T_b - T_e - T_0 \ln\left(\frac{T_b}{T_e}\right) dx \end{aligned} \tag{2.89}$$

where T_b and T_e are the temperatures in the reservoir at the beginning and end of storage. The maximum storage loss occurs after an infinite time when the thermal front has completely equilibrated. For an adiabatic store, this is achieved once the storage medium has reached a uniform temperature given by its average value

$$\bar{T} = \frac{1}{L} \int_0^L T_s(x) dx \tag{2.90}$$

2.5.7 Radiative losses

Radiative losses are a special case of availability loss, and occur when a packed bed has been segmented. Segmentation is a design feature where the packed bed may be divided into separate layers. Segmentation is discussed comprehensively in section 3.3 and a schematic is given in figure 3.8. Each segment or layer is separated by a small gap. During charge and discharge, gas flows out of one segment, through the gap and into the next segment, such that the gap may be assumed not to be present. On the other hand, there is no gas flow between segments that are inactive or during storage phases. Heat transfer still occurs between segments by conduction through the gas (which is small), convection and radiation. Convective processes are neglected by noting that the packed-beds are orientated such that hot regions are at the top in order to reduce buoyant forces.

Radiation between two successive layers is modelled with an electrical analogy similar to that in figure 2.16. For segments of area $A = \pi r^2$ with a view factor of $F = 1$ between them, the rate of heat transfer is

$$\dot{Q} = \frac{\varepsilon \sigma A}{2 - \varepsilon} \left(T_1^4 - T_2^4 \right) \tag{2.91}$$

where ε is the emissivity of the particles in the segment which may be assumed to be close to 1 for pebbles due to their low reflectivity. The irreversible entropy generation is given by

$$\dot{S}_{\text{irr}} = \left(\frac{1}{T_2} - \frac{1}{T_2} \right) \dot{Q} = \frac{\varepsilon \sigma A}{2 - \varepsilon} \frac{(T_1 - T_2)}{T_1 T_2} \left(T_1^4 - T_2^4 \right) \tag{2.92}$$

Simplifications can be made to this expression if $T_1 \approx T_2$ but this is not necessarily the case between segments. As is discussed further in section 3.3.2, heat transfer between layers reduces the benefits that segmentation is thought to provide.

2.6 Summary

In this chapter, the underlying theory of packed-bed thermal reservoirs has been described. The governing equations have been derived, appropriate methods of solution have been discussed, and a number of processes that reduce the available energy have been introduced. Whilst much of the behaviour is complex, employing a number of simplifications develops an understanding of these processes. For instance, thermal losses were seen to depend on the particle diameter, the duration of charging in cyclic operation and the variation of the specific heat capacity with temperature. c_s was also seen to have a significant impact on the shape of the thermal fronts. The value of the axial effective conductivity is a source of uncertainty, but a consideration of various correlations suggests that for the current application k_{eff}^x is sufficiently small that it does not significantly affect thermal front shapes, and that conductive losses only have a comparable magnitude to thermal losses at small particle sizes. Conduction is therefore not negligible and it is especially important in storage phases.

Other simplifications include assuming that effective conductivities and overall heat transfer coefficients remain constant throughout operation of the bed. These adjustments were

justified based on the realistic magnitudes of each process. Some confidential experimental results were made available by Isentropic Ltd., from which it has been possible to verify that the reported figures have realistic magnitudes. Moreover, a survey of the literature demonstrated that these kind of theoretical analyses were comparable to experimental results. Further experimental work is clearly required in order to justify these claims. Furthermore, there are some assumptions that may not be particularly realistic. For instance, particles are unlikely to be spherical and uniformly sized. An understanding of the impact of rough, unevenly shaped particles could be achieved through experiments or detailed CFD simulations.

Chapter 3

Behaviour of packed-bed thermal reservoirs

3.1 Introduction

In the previous chapter, a thermodynamic model of packed-bed thermal reservoirs for energy storage applications was described. Availability loss coefficients were defined and these are used to assess the performance and behaviour of thermal reservoirs in this chapter.

Packed bed behaviour is reasonably well understood [112, 113]. Thermal and pressure loss coefficients have been investigated by White [60] but this analysis is extended in this chapter to include conductive losses, heat leakage losses, and losses during the storage phase. Parametric studies are presented in section 3.2 and involve varying each design parameter individually, and quantifying its effect on each loss coefficient. These results provide an understanding of reservoir behaviour from a second law perspective that is necessary for design and optimisation of PTES systems.

Establishing the major factors that affect performance enables innovative design features to be developed and two such features are investigated. The first is 'segmentation' of the packed bed into discrete layers that the gas may be diverted around or directed into. In the context of energy storage, this idea was developed by Isentropic Ltd. [108], and papers have been written on the subject by White and McTigue [80, 81]. The present author extended the thermal reservoir model to include segmented stores, and the behaviour of these stores during charge and discharge is presented in section 3.3. The performance of segmented stores during storage phases is also of interest, and an account is given in section 3.3.2.

A second innovative design feature is radial-flow packed beds. These stores have been patented [142, 143] and some numerical and experimental results are given in [74]. In section 3.4, the governing equations are derived and a method of solution is described based on that presented in section 2.4. The behaviour of radial-flow packed beds is described in terms of loss coefficients and compared with the performance of axial-flow stores.

3.2 Parametric studies of reservoir thermodynamics

The impact of key design variables is investigated through parametric studies: each parameter is varied, whilst the others are held constant at nominal design values given in table 3.1. This approach develops an understanding of reservoir behaviour, and informs decision making during optimisation. The variables are divided into two categories: *design parameters* that are fixed once the packed bed has been constructed, and *operational parameters* that can be varied during operation.

The nominal packed bed designs in table 3.1 are chosen such that if the two reservoirs were integrated into a PTES system as described in section 1.5.3, the device would have a nominal energy storage capacity of $\Delta E_{\max} = 16$ MWh which could be delivered at $\dot{W}_{\max} = 2$ MW. The nominal charging and discharging durations are therefore 8 hours[1]. Two storage phases of four hours (after each charge and discharge period) allow the system to operate on a 24 hour cycle. Typical behaviour of the nominal reservoirs is tabulated in table 3.2 which gives the round-trip efficiency χ as defined by equation 2.44, loss coefficients as defined in section 2.5 and the available energy that is returned during discharge as given by

$$B_{\text{ret}} = \chi B_{\text{in}} \tag{3.1}$$

where B_{in} is the net flux of available energy during charge.

Control of the reservoir charging period

The normalised cycle period Π is defined as the charging duration as a fraction of the nominal charging time, $\Pi = t_{\text{chg}}/t_N$. This may also be interpreted as the reservoir *utilisation* because it corresponds to the extent to which the reservoir is charged. The reservoir charge and discharge durations can be controlled in a number of ways, and the most obvious method is to switch between charge and discharge after fixed periods of time have elapsed. However, in practice the utilisation is likely to be controlled by ending the current operation phase once the exit temperature of the packed bed reaches a certain threshold. This

[1] This is the time required to fully charge the reservoirs, in accord with equation 2.5. In practice the actual charging and discharging duration will be less than this in order to avoid large exit losses.

System properties		PTES	
Energy capacity	$\Delta E_{\max}$	16.0 MW h	
Power	$\dot{W}_{\max}$	2.0 MW	
Nominal charge time	t_N	8 hours	
Exit temperature fraction	$\theta_{c,d}$	0.25	
Charging time	t_{chg}	5.4 hours	
Working fluid		Argon (Ar)	
Gas specific heat capacity	c_p	520 J/kgK	
Heat capacity ratio	γ	1.667	
Mass flow rate	$\dot{m}$	13.7 kg/s	
Packing material		Magnetite (Fe_3O_4)	
Particle diameter	d_p	20 mm	
Void fraction	ε	0.40	
		Hot reservoir	Cold reservoir
Charging temperature	T_1	505°C	-150°C
Discharging temperature	T_2	37°C	37°C
Pressure	P	10.5 bar	1.05 bar
Effective thermal conductivity	k_{eff}	0.5 W m^{-1} K^{-1}	0.5 W m^{-1} K^{-1}
Overall heat transfer coefficient	U_w	0.16 W $m^{-2}K^{-1}$	0.09 W $m^{-2}K^{-1}$
Length	L	4.58 m	5.45 m
Diameter	D	4.58 m	5.45 m
Packing volume	V_{pack}	75.5 m^3	127.1 m^3
Insulation thickness	t_I	238 mm	342 mm
Steel thickness	t_s	16 mm	2 mm
Total volume	V_{tot}	128 m^3	222 m^3

Table 3.1: Nominal PTES and packed bed designs

method is straightforward to monitor and would prevent excessive heat rejection. Temperature thresholds for the charging and discharging periods may be varied independently. The thresholds are defined as a fraction of the temperature difference in the reservoir:

$$\begin{aligned} \theta_c &= \frac{T_x^c - T_2}{T_1 - T_2} \\ \theta_d &= \frac{T_x^d - T_1}{T_1 - T_2} \end{aligned} \tag{3.2}$$

where $\theta_{c,d}$ is the charging or discharge temperature threshold, and $T_x^{c,d}$ is the exit temperature of the gas during charge or discharge. Larger values of θ correspond to higher utilisations and energy densities, as shown in figure 3.1. For the case where $\theta_c \neq \theta_d$ charging and

	χ (%)	ζ_t (%)	ζ_p (%)	ζ_c (%)	ζ_L (%)	ζ_s (%)	B_{ret} (MW h)
Hot store	94.97	4.47	0.03	0.07	0.18	0.28	7.13
Cold store	86.55	10.90	1.47	0.20	0.29	0.59	2.96

Table 3.2: Efficiency and losses in nominal packed bed designs

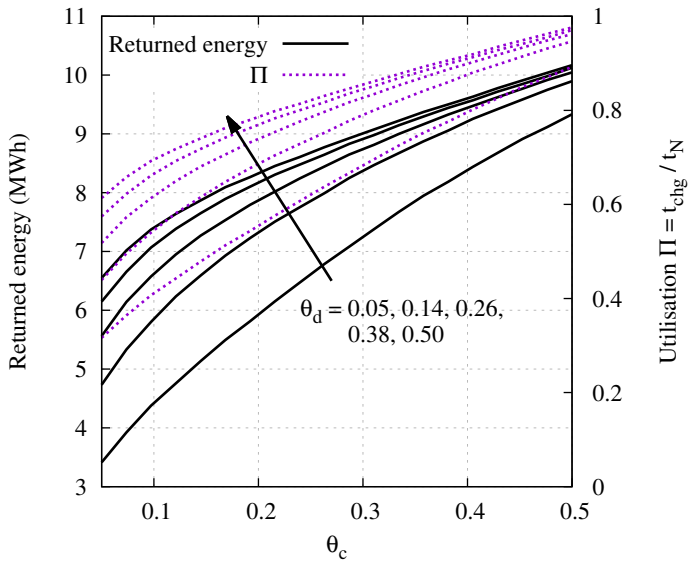

Figure 3.1: Effect of θ_c and θ_d on the returned energy and utilisation of a hot store

discharging durations are roughly equal during cyclic operation.

The following studies use $\theta_{c,d}$ to control the cycle period, and these values are fixed at 0.25 unless otherwise specified. It is worth noting that the thermal gradient is affected by the choice of design and operational variables. As a result, when $\theta_{c,d}$ are constant the utilisation may change if other parameters are varied.

Packed beds can be operated in a number of ways. 'Single-blow' operation involves a single charge-discharge cycle. On the other hand, in 'cyclic' operation the stores are repeatedly charged and discharged for the same duration each cycle. In practice, the stores may be required to operate more flexibly in order to meet constraints set by economic factors or the electrical grid. As a result, charge and discharge periods may change from cycle to cycle, while mass flow rates may be varied in order to change to power output. Understanding the impact of these erratic load cycles requires a comprehensive study and a knowledge of the

typical load cycles that may occur. The subsequent investigations use cyclic operation, as this mode could be used to smooth daily demand fluctuations.

3.2.1 Design parameters

Aspect ratio and particle diameter

The particle diameter and aspect ratio are varied whilst holding the reservoir volumes, mass flow rate and operating temperatures constant, thereby ensuring that the nominal storage capacity and power also remain constant. Figure 3.2 shows how each loss coefficient varies with d_p and L/D for hot and cold stores. As with all heat exchange processes there is an inherent trade-off between efficient heat transfer and low pressure loss, which manifests itself as an optimal particle diameter and aspect ratio. Increasing the aspect ratio and decreasing the particle size both increase frictional effects, thereby increasing ζ_p, but cause a decrease in ζ_t since the area for heat transfer is increased and dissipative effects are reduced.

The optimal shape of cold reservoirs is shorter and fatter than that of the hot stores due to the dominant effect of pressure losses: cold reservoirs have lower gas densities, larger gas velocities, and a lower pressure meaning that a given pressure drop has a greater impact. The large pressure losses in cold reservoirs also lead to larger optimal particle sizes than in hot stores. Pressure losses only become significant in hot reservoirs for rather large aspect ratios and very small particles.

Storage losses

Storage losses are less significant than thermal or pressure losses. Storage losses are composed of conductive and leakage losses during the storage phase, hence ζ_s follows a similar trend to ζ_c (which itself is closely related to the thermal gradient and therefore to ζ_t, as shown in equation 2.62). Conductive losses drop continuously as d_p is increased but storage losses show a slight increase at large particle sizes. Figure 3.3(a) shows that large particles lead to less steep thermal fronts which consequently reach the exit of the packed bed sooner. Since the full cycle is fixed at 24 hours, the impact of large particles is to reduce charging duration and increase storage duration.

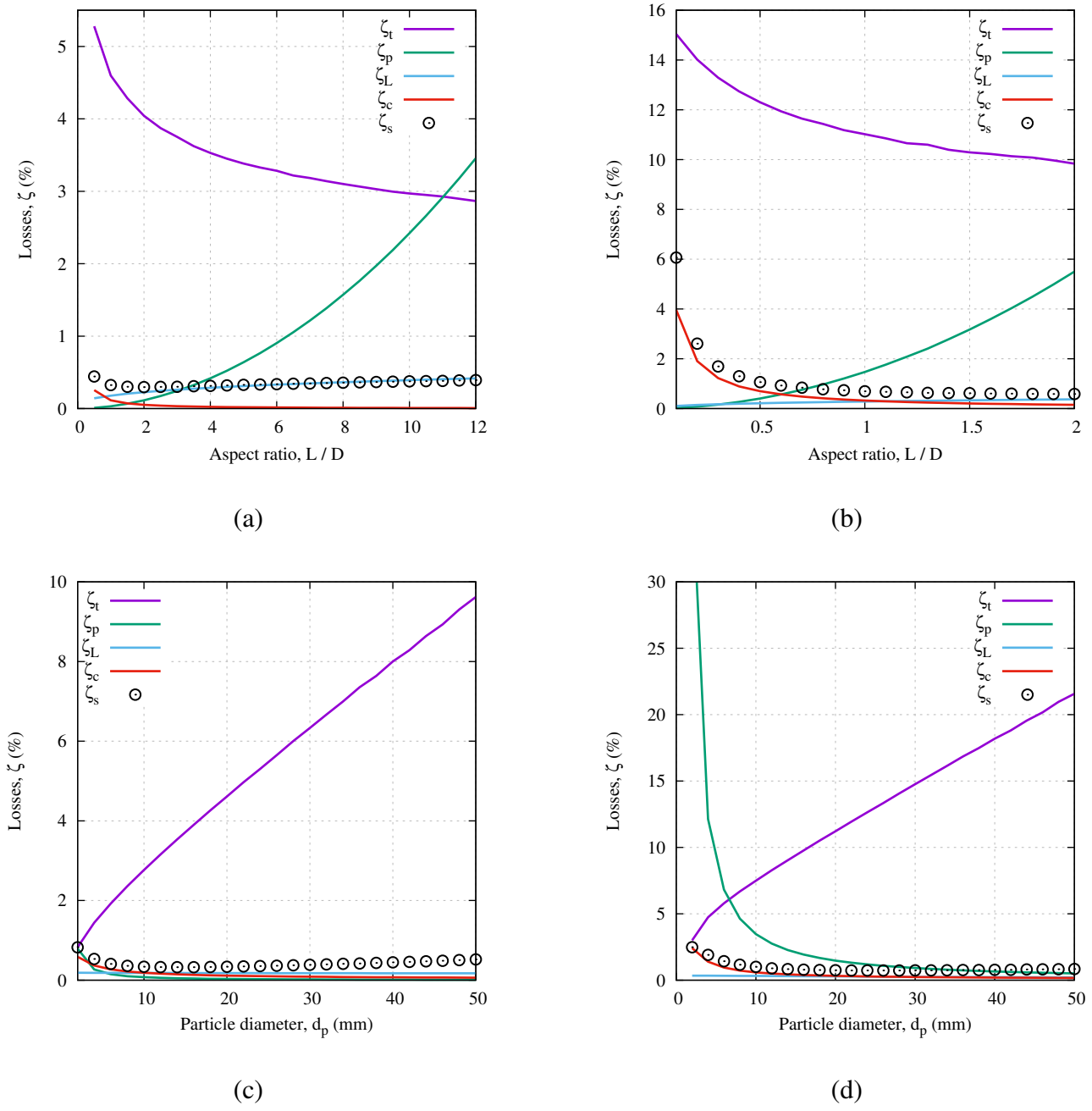

Figure 3.2: Parametric study of aspect ratio and particle diameter on hot and cold packed beds **(a)** Effect of aspect ratio on losses in a hot store (d_p = 20 mm) **(b)** Effect of aspect ratio on losses in a cold store (d_p = 20 mm) **(c)** Effect of particle diameter on losses in a hot store (L / D = 1) **(d)** Effect of particle diameter on losses in a cold store (L / D = 1)

The shape of the thermal fronts has an impact on the energy that is stored in the packed bed. Figure 3.3(b) displays the round-trip efficiency χ against the available energy that is returned during the discharge phase B_{ret}. Decreasing the particle size leads to steeper fronts and generally increases the quantity of energy that is returned during discharge. However, very small particles and large aspect ratios lead to large pressure losses, which reduces the round-trip efficiency and therefore also reduces the returned energy (consider the open point on the $d_p = 5$mm curve).

Figure 3.3(c) indicates that smaller aspect ratios lead to thermal fronts that take up a larger fractional length of the reservoir. As these fronts are 'less steep' a smaller quantity of energy is returned. Increasing the aspect ratio increases the returned energy, until pressure losses become significantly large and reduce the efficiency in a similar way to that shown in figure 3.3(b).

Packing material

The choice of storage media is an important consideration in the design of the PTES system. The material must fulfil several requirements, such as good thermal and mechanical properties – e.g. it should be able to resist the compressive forces due to its own self weight. Ideally, the material should also be cheap, widely available, environmentally friendly and non-toxic. In order to make detailed comparisons between materials, a mechanical model of the particles should be developed (e.g. particle packing and arrangement, how the particles compact or interact with one another, and how this changes with time) so that the interactions between mechanical stresses and thermodynamic behaviour can be considered such as in [144, 145]. The development of a mechanical model is outside the scope of this thesis which concentrates on the thermodynamic performance.

The availability density provides a useful metric to compare different materials and is given by

$$\rho_a = \rho_s(1-\varepsilon)\left[(e_{\mathrm{chg}} - e_{\mathrm{dis}}) - T_0(s_{\mathrm{chg}} - s_{\mathrm{dis}})\right] \tag{3.3}$$

Data for several suitable materials are given in table 3.3, where the values are calculated for the nominal design. By comparison, PHES with a height difference of 500 m has a density of 5 MJ m^{-3} of water, whilst CAES at 100 bar has a value of around 36 MJ m^{-3}

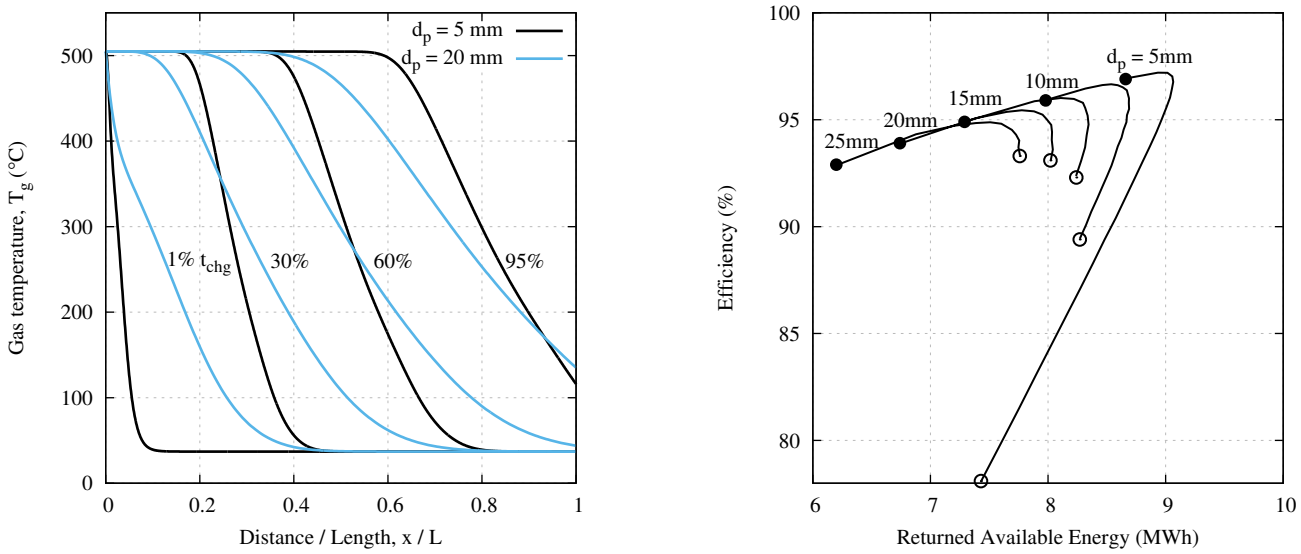

(a)

(b)

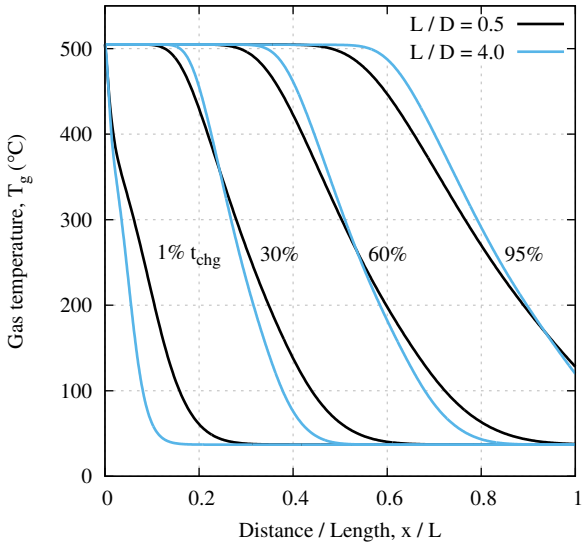

(c)

Figure 3.3: Parametric study of aspect ratio and particle diameter on hot packed beds. **(a)** Effect of particle diameter on thermal front shape in hot stores **(b)** Effect of geometric parameters on the trade-off between efficiency and returned available energy in a hot store. Lines of constant d_p are plotted and L/D is varied along the lines. Filled and open points mark the minimum and maximum L/D, respectively. **(c)** Effect of aspect ratio on thermal front shapes in hot stores

		Al_2O_3	Fe_2O_3	Fe_3O_4	SiO_2	TiO_2
Hot reservoir	ρ_s (kg m^{-3})	4040	5242	5175	2650	4230
	ρ_a (MJ m^{-3})	509	534	549	327	425
	$\bar{c}_s$ (J/kg·K)	1070	850	860	1020	855
	$\Delta c_s/\bar{c}_s$	0.347	0.367	0.468	0.433	0.242
	$\bar{k}_s$ (W/m·K)	25.50	4.83	3.50	8.20	7.50
Cold reservoir	ρ_s (kg m^{-3})	4040	5242	5175	2650	4230
	ρ_a (MJ m^{-3})	85	112	121	65	100
	$\bar{c}_s$ (J/kg·K)	540	500	520	570	550
	$\Delta c_s/\bar{c}_s$	1.048	0.774	*0.643*[a]	0.740	0.708
	$\bar{k}_s$ (W/m·K)	56.80	6.95	3.94	22.50	11.0

Table 3.3: Physical properties of materials for hot and cold thermal stores. Data for densities and heat capacities taken from [146] and [147], thermal conductivities are from [148] and [127].
[a] $\Delta c_s/\bar{c}_s$ for magnetite has been calculated as if there were no spike in c_s at 120 K (see figure 2.10), in order to give a more representative value. The true value is 0.20 but this is distorted by the presence of the spike which is apparently due to a magnetic effect. While not included in the calculation of $\Delta c_s/\bar{c}_s$ this feature has been included in the calculation of losses.

of compressed air, demonstrating that thermal stores achieve competitive energy densities [97].

The solid specific heat capacity c_s varies with temperature, as shown in figure 2.10 on page 61. This causes the length of the thermal front to fluctuate, which subsequently affects the thermal losses since the area for heat transfer is changed. The extent to which fronts steepen or spread is dependent on the range of heat capacities over which the reservoir operates. Table 3.3 gives the fractional change in heat capacity $\Delta c_s/\bar{c}_s$ for each material over the range of operating temperatures, where $\bar{c}_s$ is the average heat capacity (defined by equation 2.4). In cyclic operation, the greater the value of $\Delta c_s/\bar{c}_s$, the more the length of the thermal front changes about its average gradient, and therefore the greater the thermal losses, as discussed in section 2.5.1 and appendix A.

Figure 3.4 shows the distribution of losses for hot and cold reservoirs in cyclic operation for different materials. Pressure and leakage losses are insensitive to the choice of material. Thermal losses in the hot reservoirs do not vary significantly due to smaller variations in heat capacity at high temperatures (figure 2.10). The choice of material has a more significant effect in cold reservoirs, however, since the heat capacity curves are steeper at low temperatures. Magnetite (Fe_3O_4) is a promising material due to its low variation in

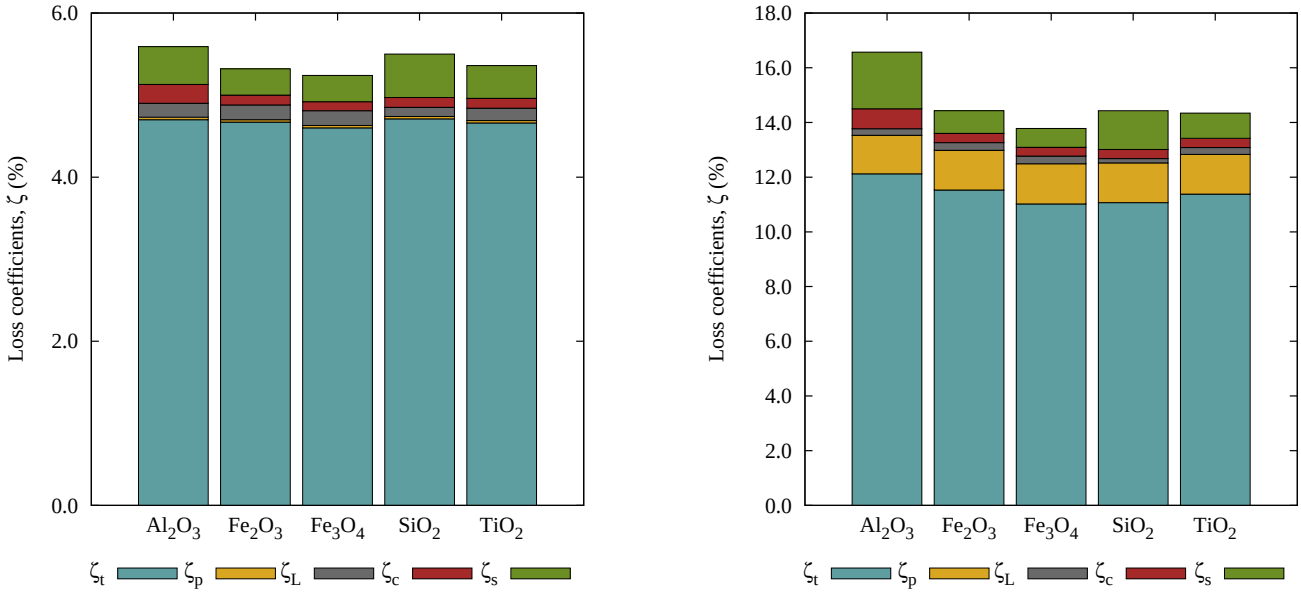

(a) Hot store

(b) Cold store

Figure 3.4: Distribution of losses for different packing materials computed at the nominal conditions of table 3.1

heat capacity.

Conductive losses are fairly similar in each of the materials. Table 3.3 indicates that each material has quite different values of average thermal conductivity $\bar{k}_s$. However, it was found that the solid conductivities did not significantly affect the effective conductivity k_{eff} which was calculated using the correlations of section 2.5.3 (i.e. k_{eff} is dominated by contributions from radiation and the turbulent transport of heat). Aluminium oxide has the largest conductive and storage loss as a result of the large solid conductivity.

These results suggest that the choice of material has an important effect on the thermal losses, particularly in cold stores. For the temperature ranges considered, magnetite appears to be the most suitable material, and aluminium oxide the least suitable. However, this choice may change if different temperature ranges are chosen. It is conceivable that hot and cold reservoirs may use different materials in order to exploit the material with the best heat capacity profile for that temperature range. Furthermore, mechanical properties and cost will play an important role in material selection.

Reservoir sizing

Reservoirs of different volumes are compared in this section. The operating temperatures of the packed beds are fixed and the availability capacity of the stores therefore varies in proportion with the volume. The nominal charge time t_N of the reservoirs is held constant at 8 hours, and the stores are cycled with a period of $\Pi = t_c/t_N = 0.75$ (6 hours). The mass flow rate is varied in order to keep t_N constant and is thus

$$\dot{m} = \frac{\rho_s c_s (1-\varepsilon) V_{\text{pack}}}{c_p t_N} \tag{3.4}$$

where V_{pack} is the volume of the packing material.

The mass flow rate scales with the cube of the packed-bed length scale, such that the mass flow rate per unit area is proportional to the length scale,

$$G = \frac{\rho_s c_s (1-\varepsilon)}{c_p t_N} L \tag{3.5}$$

The variation in mass flow rate per unit area is directly responsible for an increase of ζ_p with volume, and for a decrease in ζ_t and ζ_c as the volume increases as shown in figure 3.5(b). Leakage losses also decrease as the volume is increased at constant aspect ratio since the surface area to volume ratio is given by $4/D$.

The trade-off between thermal losses and pressure losses leads to an optimal packing volume. As the aspect ratio is increased, this optimal point occurs at smaller volumes due to the increased pressure losses that occur. Comparable behaviour was observed in the cold store.

3.2.2 Operational parameters

Cycle frequency

Once the packed bed has been constructed the geometric parameters are fixed. Operational parameters, such as the cycle frequency and the operating temperatures influence the efficiency and energy density. Previous work [60, 84] has indicated that one of the most

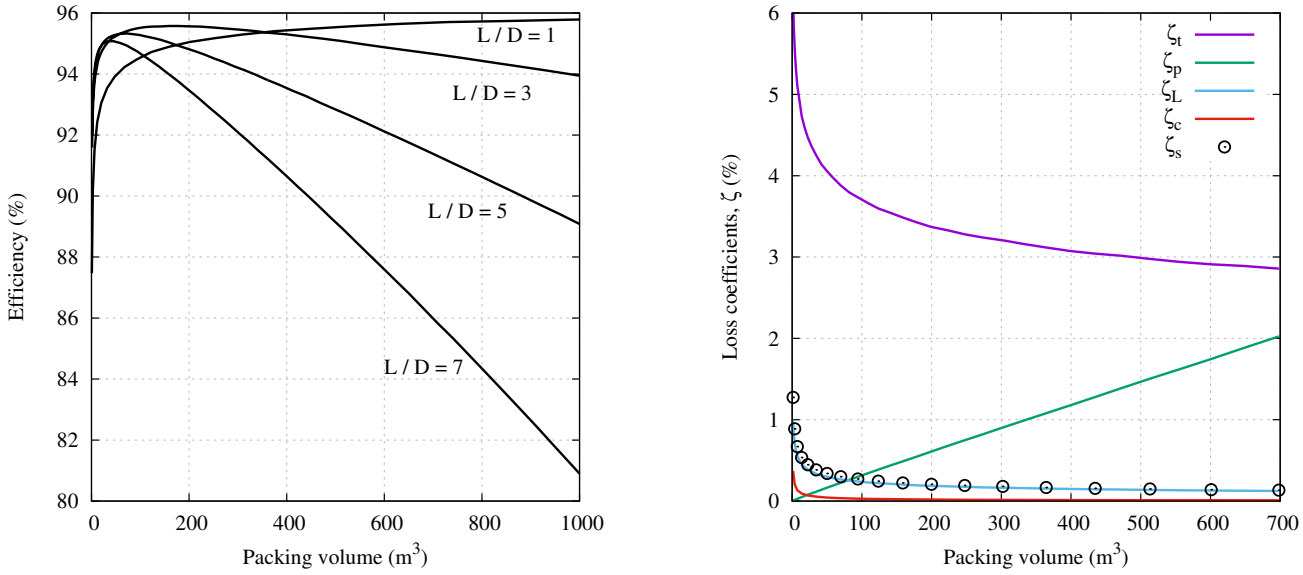

(a) (b)

Figure 3.5: Effect of reservoir sizing on availability losses in packed beds for $\Pi = 0.75$ **(a)** Round-trip efficiency of hot stores for different volumes and aspect ratios **(b)** Breakdown of availability losses in a hot store for $L/D = 3$

significant parameters is the normalised cycle period, Π.

During cyclic operation, instantaneous temperature profiles are identical from one cycle to the next and the packed bed returns to its original state at the end of the cycle. Information must be propagated along the entire length of the reservoir in order to flush out entropy that was generated irreversibly within the packed bed. When $\theta_{c,d}$ (or Π) is low, the thermal front moves only a small fraction of the reservoir length. The thermal front must therefore become longer and less steep, as shown in figure 3.6(a). Heat transfer then occurs over a larger surface area reducing thermal losses, although the energy density of the storage is compromised, as shown in figure 3.1. The utilisation therefore controls the trade-off between efficiency and energy density.

Figures 3.6(b) and 3.6(c) indicate that lower $\theta_{c,d}$ lead to larger efficiencies. However, the orientation of the constant efficiency lines indicate that these parameters do not have an equal impact. The efficiency is more sensitive to θ_c than θ_d in hot packed beds, and the opposite is true in cold packed beds. Calculating the correlation coefficients between θ and

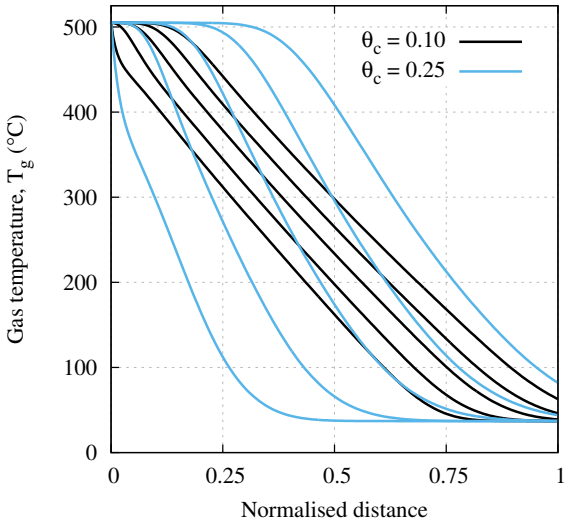

(a)

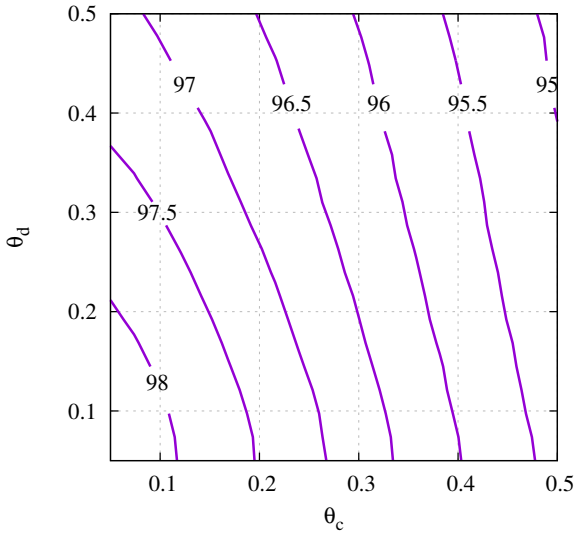

(b)

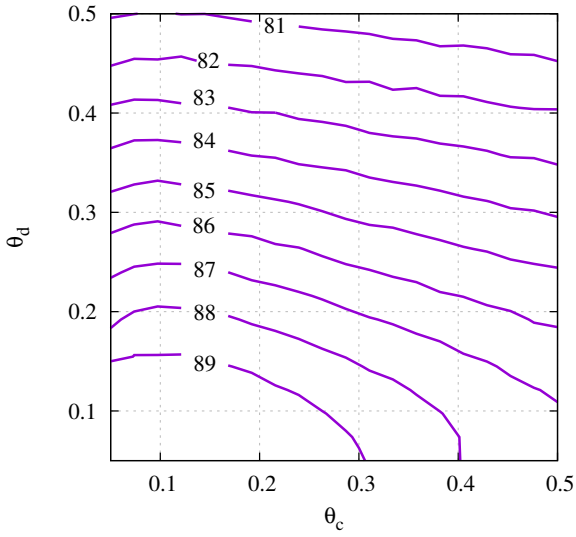

(c)

Figure 3.6: Parametric study of θ_c and θ_d on hot and cold packed beds **(a)** Effect of θ_c and θ_d on thermal front shapes in a hot store **(b)** Contours of constant efficiency in a hot store. **(c)** Contours of constant efficiency in a cold store.

the round-trip efficiency χ for this data emphasises this result, since $\mathrm{corr}(\theta_c, \chi) = -0.95$ and $\mathrm{corr}(\theta_d, \chi) = -0.30$ for a hot store, and $\mathrm{corr}(\theta_c, \chi) = -0.21$ and $\mathrm{corr}(\theta_d, \chi) = -0.96$ for a cold store.

Operating temperatures

For PTES systems reservoir temperatures are not independent as setting the temperatures of one reservoir impacts on those in the other reservoir. For instance, during charge the inlet temperature of the hot reservoir cannot be varied without changing either the pressure ratio or the outlet temperature of the cold reservoir. Changing these quantities also affects the rated power and energy density of the system. Furthermore, these factors affect the operating point on the mass flow rate–pressure ratio characteristic of the reciprocating devices, see section 4.2.

A parametric study of the operating temperatures and pressure ratios within the context of the full PTES system is presented in chapter 4. The above constraints are relaxed in this analysis which considers the thermal stores in isolation, and is applicable to storage systems that use a single reservoir.

The charging and discharging temperatures of hot and cold reservoirs are varied independently. The reservoir volume and geometry is fixed, as is the mass flow rate such that the nominal storage time is constant. Contours of constant $\Delta T = T_1 - T_2$ are plotted in figures 3.7(a) and 3.7(b) and are approximately proportional to the internal energy density of the system. For hot stores, increasing the charging temperature T_1 at a constant ΔT leads to higher efficiencies since thermal losses decrease (compare with equation 2.50 where $\zeta_t \sim \Delta T^2 / T_1 T_2$). On the other hand, T_1 should be minimised in cold reservoirs.

In figures 3.7(c) and 3.7(d) the charging temperature is varied while the discharging temperature is held constant (i.e. ΔT varies). As ΔT increases, thermal losses increase and pressure losses are reduced due to lower gas densities. Heat leakage losses also reduce which seems counter-intuitive. However, whilst the real heat leakage rate does increase with T_1, the inlet available energy B_{in} (the denominator in the loss coefficients) increases at a greater rate than the heat leakage, so that the leakage loss *coefficient* decreases.

These results suggest that the charging temperature should be increased (or decreased for

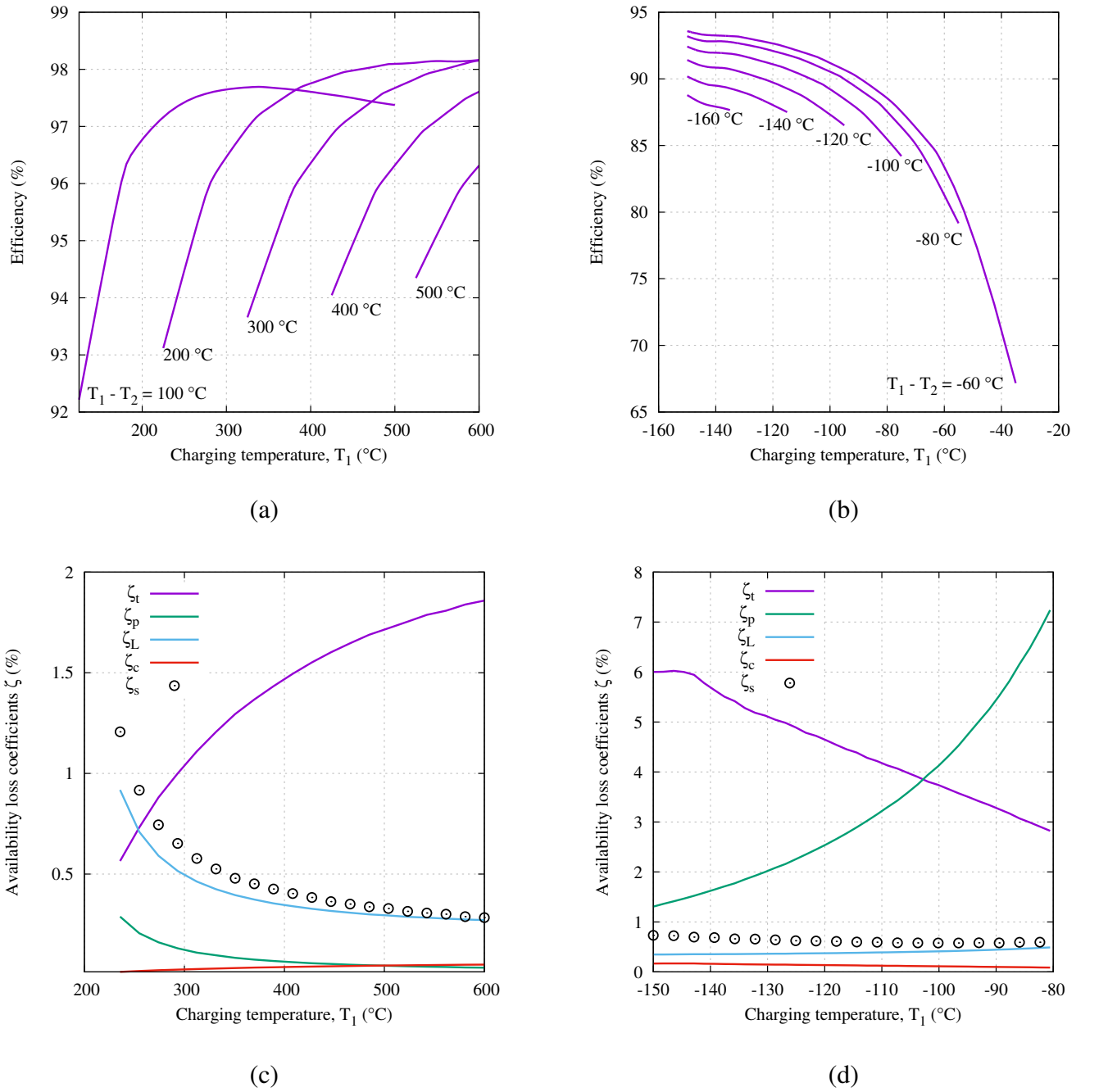

Figure 3.7: Parametric study of operating temperatures in hot and cold packed beds. **(a)** Contours of constant $T_1 - T_2$ in a hot store. **(b)** Contours of constant $T_1 - T_2$ in a cold store. **(c)** Loss coefficients in a hot store as the charging temperature T_1 is varied. The discharging temperature T_2 is fixed at 185°C **(d)** Loss coefficients in a cold store as the charging temperature T_1 is varied. The discharging temperature T_2 is fixed at -30°C

a cold store) as much as possible, and that the discharging temperature should be as close as possible to T_1 for high efficiencies. As a result, there is a trade-off with maximising the energy density which requires large values of $T_1 - T_2$.

3.3 Segmented packed beds

The previous section emphasised the conflict between thermal and pressure losses and their impact on the optimal value of variables such as the particle diameter and aspect ratio. Pressure losses occur over the full length of the packed bed whilst heat exchange only occurs in the fraction of the reservoir where the thermal front is present. The magnitude of the pressure losses could be reduced by dividing the packed bed into several segments and only directing flow through those segments where the thermal front is present. By diverting the flow around the remaining segments the pressure losses are reduced.

Segmentation of thermal stores has been proposed in the literature for different applications. Crandall and Thatcher [78] suggested that it could be used to maintain thermal stratification in solar air heating applications. Similarly, Dickinson et al. [149] employed multiple hot water tanks for a solar hot water scheme. These authors noted that segmentation could reduce the extent of de-stratification of the temperature gradients. This would be beneficial during the storage periods of packed beds where conduction erodes the thermal fronts. Segmentation has recently been patented for thermal energy storage applications by Isentropic Ltd. [108] who cite greater control over the thermal front in addition to the above advantages.

3.3.1 Segment control and spacing requirements

Segment control is the process by which segments are activated (gas flow is directed into the segment) and de-activated (gas flow is diverted around the segment). Various possibilities exist for activation/deactivation and two schemes suggested by Isentropic Ltd. [108] are illustrated in figure 3.8. In 3.8(a) the central valve/baffle system moves down through the reservoir during charge, tracking the thermal front. Most of the flow takes the path of least resistance so that, as shown, only layers B, C and D are active. As shown in Ref. [80] this

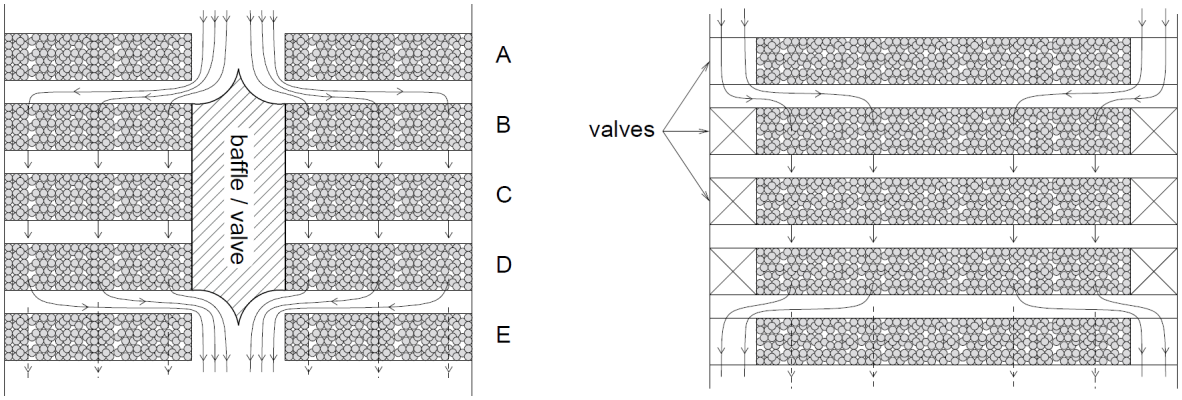

Figure 3.8: Possible segmented packed bed arrangements based on [108]. **(a)** A fixed number of layers are maintained active by means of the baffle/valve arrangement **(b)** Independent valving of each segment allows greater flexibility.

leads to impractical temperature distributions. Alternatively, in the design of 3.8(b) each layer is individually gated (with gates B, C and D shut, as shown). This allows each segment to be controlled independently. In practice, some flow will leak through the bypassed layers (as indicated by the dashed lines through layer E), depending on the relative resistance of the layers and the bypass channels.

For segmented beds, additional space is required between each segment and in the case of design 3.8(b) in an annular ring around the segments. The space required may be estimated by setting the pressure drop through the spaces between and around the segments to be a small fraction (denoted by ϕ) of the pressure drop that would occur if the flow passed through an optimised unsegmented reservoir[2]. The pressure drop of the bypass flow takes into account the loss due to turning the flow and is estimated from

$$\Delta p_b = \frac{1}{2} k \rho u^2 = \frac{k}{2\rho} \left(\frac{\dot{m}}{A_b} \right)^2 \tag{3.6}$$

where A_b is the area through which the bypass flow travels and k is an empirical factor which is of the order of unity [150]. The pressure drop along an unsegmented packed bed

[2]The objective of segmentation is to reduce pressure losses. Therefore, the losses in the bypass areas should be small compared to that in an optimal unsegmented store.

is given by

$$\Delta p_p = \frac{1}{2\rho\varepsilon^3}\frac{C_f}{\mathrm{St}}\left(\frac{\dot{m}}{A}\right)^2\frac{L}{\ell^*} \tag{3.7}$$

where A is the cross sectional area of the packed bed, L is the total length of the bed, and ℓ^* is the optimal value of ℓ for an unsegmented store. Note that the density ρ, and the other thermodynamic properties (C_f, St, and ℓ^*) are taken at their average values along the bed. Consequently this leads to

$$\frac{A_b}{A} = \sqrt{\frac{k\varepsilon^3}{\phi}\frac{\ell^*}{L}\frac{\mathrm{St}}{C_f}} \tag{3.8}$$

The spacing s between segments must also have the same area as the bypass flow ratio and is given by

$$\frac{A_b}{A} = \frac{2\pi Rs}{\pi R^2} \Rightarrow \frac{s}{D} = \frac{1}{4}\frac{A_b}{A} \tag{3.9}$$

As a result, the space between segments is approximately equal to the size of the gap outside the segments. Estimates using the nominal reservoir design suggest a spacing of 11 mm in hot stores (an increase in cross-sectional area A of 1%) and 21 mm in cold stores (an increase in A of 1.5%).

Further additional space may be required to provide room for the valve mechanisms, other control systems, and structural support. Although segmented beds could lead to an increased utilisation of the packed beds, the extra space required may in fact decrease the energy density of the stores.

3.3.2 Availability losses in segmented reservoirs

Operational losses

The evolution of the thermal front within a segmented store is affected by the way the individual segments are activated and deactivated. Figure 3.9(a) illustrates the temperature profiles at the end of charge and discharge for packed beds with one segment and eight segments. During cyclic operation using the valve arrangement shown in figure 3.8(b) new segments are activated at the leading edge of the thermal front when the normalised exit temperature from the previous segment exceeds $\theta_l = 0.1$, where $\theta_l = (T_o - T_2)/(T_1 - T_2)$

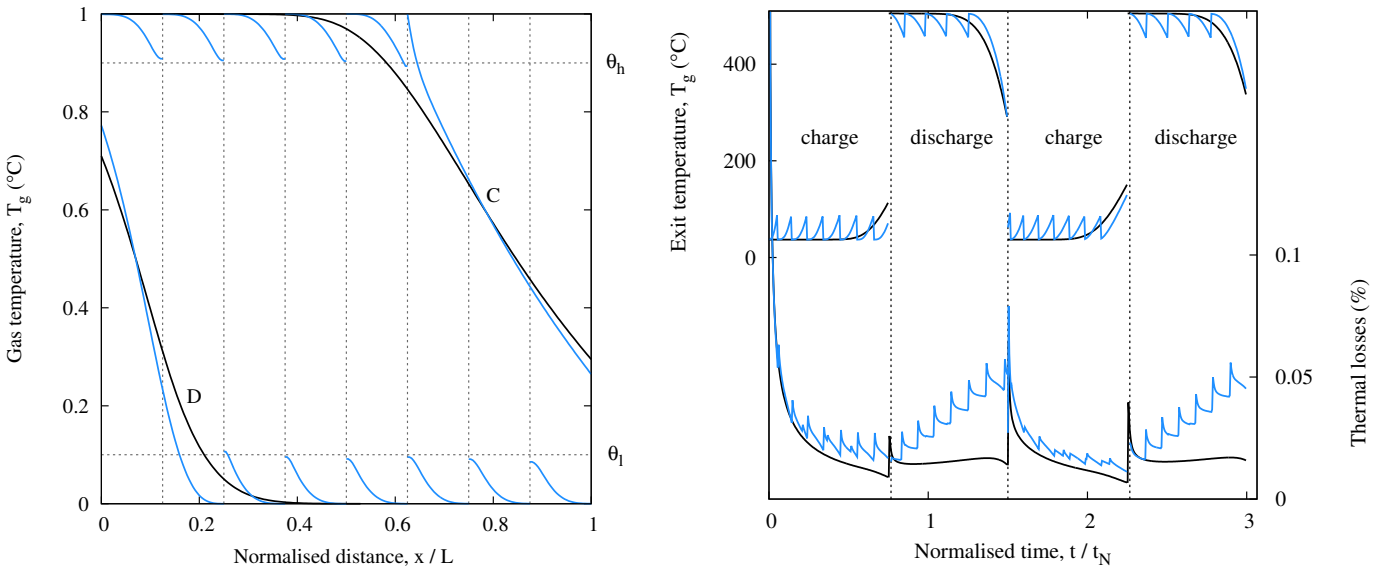

Figure 3.9: Behaviour of an unsegmented packed bed (black) and a segmented packed bed (blue) with eight segments. Cyclic operation with $\Pi = 0.75$, $d_p = 20$ mm. **(a)** Temperature profiles at the end of charge (C) and discharge (D) **(b)** Exit temperatures and instantaneous thermal losses for the first two cycles of operation

and T_o is its outlet temperature. The segments at the trailing edge of the thermal front are then deactivated when their exit temperature exceeds $\theta_h = 0.9$ where θ_h is defined in the same way as θ_l.

Truncation of the nose and tail of the thermal front in segmented stores leads to steeper temperature profiles, but also generates a 'sawtooth wake' in the deactivated segments that gradually decays as a result of axial conduction. Figure 3.9(b) (top) shows how the exit temperature from the packed bed varies for the first two cycles of operation. The exit temperature displays the same sawtooth behaviour and implies that there are exit losses through much of the duration of the cycle. This counteracts the increased utilisation of the reservoir due to the steeper fronts, and as a result the packed beds do not store more available energy per cycle. On the other hand, the exit flow does not reach such high temperatures as the unsegmented case.

Figure 3.9(b) (bottom) shows the importance of the switching temperatures $\theta_{l,h}$ on thermal losses. During the first charging cycle, whenever a segment is activated a temperature

difference exists between the exit gas of the previous segment (which is $T = T_2 + \theta_l(T_1 - T_2)$) and the solid temperature near the inlet of the new segment (which is T_2). This causes spikes in the instantaneous thermal losses, the extent of which will clearly depend on the size of θ_l. Notably, figure 3.9(b) shows that the spikes are substantially smaller during the second charging period compared to the first. This is because the remnants of the sawtooth wake from the previous cycle reduce the temperature difference between the inlet gas and the existing solid temperature.

When a segment is deactivated, flow is diverted around this segment and is directed into the next segment. Consequently, there is also a large temperature difference at the trailing edge of the front. For instance, during charge the inlet gas is at T_1 whereas the solid temperature near the inlet of the first activated segment is $T = T_2 + \theta_h(T_1 - T_2)$. During the first charge cycle these losses are observed in figure 3.9(b) (bottom) as small spikes between the larger spikes. (The instantaneous losses are smaller than those at the leading edge of the front due to the higher average temperature). The large spikes shown during discharge are trailing edge losses. These are much larger during the discharging phases where temperatures are low. Unlike the leading edge losses which are reduced in subsequent cycles, the trailing edge losses cannot be avoided, and the loss spikes are particularly pronounced throughout all discharge cycles. Note that the charging losses gradually decrease, and discharge losses increase due to the spreading and steepening of the thermal front.

The impact of particle diameter

Figure 3.10 illustrates the impact of segmentation on availability losses in cold reservoirs. As expected, segmenting the bed significantly reduces the pressure losses, especially at small particle diameters. On the other hand, thermal losses increase slightly due to the losses caused when activating and deactivating segments. There is a trade-off in the value of $\theta_{l/h}$; smaller values reduce thermal losses with a penalty for pressure losses.

The round-trip efficiency is maximised at smaller particle diameters when segmented, as illustrated by the filled in dots in figure 3.10(a). This has an additional benefit: smaller particles form steeper fronts and therefore more available energy is stored. Figure 3.10(b) compares the performance of three cold packed beds which use the optimal particle size for the given number of segments, with $\theta_{c,d} = 0.25$. The figure is created by varying $\theta_{c,d}$

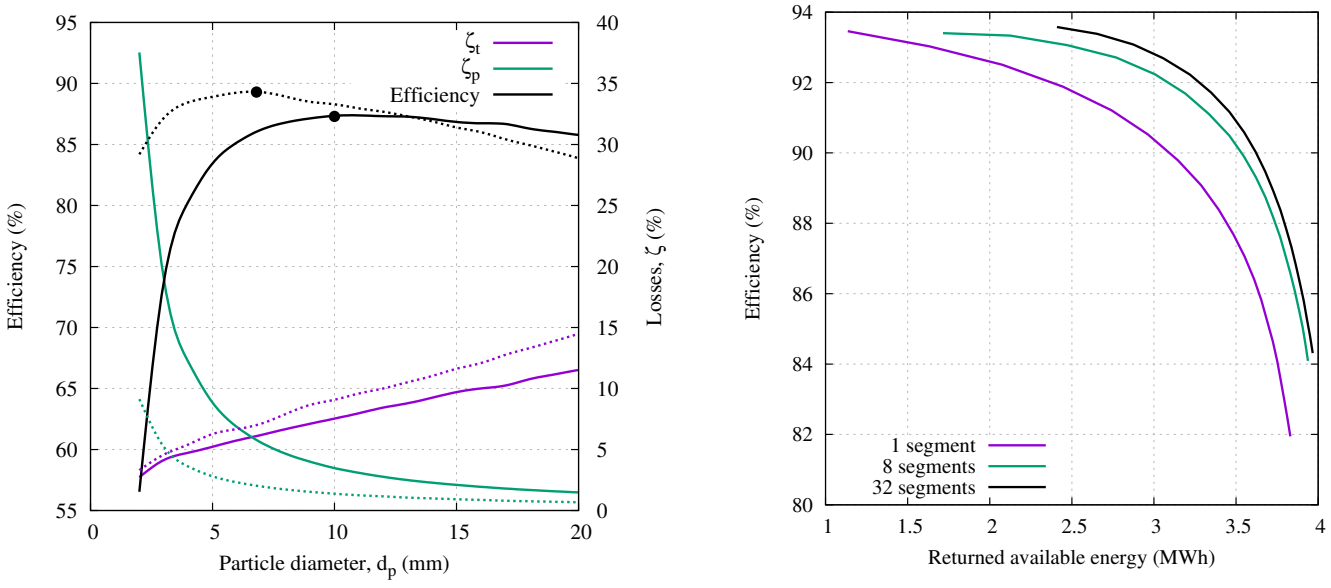

(a) (b)

Figure 3.10: Availability losses of cold segmented packed beds. **(a)** Efficiency and availability losses in cyclic operation of packed beds with one segment (solid lines) and 32 segments (dashed lines). Solid dots represent 'optimal' points at $\theta_{c,d} = 0.25$ **(b)** Particle diameter is set at the optimal value for efficiency (figure 3.10(a)) which is 10 mm for 1 segment, 8 mm for 8 segments and 7mm for 32 segments. θ_c is varied to generate the plot.

and it therefore displays 'off-design' performance in the sense that the optimal particle size also depends on the utilisation: longer charging periods imply steeper, shorter thermal fronts (see section 3.2.2). The benefits derived from segmentation are clear and may be interpreted as either an increase in efficiency at high utilisation (by up to 4 percentage points) or a substantial improvement in returned energy at fixed efficiency (e.g. an increase of 30% at an efficiency of 92%). Note that this improvement will be offset to some degree by the additional space required for bypass flows etc. In addition, it is clear that there are diminishing returns to installing a greater number of segments, and that the majority of the potential benefit can be achieved with just eight segments.

Storage losses

Segmentation can reduce the losses that occur during the storage phase, when conduction and heat leakage cause equilibration of the solid temperature. Conductive losses in particular can be reduced and figures 3.11 and 3.12(a) illustrate a simplified scenario where conduction acts on thermal fronts that are assumed to be linear. In this scenario, the gas and solid are assumed to have the same temperature, and the front behaviour is governed by the heat equation

$$\frac{\partial T}{\partial t} = \alpha \frac{\partial^2 T}{\partial x^2} \tag{3.10}$$

where $\alpha = k_{\text{eff}}/\rho_s c_s(1-\varepsilon)$. The reservoir inlet and outlet are assumed fully insulated (i.e. adiabatic) as are the boundaries between segments so that the boundary conditions are

$$\frac{\partial T(0,t)}{\partial x} = \frac{\partial T(L,t)}{\partial x} = 0 \tag{3.11}$$

For a linear front which varies from T_1 at the inlet to T_2 at the exit, the initial condition is given by

$$T(x,0) = T_1 - \frac{(T_1 - T_2)x}{L} \tag{3.12}$$

Separation of variables and use of the Fourier Series gives the analytical solution:

$$\begin{aligned} T(x,t) &= \left(\frac{T_1+T_2}{2}\right) \\ &+ \frac{2(T_1-T_2)}{\pi^2}\sum_{n=1}^{\infty}\frac{1-(-1)^n}{n^2}\cos\left(\frac{n\pi x}{L}\right)\exp\left\{-\alpha\left(\frac{n\pi}{L}\right)^2 t\right\} \end{aligned} \tag{3.13}$$

Figures 3.11(a) and 3.11(b) show how the thermal front equilibrates in reservoirs with one and four segments, respectively. In the segmented case, the thermal front is constrained to equilibrate within its respective segment, rather than level out over the full length of the reservoir. Consequently, the thermal profile is preserved, albeit, with a stepped profile. For figures 3.11(a) and 3.11(b) the temperature profiles have the same energy content. However, the stepped profile of the segmented store has a greater *available* energy content.

The instantaneous conductive loss coefficient at each x position for the above cases is shown in figures 3.11(c) and 3.11(d). (In this section loss coefficients are defined as the

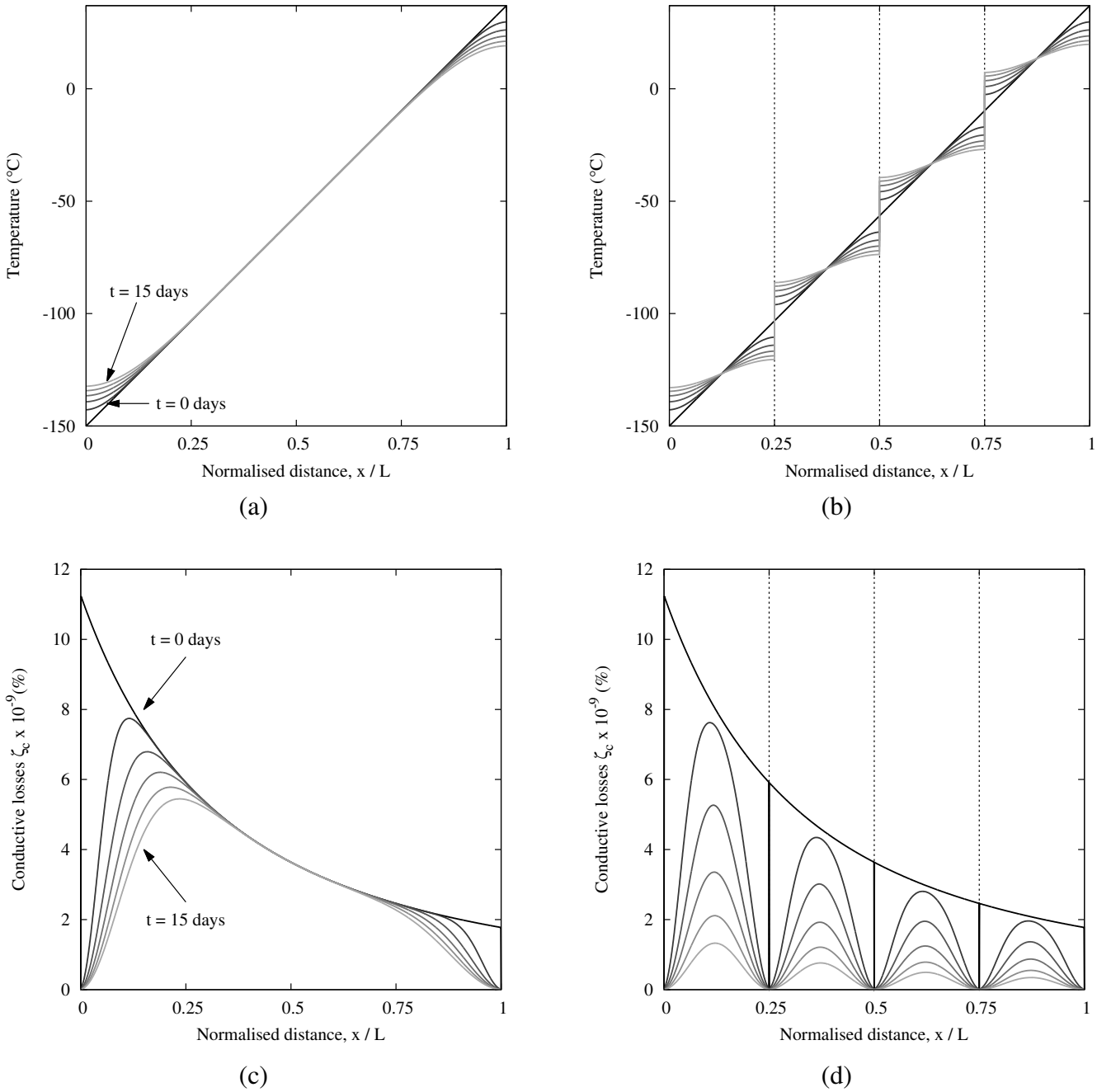

Figure 3.11: Conductive effects in the storage phase of segmented reservoirs. Boundaries of the reservoir and each segment are adiabatic. Each line shows the profile at intervals of 3 days with the darkest line being at 0 days. **(a)** Equilibration of a linear temperature profile during the storage phase of an unsegmented cold reservoir **(b)** Equilibration of a linear temperature profile during storage in a cold reservoir with four segments **(c)** Instantaneous conductive losses in an unsegmented cold reservoir **(d)** Instantaneous conductive losses in a cold reservoir with four segments

available energy lost divided by the total available energy in the packed bed at the beginning of storage.) By comparing these figures with equation 2.60 on page 66 it is clear that the largest conductive losses are generated at points where the thermal gradient is steepest and where the temperature is lowest. Conductive losses decrease at the boundaries first, where the thermal gradient reduces most rapidly. The segmented store has the same conductive loss generation as the unsegmented store at zero days. However, the larger number of boundaries means that the thermal gradient is reduced at more points in the segmented reservoir. As a result, the total conductive loss at each time-step is less than in the unsegmented reservoir. (This can be seen by observing that the total area under each curve for the segmented reservoir is always equal to or less than the corresponding unsegmented curve).

Conductive and leakage losses during the storage phase

Segmented reservoirs are compared by considering designs that would minimise the pressure losses. Thus, it is assumed that the thermal front length is equal to the length of the segments. At the end of charge, the thermal profile is given by a linear gradient in the final segment, while all the other segments are fully charged. Figure 3.12(a) shows how the conductive losses vary with time for different numbers of segments with $k_{\text{eff}} = 0.5$ W m^{-1}K^{-1}. Conductive losses increase more quickly in packed beds with more segments due to the steeper thermal gradient in the final layer. However, over a longer period of time the benefit of segmenting the reservoirs is obvious, for instance conductive losses in a reservoir with 32 layers are around one fifth of those in an unsegmented store.

Heat leakage occurs during storage periods and its behaviour is included by adding an additional term to the heat equation, such that

$$\frac{\partial T}{\partial t} = \alpha \frac{\partial^2 T}{\partial x^2} + \beta(T - T_0) \tag{3.14}$$

where $\beta = 4U_s/((1-\varepsilon)\rho_s c_s D)$. For insulated boundaries, the analytical solution can be obtained in the same manner as equation 3.14 and is given by

$$T(x,t) = \Theta(x,t)\exp(-\beta t) \tag{3.15}$$

where $\Theta(x,t)$ is the solution given in equation 3.14. When the boundaries are no longer

insulated and heat transfer occurs between segments and from the top and bottom of the stores, the heat equation can be most easily and accurately solved using the Crank-Nicolson method [121].

The impact of leakage in a segmented cold store with a linear temperature profile in the final layer is investigated. The overall heat transfer coefficient is $U_s = U_t = U_b = 0.16$ W/mK which is consistent with U_L for the nominal designs. Leakage occurs from the side walls and from the top and bottom of the store. Radiative heat transfer also occurs between the layers and generates thermal gradients which are then eroded by conduction as shown in figure 3.13. Thermal gradients also develop in the first layer as a result of heat leakage to the environment through the bottom of the reservoir.

The variation of each loss with time is shown in figure 3.12(b) for a 16 segment reservoir (radiative losses as defined in section 2.5.7 are included in $\zeta_{\mathrm{L,t}}$). Leakage losses are a similar order of magnitude to conductive losses in this example, but in practice could be reduced by using more insulation. The effect of heat transfer between the segments and from the reservoir ends is to substantially increase the conductive losses compared to the adiabatic case. Furthermore, the conductive losses continually increase rather than levelling off.

Once leakage and conduction are both included in the analysis, the benefit of segmented reservoirs is significantly reduced as shown in figure 3.12(c). This analysis highlights the importance of several factors when designing the packed beds. If the reservoir is likely to have storage phases that last several days, then segmentation would significantly reduce conductive losses. However, the packed bed should be sufficiently insulated to reduce leakage losses to a small fraction of the conduction losses. This is particularly important since leakage losses exacerbate conductive losses. On the other hand, if the storage duration is short (e.g. a number of hours) then conductive losses are likely to be small compared to other losses in the system, and the system should be designed with an emphasis on the operational periods.

The analysis in this section suggests that segmentation may have reasonable benefits during operational periods. Furthermore, segmented reservoirs could reduce losses during storage phases that last several days.

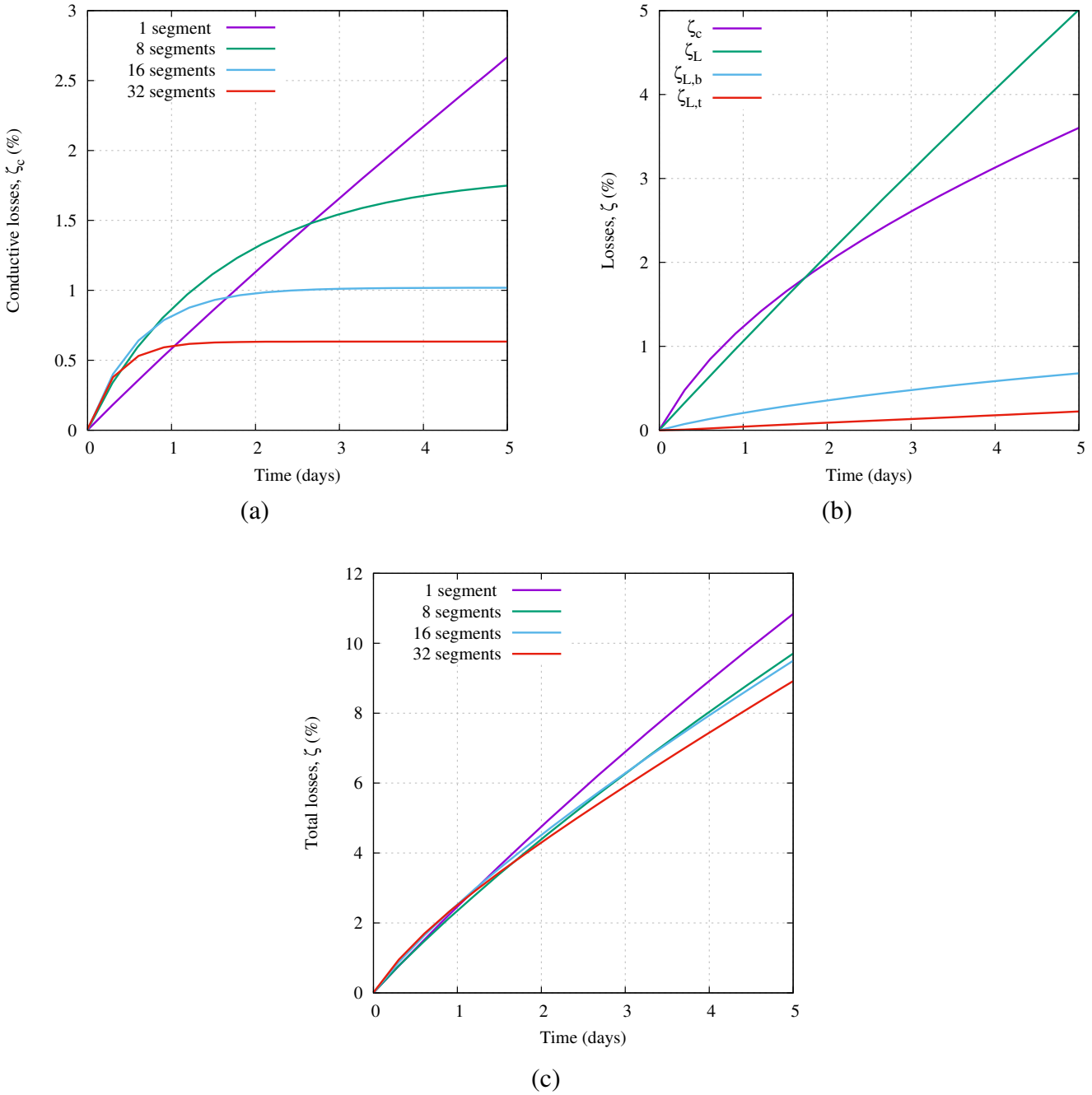

Figure 3.12: Combined effect of conduction and heat leakage on loss coefficients during the storage phase of segmented packed beds. **(a)** Conductive losses in cold segmented packed beds with no heat leakage and with adiabatic boundaries. **(b)** Loss coefficients in a cold packed beds with 16 segments and with heat leakage **(c)** Total losses from cold segmented packed beds with the thermal front in the final segment

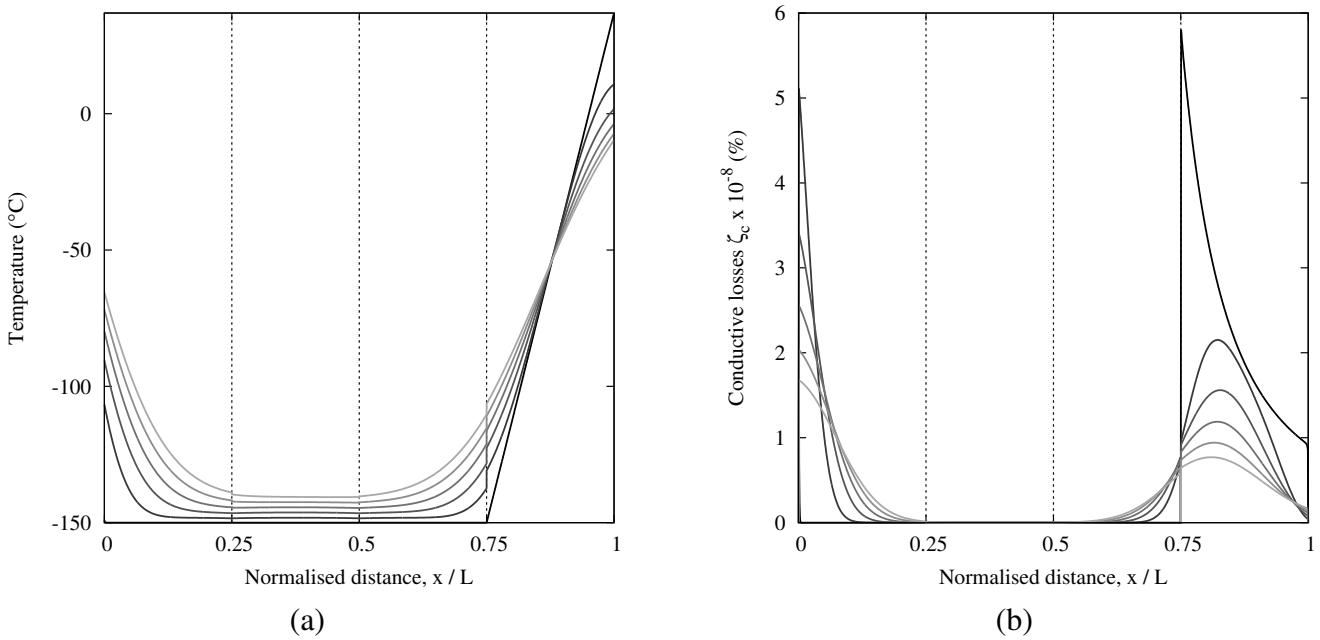

Figure 3.13: Combined effect of conduction and heat leakage during the storage phase of packed beds with four segments. Segments do not have adiabatic boundaries (there is heat leakage to the atmosphere and radiation between the segments). Profiles plotted every 3 days with the darkest line being 0 days. **(a)** Conduction and heat leakage acting on a profile with the thermal front in the final segment of a segmented cold store. **(b)** Instantaneous conductive loss coefficients for a reservoir with the thermal front in the final segment of a segmented cold store.

3.4 Radial-flow packed beds

Radial-flow packed beds are one alternative to the packed beds that have been described so far. Figure 3.14 is a schematic for a radial-flow packed bed, where gas enters a chamber in the centre of the cylindrical container, before flowing through the bed along the radial co-ordinate and exiting through an outer plenum. The packing material is contained by a grid through which the gas can flow. Various aspects of these packed beds have been studied, including the effective conductivity [151, 152], flow distributions [153] and applications in air filters [154, 155] and the synthesis of ammonia [156, 157]. These models typically include reaction terms and mass transfer, and the emphasis of these papers tends to be on the chemical conversion efficiency. For electrical energy storage applications particular consideration must be given the heat transfer processes and available energy losses.

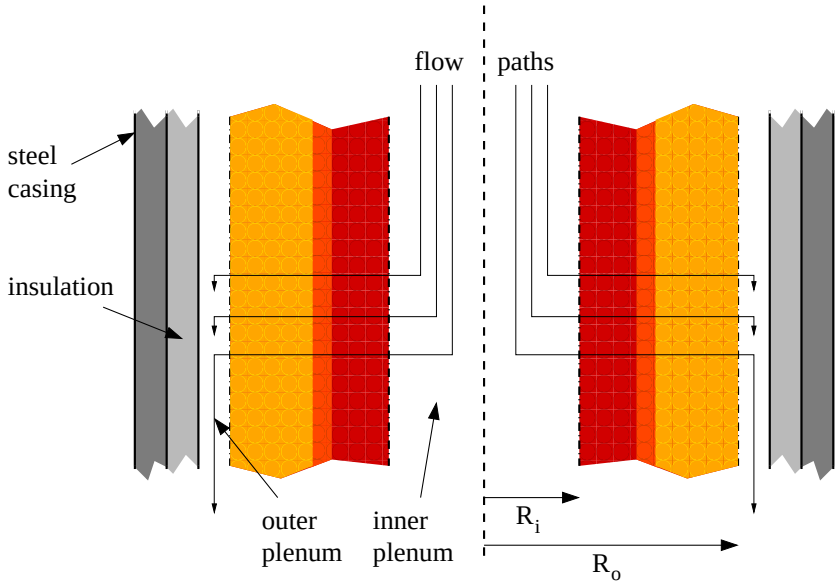

Figure 3.14: Schematic of a radial-flow packed bed during charge. Hot gas enters the inner plenum, and flows radially through the bed from R_i to R_o and into the outer plenum.

Radial-flow packed beds were first patented for thermal energy storage in 1942 by Bradley [158]. In this patent, the thermal store heated input air to 1030°C for use in a blast furnace for smelting iron ore. Bradley suggested that particles of different sizes could be used. The mass flow rate decreases along the radius, such that pressure losses are lowest at the outer plenum. Smaller particles can then be placed near the outer plenum in order to reduce thermal losses. (The decreasing mass flow rate alters the trade-off between thermal losses and pressure losses, such that the optimal particle size also varies with radius). Grids would have to be installed at intervals along the radius to keep particles in their respective positions.

Two further patents [142, 143] in the 1990s aimed to make Bradley's concept more practicable. It was thought that the packing material might flow with the gas into the inner and outer plena. Thermal expansion could cause disintegration of the rocks, damage to the containment, or non-uniformities in the packing structure. Fassbinder's [142] and Emmel et al.'s [143] patents provided specific design features to tackle these problems. A subsequent patent [159] described a system for converting thermal energy into mechanical work which specifically used radial-flow thermal stores.

Daschner et al. [74] carried out experimental work on Emmel et al.'s design and described

results from a 80 kW h, 235 kW packed bed that was operated between 710°C and 50°C. The store recorded a first law thermal efficiency of 92%. Daschner noted that because the hot gas enters the inner plenum, the exit flow will always be close to ambient temperature so that smaller quantities of insulation will be required. This may result in a cheaper design and lower heat leakage losses. However, the outer surface of the packed bed is not designed for high temperatures which may compromise flexibility of operation. Furthermore, the need for an inner and outer plenum means that the radial-flow design may have a lower energy density than an axial-flow device of the same energy capacity.

The governing equations for radial-flow packed beds are now described, and their behaviour is investigated. The thermal front length is found to vary with the radial position and this has consequences for thermal losses and energy stored. In section 3.4.4 the performance of radial-flow stores is compared to axial-flow stores. This will establish, for example, which design results in lower pressure losses and higher energy densities once factors such as aspect ratio and segmentation are included.

3.4.1 Radial-flow packed bed governing equations

Daschner et al. [74] employed a one-temperature model of the thermal store to generate numerical results, but a two-temperature model is required here so that the thermal loss coefficient can be calculated. The analysis and derivation of governing equations follows the same methodology as for axial-flow packed beds that was described in section 2.3. Figure 3.15 shows a control volume for the radial-flow packed bed. The mass continuity equation for radial-flow is given by

$$\varepsilon \frac{\partial \rho}{\partial t} = -\frac{1}{r}\frac{\partial \left(rG\right)}{\partial r} \tag{3.16}$$

When mass accumulation is small and the mass flow rate is constant, the mass flow rate per unit area decreases with radius

$$G = \frac{G_i R_i}{r} \tag{3.17}$$

where G_i is the mass flow rate per unit area at the inlet radius R_i. As a result, the thermal wave speed (which can be found from an energy balance like equation 2.3) is also a function

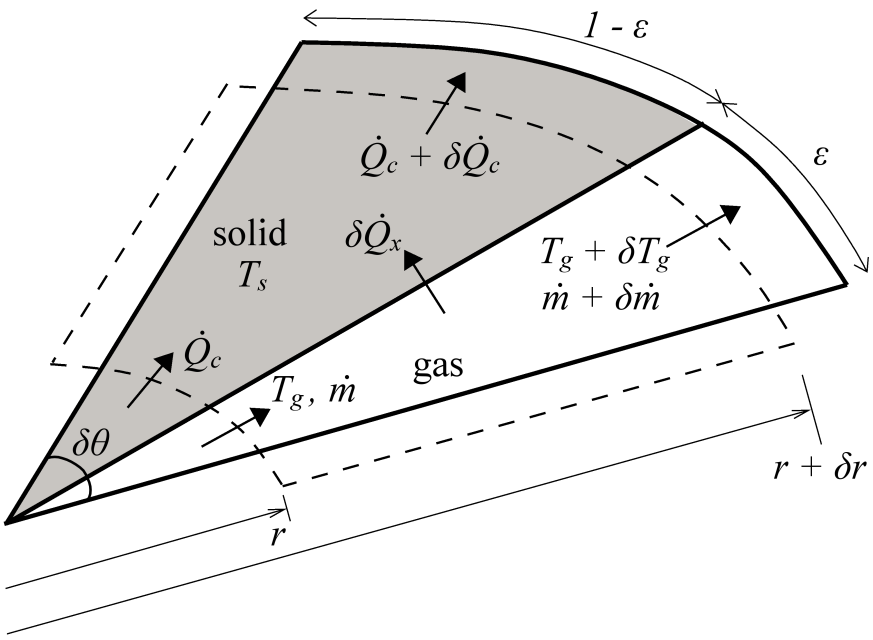

Figure 3.15: Control volume of a radial-flow packed bed during charge, where T_g is the gas temperature, T_s is the solid temperature, $\dot{Q}_x$ is the gas-solid heat transfer, $\dot{Q}_c$ is heat transfer due to conduction along the bed and $\dot{m}$ is the mass flow rate.

of radius

$$V_f^r = \frac{c_p G_i R_i}{\rho_s c_s (1-\varepsilon) r} \tag{3.18}$$

The wave speed thus depends on the radial position of the front; for gas flow from the inner surface to outer surface, points in the front that are more advanced travel more slowly and the front shape will be affected. For instance, figure 3.16 shows how the shape of an initially linear front in hot and cold reservoirs changes during the first charging period. When the specific heat capacity c_s is held constant the front steepens. As discussed in section 2.5.1, the dependence of the wave speed on c_s effects the thermal front shape. For instance, it causes spreading of the front in hot stores, thereby counteracting the steepening caused by radial position. A similar effect is seen in the cold reservoir. Variable c_s in the cold store contributes to the wave steepening during charge and causes thermal shocks to form. If the gas were to pass in the opposite direction (i.e. from the outer plenum towards the inner plenum) during charge then the steepening impact of variable c_s may be reduced by the wave slackening effect of the mass flow rate. Consequently, thermal losses may be

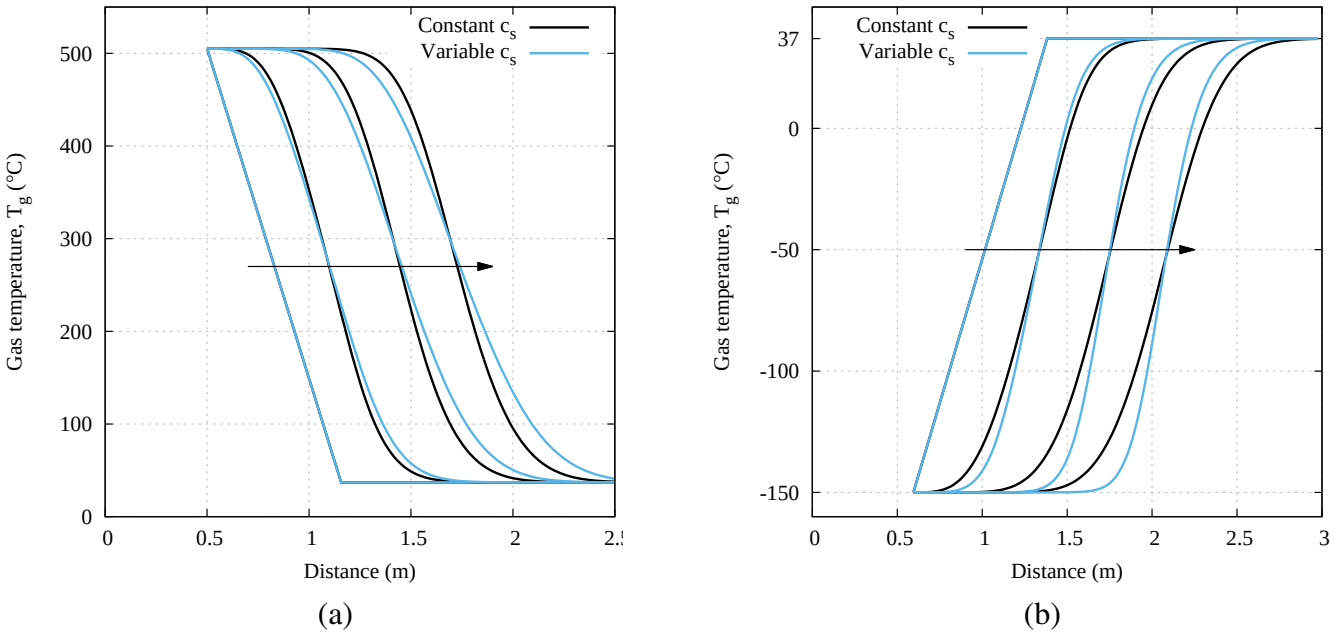

Figure 3.16: Thermal front steepening due to decreasing mass flow rate per unit area in radial packed beds during the first charging period. **(a)** Hot radial packed beds. **(b)** Cold radial packed beds.

reduced as the thermal gradients are reduced. A disadvantage of this mode of operation is that the cold gas would be in direct contact with the outer plenum, and the 'self-insulating' benefits of the radial store would not occur. Also, since the thermal front shape changes are undone during the discharging phase, wave steepening is not as prominent in cyclic operation as it is in the single blow case. As a result, there may not be very much to gain by charging cold reservoirs from the outer plenum.

The governing equations can be derived in a similar way to section 2.3 by considering an infinitesimal control volume, see figure 3.15. The heat transfer rate between gas and solid is given by

$$\delta \dot{Q}_x = (1-\varepsilon) S_v h (T_g - T_s) r \delta r \delta\theta \delta z \tag{3.19}$$

The net heat flux due to conduction through the control volume is given by

$$\dot{Q}_c^{\text{net}} = -\frac{\partial}{\partial r}\left(r k_{\text{eff}} \frac{\partial T_s}{\partial r} \delta\theta \delta z \right) \delta r \tag{3.20}$$

The energy equations are then given by

$$\varepsilon \frac{\partial}{\partial t}\left(\rho_g e_g\right) + \frac{1}{r}\frac{\partial}{\partial r}\left(rGh_g\right) = (1-\varepsilon)S_v h(T_s - T_g) \tag{3.21}$$

$$\rho_s c_s \left(1-\varepsilon\right)\frac{\partial T_s}{\partial t} = S_v h \left(1-\varepsilon\right)\left(T_g - T_s\right) + \frac{1}{r}\frac{\partial}{\partial r}\left(r k_{\text{eff}} \frac{\partial T_s}{\partial r}\right) \tag{3.22}$$

The gas equation can be simplified for the case where mass accumulation is zero since the continuity equation gives

$$\frac{\partial (rG)}{\partial r} \approx 0 \tag{3.23}$$

meaning that

$$\frac{1}{r}\frac{\partial}{\partial r}\left(rGh_g\right) \approx G\frac{\partial h}{\partial r} \tag{3.24}$$

Using these simplifications, and re-writing the equations to highlight the dependence on radius r and be comparable with the axial-flow equations of section 2.3 produces

$$\frac{\partial T_g}{\partial r} = \frac{T_s - T_g}{\ell} + \frac{r}{R_i}\mathcal{C}_i \tag{3.25}$$

$$\frac{\partial T_s}{\partial t} = \frac{R_i}{r}\frac{T_g - T_s}{\tau_i} + \frac{\alpha}{r}\frac{\partial}{\partial r}\left(r\frac{\partial T_g}{\partial r}\right) \tag{3.26}$$

where ℓ, τ_i, α and $\mathcal{C}_i$ have the same form as in section 2.3. However, these factors are all functions of the radius through the mass flow rate per unit area G, and must be integrated appropriately.

These equations are solved using the semi-implicit method described for axial packed beds in section 2.4 using the stencil in figure 2.8. The conductive term on the right-hand-side of the solid equation is expanded and the $\partial T_s/\partial r$ term is incorporated into this method. The second derivative is then evaluated in a second step after the main integration as described in section 2.4. Heat leakage is also included in this second step and only occurs at the final node. This approach therefore generates the following matrix for each grid-step i at each time-step n:

$$\begin{bmatrix} (1+\phi) & -\phi \\ -\psi_1 & (1+\psi_1+\psi_2) \end{bmatrix} \begin{Bmatrix} T^n_{g,i} \\ T^n_{s,i} \end{Bmatrix} = \begin{Bmatrix} K_1 \\ K_2 \end{Bmatrix} \tag{3.27}$$

where

$$\phi = \frac{\Delta r}{2\ell} \tag{3.28}$$

$$\psi_1 = \frac{\Delta t}{2\tau} \tag{3.29}$$

$$\psi_2 = \frac{\alpha \Delta t}{\bar{r} \Delta r} \tag{3.30}$$

where $\bar{r}$ is the average radius between grid points i and $i-1$. The constants are given by

$$K_1 = (1-\phi) T^n_{g,i-1} + \phi T^n_{s,i-1} + \Delta r \mathcal{C}^{n-1}_i \tag{3.31}$$

$$K_2 = (1-\psi_1) T^{n-1}_{s,i} - \psi_2 T^n_{s,i-1} + \psi_1 T^{n-1}_{g,i} \tag{3.32}$$

3.4.2 Size of the empty column

The size of the inner plenum can be estimated by requiring the pressure loss down the central column Δp_c to be small compared to the pressure loss along the radius Δp_r in order to maintain uniform flow. The inner plenum is similar to a pipe, so that Δp_c is given by

$$\Delta p_c = \frac{4 C^p_f L}{2 R_i} 1/2 \rho V^2 = \left(\frac{\dot{m}}{\pi} \right)^2 \frac{C^p_f L}{\rho R^5_i} \tag{3.33}$$

where C^p_f is the coefficient of friction in a pipe which is approximately 0.02.

The pressure drop through the packed bed varies with radius as the mass flow rate per unit area varies. Assuming dimensionless numbers do not vary significantly, and integrating gives

$$\Delta p_r = \frac{1}{2\rho\varepsilon^3} \frac{C_f}{\mathrm{St}} \frac{1}{\ell} \int_{R_i}^{R_o} \left(\frac{\dot{m}}{2\pi R L} \right) dR \tag{3.34}$$

$$= \frac{1}{2\rho\varepsilon^3} \frac{C_f}{\mathrm{St}} \frac{1}{\ell} \left(\frac{\dot{m}}{2\pi L} \right)^2 \left(\frac{R_o - R_i}{R_o R_i} \right) \tag{3.35}$$

Setting Δp_c as a fraction $\phi = 0.1$ of Δp_r and solving for R_i iteratively suggests that the inner column should have a radius of around $R_i/R_o \approx 0.25$. The column then occupies around 5% of the volume of the packed bed (not including insulation and steel volume).

The increase in volume compared to a reservoir which has the same volume of packing material but no inner column is approximately 7%.

Radial-flow packed beds also require an outer plenum (see figure 3.14) through which the gas can exit the reservoir. The space occupied can be found by the same method as above and the required area is the same as for the inner plenum (although the additional increase to the radius is much smaller).

For comparison, the patent by Bradley [158] suggested a system with $R_i = 5$ feet (1.52 m), $R_o = 10$ feet (3.05 m), meaning that $R_i/R_o = 0.5$. Bradley's store had a height of 50 feet (15.24 m) such that the aspect ratio is 5. The prototype developed by Daschner et al. [74] used $R_i = 200$ mm and $R_o = 850$ mm such that $R_i/R_o = 0.24$. The prototype had a height of 900 mm so that the aspect ratio is 0.82.

3.4.3 Parametric studies of radial-flow packed beds

The nominal bed design is chosen to be similar to the axial-flow nominal designs: reservoirs have the same energy capacity and the same power rating and thereby have the same nominal charging time t_N. Magnetite is used as the packing material, and the operating temperatures, pressures, mass flow rates and packing volumes are the same. The nominal particle diameter is 20 mm. The main parameters free to be varied are the particle diameter and the aspect ratio which is defined as $H/2(R_o - R_i)$ for radial-flow packed beds. The geometry of a nominal design for a radial packed bed with an aspect ratio of 1 is described in table 3.4.

Geometry	Hot reservoir	Cold reservoir
H	4.0 m	4.76 m
R_i/R_o	0.20	0.20
R_i	0.50 m	0.60 m
R_o	2.50 m	2.98 m
Packing volume	75.5 m^3	127.1 m^3
Outer plenum thickness	50 mm	60 mm
t_I	224 mm	321 mm
t_s	17 mm	2 mm
Total volume	189 m^3	328 m^3

Table 3.4: Nominal radial-flow packed bed designs

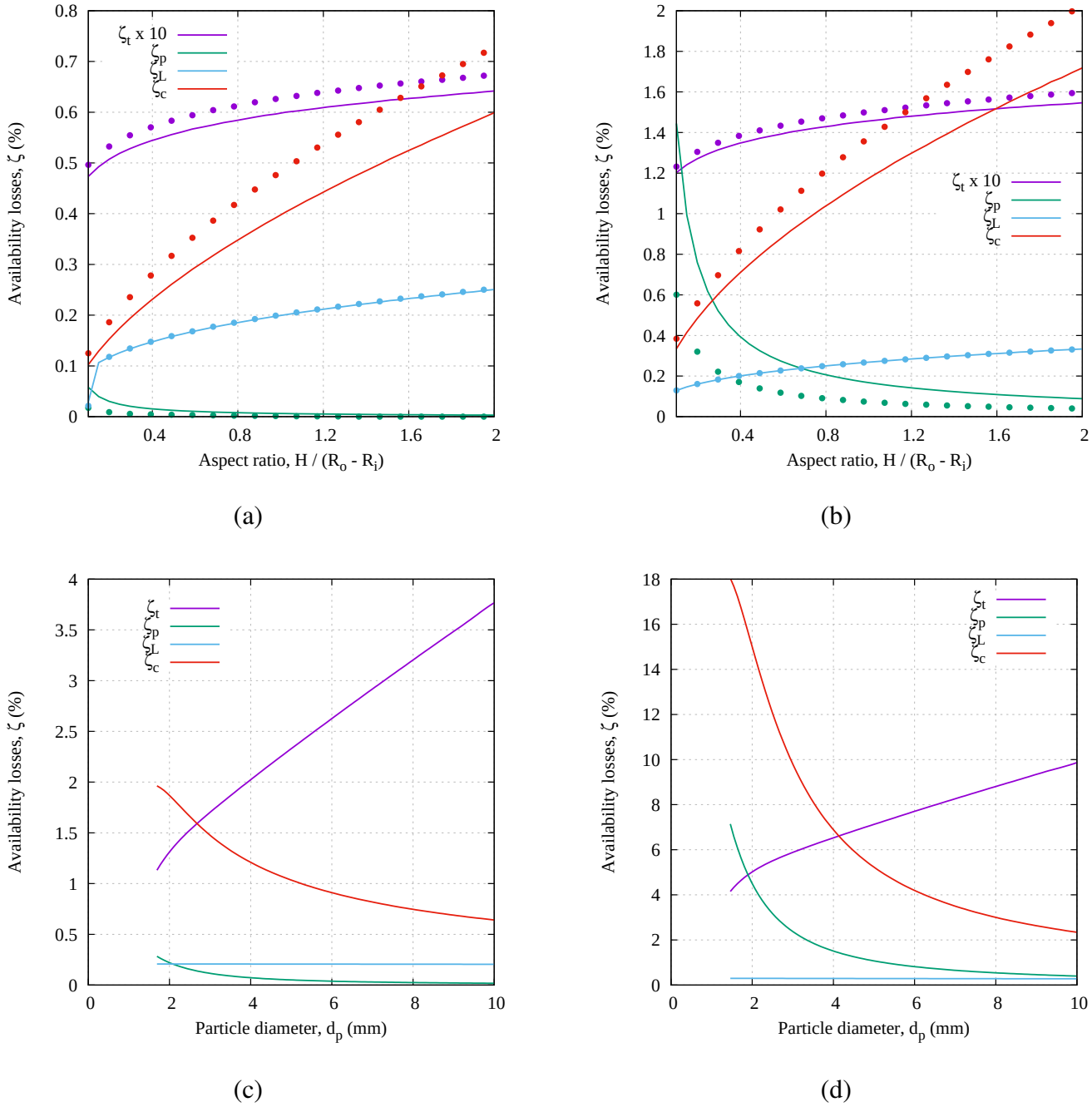

Figure 3.17: Parametric study on aspect ratio and particle diameter on hot and cold radial-flow packed beds. **(a)** Hot store ($d_p = 20$ mm. Solid lines have $R_i/R_o = 0.2$ and dotted points are $R_i/R_o = 0.5$) **(b)** Cold store ($d_p = 20$ mm. Solid lines have $R_i/R_o = 0.2$ and dotted points are $R_i/R_o = 0.5$) **(c)** Hot store ($H/2(R_o - R_i) = 1$, $R_i/R_o = 0.2$) **(d)** Cold store ($H/2(R_o - R_i) = 1$, $R_i/R_o = 0.2$)

In this section availability losses during the storage phase are not considered. A simple treatment of storage losses in radial-flow stores will be discussed in section 3.4.5.

Parametric studies of aspect ratio and particle diameter for hot and cold radial-flow reservoirs are shown in figure 3.17. The trends in each loss are very similar to those in axial-flow packed beds and as expected a trade-off between thermal and pressure losses is observed. However, it is apparent that pressure losses are significantly smaller than in axial-flow reservoirs as shown in figure 3.2 on page 92 [3]. This suggests that it may be possible to use smaller particles thereby further reducing thermal and conductive losses.

Varying the size of the central empty column only changes the losses by a small amount. As expected, figures 3.17(a) and 3.17(b) show that pressure losses decrease slightly as R_i/R_o is increased since the mass flow rate undergoes a commensurate reduction. Increasing R_i/R_o reduces the distance the gas passes through $R_o - R_i$ for a fixed volume and aspect ratio. Steeper thermal gradients are then formed which causes the slight increase in thermal losses.

[3]Note that the axial-flow results include storage losses whereas the radial-flow results do not. Inclusion of storage phases does not significantly effect the size of the pressure losses, nor the optimal particle size

3.4.4 Comparison of radial-flow and axial-flow packed beds

To make a comparison of radial-flow and axial-flow reservoirs, the stores are set up so that they are dimensionally similar. This requires matching of the dimensionless length scale $\Lambda = L/\ell$ and the dimensionless time scale $\Gamma = t_c/\tau$. The reservoirs have the same volume, mass flow rates, temperatures and pressures as the nominal designs that have been discussed so far. The axial-flow store has the nominal design geometry as in table 3.1. The radial-flow geometry (aspect ratio and particle diameter) are then chosen such that Λ and Γ are the same for both reservoir types. Since the dimensionless numbers vary with temperature and mass flow rate and the numbers that are matched correspond to the average reservoir conditions. Table 3.5 provides details of the selected geometry for a cold reservoir.

		Axial-flow store	Radial-flow store
Length L[a]	(m)	5.45	3.00
Aspect ratio[b]		1.0	0.5
d_p	(mm)	20	16
V	(m^3)	127	127
t_c	(h)	6	6
ℓ	(mm)	50.6	28.4
τ	(s)	280	280
Λ		108	106
Γ		77	77

Table 3.5: Geometry of dimensionally similar axial-flow and radial-flow cold packed-beds.
[a] L is the length of the flow path through the store. For an axial-flow reservoir it is equal to the height of the store. For a radial-flow store it is given by $r_o - r_i$.
[b] The aspect ratio is defined as L/D for an axial-flow store, and as $H/2(r_o - r_i)$ in a radial-flow store.

Comparison of pressure losses

The cycle period $\Pi = t_c/t_N = \Gamma/\Lambda$ was varied and results are shown in figure 3.18. As indicated by the parametric studies, pressure losses in the radial-flow store are smaller than those in the axial-flow store. This is predominantly the result of smaller mass flow rates per unit area. For instance, the average G in the radial-flow store is 0.39 kg $m^{-2}s^{-1}$, whereas in an axial-flow store, $G = 0.59$ kg $m^{-2}s^{-1}$. Furthermore, the pressure drop depends on

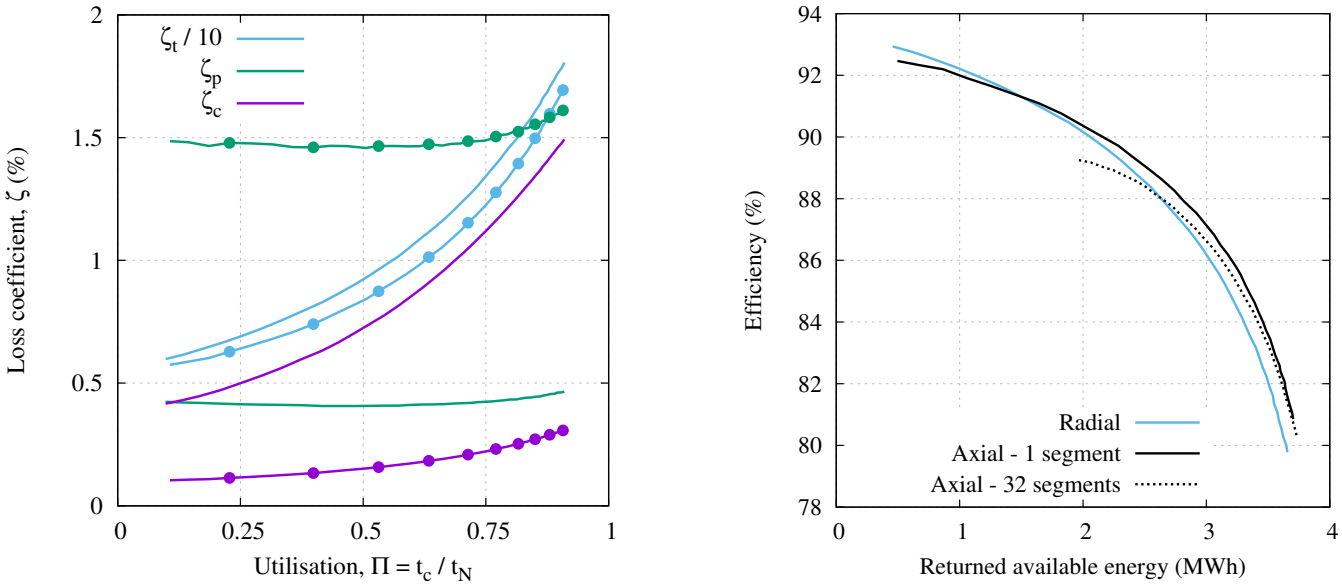

Figure 3.18: Comparison of dimensionally similar axial-flow packed beds and radial-flow packed beds as the cycle frequency $\Pi = t_c/t_N$ is varied. Curves generated by varying $\theta_{c,d}$ between 5% and 50%. **(a)** Loss coefficients. Lines correspond to radial-flow stores. Dotted lines correspond to axial-flow stores. Note that thermal losses are 10 times larger than those displayed. **(b)** Trade-off between efficiency and returned available energy.

the square of G. The pressure gradient in equation 2.53 can be reformulated as

$$\frac{\partial p}{\partial x} = -\frac{G^2}{2\rho_g \varepsilon^3 \ell}\frac{C_f}{\mathrm{St}} \tag{3.36}$$

Integrating this expression over the length of the reservoir to give the pressure drop and for an axial-flow reservoir this is

$$\Delta p_x = -\frac{\dot{m}^2}{2\pi^2 \varepsilon^3 \bar{\rho}_g}\frac{C_f}{\mathrm{St}}\frac{L}{\ell}\frac{1}{R_x^4} \tag{3.37}$$

where $\bar{\rho}_g$ is the average gas density and R_x is the radius. For a radial-flow reservoir the total pressure drop is

$$\Delta p_r = -\frac{\dot{m}^2}{8\pi^2 \varepsilon^3 \bar{\rho}_g}\frac{C_f}{\mathrm{St}}\frac{R_o - R_i}{\ell}\frac{1}{R_o R_i H^2} \tag{3.38}$$

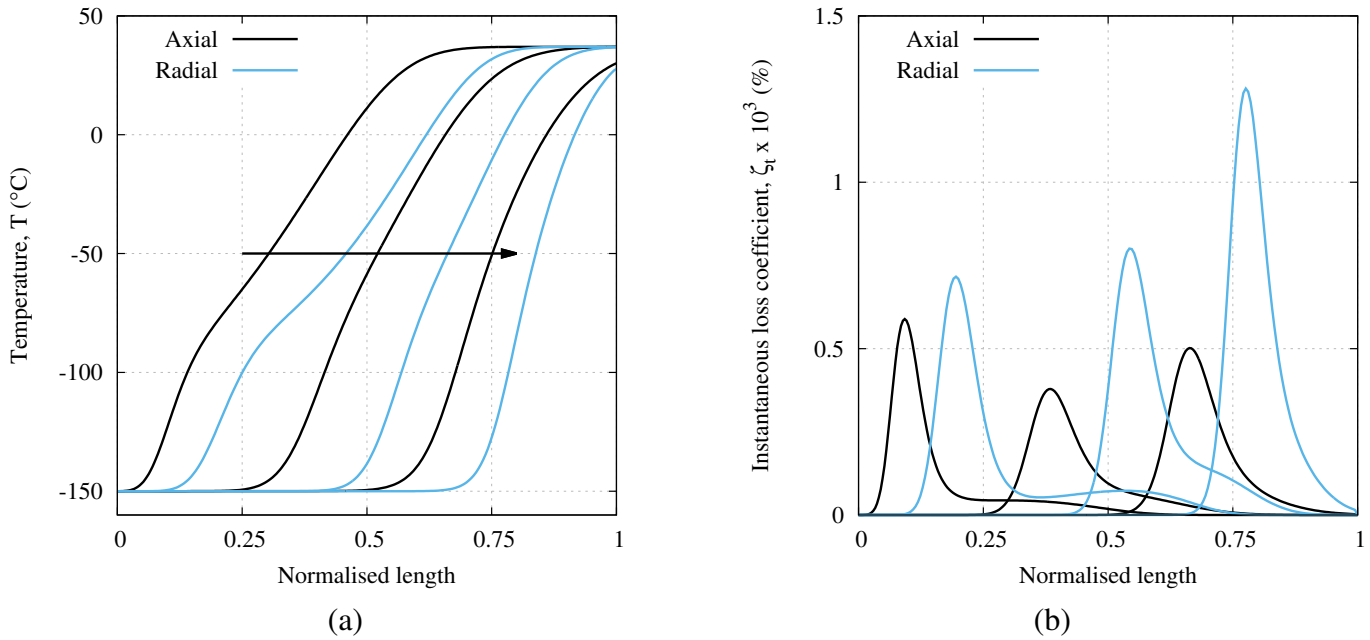

Figure 3.19: Comparison of thermal fronts formed in dimensionally similar axial-flow and radial-flow packed beds for $\Pi = 0.75$. Profiles are plotted at $t/t_c = 10\%$, 40% and 70% during charge. 'Normalised length' is x/L in axial-flow stores and $(r - r_i)/(r_o - r_i)$ in radial-flow stores. **(a)** Thermal front shapes **(b)** Instantaneous thermal loss coefficient at each x position

where H is the height of the radial reservoir. $C_f/\mathrm{St} \approx 4$ and $L/\ell = (R_o - R_i)/\ell = \Lambda$ for both radial and axial packed beds. Consequently, the ratio of the pressure losses is given by

$$\frac{\Delta p_r}{\Delta p_x} = \frac{R_x^4}{4R_i R_o H^2} \tag{3.39}$$

which is 0.5 for the dimensionally similar designs in table 3.5. This simplified analysis supports the results above, although it does not take into account the variation of parameters such as ℓ which depends on the mass flow rate per unit area.

Comparison of thermal and conductive losses

Figure 3.18(a) indicates that thermal and conductive losses are larger in radial-flow stores. For the same Π a radial-flow store forms a steeper thermal front *on average* than in the equivalent axial-flow store. As discussed in section 2.5.1 shorter thermal fronts lead to larger thermal losses as there is a smaller area for heat transfer. In addition, the front length

changes due to the variation in the mass flow rate per unit area with radius. Figure 3.19 compares the thermal fronts in dimensionally similar axial-flow and radial-flow stores. At the start of charge the radial-flow front is slightly longer than the axial flow front. However, as the front progresses it becomes steeper than the axial-flow front. A simplified analysis in Appendix A.2 indicates that the average radial-flow front length is less than the average axial-flow front length. Moreover, the fluctuations in front length lead to larger thermal losses than if the front was kept at its average value, as described in section 2.5.1 and Appendix A. The thermal loss coefficient is calculated at each x position along the thermal fronts and is plotted in figure 3.19(b). This illustrates that larger thermal losses are generated in radial-flow stores. Furthermore, steeper thermal gradients increase conductive losses.

Figure 3.18(b) illustrates the trade-off between efficiency and returned available energy as the charging frequency Π is varied. Axial-flow and radial-flow packed beds that are dimensionally similar perform equally well. Radial-flow stores attain slightly higher efficiencies, but axial-flow reservoirs can store slightly more available energy. The figure also shows results for an axial-flow store with 32 segments. The segmented store does not attain high efficiencies since its design has not been optimised.

The above studies indicate the radial-flow stores have a comparable performance to axial-flow stores. An optimisation algorithm can be used to compare the best possible designs of radial-flow and axial-flow stores. Additional factors and objectives such as economic considerations and/or space requirements can be included. For instance, it is important to determine the impact of the volume requirements of the inner and outer plenum on the energy density. Optimisation studies are carried out in chapter 5.

3.4.5 Storage losses in radial-flow stores

The impact of conductive and leakage losses in radial packed beds during the storage phase is evaluated in the same way as described in section 3.3.2. The radial heat equation is

$$\frac{\partial T}{\partial t} = \frac{\alpha}{r}\frac{\partial}{\partial r}\left(r\frac{\partial T}{\partial r}\right) \tag{3.40}$$

where $\alpha = k_{\text{eff}}/\rho_s c_s(1-\varepsilon)$. The heat equation is solved using the Crank-Nicolson numerical scheme.

The development of conductive losses with time is shown in figure 3.20. As in section 3.3.2 the thermal front is initially linear and either crosses the full radius of the reservoir ("Full profile") or only the final fifth of the reservoir ("Realistic profile"). The "realistic" profile is similar to the thermal profiles that were observed at the end of the charging phase. Conductive losses are initially larger in the realistic profile due to steeper thermal gradients, but the long-term losses are lower.

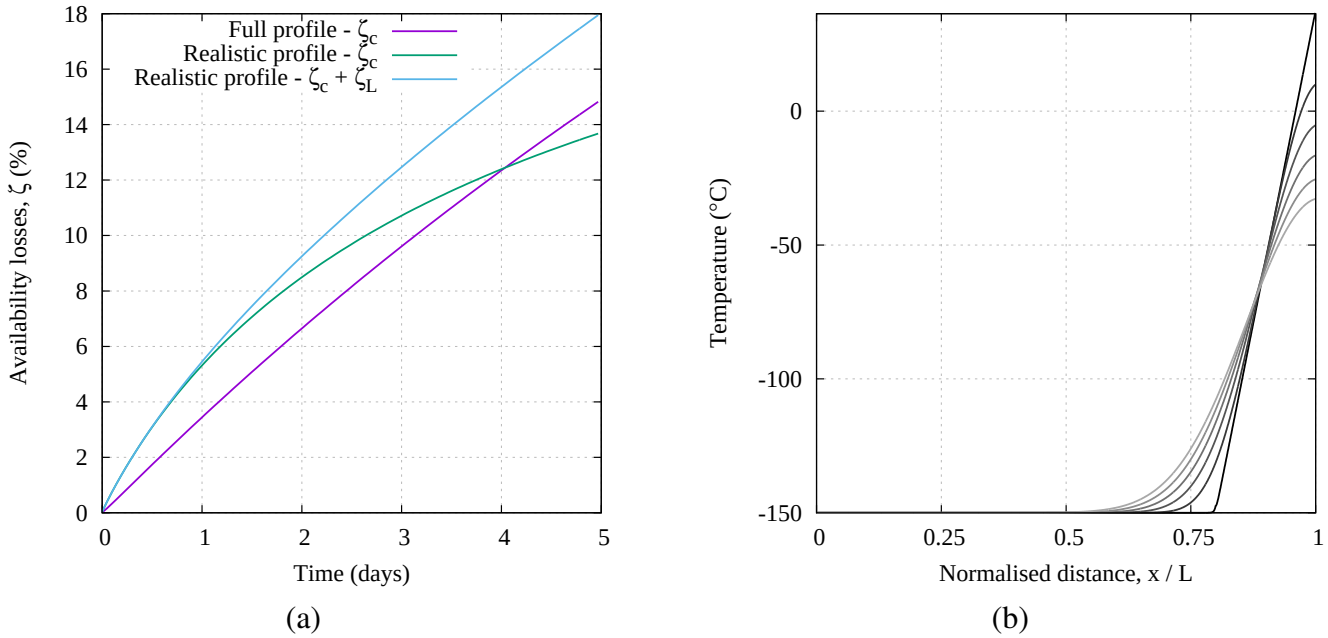

Figure 3.20: Conductive and leakage losses during the storage phase of a cold radial-flow packed bed reservoir with a linear thermal front. **(a)** Conductive losses during the storage phase of a cold radial reservoir. The thermal front crosses either the full reservoir, or only the final fifth. The final curve includes heat leakage losses and the profile crosses the final fifth of the reservoir. **(b)** Thermal fronts in a cold radial reservoir. The front initially covers the final fifth of the reservoir. Profiles are plotted every 3 days with the darkest line being 0 days.

It is clear that the conductive losses are substantially larger than those that occur in axial reservoirs (see figure 3.12). This is partly because the thermal front is initially much steeper. In addition, conduction occurs across the full radius of the radial store unlike segmented stores.

Heat leakage was included in a radial reservoir with a realistic profile in figure 3.20(a). Leakage does not add significantly to the total availability losses due to the 'self-insulating' behaviour: unlike axial stores, the external surface temperature of the radial stores is never significantly different from ambient temperature. However, as section 3.3.2 noted, sufficient levels of insulation in axial-flow stores could reduce the leakage losses and also conductive losses.

3.5 Summary

In this chapter, the detailed thermodynamic behaviour of packed-bed thermal reservoirs was investigated. Nominal designs for hot and cold reservoirs were developed, and key parameters were varied about these nominal values. These investigations improve understanding of packed bed thermal store behaviour. The uncertainties in the modelling and the correlations used should be borne in mind when considering the quantitative results. Experiments would provide useful validation for these methods. Nonetheless, the trends that emerge are useful and can be thought of as design guidelines. The expected trade-off between thermal losses and pressure losses was observed when geometric parameters such as aspect ratio and particle diameter were varied. Pressure losses are less significant in hot stores, meaning that optimal particle diameters are smaller, and optimal aspect ratios are larger. The optimal value of these parameters typically depends on other variables, such as the charging time, however.

Several different packing materials were compared, and it was found that the variation in specific heat capacity over the range of operation was a key factor in determining the thermal losses. The physical size of the packed beds was investigated by comparing stores with different volumes but the same charging period. Again, a trade-off between thermal and pressure losses led to there being an optimal volume. It was also found that larger packed beds would benefit from having a lower aspect ratio, L/D and that the heat leakage losses decreased as the reservoir volume was increased.

Parametric studies of the charging period revealed further conflicts between the round-trip efficiency and the available energy that was returned during discharge: longer charging periods created steeper fronts, leading to lower efficiencies and higher utilisation of the

packed beds.

The operating temperatures were varied and it was seen that the charging temperature should be as large as possible for hot stores and as small as possible for cold stores to increase efficiency. The study also suggested that the difference between charging and discharging temperature should be minimised, although this is not practical as it would minimise the storage density. The operating temperature results are only applicable to packed beds considered in isolation, since in PTES schemes the temperatures of the hot and cold reservoirs are dependent on one another.

The concept of segmenting the packed beds in order to reduce the pressure losses was introduced. By reducing pressure losses, segmentation allows smaller particles to be used, thereby reducing thermal losses and creating steeper thermal gradients. As a result, segmented packed beds were found to increase the efficiency and returned available energy during operational periods. Segmentation also significantly reduced conductive losses during storage periods. However, heat leakage during storage exacerbates the conductive losses and the packed bed should be sufficiently insulated to avoid this.

Radial-flow packed beds were introduced. The governing equations were derived and some simple parametric studies were undertaken. The radial-flow causes the mass flow rate per unit area to decrease with radius which can affect the shape of the thermal front, and most notably, significantly reduces the pressure losses. Radial-flow packed beds were found to have comparable performance to segmented and unsegmented packed beds, and more detailed investigations are recommended.

Chapter 4

Pumped Thermal Energy Storage (PTES)

4.1 Introduction

Pumped Thermal Energy Storage (PTES) is a novel energy storage system. Several variations exist and an overview is given in the literature review. This chapter is mainly concerned with the PTES system that was under development by Isentropic Ltd. Energy is stored in two packed-bed thermal reservoirs (one hot, one cold). During charge, the system operates as a heat pump, moving energy from the cold store to the hot store. The process is reversed in discharge, where the system behaves as a heat engine.

Figure 4.1 shows a schematic of the PTES layout, and a *T–s* diagram of ideal cycles proposed by Isentropic Ltd. and Saipem. The main system components are two compression-expansion devices (CE and EC) and two thermal stores (one hot, HS, and one cold, CS). The discharged state of the reservoirs is set close to ambient temperature: 310 K in the present case. With argon as the working fluid (as proposed in [107]), and with a pressure ratio of 10:1, the nominal hot and cold storage temperatures (based on isentropic compression and expansion) are then 778 K and 123 K.

Following previous work, investigations centre on a nominal design with an energy storage capacity of 16 MW h, and a power rating on 2 MW. For a reversible, adiabatic system, the stored energy that can be converted back to useful work (i.e. the available energy) is the difference between the stored internal energies of the two reservoirs

$$E = M_s^h c_s^h (T_2 - T_3) - M_s^c c_s^c (T_1 - T_4) \tag{4.1}$$

where M_s is the mass of storage material, c_s is its average specific heat capacity over the relevant temperature range, and the superscripts h and c refer to the hot and cold reservoirs respectively. The mass of storage material in a reservoir is given by $M_s = \rho_s(1-\varepsilon)V_s$ where ε is the void fraction. The reservoirs are sized by specifying that they charge in the same period of time. Since the nominal charging time is given by $t_N = M_s c_s / \dot{m} c_{p,g}$ where $\dot{m}$ is the mass flow rate and $c_{p,g}$ is the specific heat capacity of the gas, if the reservoirs are to charge in the same time then $M_s^h c_s^h = M_s^c c_s^c$. Consequently, the stored energy is

$$E = M_s^h c_s^h (T_2 - T_3 - T_1 + T_4) = M_s^c c_s^c (T_2 - T_3 - T_1 + T_4) \tag{4.2}$$

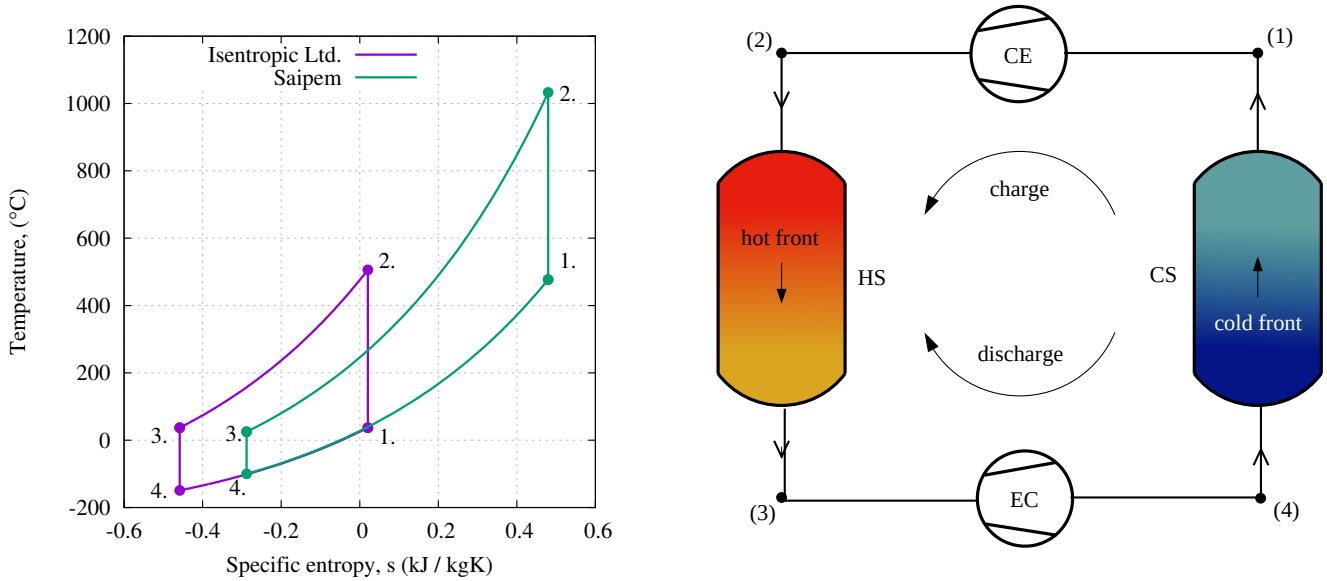

Figure 4.1: **(a)** *T*–*s* diagrams of ideal Joule-Brayton based PTES systems as proposed by Isentropic Ltd. and SAIPEM. During charge the diagrams are traversed in the anti-clockwise direction. **(b)** Schematic layout of an ideal PTES system during charge. Key: HS/CS hot/cold store; CE/EC reversible compressor–expanders.

Therefore the hot reservoir volume can be calculated given a specific energy storage capacity, and the cold store volume can be calculated from the equality of heat capacities.

As discussed in the previous chapters, magnetite (Fe_3O_4) provides a suitable storage material due to its high heat capacity per unit volume, and its low fractional variation of heat capacity over the temperature ranges of interest. Data for magnetite are given in table 4.1, together with the required storage masses computed from equation 4.2 for 16 MWh of storage. The reservoir volumes are also given in the table, calculated with an average void fraction of 0.40. The nominal stores have an aspect ratio of $L/D = 1$, such that the internal diameters are 4.5 m and 5.3 m for the hot and cold stores respectively.

The power output for a reversible, adiabatic PTES system is given by

$$\dot{W}_x = \dot{m} c_{p,g} \left[(T_2 - T_1) - (T_3 - T_4) \right] \tag{4.3}$$

Using the temperatures listed above and data for argon ($c_{p,g} = 520$ J kg^{-1}K^{-1}), the mass flow rate required for a 2 MW device is 13.7 kg s^{-1}.

	P (bar)	T (K)	ρ_g (kg m^{-3})	M_g (kg)	$\bar{c}_s$ (J kg^{-1}K^{-1})	M_s (tonne)	V (m^3)
Hot							
Charge	10.5	778	6.5	196	860	234	75.5
Discharge	10.5	310	16.3	492			
Cold							
Charge	1.05	123	4.1	208	520	395	127.1
Discharge	1.05	310	1.63	83			

Table 4.1: Hot and cold reservoir details for a nominal 16 MWh PTES system. The storage material is Fe_3O_4 (density 5.175 tonne m^{-3}) in the form of a packed bed with an assumed void fraction of $\varepsilon = 0.40$. Further reservoir details are given in table 3.1.

Isentropic Ltd.'s design uses reciprocating machines as the compression and expansion devices. A similar thermal energy storage scheme developed in France (SEPT) uses turbomachinery as described in chapter 1 and displayed in figure 4.1(a). The Isentropic design has the advantage that only two machines are required: by changing the valve timings a reciprocating device may operate as a compressor or an expander. This could potentially lead to lower system costs, and as a result reciprocating devices are investigated rather than turbomachinery.

Simple models of reciprocating devices are developed in this chapter which allow the required geometry to be calculated, and describe their behaviour. Developing realistic models of these components is important because preliminary studies have suggested that the round-trip efficiency depends heavily on the compression and expansion efficiency, particularly since a full charge-discharge cycle involves four compression-expansion processes. Other components, such as heat exchangers, buffer vessels, and electrical heaters are also discussed. The previous chapter suggested that high efficiencies could be achieved in the packed-beds and optimisation studies in chapter 5 suggest that efficiencies could reach 99.5% in hot stores and 95% in cold stores. Therefore, careful design of the reciprocating devices is a necessity for PTES to be a competitive option.

4.1.1 Metrics of PTES performance

Generally, the round-trip efficiency of energy storage systems is defined as the ratio of net work output during discharge to the net work input during charge[1]. In the present study, only the "thermodynamic" efficiency χ is considered – i.e. excluding losses due to electrical and mechanical processes. χ is given by

$$\chi = \frac{\text{Net work output}}{\text{Net work input}} = \frac{W_{\text{dis}}^{\text{net}}}{W_{\text{chg}}^{\text{net}}} \tag{4.4}$$

For a 2 MW machine using an induction motor-generator, electrical efficiencies of 97% in each direction are commonplace, but mechanical losses for a custom-built reciprocating devices are less easy to estimate. Howes [5] suggests a mechanical efficiency of 92% might be possible in each direction. Together with the electrical losses, the electricity-to-electricity round-trip efficiency is $(\eta_{\text{mech}}\eta_{\text{elec}})^2\chi \approx 0.8\chi$.

In chapter 1 simplified expressions for χ were developed and revealed the impact of design parameters on the system performance. In this chapter, χ is evaluated by integrating the power input and output over the duration of the charge-discharge cycle. This is necessary because the power output changes as the hot and cold fronts reach the exits of the reservoirs.

Other useful performance metrics are the energy density ρ_E and power density ρ_P which are defined as:

$$\rho_E = \frac{\text{Net work output}}{\text{Reservoir volume}} = \frac{W_{\text{dis}}^{\text{net}}}{V_{\text{CR}} + V_{\text{HR}}} \tag{4.5}$$

$$\rho_P = \frac{\text{Net work output}}{\text{Hot cylinder volume}} = \frac{W_{\text{dis}}^{\text{net}}}{V_s^{\text{CE}}} \tag{4.6}$$

where V_s indicates the swept volume which is discussed in more detail in section 4.2. The power density typically increases monotonically with χ [84]. Maximising energy density typically leads to a trade-off with efficiency and therefore ρ_E is related to cost. This chapter focuses on thermodynamic metrics as economic factors tend to be uncertain (see chapter 5).

[1] Some storage systems, such as CAES, have a dual role of storage and generation, and a different definition of the round-trip efficiency is required.

4.2 Modelling of reciprocating devices

The theory of reciprocating compressors and expanders is less fully developed than for packed beds. Their performance is compromised by mechanical irreversibilities (such as friction and pressure losses) and thermal irreversibilities caused by heat transfer between the fluid and the cylinder walls. A simplified model of reciprocating devices was developed by White [160]. Heat losses are quantified by a fractional heat loss factor ν defined as

$$dq_c = \nu dw_c \tag{4.7}$$

where dq_c is the heat loss and dw_c is the work input during an infinitesimal compression process. The corresponding reversible work input is dp/ρ, regardless of whether the process is adiabatic. Irreversibility may then be defined by introducing the (compression) polytropic efficiency η_c, where

$$dw_c = \frac{dp}{\rho \eta_c} \tag{4.8}$$

As shown in Ref. [160] this leads to a polytropic expression of the form

$$\tau_c = \beta_c^{\phi_c} \tag{4.9}$$

where τ_c and β_c are the compression temperature and pressure ratios, and ϕ_c is the compression polytropic exponent,

$$\phi_c = \frac{\gamma - 1}{\gamma} \left(\frac{1 - \nu_c}{\eta_c} \right) \tag{4.10}$$

Similar expressions exist for the expander. In the polytropic model heat leakage losses and irreversibilities are accounted for independently. On the other hand, isentropic models are only suitable for adiabatic processes and cannot resolve the individual influences of heat transfer and other irreversibilities. For example, during compression the effects of irreversibility and heat transfer could 'cancel' one another out thereby leading to a process which is isentropic but not ideal.

Pressure losses occur in pipework and valves and are included by specifying a fractional pressure loss factor $f_p = \Delta p/p$. Losses occur at the inlet and outlet valves of the reciprocat-

ing devices such that each component has two pressure loss factors. For example, for the inlet valve with an inlet p_1 and outlet p_1' the pressure loss factor is given by $f_p = (p_1 - p_1')/p_1$. This is a convenient definition, since the pressure loss factors are closely related to the exergetic pressure loss ζ_p (see equation 2.55). Thus, a given absolute pressure loss Δp has a greater impact on performance if it occurs in the low pressure part of the cycle.

Availability loss coefficients ζ

Second law analysis of the PTES system requires the loss in available energy in each component to be calculated. Loss coefficients for various loss generating mechanisms in the packed-bed thermal reservoirs were discussed in section 2.5. In reciprocating devices availability loss coefficients are given by the loss in available energy divided by the net work input during charge, such that

$$\zeta = \frac{B_{\text{lost}}}{W_{\text{chg}}^{\text{net}}} \tag{4.11}$$

whereas the availability loss coefficients derived in section 2.5 were divided by the net inlet available energy into the thermal store. Note the terminology *loss coefficient* refers to a fractional loss in available energy, whilst *loss factor* refers to an empirical factor that determines the magnitude of a loss generating mechanism (η, ν or f_p).

The irreversible entropy generation due to the pressure loss at each valve is given by:

$$\dot{S}_{\text{irr}} = -\dot{m}R\ln(1 - f_p) \tag{4.12}$$

so that the pressure loss coefficient in the reciprocating devices is

$$\zeta_p = -\frac{\dot{m}RT_0\ln(1 - f_p)}{W_{\text{chg}}^{\text{net}}} \tag{4.13}$$

In a compressor, the available energy loss coefficient corresponding to the polytropic efficiency η is found by substituting $\nu_c = 0$ into the expression for the polytropic exponent ϕ_c and calculating the increase in entropy which leads to

$$\zeta_t = \left(\frac{1 - \eta}{\eta}\right)\frac{\dot{m}RT_0\ln\beta}{W_{\text{chg}}^{\text{net}}} \tag{4.14}$$

The availability loss coefficient associated with heat addition ζ_Q can then by found by taking the increase in availability for the compression process (after the inlet valve and before the outlet valve) and subtracting from it the thermal loss ζ_t and the work input w_c which leads to

$$\zeta_Q = \frac{\dot{m}}{W_{\text{chg}}^{\text{net}}} \left[\frac{\nu_c c_p T_1 \left(\beta^{\phi_c} - 1\right)}{\nu_c - 1} + 2 \left(\frac{\eta - 1}{\eta} \right) R T_0 \ln \beta \right] \tag{4.15}$$

Similar expressions can be derived for the expander.

The general model described above is equally applicable to turbomacinery and reciprocating devices but the present work focuses on the latter. Evaluating the availability loss coefficients requires values for each of the loss factors η, ν and f_p. In the next section a simplified model of reciprocating device geometry is used to obtain order of magnitude estimates of ν and f_p. More detailed models of turbomachinery or reciprocating devices could have been employed. However, the aim is to develop simple expressions that reveal the influence of design parameters on the loss factors. Due to the uncertainty of these results, the sensitivity of PTES performance to each loss factor is explored in section. 4.4.1.

Simplified model of a reciprocating compressor

A schematic diagram of a reciprocating compressor is shown in figure 4.2(a). The compressor has a diameter d and a stroke length $L_s = 2r$ (where r is the crank length), and rotates at an angular velocity ω. The pressure-volume diagram for the ideal compression process is shown in figure 4.2(b) (ideal expansion processes are represented by the same curve traversed in the opposite direction). After compression, the valves are opened at (2) and the flow is discharged until the piston reaches top dead centre (TDC) at (3). At this point the valves are closed and the piston reverses direction, thereby expanding the gas. The valves are then re-opened at (4) for the suction phase, and closed again at bottom dead centre (BDC) at (1). In the absence of heat leakage and irreversibility, processes (1)–(2) and (3)–(4) are isentropic. The volumetric compression ratio is therefore

$$r_v = \frac{V_1}{V_2} = \frac{V_4}{V_3} = \beta^{1/\gamma} \tag{4.16}$$

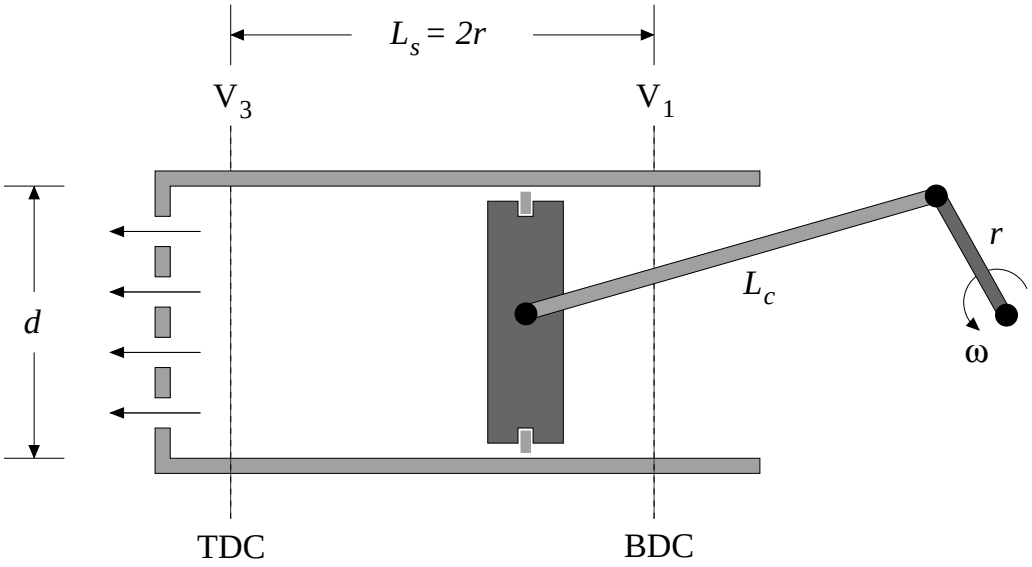

(a)

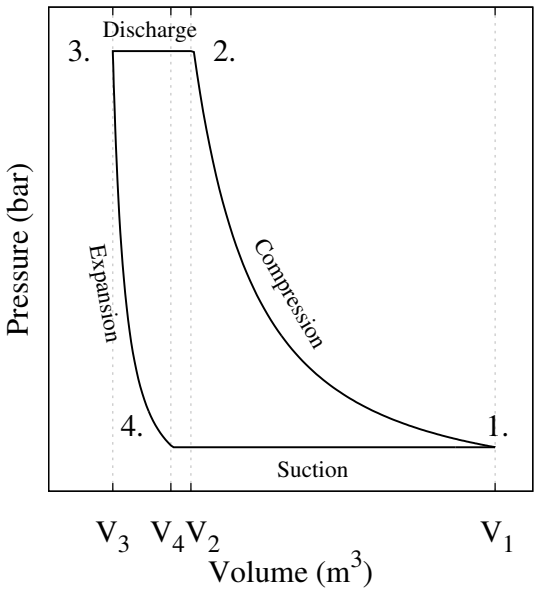

(b)

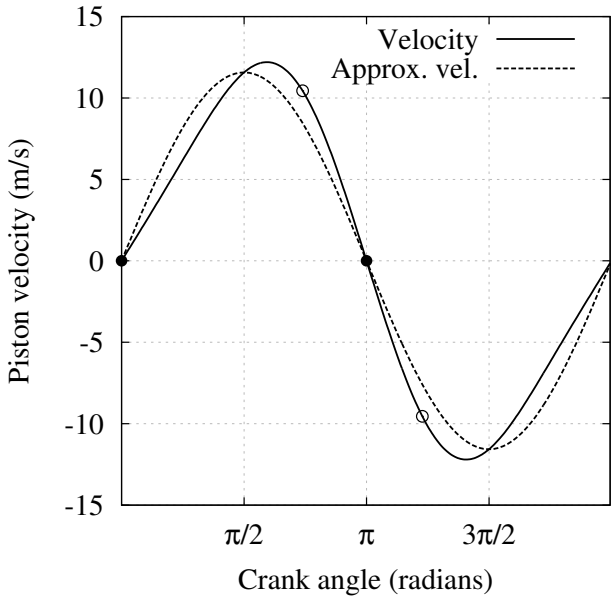

(c)

Figure 4.2: **(a)** Schematic diagram of reciprocating piston. **(b)** p-V diagram for an ideal reciprocating compressor. The lines are followed anti-clockwise. The direction is reversed (but otherwise identical) for an expander **(c)** Velocity variation in an ideal reciprocating compressor given by 4.23. Approximate velocities given by $v_p = wr \sin\theta$. Filled circles indicate where valves close and open circles indicate valves opening for a cycle with a pressure ratio of 10.

where β is the pressure ratio. If the inlet valve pressure losses are small then the mass of gas entering the cylinder during the suction stroke (4–1) is

$$m_{\text{in}} = \rho_{\text{in}}(V_1 - V_4) = \rho_{\text{in}} V_1 (1 - \varepsilon r_v) \tag{4.17}$$

where ρ_{in} is the inlet density and ε is the clearance (or dead) volume ratio given by $\varepsilon = V_3/V_1$. The volumetric efficiency is therefore given by

$$\eta_v = \frac{m}{\rho_{\text{in}} V_s} = \frac{1 - \varepsilon r_v}{1 - \varepsilon} \tag{4.18}$$

where $V_s = V_1 - V_3$ is the swept volume. The same expression for volumetric efficiency may be applied to expanders but with the density evaluated at the outlet rather than the inlet. (For instance, for the PTES scheme illustrated in figure 4.1, for charging compressors use ρ_1 and for charging expanders use ρ_4).

The mass flow rate versus pressure ratio characteristic curve for the compressor is developed by considering the mass flow rate in and is thus,

$$\dot{m} = \frac{\rho_1 V_s \omega}{2\pi} \eta_v = \frac{\rho_1 V_s \omega}{2\pi} \frac{\left(1 - \varepsilon \beta^{1/\gamma}\right)}{(1 - \varepsilon)} \tag{4.19}$$

This model is used to size the reciprocating devices for the PTES system. The mass flow rate is fixed by the power rating (equation 4.3) and the swept volumes are then found from equation 4.19. Nominal reciprocating device details are tabulated in table 4.2. These designs have 6 cylinders, a nominal dead space ratio of 0.05, a speed of 1200 RPM and an aspect ratio (stroke / diameter) of 0.25. This low aspect ratio is proposed in preliminary designs by Isentropic Ltd. [5] on the grounds that the resulting low piston velocity leads to low valve pressure losses and low inertial loading. Figure 4.3 illustrates the mass flow characteristics of these nominal designs for different dead volume ratios. (Characteristics for the compressor and expander are coincident, since the devices are sized to have the same mass flow rate at the same pressure ratio). At low dead volume ratios the pressure ratio can be varied without significantly effecting the mass flow rate. Small ε also increases the volumetric efficiency of the device. However, in practice it may be challenging to reduce ε too much below 5%.

	Speed (RPM)	V_s (total) (m^3)	N_{cyl}	Bore d (m)	Stroke L_s (m)	Clearance (mm)
Hot cylinders	1200	0.50	6	0.75	0.19	10
Cold cylinders	1200	0.20	6	0.55	0.14	7.4

Table 4.2: Details of the compression-expansion devices for a nominal power rating of 2 MW. The nominal designs have a clearance ratio of $\varepsilon = 5\%$ and a cylinder aspect ratio of $L_s/d = 0.25$.

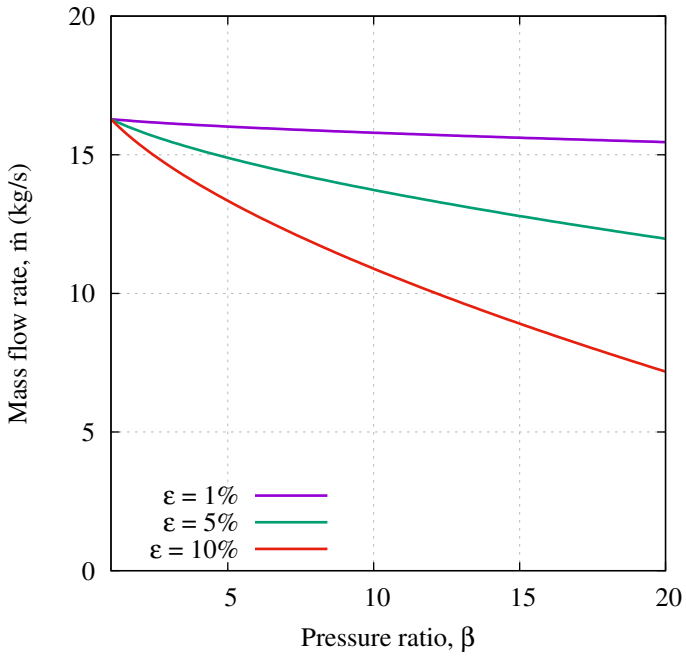

Figure 4.3: Mass flow rate–pressure ratio characteristic for reciprocating devices calculated using equation 4.19 and data from table 4.2. Characteristics for the hot and cold cylinders are coincident.

4.2.1 Pressure loss estimation

Pressure losses occur in the reciprocating devices as the gas enters and exits the piston chamber during the suction and discharge steps, respectively. These losses can be minimised by actuating the valves when there is no pressure difference across them and if the valves open and close rapidly. An indicator diagram for a prototype device developed by Isentropic Ltd [5] is shown in figure 4.4 and shows behaviour that is reasonably similar to the ideal *p*–*V* diagram of figure 4.2(b). This suggests that the objective of significantly reducing pressure losses may be achievable in practice. Isentropic Ltd. designed valves that comprise two thin sheets of metal which are perforated with rectangular openings, as

shown in figure 4.5. When the valves are closed, the sheets lie over one another such that there are no openings for the gas to flow through. The pressure difference keeps the sheets in place until the pressure equilibrates across both sides and the opening force causes one sheet to slide over the other, and allows the gas to flow through the perforations. This design allows careful control of valve opening and closing times, and maximises the valve open area which Isentropic Ltd. estimates is around 30% of the bore area [5]. Reportedly, this design configuration also helps to reduce large scale turbulence after the valve. Pressure

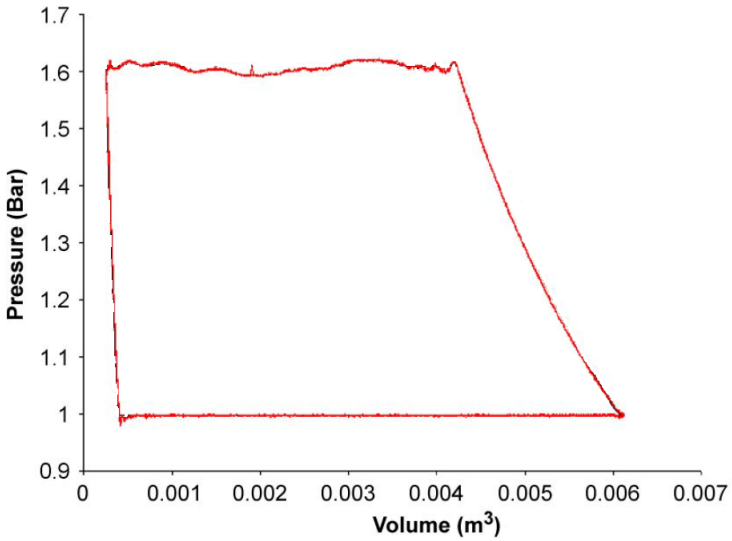

Figure 4.4: *p–V* diagram from a prototype piston developed by Isentropic Ltd. which shows a comparable shape to the ideal *p–V* diagram in figure 4.2(b). Figure is reproduced from [5].

losses are included in computational models by specifying a pressure loss factor f_p for each valve. These factors can be estimated by considering the schematic diagram in figure 4.6 whereby a single orifice represents the rectangular grid that makes up Isentropic's valves. Miller [150] suggests that this is a reasonable assumption, especially if the plate is thin in comparison to the hole diameter. The orifice has an area A_v such that it equals the open area of the real valve (therefore $\sigma = A_v/A_p \approx 0.30$). A *vena contracta* (or narrowing of the fluid jet due to streamline curvature) occurs after the valve and the contraction area is typically given by $\sigma_{vc} = A_{vc}/A_v \approx 0.64$.

Assuming that the gas travels at the piston velocity, making use of the mass continuity equation, and by applying the steady flow momentum equation between B–C and the steady

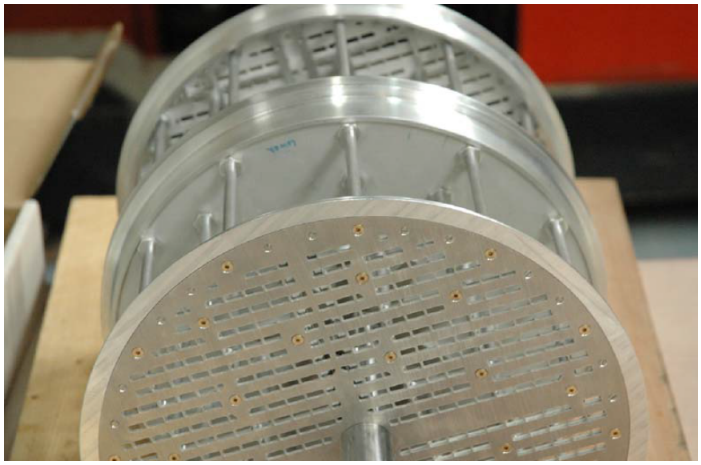

Figure 4.5: Prototype piston developed by Isentropic Ltd. [5] which illustrates the valve arrangement that consists of many rectangular orifices.

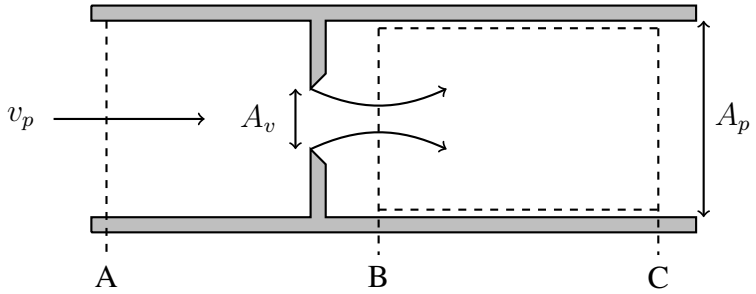

Figure 4.6: Schematic diagram of gas at velocity v_p passing through a valve of area A_v into the piston cylinder of area A_p

flow energy equation between A–B, the pressure loss is thus

$$\Delta p = p_A - p_C = \frac{\rho v_p^2}{2}\left(\frac{\sigma\sigma_{vc} - 1}{\sigma\sigma_{vc}}\right)^2 \tag{4.20}$$

Where the density is approximately constant across the control volume at this instant in time. The pressure loss factor is given by

$$f_p = \frac{\Delta p}{p} = \frac{v_p^2}{2RT}\left(\frac{\sigma\sigma_{vc} - 1}{\sigma\sigma_{vc}}\right)^2 \tag{4.21}$$

Evaluation of f_p requires the piston velocity v_p, which can be derived by considering fig-

ure 4.2(a). The piston position x_p is given by

$$x_p = \sqrt{L_c^2 - r^2 \sin^2 \theta} - r \cos \theta \tag{4.22}$$

where L_c is the length of the connecting rod, r is the length of the crank arm, and θ is the crank angle. Differentiating this expression gives the piston velocity as

$$v_p = \omega \left(r \sin \theta - \frac{r^2 \sin \theta \cos \theta}{\left(L_c^2 - r^2 \sin^2 \theta\right)^{\frac{1}{2}}} \right) \tag{4.23}$$

A conservative pressure loss factor f_p is estimated by taking the piston velocity at its maximum value $v_p = \omega r$ [84] to give

$$f_p = \frac{\omega^2 L_s^2}{8RT} \left(\frac{\sigma\sigma_{vc} - 1}{\sigma\sigma_{vc}} \right)^2 \tag{4.24}$$

where L_s is the stroke length. Estimated values for the loss factors at inlet and outlet of the compressor and expander are given in table 4.3. A more accurate estimate is obtained by considering how the instantaneous pressure loss factor varies with piston velocity. An average pressure loss factor $\bar{f}_p$ is given by the value which produces the same irreversible entropy generation as that calculated by integrating instantaneous values of f_p. For instance, the irreversible entropy generation caused by an instantaneous pressure loss is given by (compare with equation 2.55)

$$\dot{S}_{\text{irr}} = -\dot{m} R \ln (1 - f_p) \tag{4.25}$$

The total irreversible entropy generation is found by integrating over the time that the valves are open

$$\begin{aligned} S_{\text{irr}} &= -R \int \ln (1 - f_p)\, dm \\ &= -\rho_{\text{ref}} R A_p \int \ln (1 - f_p)\, dx \\ &= -\frac{\rho_{\text{ref}} R A_p}{\omega} \int_{\theta_1}^{\theta_2} v_p \ln (1 - f_p)\, d\theta \end{aligned} \tag{4.26}$$

	$L_s/d = 0.25$			$L_s/d = 1.00$		
	$v_{\mathrm{p,max}}$ (m/s)	f_{p} (%)	$\bar{f}_{\mathrm{p}}$ (%)	$v_{\mathrm{p,max}}$ (m/s)	f_{p} (%)	$\bar{f}_{\mathrm{p}}$ (%)
Hot cylinder inlet	11.9	1.96	1.43	29.5	12.2	6.92
Hot cylinder outlet		0.78	0.33		4.84	1.49
Cold cylinder inlet	8.8	1.06	0.45	21.9	6.60	2.90
Cold cylinder outlet		2.67	1.96		16.6	12.54

Table 4.3: Pressure loss factors in reciprocating devices. f_p is calculated using the maximum velocity (as in [84]) whereas $\bar{f}_p$ is calculated from equation 4.28. Values are calculated for charging compressors (hot cylinder) and charging expanders (cold cylinder).

In these expressions ρ_{ref} is the gas density for the particular process. For instance, in the charging compressor, $\rho_{\mathrm{ref}} = \rho_1$ for the suction pressure loss factor, and $\rho_{\mathrm{ref}} = \rho_2$ for the discharge pressure loss factor. θ_1 and θ_2 represent the crank angles at which the valves open and close respectively. The crank angle at which the charge compressor opens its valves during suction can be found by considering the volume (and thereby x_p) at which the correct pressure ratio is achieved. In this case, the valve closing crank angle is simply given by $\theta_2 = 2\pi$.

Setting equation 4.26 equal to the entropy generation that would occur for some average value of pressure loss factor $\bar{f}_p$ gives

$$-\rho_{\mathrm{ref}} A_p L R \ln\left(1-\bar{f}_p\right) = -\frac{\rho_{\mathrm{ref}} R A_p}{\omega}\int_{\theta_1}^{\theta_2} v_p \ln\left(1-f_p\right) d\theta \tag{4.27}$$

where L is the distance that the piston travels whilst the valves are open. In the charge compressor, during suction $L = x_1 - x_4$ and during discharge $L = x_2 - x_3$. Consequently, the entropy averaged value of pressure loss factor is given by

$$\bar{f}_p = 1 - \exp\left\{\frac{1}{\omega L}\int_{\theta_1}^{\theta_2} v_p \ln\left(1-f_p\right) d\theta\right\} \tag{4.28}$$

Calculated values for $\bar{f}_p$ are given in table 4.3. As expected, these values are lower than the pressure loss factors using the maximum gas velocity, and indicate that for the given design, values of f_p of around 1% are reasonable. Table 4.3 also indicates that the lower the aspect ratio L_s/d, the lower the valve pressure losses.

4.2.2 Heat transfer losses

In theory, the time-mean heat leakage can be reduced to very small levels with sufficient insulation. Heat leakage factors have therefore been set to 2% for baseline calculations. However, even if the processes are globally adiabatic, losses are still incurred due to time-varying heat transfer to and from the cylinder walls. To estimate the magnitude of this loss, the irreversibility is divided into three parts: heat transfer between the cylinder walls and the inlet (or outlet) gas, heat transfer between the gas and the walls during the compression and expansion strokes, and a mixing loss between the residual gas and the inlet gas. The loss in efficiency due to these three processes is estimated for compression, and it is assumed a similar loss factor applies to expanders.

Heat transfer during induction and delivery

The walls of the compressor have thermal inertia and are likely to be at a temperature greater than the cool inlet gas, and lower than the compressed outlet gas. The gas that enters the compressor is preheated by the walls prior to the compression stroke. Similarly, the gas is cooled by the walls during the delivery stroke. The net effect is that heat is transferred from the high exit temperature down to the low inlet temperature, as illustrated schematically in figure 4.7. Analysis of this problem was carried out in the appendix of [84]. To simplify the problem, the complete process (1–2) is assumed adiabatic and the compressor (1'–2') is isentropic. Since the wall temperature is between the inlet and outlet temperatures it is written as $T_w = T_1 + \theta(T_2 - T_1)$ where $0 < \theta < 1$. The heat transferred to the inlet gas can be written as

$$Q = hS(T_w - T_1)\tau = hS\theta(T_2 - T_1)\tau \tag{4.29}$$

where h is an average heat transfer coefficient, S is the average internal surface area and τ is the duration of the induction stroke. The heat transfer increases the enthalpy of the inlet mass according to

$$Q = mc_p(T_1' - T_1) = \rho_1 v_p A c_p(T_1' - T_1)\tau \tag{4.30}$$

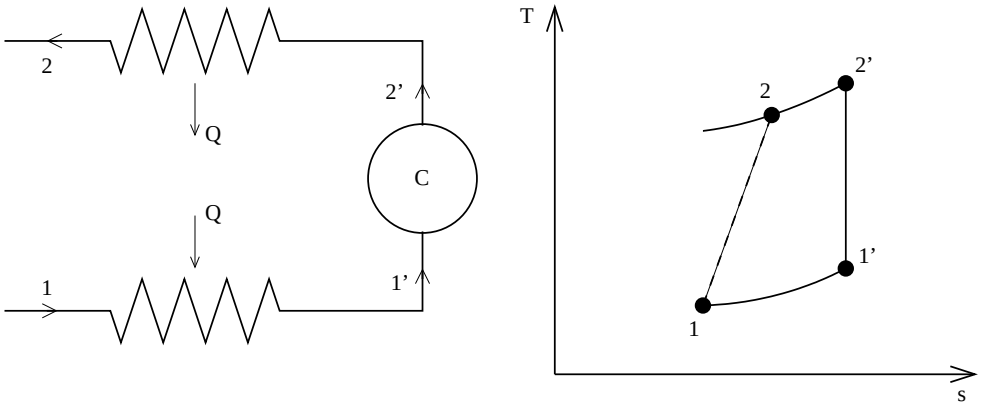

Figure 4.7: Simplified model of the irreversibility associated with preheating during induction and cooling during delivery, shown for a compression process. The overall process 1–2 is assumed to be adiabatic.

where v_p is the average piston speed during induction and A is the piston face area. Equating the two expressions for Q gives

$$T_1' - T_1 = \mathrm{St}\theta\frac{S}{A}(T_2 - T_1) = T_2' - T_2 \tag{4.31}$$

where St is the Stanton number (based on average piston speed). The equality on the right-hand side is a result of the full process being adiabatic. By inspection of the *T–s* diagram of figure 4.7 and using the above equations, the *isentropic* efficiency is given by

$$\eta = \frac{T_2' - T_1'}{T_2 - T_1} \tag{4.32}$$

$$= 1 - \kappa\left[\beta^{(\gamma-1)/\gamma} - 1\right] \tag{4.33}$$

where $\kappa = \mathrm{St}\theta S/A$ which represents the heat transferred during induction as a fraction of the work transfer. As expected, this fraction is independent of the pressure ratio β although efficiency losses are larger at high pressure ratios due to the larger temperature difference across which heat is transferred. The fraction κ is difficult to accurately determine. A rough estimate involves setting $\theta = 1/2$ and approximating the Stanton number from a turbulent pipe flow correlation, such as $\mathrm{St} = 0.023\mathrm{Re}^{-1/5}\mathrm{Pr}^{-3/5}$. For the nominal design conditions given in table 4.2 this gives $\kappa = 0.0025$ which corresponds to an efficiency loss of approximately 0.4% at a pressure ratio of 10:1.

Heat transfer during compression and expansion strokes

Heat transfer occurs during the compression and expansion strokes (1–2 and 3–4 on figure 4.2(b), respectively). It is no longer appropriate to use a simple heat transfer coefficient due to the interaction between heat and work transfers, and the inherently unsteady behaviour of these two processes. Lawton [8] explains this behaviour and notes that in general the heat flux is not in phase with the temperature difference. For instance, figure 4.8 is a schematic of the temperature variation across a cylinder during compression which illustrates the interaction between the heat (diffusion in the boundary layer) and work (adiabatic compression) transfers. At the beginning of compression, the wall temperature is greater than the core temperature, and heat transfer occurs from the wall to the gas. During compression the temperature of the gas increases. In the absence of conduction, the temperature at point 1 which is located in the thermal boundary layer increases above the wall temperature. Consequently, the wall is heated by the gas despite the core gas temperature being lower than the wall temperature. During expansion, the reverse effect occurs, and the wall is cooled even though the core is hotter than the wall. As a result, the heat flux is not always in phase with the temperature difference and this can be modelled with a complex Nusselt number.

A number of studies have attempted to quantify the above effect in the context of gas springs. These comprise a fixed mass of gas enclosed in a cylinder and a piston but with no flow of gas into or out of the system. Ideal gas springs are fully reversible, such that compression and expansion lines on the *p*–*V* diagram are coincident. However, heat transfer irreversibilities result in a hysteresis loss such that there is a net work input into the system. Early work by Lee [7] led to the development of a simple analytical expression for this loss which fits experimental data reasonably well, as reported by Kornhauser and Smith [6] and reproduced in figure 4.9. Minor modifications were made to the theory in [6] to improve the fit. In more recent work by Mathie et al. [161] an extended semi-analytical model was proposed for the full conjugate (solid-gas) thermal problem in gas-springs.

Kornhauser et al.'s results are shown in figure 4.10. The loss is expressed as a reduction in the polytropic efficiency where half of the hysteresis loss is attributed to the compression stroke. The horizontal axis in this figure is the Peclet number, $\mathrm{Pe} = \omega D_h^2 / 2\alpha_t$, where D_h is the cylinder mean hydraulic diameter, and α_t is the mean thermal diffusivity of the

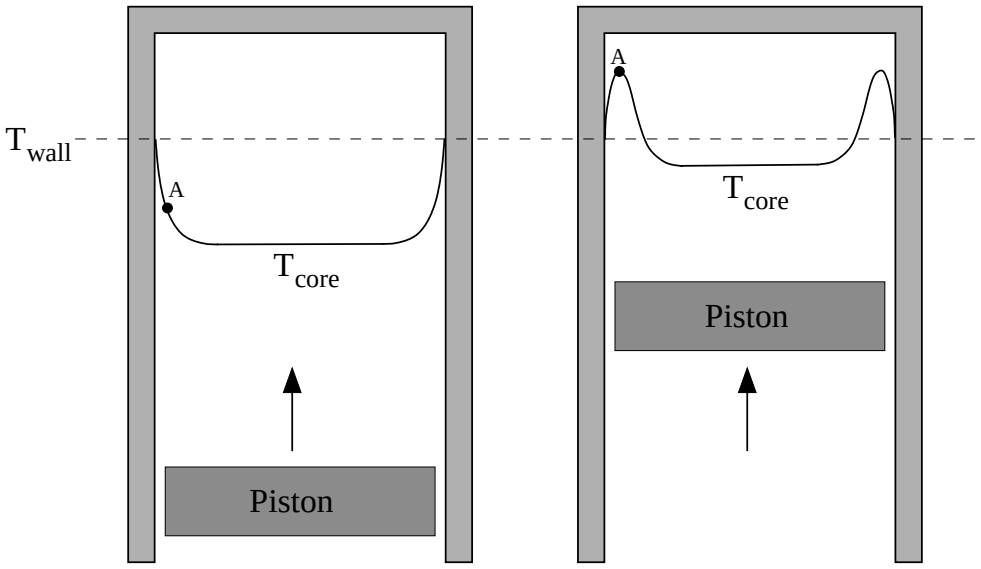

Figure 4.8: Schematic of heat transfer in a reciprocating device during compression. The figure on the left shows the beginning of compression where the wall temperature is greater than the core fluid temperature. The right-hand figure shows the compression at a later stage, where at some points (e.g. A) the boundary layer gas temperature is greater than the wall temperature.

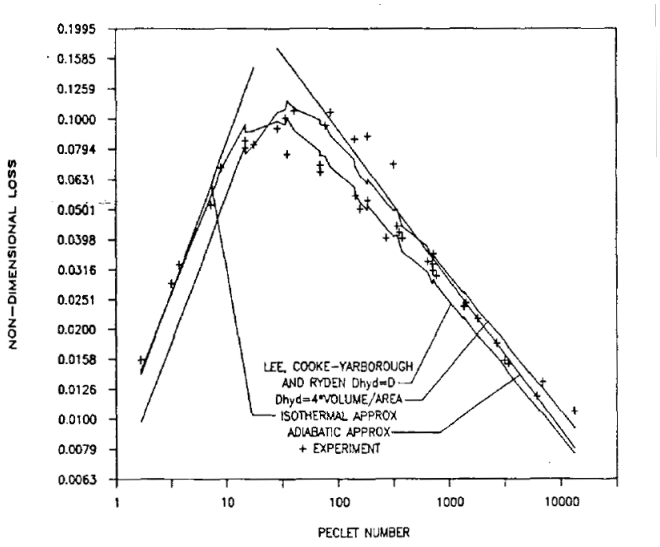

Figure 4.9: Experimental and theoretical results for heat transfer losses in gas springs. Figure is taken from Lee [6]. The figure shows the analytical expression developed by Lee [7] as well as isothermal and adiabatic limits, and experimental results.

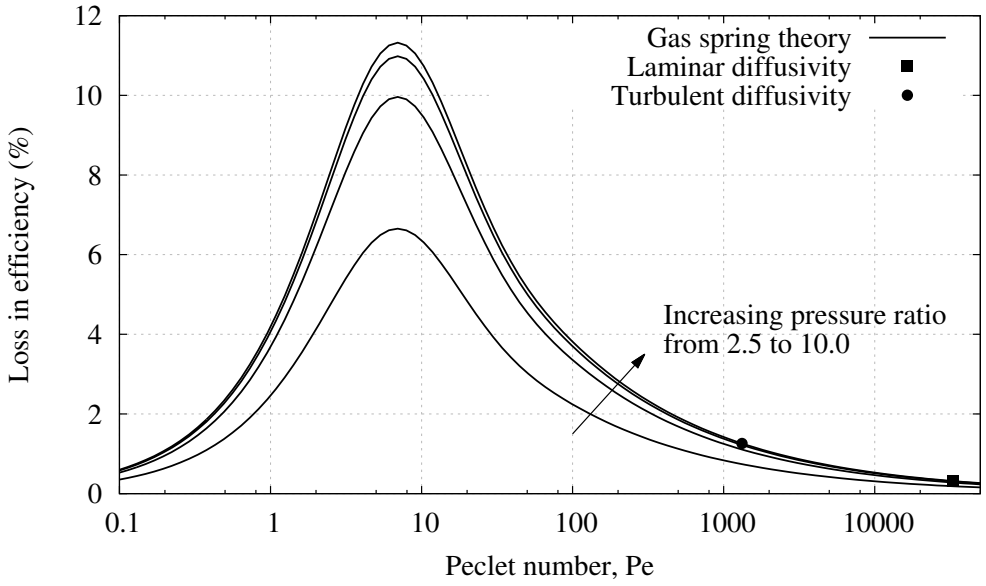

Figure 4.10: Loss in efficiency due to heat transfer irreversibilities in gas springs. Gas spring theory uses the expression by Kornhauser [6].

gas. The Peclet number for the nominal design of hot cylinder is 34 000, suggesting an efficiency loss of around 0.3%. However, the thermal dissipation loss in a real compressor (as opposed to a gas spring) may be considerably larger because the eddying and turbulent motion generated by the inlet valve is likely to enhance the effective diffusivity. In this context, Lawton [8] found that good agreement between theory and experiment for heat transfer rates in a motored piston engine (albeit with a different valve design) could be obtained by multiplying the gas conductivity by 25 as shown in figure 4.11. This would reduce the Peclet number to 1360 and thereby increase the loss to 1.3%. Other models (such as that in [161]) predict higher losses than this.

Mixing losses

Due to irreversibility and heat transfer during processes 1→4, the residual gas in the cylinder may end up at a different temperature to that entering the cylinder, thereby giving rise to an additional mixing loss. The mixing loss can be estimated in the following way. The

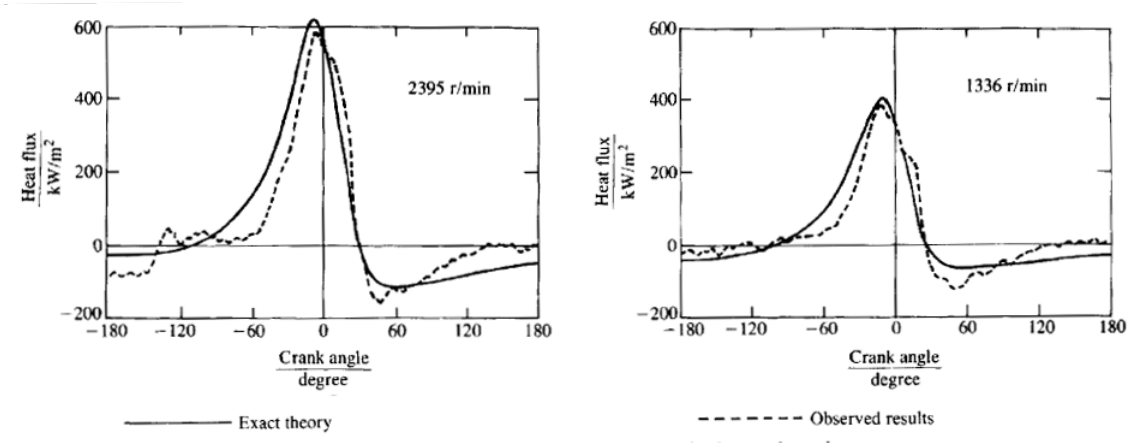

Figure 4.11: Experimental and theoretical results for heat transfer in reciprocating devices. Figure is from Lawton [8] and shows the cylinder wall heat flux against the crank angle.

gas that enters the cylinder has temperature T_1 and its mass m_i is

$$m_i = \rho_1 V_1 \left(1 - \varepsilon \beta^{1/\gamma}\right) \tag{4.34}$$

The residual gas has temperature T_4 which can be estimated from polytropic relationships. For a polytropic efficiency of 97.5%, $T_4 \approx 325$ K. The mass of the residual gas m_r is approximately given by

$$m_r = \rho_4 \varepsilon V_1 \left(\beta^{1/\gamma} - 1\right) \tag{4.35}$$

The temperature at which the inlet and residual gas equilibrate T_f is found by equating the heat flux, for example

$$m_r c_p (T_4 - T_f) = m_i c_p (T_f - T_1) \tag{4.36}$$

For the current case, the final temperature is approximately 314 K. The entropy increase due to mixing is given by

$$\Delta S_{\text{irr}} = (m_i + m_r) c_p \ln\left(\frac{T_f}{T_0}\right) - m_i c_p \ln\left(\frac{T_1}{T_0}\right) - m_r c_p \ln\left(\frac{T_4}{T_0}\right) \tag{4.37}$$

The loss factor is then given the loss of available energy normalised by the work input in the adiabatic case W_{ad}

$$\zeta = \frac{T_0 \Delta S_{\text{irr}}}{W_{\text{ad}}} \tag{4.38}$$

The adiabatic work is the work input during compression for a gas-spring (rather than a compressor) so that the mixing loss factors are calculated in a consistent manner with the other heat transfer irreversibilities. For a gas spring where compression occurs between V_1 and V_3 the adiabatic work input is

$$W_{\mathrm{ad}} = \int_1^3 p dV = \frac{p_1 V_1}{1-\gamma}\left(\varepsilon^{1-\gamma} - 1\right) \tag{4.39}$$

For the case described above, the mixing loss factor is around 0.01%. When the residual gas is above the expected temperature, the residual mass is small compared to the inlet mass thereby giving rise to the small mixing losses.

Concluding remarks on heat transfer losses

The simplified analysis above is somewhat uncertain due to the interplay between a number of heat transfer processes within the reciprocating devices. In addition, it is unclear exactly what impact the turbulent eddies of the gas flow through the valves will have. As a result, accurate estimates of efficiency require detailed experimental investigations.

4.3 Other components

4.3.1 Heat Exchangers

Heat exchangers reject heat and are required for steady state cyclic operation to be achieved. They are placed at points 1 and 3 in figure 4.12 where they are labelled HX1 and HX3. These locations are closest to ambient temperature and are therefore the most efficient locations for heat rejection to occur. Figure 4.12(b) illustrates the *T*–*s* diagram for a non-ideal PTES system. Irreversibilities in the compressors and expanders, plus the progression of the thermal fronts out of the stores leads to a need for heat rejection.

Heat exchanger design should consider a wide range of factors such as the required inlet and outlet temperatures of gas flow, the heat exchanger geometry (shell and tube, cross flow, multiple passes, fin shapes and sizes etc.), the gas or liquid to which heat is rejected

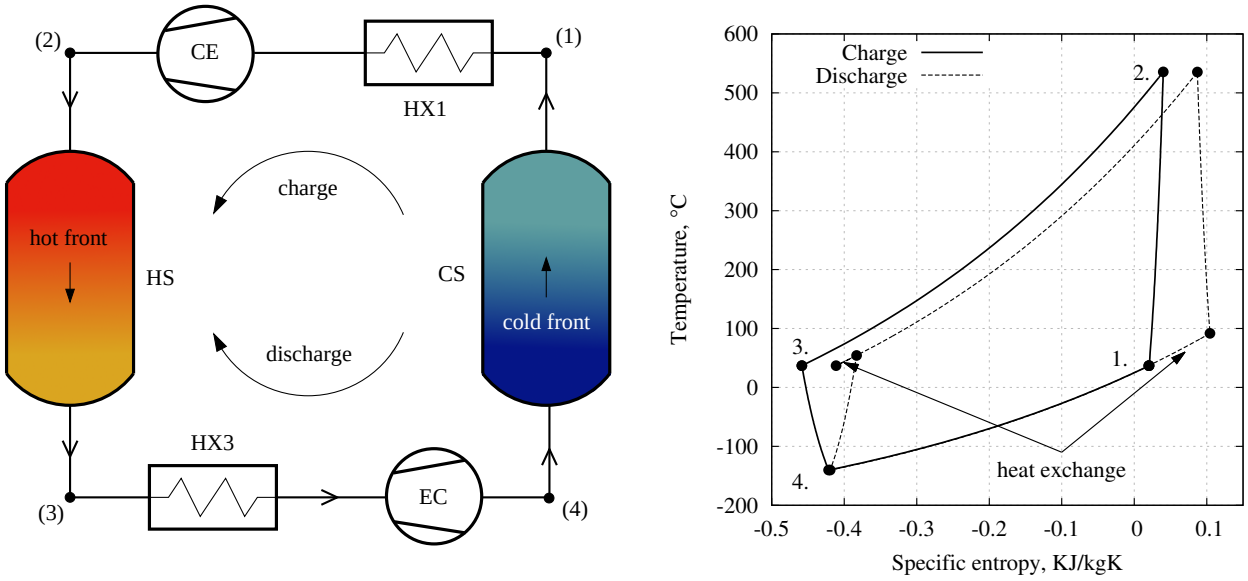

Figure 4.12: **(a)** Schematic layout of a PTES system during charge. Key: HS/CS hot/cold store; CE/EC reversible compressor–expanders; HX1/HX3 heat exchangers. **(b)** *T*–*s* diagrams of a PTES system during charge and discharge. During charge the diagrams are traversed in the anti-clockwise direction. In this example, the discharging cycle operates at a lower pressure ratio and heat rejection occurs at both HX1 and HX3.

(and its mass flow rate), the desired performance and the economic cost of these design requirements [162]. The modelling is simplified here by considering two parameters: the effectiveness ϵ governs the efficiency of the heat transfer processes, and a pressure loss factor f_p which accounts for frictional pressure drops.

The effectiveness is defined as the ratio between the actual rate of heat transfer and the maximum possible rate of heat transfer. For a heat exchanger where gas enters at a high temperature $T_{g,i}$ and is cooled to $T_{g,o}$ by water which enters at $T_{w,i}$, the effectiveness is given by

$$\epsilon = \frac{\dot{m}_g c_{p,g}(T_{g,i} - T_{g,o})}{(\dot{m}c_p)_{\min}(T_{g,i} - T_{w,i})} \tag{4.40}$$

where $(\dot{m}c_p)_{\min}$ is the minimum heat capacity rate of the two flows. For the outlet gas flow to be as close to the water inlet temperature as possible (i.e. to maximise the heat transfer) the minimum heat capacity rate should equal that of the gas. The outlet gas temperature is

thus

$$T_{g,o} = T_{g,i} - \epsilon \left(T_{g,i} - T_{w,i} \right) \tag{4.41}$$

The lost work associated with heat rejection may be calculated by finding the change in available energy between the inlet and oulet gas, which, in the case of zero pressure losses is given by

$$\dot{S}_{\mathrm{irr}} = \dot{m}(b_{\mathrm{i}} - b_{\mathrm{o}}) = \dot{m} c_p \left(T_{g,i} - T_{g,o} - T_0 \ln \left(\frac{T_{g,i}}{T_{g,o}} \right) \right) \tag{4.42}$$

The effectiveness may be calculated using approaches such as the NTU-ϵ method. However, this requires geometric data, and it is more revealing to choose a value of ϵ and consider its impact on the behaviour of the cycle. Heat exchanger design can begin in earnest once its importance relative to other component parameters has been determined. Nonetheless, it is useful to estimate the magnitude of ϵ and, following [160], data from a compact heat exchanger of surface type $8.0 - 3/8T$ has been employed. This design has finned cylindrical tubes which are perpendicular to the flow direction. The purpose of the fins is to enhance the heat transfer rate and provide structural support. The fin geometry means that the exchanger can be used in scenarios where one stream is at a higher pressure than the other, as may be the case in PTES systems [162]. Data for an $8.0 - 3/8T$ exchanger is available in Kays and London [163]. Heat transfer results correlate the Colburn j factor $j_H = \mathrm{StPr}^{2/3}$ against Reynolds number from which it is possible to calculate the overall heat transfer coefficient. An approximate value of the effectiveness can be obtained by using the standard result for a cross-flow heat exchanger [137]. The effectiveness is evaluated for several heat exchangers (HX3) of different volumes in table 4.4. These results use $8.0 - 3/8T$ exchanger data and assume the heat capacity flow rates of water and gas are equal (resulting in a water mass-flow-rate of $\sim$1.7 kg s^{-1}). An average inlet gas temperature is 50°C is also assumed. An effectiveness of 80% is achieved using a reasonably compact heat exchanger that has a total volume of 1 m^3. To achieve an effectiveness close to 90% requires a much larger heat exchanger of 5m^3. Sensitivity of PTES performance to the heat exchanger effectiveness is investigated in section 4.4.1.

Pressure losses are the result of friction along the heat exchanger, and losses at the inlet/outlet manifolds and in the inlet/outlet ducts or valves. Like the reciprocating devices, losses are defined using pressure loss factors where $f_p = \Delta p / p$. Losses in the core of the heat exchanger are estimated in this section, whilst those that arise in the connecting

HX3 volume (m^3)	0.5	1.0	5.0
Side wall length, L_{hx} (m)	0.80	1.0	1.70
Heat exchange area, A_x (m^2)	290	590	2900
Reynolds number, Re	5400	3400	1200
Overall heat transfer coefficient, U (W $m^{-2}K^{-1}$)	145	116	63
Effectiveness, ϵ	0.77	0.81	0.87
Friction factor, f_v	0.022	0.025	0.03
Pressure loss factor, $f_p = \Delta p/p$ (%)	0.11	0.06	0.014

Table 4.4: Approximate effectiveness and pressure loss factors for several heat exchangers of different sizes for HX3 with a $8.0 - 3/8T$ surface [160, 162, 163].

pipes/manifolds are discussed in 4.3.3.

Losses are estimated for the $8.0-3/8T$ exchanger described above. Kays and London [163] provide correlations for the friction factor f_v and Reynolds number. The pressure drop across the cylinders is given by [160, 162]

$$\Delta P = 1/2\rho v_x^2 f_v \frac{A_x}{A_{\text{ff}}} \tag{4.43}$$

where v_x is the maximum gas velocity in the heat exchanger which occurs at the minimum free flow area A_{ff}, and A_x is the area over which heat transfer takes place. Pressure losses for several heat exchangers are tabulated in table 4.4 from which it is clear that within the heat exchanger they are very small (around 0.1%). Losses in additional pipework are more significant and should be included.

The above discussion gives an indication of the typical performance and size of the heat exchangers in a PTES system. There are a number of additional practical considerations. For instance, the inlet water temperature $T_{w,i}$ may typically be around 15°C, whereas for the nominal PTES design the desired gas outlet temperature from the heat exchanger is 37°C. Consequently, the heat exchanger would not seek to cool the inlet gas down to $T_{w,i}$, but rather increase the water temperature to that of the inlet gas flow. Furthermore, as the thermal front emerges from the packed bed, the inlet gas temperature changes. To maintain a constant outlet gas temperature, the mass flow rate of water should be varied. As the operating point changes, the performance of the heat exchanger may also be affected.

For the cycle calculations presented in the rest of this chapter, the heat exchanger behaviour

is simplified and its performance is governed by a factor ϵ^* that corresponds to the change in temperature of the gas as a fraction of the total required change, that is:

$$\epsilon^* = \frac{T_{g,i} - T_{g,x}}{T_{g,i} - T_{g,o}} \tag{4.44}$$

where $T_{g,o}$ and $T_{g,x}$ are the ideal scenario and obtained outlet gas temperatures respectively. This definition simplifies the integration of heat exchangers into the PTES system, and gives a sufficient indication of their influence on PTES behaviour.

4.3.2 Electric heater

In some cases, the outlet temperature of a packed bed may fall below the desired value. For instance, during charge the thermal front in the cold reservoir will eventually emerge from the exit. The exit temperature will then be less than T_1 and heat addition is required to maintain cyclic operation. Heat addition may be provided by an electric heater, for which the *work* input is given by

$$\dot{W}_h = \dot{m} c_{p,g} \left(T_{g,o} - T_{g,i} \right) \tag{4.45}$$

If the heater does not heat the gas back up to the required temperature, a 'heater effectiveness' ϵ_h can be defined in the same way as ϵ^* for the heat exchangers. Availability losses are given by the work input minus the increase in availability of the gas. In this chapter, heater losses are combined with the heat exchanger loss.

These additional work inputs (plus the expense of installing a heater) should be avoided, and section 4.5 investigates designs that achieve this.

4.3.3 Pipe work and valves

Pressure losses occur in the pipes that connect the packed beds, reciprocating devices and heat exchangers. Without detailed knowledge of the geometry it is difficult to accurately calculate these losses. Factors that should be considered are the length, diameter and roughness of the pipes, the number of bends, expansions and contractions and the precise geometry of these individual features [164]. For instance, a sudden expansion will cause a greater

Pipe location	Pressure (bar)	Temperature (K)	Diameter (m)	$\Delta P/P^*$ (%)
1.	1.05	310	0.55	1.0
2.	10.5	778	0.22	0.026
3.	10.5	310	0.17	0.010
4.	1.05	123	0.43	0.41

Table 4.5: Pressure loss factors in pipes. Each pipe section corresponds to a point on the PTES schematic in figure 4.1. The diameters are those which give a pressure loss factor of 1%. * The final column is the pressure loss factor for a pipe of diameter 0.55 m.

pressure loss than a gradual expansion, and a tight bend could lead to flow separation and secondary flows [165].

The pressure loss ΔP can be written as

$$\Delta P = 1/2\rho V^2 K \tag{4.46}$$

where K is an empirical factor that depends on the flow conditions and geometry. Values of K are given in several textbooks [164, 165], and Miller [150] provides data for a wide range of pipe types. Use of this data requires detailed geometric information, which at this early design stage is unspecified. Instead, the pressure losses are assumed to be of the order of $1/2\rho V^2$, as generally $K \sim 1$. By keeping these losses within 1% of the local pressure it is possible to calculate the required pipe diameters at each point around the cycle as in [84], and these are shown in table 4.5. The largest pipe diameter occurs in section 1 and is around 0.55 m. The pressure loss factors are also evaluated for the case where all the pipes are identical with diameter 0.55 m.

In the PTES model pressure loss factors are incorporated with the compressor and expander valve pressure losses to reduce the number of variables. This is appropriate because these loss factors are additive if they are reasonably small, as is the case here: the new pressure P_2 after a number of loss factors f_i have been applied is $P_2 = P_1 \prod(1 - f_i)$. If the f_i are small then the expression becomes $P_2 \approx P_1(1 - \sum f_i)$.

4.3.4 Buffer tank

A buffer tank is required because the total mass of gas within the packed beds changes during charge. The change in mass of gas is given by

$$\Delta m = \frac{\varepsilon V P}{R}\left(\frac{1}{T_{\text{chg}}} - \frac{1}{T_{\text{dis}}}\right) \tag{4.47}$$

where V is the volume of the reservoir, and T_{chg} and T_{dis} are the charging and the discharging temperatures. Table 4.1 shows the masses of charged and discharged hot and cold reservoirs, and indicates that the total change in mass between charge and discharge is 171 kg. Locating the buffer tank at point 3 on diagram 4.1 minimises the required volume which is then 10.5 m^3, but this does require the vessel to be pressurised, and insulation may also be necessary. Pressure losses occur in the valves and pipes for both filling and emptying of the tanks. These losses are taken into account by the other pressure loss factors in the cycle.

4.4 Behaviour of PTES systems

The behaviour of PTES systems is investigated using parametric studies. A nominal 16 MWh, 2 MW design has been chosen as described at the beginning of chapter 3. The nominal design has a thermodynamic efficiency of $\chi = 67.4\%$, an energy density of $\rho_E =$ 34.3 kWh m^{-3} (123.5 MJ m^{-3}) and a power density of $\rho_P = 2.9$ MW m^{-3}. Values for each of the nominal design parameters are given in table 3.1. These parameters are individually varied through a range of values to investigate the impact on PTES performance. The nominal design uses a polytropic efficiency of 98% and values in this range have been used in the literature before [160, 166]. Detailed simulation results suggest that reciprocating devices could achieve indicated efficiencies of 87–93% if leakage flow and pressure losses are reduced [167].

	f_{p}	$1-\eta$	ν	$f_{\mathrm{p,hx}}$	$1-\epsilon^{*}$
Nominal	0.02	0.02	0.02	0.02	0.20
Minimum	0.00	0.00	0.00	0.00	0.00
Maximum	0.04	0.04	0.04	0.04	0.40

Table 4.6: Nominal values of loss factors, and minimum and maximum values used in parametric studies

4.4.1 Sensitivity to loss factors

As discussed above, the availability losses that occur in the reciprocating devices, heat exchangers and pipe work are defined in terms of loss factors. The sensitivity of the round-trip efficiency to each of the loss factors was investigated by White et al. [83] as part of a simplified analysis of a PTES system. Ref. [83] developed an expression for the round-trip efficiency χ in terms of the temperature ratios $\tau = T_2/T_1$ and $\theta = T_3/T_1$ and included the effect of pressure loss f_p, heat leakage ν and irreversibilities η. Partial derivatives of χ with each loss factor indicate the sensitivity to these factors. For instance, the sensitivity to the compression/expansion heat leakage factor is defined as

$$S_\nu = -\frac{\partial \chi}{\partial \nu} \tag{4.48}$$

According to [83] $S_\nu = 2.0$ and is independent of τ which means that there will be a 2% increase in losses for each 1% of heat leakage. Results from [83] are shown in figure 4.13 for various values of the isentropic temperature ratio τ. For the nominal design, $\tau = 2.5$, and from the figure 4.13 it can be seen that $S_\eta = 2.0$, $S_\nu = 2.0$ and $S_{f_p} = 0.9$. This analysis suggests that the PTES round-trip efficiency is susceptible to polytropic efficiencies, especially at low pressure ratios.

Sensitivity to the loss factors was explored using the full PTES thermodynamic model. Nominal values for the loss factors are given in table 4.6, as are the maximum and minimum values. Figure 4.14 shows how the round-trip efficiency changes as the loss factors are varied and the results support the simplified analysis of Ref. [83]. For instance, the efficiency drops around 2% for every 1% decrease in the polytropic efficiency. Figure 4.15(a) shows the distribution of availability losses in each component, from which it can be seen that the polytropic efficiency significantly affects the losses in the reciprocating devices.

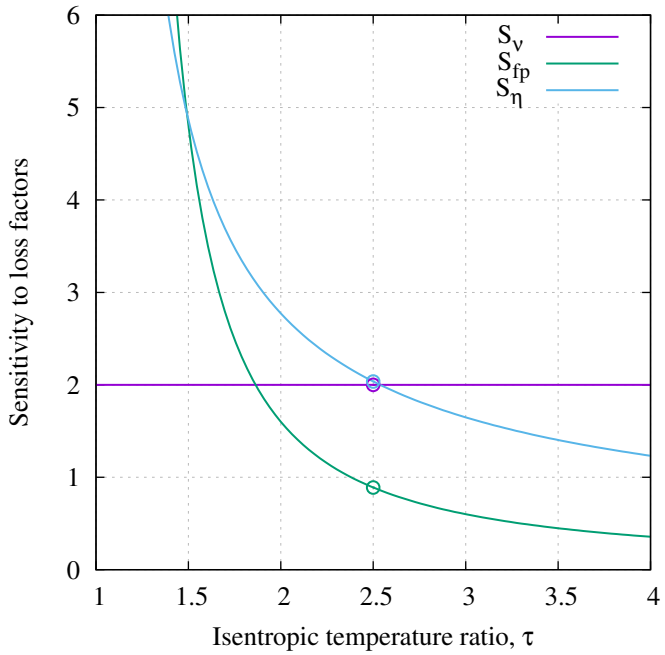

Figure 4.13: Sensitivity of thermodynamic PTES round-trip efficiency to loss factors. Results are from a simplified model of PTES in [83]. Open circles indicate the sensitivities at $\tau = 2.5$, the nominal PTES design.

Heat exchanger losses are also affected, although the net impact remains fairly constant.

The heat loss factor ν has a slightly larger impact than that predicted by Ref. [83]. Figure 4.15(b) indicates that the reciprocating device losses significantly affected by ν as expected. In addition, heat exchanger losses increase to a similar extent because of increased exit losses from the packed beds. Heat exchanger behaviour was not included in the analysis of Ref. [83] which accounts for the difference in the results.

These results highlight the importance of minimising heat leakage from the reciprocating devices, and for more thoroughly understanding the thermal irreversibility that occurs within them.

Note that these results are also applicable to compression and expansion with turbomachinery. Heat leakage losses may be less significant in turbomachines but the polytropic efficiency will be just as influential.

The heat exchanger loss factor $1 - \epsilon^*$ has quite a small effect on the round-trip efficiency. As figure 4.16(a) shows, losses in the thermal reservoirs increase if the heat exchanger ef-

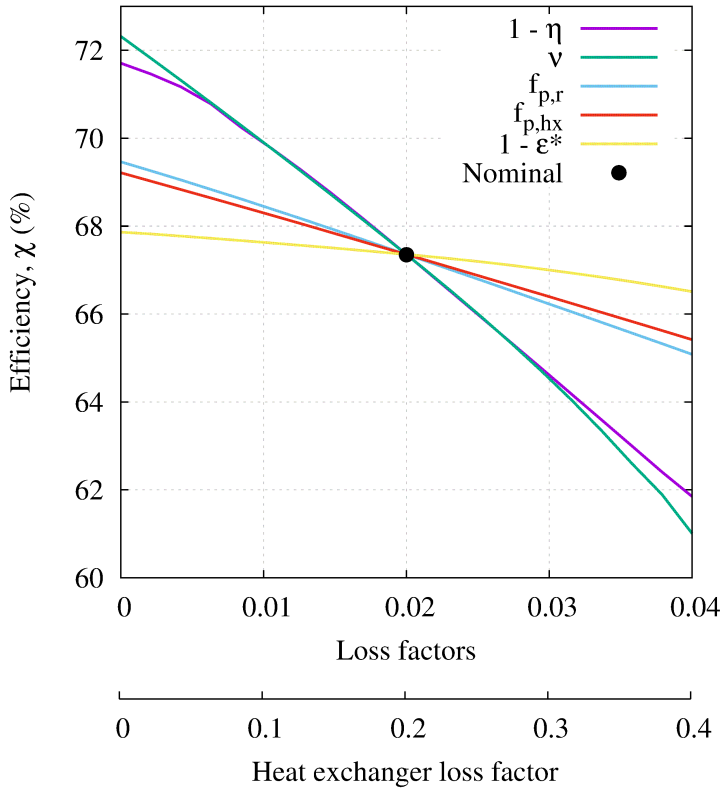

Figure 4.14: Sensitivity of thermodynamic round-trip efficiency to loss factors

fectiveness is increased. This is surprising, but is due to changes in the inlet temperature of the reservoirs when $\epsilon^* < 1$, as shown in figure 4.16(b). For instance, during discharge, the inlet temperature to the discharge compressor increases above T_4 as the cold front emerges, and this leads to a compressor outlet temperature above T_3. As HX3 does not reject all the required heat, the hot reservoir inlet temperature during discharge is greater than the design value of T_3.

Figure 4.16(b) illustrates how hot store thermal profiles are affected by the heat exchanger effectiveness. When $\epsilon^* < 1$, the thermal gradients occur across a greater proportion of the store. However, the thermal front is typically less steep and as a result, thermal losses actually reduce as indicated by considering the area under the curve of $(T_g - T_s)^2 / T_g T_s$ in figure 4.16(b). (This expression scales with the thermal losses, see section 2.5.1.)

Overall, reducing the heat exchanger performance ϵ^* has a negative effect on the round-

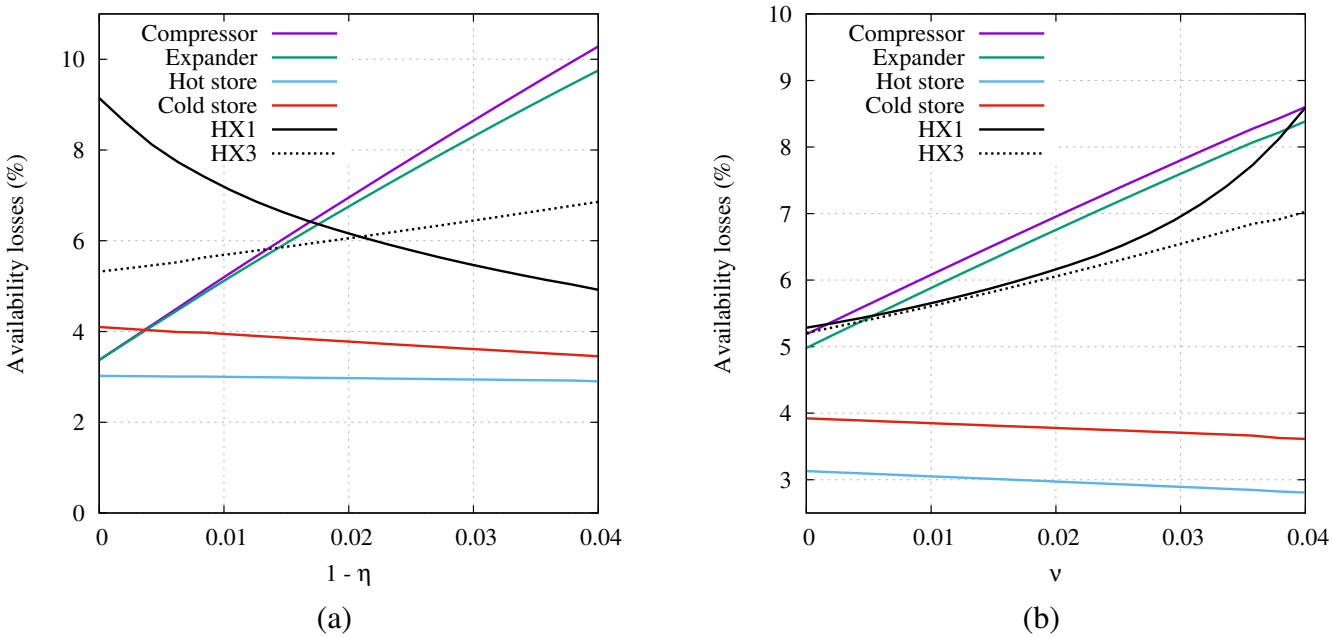

Figure 4.15: Sensitivity of availability losses in each PTES component to variations in **(a)** polytropic efficiency η **(b)** heat leakage factor ν

trip efficiency, which is due to an increase in losses in the heat exchangers themselves: the irregular thermal fronts mean that the packed-bed outlet temperatures are never at the design value such that heat is rejected over the entire duration of the cycle.

4.4.2 Further parametric studies

Parametric studies of the main PTES design variables are now carried out. Parameters are varied about their nominal values as given in table 4.7, whilst the remaining variables are fixed at their nominal values.

	Geometric parameters				Operating conditions				
	$(L/D)^{\mathrm{HS}}$	$(L/D)^{\mathrm{CS}}$	d_p (mm)	N_{seg}	T_1 (K)	T_3 (K)	β_{chg}	β_{dis}	Π
Nominal	1.00	1.00	20.0	1	310	310	10.0	10.0	0.75
Minimum	0.10	0.10	2.0	1	273	273	5.0	5.0	0.10
Maximum	10.0	2.0	50.0	32	347	347	15.0	15.0	1.00

Table 4.7: PTES variables that are used in the parametric study. Minimum and maximum values indicate the range through which the parameters are varied.

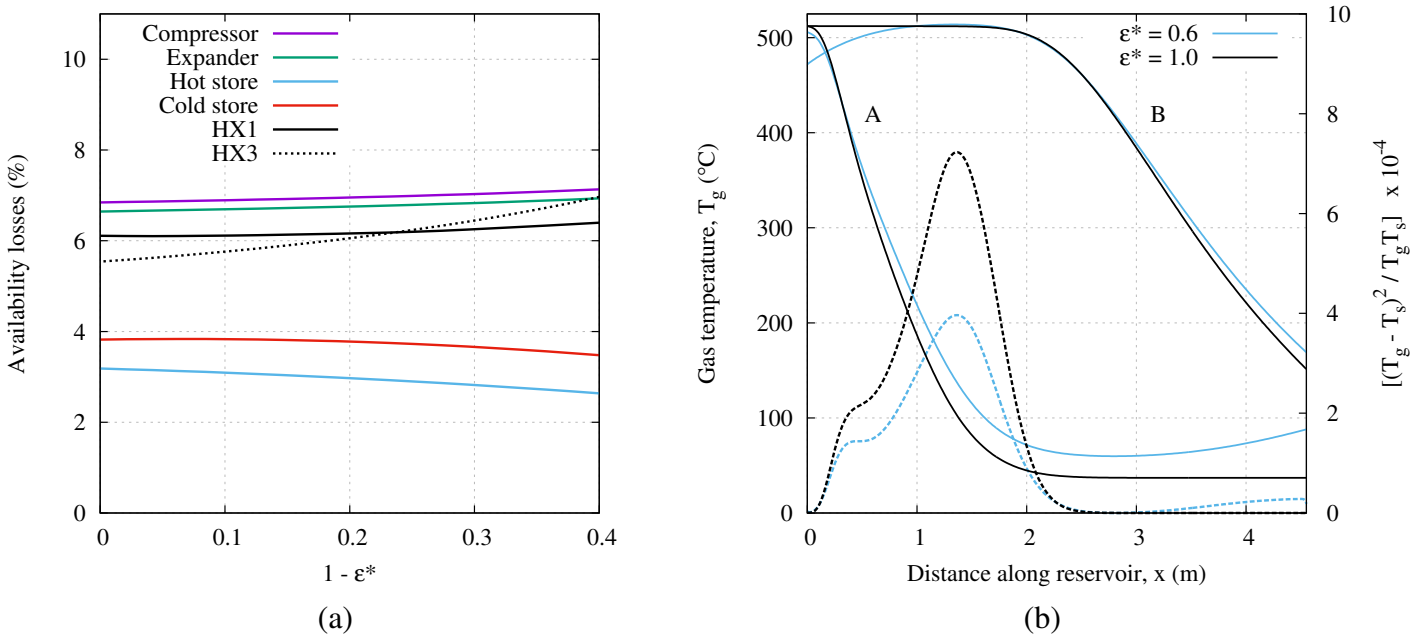

Figure 4.16: Impact of heat exchanger loss factor ϵ^* on PTES performance **(a)** Distribution of availability losses in various components **(b)** Influence of ϵ^* on thermal profiles in a hot packed bed. Profiles are shown at the start of charge (A) and the end of charge (B). Dashed lines show thermal losses of (A) on the right-hand axis.

Geometric parameters

The geometric parameters that are varied are the hot and cold reservoir aspect ratio (L/D), particle diameter (d_p) and number of segments (N_{seg}). The maximum in efficiency that is evident in figure 4.17 reflects the trade-off between heat transfer losses and pressure losses as discussed in detail in chapter 3. For example, small particles give large heat exchange area but increase the frictional effects. Likewise, long reservoirs give lower thermal losses, but the associated reduction in cross-sectional area implies higher fluid velocities and hence higher pressure drop. Due to the lower average gas density, pressure losses are more significant in the cold reservoir and consequently the optimal aspect ratio is lower and the optimal particle size larger than for the hot reservoir. However, it should be recalled that these results have been obtained with all the other parameters fixed at their nominal values, and the picture changes when overall system optimisation is considered.

In chapter 3 it was found that segmentation of the packed-beds could have a number of

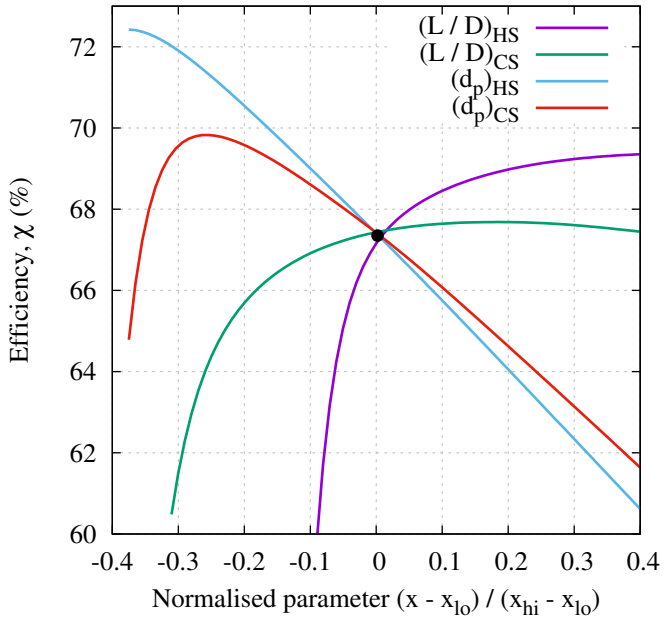

Figure 4.17: Variation of thermodynamic round-trip efficiency with packed-bed geometric parameters. Minimum, nominal and maximum values are given in table 4.7.

advantages, such as reduced pressure and storage losses, increased utilisation of the reservoirs, and more uniform power output. However, these benefits could only be achieved under certain conditions. For instance, storage losses were only reduced if heat leakage was small compared to axial conduction. Furthermore, the main benefit of segmentation was that it allows smaller particles to be used thereby reducing thermal losses without incurring significant pressure losses. As a result, segmentation is most beneficial in cold packed beds where pressure losses are reasonably large.

Figure 4.18 illustrates the impact of a layered cold store on the round-trip efficiency of a PTES system. Calculations are carried out using particle diameters in the cold store of 4 mm and 10 mm, since there is no benefit to segmenting the packed bed at larger particle sizes. For instance, losses can be reduced by 1.4% when $d_p = 4$ mm, but only by 0.4% for $d_p = 10$ mm. Furthermore, most of the loss reduction can be achieved with only eight segments, and the benefit of additional segments diminishes. Figure 4.18 shows that segmentation has no impact on the performance of the reciprocating devices or the hot store. However, heat exchanger losses do increase by a small amount as a result of the presence of the saw-tooth wake discussed in section 3.3. For the particular case when $(d_p)_{\mathrm{CS}} = 4$

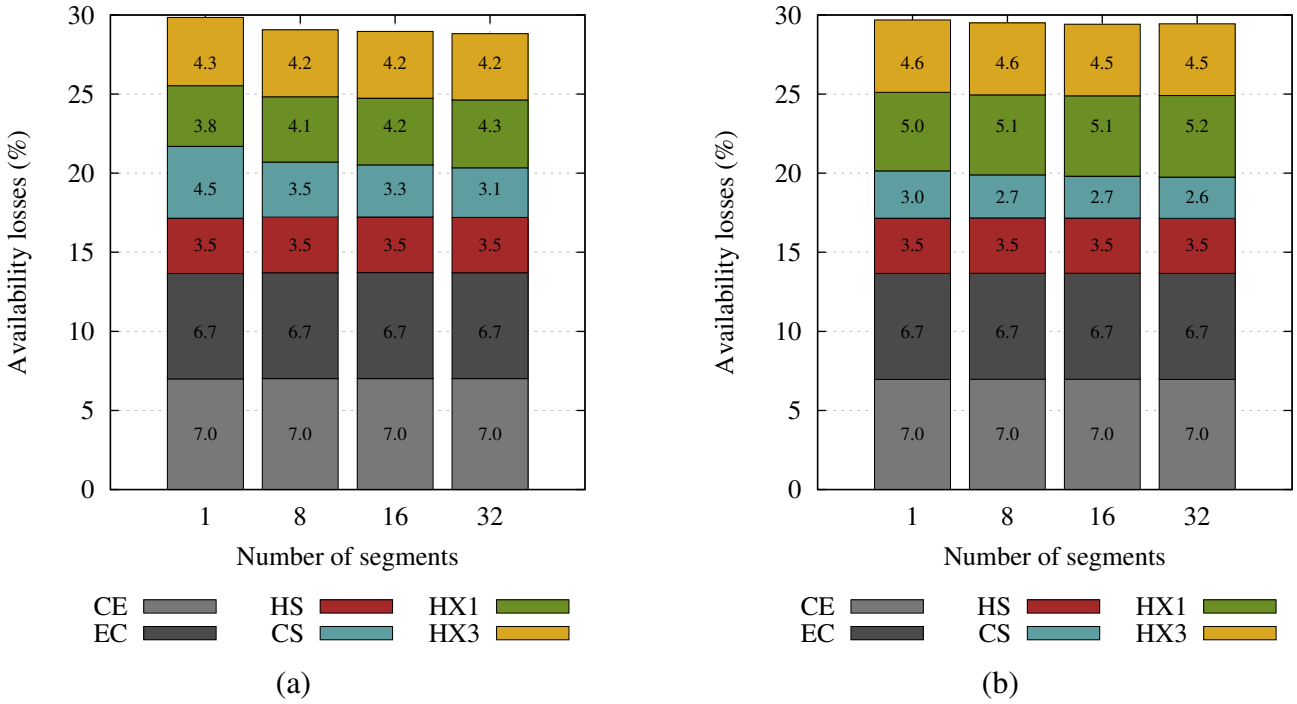

Figure 4.18: Distribution of available energy losses in a PTES system as the number of layers in the cold store is varied. In **(a)** $d_p = 4$ mm and **(b)** $d_p = 10$ mm

mm, the thermodynamic round-trip efficiency (i.e. excluding mechanical and electrical losses) is improved from 70.2% to 71.2% when the number of segments is increased from 1 to 32. Detailed economic analysis is required to determine whether the additional cost of installing the segments, valving and control systems is covered by the 1% increase in efficiency.

Operational parameters

Figure 4.19 shows the effect of various cycle operating conditions on the efficiency and energy density. In varying these parameters, the nominal power and storage capacity have been held constant by adjusting the size of the reservoirs and the mass flow rate.

At fixed pressure ratio, the efficiency and energy density are both improved by either increasing T_1 or decreasing T_3. Increasing the pressure ratio at fixed T_1 and T_3 has a similar effect as shown in figure 4.19(a). These trends are consistent with the findings in refer-

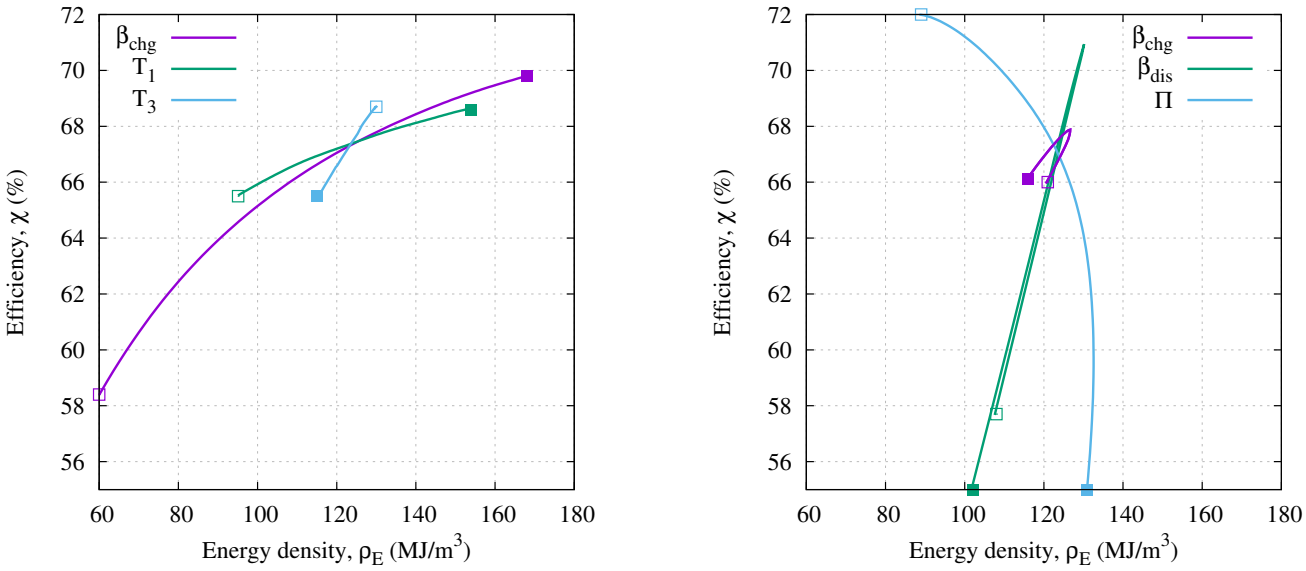

Figure 4.19: Variation of round-trip efficiency and energy density with PTES operational parameters. For each curve the open and solid square symbols are at the minimum and maximum values of each parameter in accord with table 4.7. **(a)** Variation with T_1, T_3 and charging pressure ratio β_{chg} (with T_1 and T_3 fixed). **(b)** Variation with β_{chg} (with T_2 and T_4 fixed), discharge pressure ratio β_{dis} and utilisation factor Π.

ence [83] where it was argued that, if compression and expansion losses dominate, then the efficiency is governed mainly by the ratio T_2/T_3 since this determines the ratio between compression and expansion work. Increasing this ratio (as all of the above variations in T_1, T_3 and β_{chg} will achieve) thus makes the cycle less susceptible to compression and expansion losses. However, improvements along these lines will almost certainly result in increased costs and technical challenges since they imply higher top temperatures or pressures, or lower bottom temperatures. A more detailed examination of the distribution of losses also reveals that the benefits of higher work ratio are partly offset by increased thermal losses in the reservoirs, as indicated in figure 4.20(a).

If the maximum and minimum cycle temperatures (T_2 and T_4) are fixed, instead of fixing T_1 and T_3, then variation of the pressure ratio gives trends similar to those observed for gas turbine cycles for which there are optimum pressure ratios, as shown in figure 4.19(b). The optimum pressure ratios for energy density and efficiency are the same, and in this case are 8.8, but the corresponding value of T_3 (10.6°C) lies below ambient temperature. This

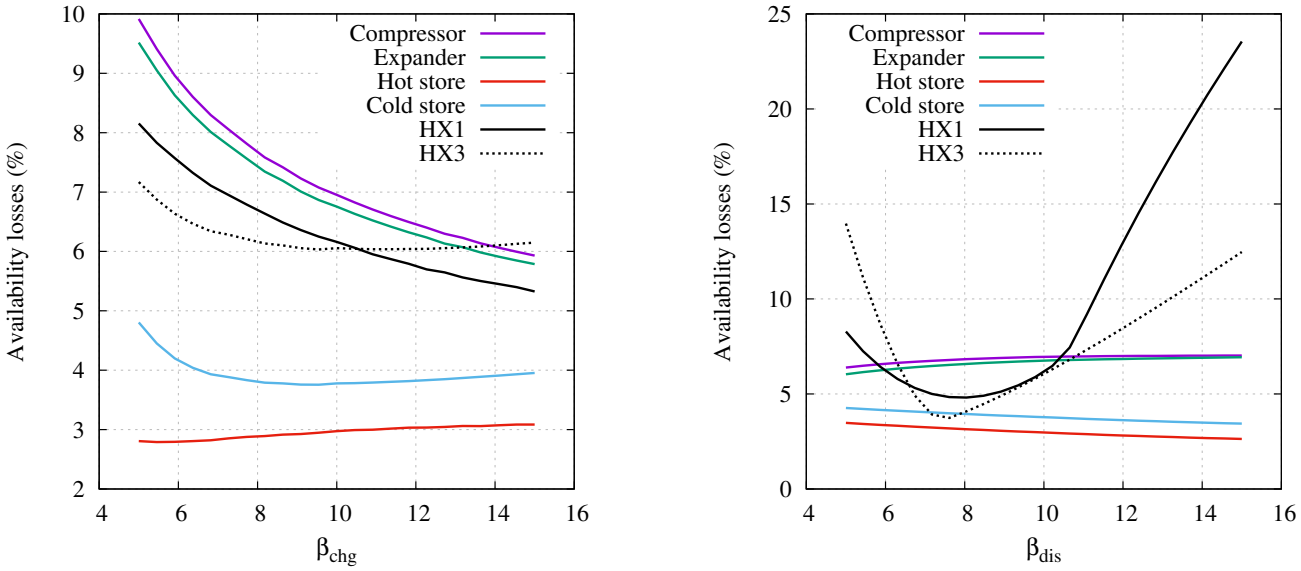

Figure 4.20: Distribution of availability losses in PTES components as β_{chg} and β_{dis} are varied. **(a)** Variation with charging pressure ratio with T_1 and T_3 held constant **(b)** Variation with the discharging pressure ratio

precludes the possibility of rejecting heat in HX3, making it difficult to manage the thermal fronts as they emerge from the reservoirs.

Figure 4.19(b) also shows the influence of the 'utilisation factor' Π and the discharge pressure ratio. Increasing Π (i.e. longer charge and discharge period) obviously increases the energy stored per cycle, but this is at the expense of lower efficiency. This is due to steeper temperature gradients within the reservoirs, which imply that gas-solid heat exchange occurs over a smaller interfacial area and hence with a larger temperature difference.

Varying β_{dis} effectively controls the balance of heat rejection between HX1 and HX3, as can be seen by examining the *T*–*s* diagram shown in figure 4.12(b). A sharp optimum in this pressure ratio is observed in figure 4.19(b) and occurs at around $\beta_{\text{dis}} = 7.60$. Inspection of figure 4.20(b) indicates that this optimum corresponds to when heat rejection is roughly evenly divided between the two heat exchangers.

4.5 Avoiding electric heat addition

When the exit temperatures of the thermal reservoirs change heat addition and rejection from the cycle is necessary. Heat rejection is unavoidable due to irreversibilities within the cycle. On the other hand, it should be possible to avoid heat addition which increases the work input and requires an electric heater as described in section 4.3.2.

Heat addition is apparent in the *T–s* diagram of the nominal PTES cycle, as shown in figure 4.21. During charge, temperature T_1 decreases as the thermal front emerges from the cold store. Figure 4.21(c) shows that T_1 drops below the required compressor inlet temperature of 37°C, and a heat input is required. Heat addition is also required during discharge: as the thermal front reaches the end of the discharging hot store T_2 reduces below the design value of 505°C. Consequently, after expansion the temperature T_1 drops below 37°C. Furthermore, changes in the exit temperature lead to reduced power output and a system that has constant power output is preferable.

In this section, alternative methods of operating the PTES cycle to avoid heat addition are described. Solutions include neglecting the need for heat addition, placing a recuperator between T_3 and T_1 or varying pressure ratios throughout operation of the cycle. A number of other solutions exist, and more detailed investigations could compare these as well as taking into account other factors such as reciprocating device behaviour.

Calculations are carried out using the nominal PTES design as described in section 4.4 and table 3.1, albeit with all pressure loss factors set to $f_p = 0.0$ and heat exchanger effectiveness set to $\epsilon^* = 1.0$. These modifications are made in order to simplify the analysis and ensure that the effect of any modifications can be observed more clearly. Under these conditions the thermodynamic efficiency is $\chi = 72.6\%$. When electrical heating is used, the electrical work is added to the work input during charge, and subtracted from the work output during discharge. During charge 3.1% of the work input is heat addition. During discharge the electrical work is 3.4% of the work output. By avoiding electrical heat addition the efficiency could therefore be increased by

$$\chi_{\text{new}} = \frac{(1+0.034)W^{\text{net}}_{\text{dis}}}{(1-0.031)W^{\text{net}}_{\text{chg}}} = \frac{(1+0.034)}{(1-0.031)}\chi = 1.07\chi \tag{4.49}$$

Therefore, the efficiency could potentially rise by 7% to 77.5%.

4.5.1 Neglecting heat addition

The simplest way to avoid heat addition is to ignore the need for it. When the temperature at T_1 or T_3 falls below the required value of 37°C, the gas is simply fed through to the next component with no heat addition. Varying the inlet temperatures to the thermal stores leads to unusual thermal fronts shapes, and cyclic operation cannot be achieved. After 20 cycles the round-trip efficiency is 37.0% compared to 72.6% of the nominal cycle above.

The stores develop profiles without a clearly defined thermal front which leads to the packed beds storing less energy, while thermal and conductive losses are exacerbated by the increased rate of heat transfer. Ideally the power should be constant, or at least easy to predict so that the energy store can be a useful asset to the electrical grid. However, the large temperature variation across the compressors and expanders also causes significant variation in the input and output power.

This option would be simple and cheap to implement. However, it significantly compromises the efficiency and energy density of the PTES plant and is not a sensible solution.

4.5.2 Recuperated cycles

Figure 4.21 indicates that heat is rejected at 3. and added at 1. in both charge and discharge cycles. The heat that is rejected at 3. could be used as a heat input at 1. as illustrated in the schematic layout in figure 4.22. The temperature traces in figure 4.21(c) and 4.21(d) suggest that T_3 is always high enough to be able to heat the gas at T_3 up to 37°C, even considering heat exchanger inefficiencies. For instance, at the end of charging $T_3 = 168$°C while $T_1 = -25$°C. Using a heat exchanger with an effectiveness of $\epsilon = 0.7$, both outlet streams could reach 37°C if the ratio of mass flow rates was $\dot{m}_3/\dot{m}_1 = 0.46$. The remaining 54% of the T_3 would pass through HX3 as usual and could conceivably be used in other waste heat purposes. The true behaviour would be more complicated than this since the inlet temperatures to the recuperator would vary as the thermal fronts emerge from the stores. Consequently, $\dot{m}_3/\dot{m}_1$ may be required to change (although preliminary analysis

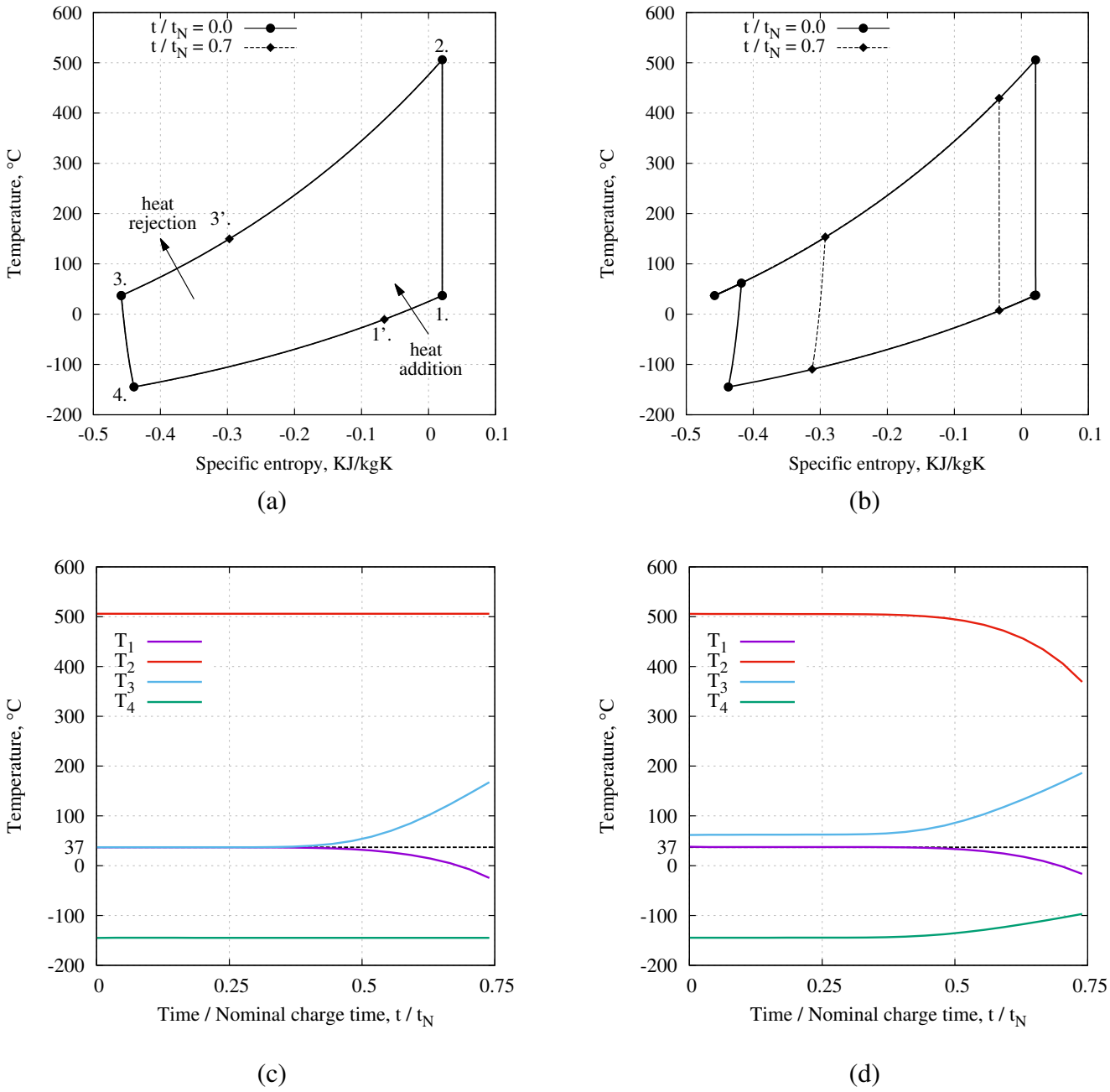

Figure 4.21: *T–s* diagrams and temperature traces for the nominal PTES design. **(a)** *T–s* diagram during charge. Points 1'. and 3'. indicate how the exit temperature of the stores changes towards the end of the charging phase and leads to heat being rejected and added. **(b)** *T–s* diagram during discharge **(c)** Reservoir inlet and exit temperatures during charge **(d)** Reservoir inlet and exit temperatures during discharge

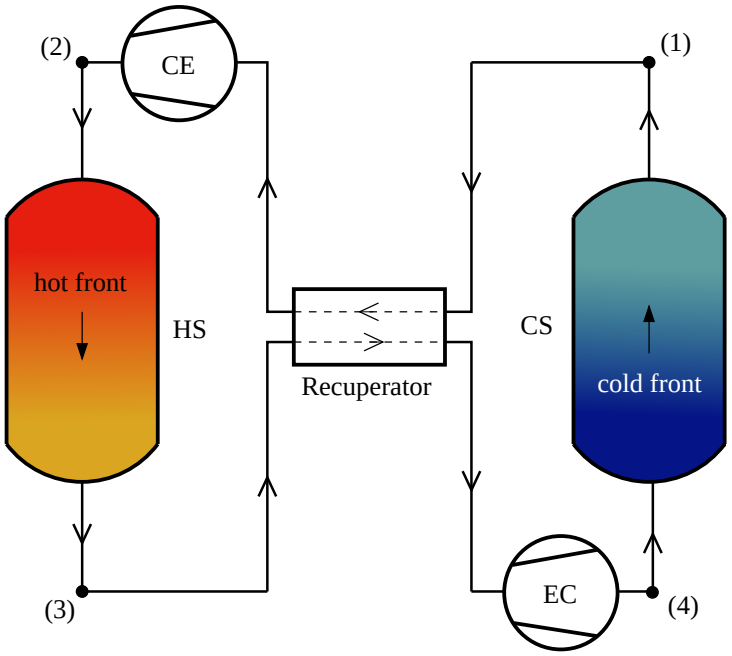

Figure 4.22: Simplified schematic of a PTES system using recuperation. Heat exchangers are not shown for clarity. As the thermal fronts exit the stores, the hot store gas at 3. is used to reheat the cold store gas at 1.

suggests only by a small amount). Integration of a recuperator in a PTES system therefore requires a thorough analysis of the off-design operating behaviour.

The benefit of recuperation is difficult to evaluate without detailed calculations. However, as noted above, if heat addition is avoided the efficiency could potentially increase from 72.6% to 77.5% which provides a strong case for including a recuperator in the PTES system. Furthermore, it may be possible to avoid any increase in capital cost by re-directing water between the existing heat exchangers to achieve the recuperation.

If different operating temperatures are used then recuperation may not be possible. Parametric studies in section 4.4.2 and [84] showed that the round-trip efficiency could be improved by decreasing T_3 and increasing T_1. Furthermore, optimisation studies of a PTES system [84] found that the cheapest designs often had lower pressure ratios and values of T_1 greater than T_3. Figure 4.23 shows *T*–*s* plots and temperature traces for a system similar to the nominal design albeit with $T_1 = 117$°C, $T_3 = 37$°C, $\beta_{\text{chg}} = 7.6$ and $\beta_{\text{dis}} = 7.2$. These values have been taken from the optimised results in [84]. In both charge and discharge, T_1 drops below the design value of 117°C for some time before T_3 becomes high

enough for recuperation to be possible. One option would be to avoid heat addition during the times it is required which would create irregular thermal front shapes and reduce the efficiency. However, T_1 decreases only a small amount below 117°C before recuperation would be possible (during charge T_1 drops by around 30°C, and in discharge it drops by around 5°C). Therefore, the impact of neglecting heat addition may not be as dramatic as in the previous section.

Recuperation could be a promising technique to avoid heat addition. However, further analysis is required to quantify the benefit, assess the economic cost, and to investigate the feasibility of recuperation in designs with alternative operating conditions.

4.5.3 Variable pressure ratios

Heat addition can be avoided by varying the pressure ratio throughout the charge and discharge cycles. The wider impacts are currently unclear since changing β requires either the mass flow rate or rotational speed of the compressors and expanders to change according to the characteristic equation derived in section 4.2. Changing the pressure ratio therefore moves the devices away from their design point. In this section it is assumed that the rotational speed changes so that the mass flow rate remains constant. If such a system were to be used, then a variable speed motor-generator would be required.

Variable pressure ratio during charging

Heat addition is required during charge when the thermal front reaches the end of the cold store causing a drop in the temperature T_1. Passing the reduced value of T_1 into the compressor leads to lower T_2. Increasing the charging pressure ratio β_{chg} to keep T_2 constant, that is, $\beta_{\mathrm{chg}} = (T_2/T_1)^{1/\phi_c}$. Figure 4.24 shows the *T*–*s* plot and temperature traces for this scheme. It is notable that the pressure ratio increases from 10 to 17 which will significantly increase the cost of the stores. However, the round-trip efficiency increases from 72.6% to 75.2% if the nominal discharging cycle is used (i.e. heat addition still occurs during discharge).

Deployment of this scheme requires flexible operation of HX3: if the output of the heat

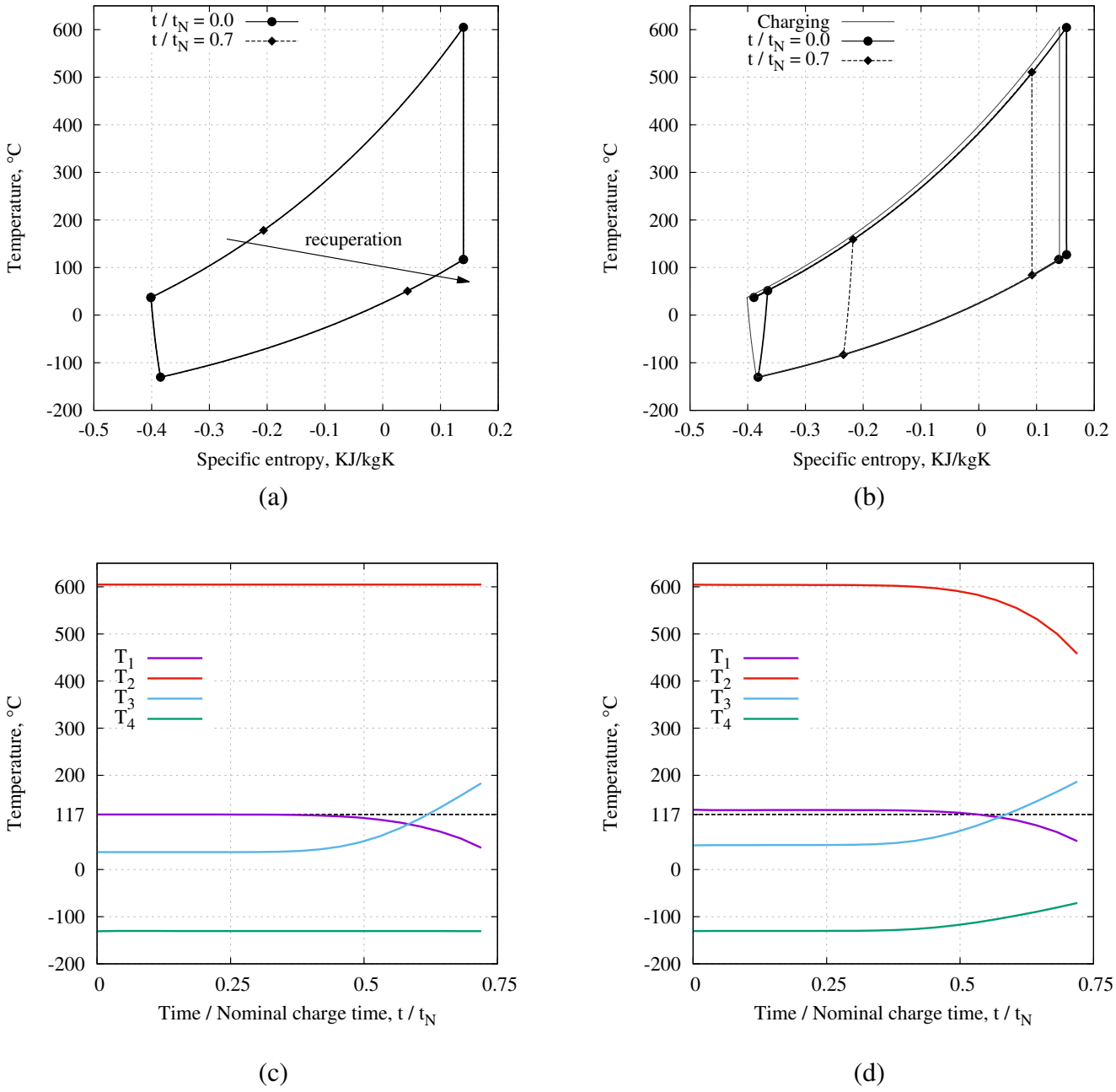

Figure 4.23: *T–s* diagrams and temperature traces for a PTES design with $T_1 > T_3$. **(a)** *T–s* diagram during charge. For the $t/t_N = 0.7$ curve recuperation can occur between the hot store exit and the cold store exit as indicated. **(b)** *T–s* diagram during discharge **(c)** Reservoir inlet and exit temperatures during charge **(d)** Reservoir inlet and exit temperatures during discharge

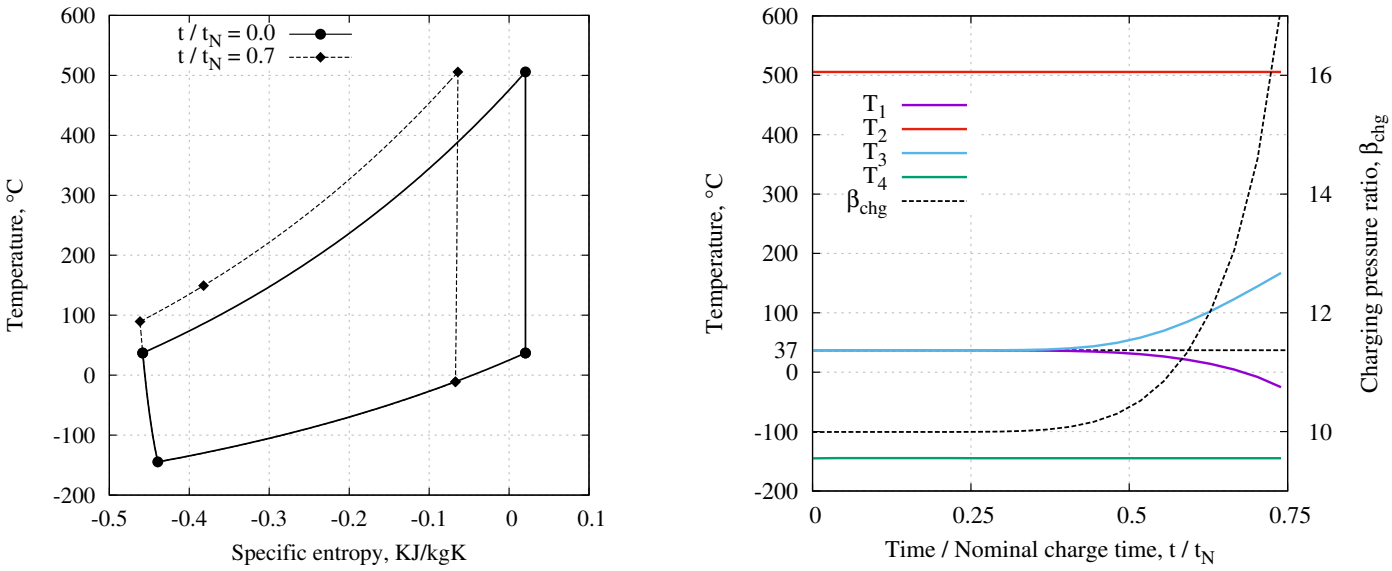

(a) (b)

Figure 4.24: Charging profiles of a PTES scheme where the charging pressure ratio β_{chg} is increased such that T_2 is constant **(a)** *T–s* diagram during charge **(b)** Temperatures at the reservoir inlets and outlets during charge

exchanger was fixed at $T_3 = 37$°C then the increased pressure ratio would reduce T_4. This would create problems with the thermal fronts in the discharging phase. Keeping T_4 constant sets the outlet temperature from HX3 to be $T_3 = T_4\beta_{\text{chg}}^{\phi_e}$. For instance, figure 4.24(a) shows that HX3 exit needs to rise to 100°C, so that T_4 is constant at -150°C. Operating HX3 in this way should reduce the quantity of heat rejected, although the heat is rejected at a higher average temperature.

Variable pressure ratio during discharging

Heat addition occurs in the discharging phase when the thermal front exits the hot store. The reduction in T_2 leads to a decrease in the expander exit temperature T_1. The pressure ratio can be varied in a number of ways. For instance β_{dis} could be varied such that the exit of the compressor remains constant at $T_3 = 37$°C. As a result, heat rejection would occur exclusively in HX1. As noted in section 4.4.2, an optimal value of β_{dis} occurs when heat rejection is evenly divided between the two heat exchangers. This can be achieved

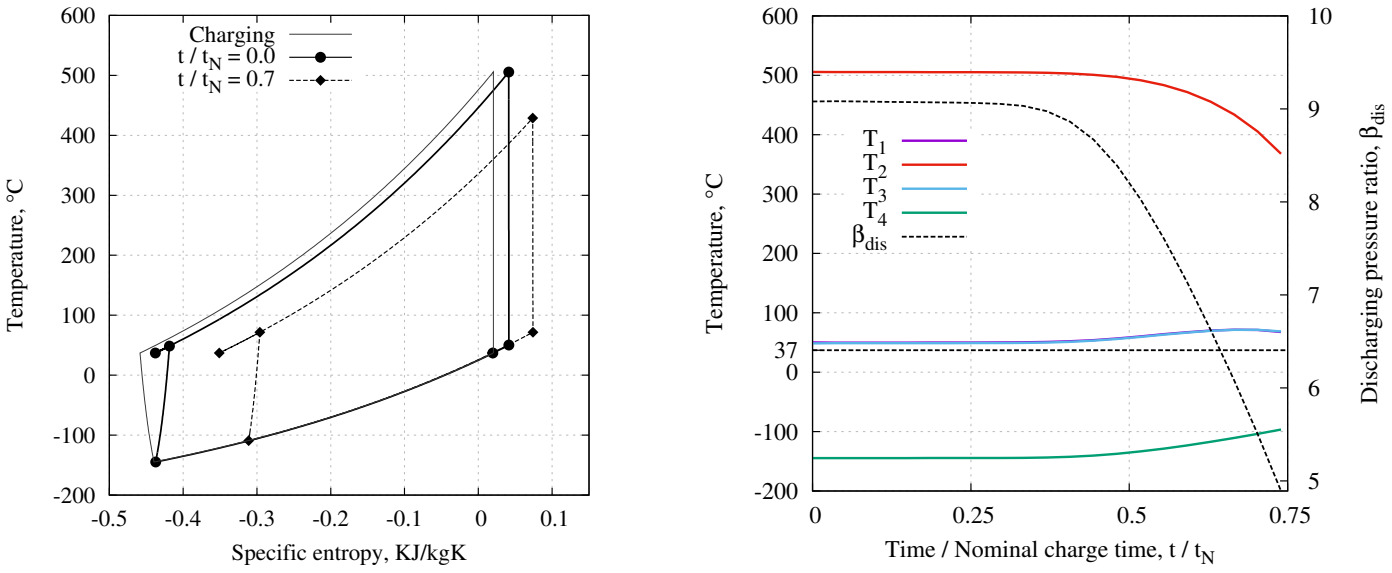

(a) (b)

Figure 4.25: Discharging profiles of a PTES scheme where the discharging pressure ratio β_{dis} is varied such that approximately equal amounts of heat are rejected in each heat exchanger. **(a)** *T*–*s* diagram during discharge **(b)** Temperatures at the reservoir inlets and outlets during discharge

by choosing a pressure ratio that leads to $T_1 = T_3$. By noting that $T_2/T_1 = \beta_{\text{dis}}^{\phi_e}$ and $T_3/T_4 = \beta_{\text{dis}}^{\phi_c}$, rearranging such that $T_1 = T_3$ leads to

$$\beta_{\text{dis}} = \left(\frac{T_2}{T_4}\right)^{\frac{1}{\phi_c+\phi_d}} \tag{4.50}$$

Figure 4.25 illustrates the *T*–*s* diagram and temperature traces. It is clear that heat addition is not required and that T_1 and T_3 are equal. The pressure ratio reduces from 9.1 to 5.1. Varying only β_{dis} (i.e. β_{chg} is constant) increases the round-trip efficiency from 72.6% to 76.9%.

Varying the pressure ratio in both the charging and discharging cycle successfully avoids undesirable heat addition and leads to a 7% increase in efficiency. There are two major disadvantages to this approach. Firstly, the pressure ratio varies between 5 and 17 which will require reciprocating devices with good off-design performance. Such wide variation could lead to low polytropic efficiencies thereby compromising the increase in efficiency. Secondly, the components have to be able to withstand a maximum pressure of 17 bar rather

than 10 bar which will significantly increase the cost of the reciprocating devices and hot store.

Rather than operating the reciprocating devices at fixed mass flow rate as above, they could be operated at a fixed speed. Thus, as the pressure ratio decreases the mass flow rate would increase (see figure 4.3) which would help to maintain constant power output.

4.5.4 Variable cold store outlet temperature

Varying the operating temperatures of the cold store is another way to avoid electric heat addition. The cold store is operated between T_1' and T_4 where T_1' is higher than the nominal temperature T_1 (i.e. the compressor inlet temperature during charge). During charge, gas exits the cold store at T_1' and is cooled in HX1 to T_1 before continuing into the charge compressor. As the thermal front emerges from the cold store T_1' decreases until at the end of charge $T_1' = T_1$. As a result, heat is continually rejected between T_1' and T_1 thereby avoiding heat addition during charge. The position of T_1' is shown on figure 4.26(a) and heat rejection from T_1' to T_1 is shaded in on figure 4.26(c).

The discharging phase needs to be carefully controlled to ensure that $T_1' > T_1$. In this example, β_{dis} is varied so that T_3 is held constant. During discharge, this leads to an increase in the discharge expander exit temperature T_1', as shown on figure 4.26(c). This gas is fed directly into the cold store rather than HX1. As a result, the cold reservoir has a temperature above the design value of $T_1 = 37$°C at this end of the store. During the next charging cycle, the gas that exits the reservoir is therefore also above 37°C, and heat addition is avoided.

During discharge the inlet temperature to the cold store T_1' is not constant. The varying discharging pressure ratio causes T_1' to steadily increase to a maximum, and then reduce slightly towards the end of discharge. Consequently, thermal fronts in the cold store have irregular shapes, as shown in figure 4.27. Rather than being a smooth curve, the thermal front actually has a maximum temperature of about 120°C at the warm end. This impacts the charging cycle where the output temperature of the cold reservoir increases before decreasing. Figure 4.27 demonstrates that the thermal profiles are quite different to the nominal case.

Generating unusual thermal fronts leads to increased heat transfer and conduction losses,

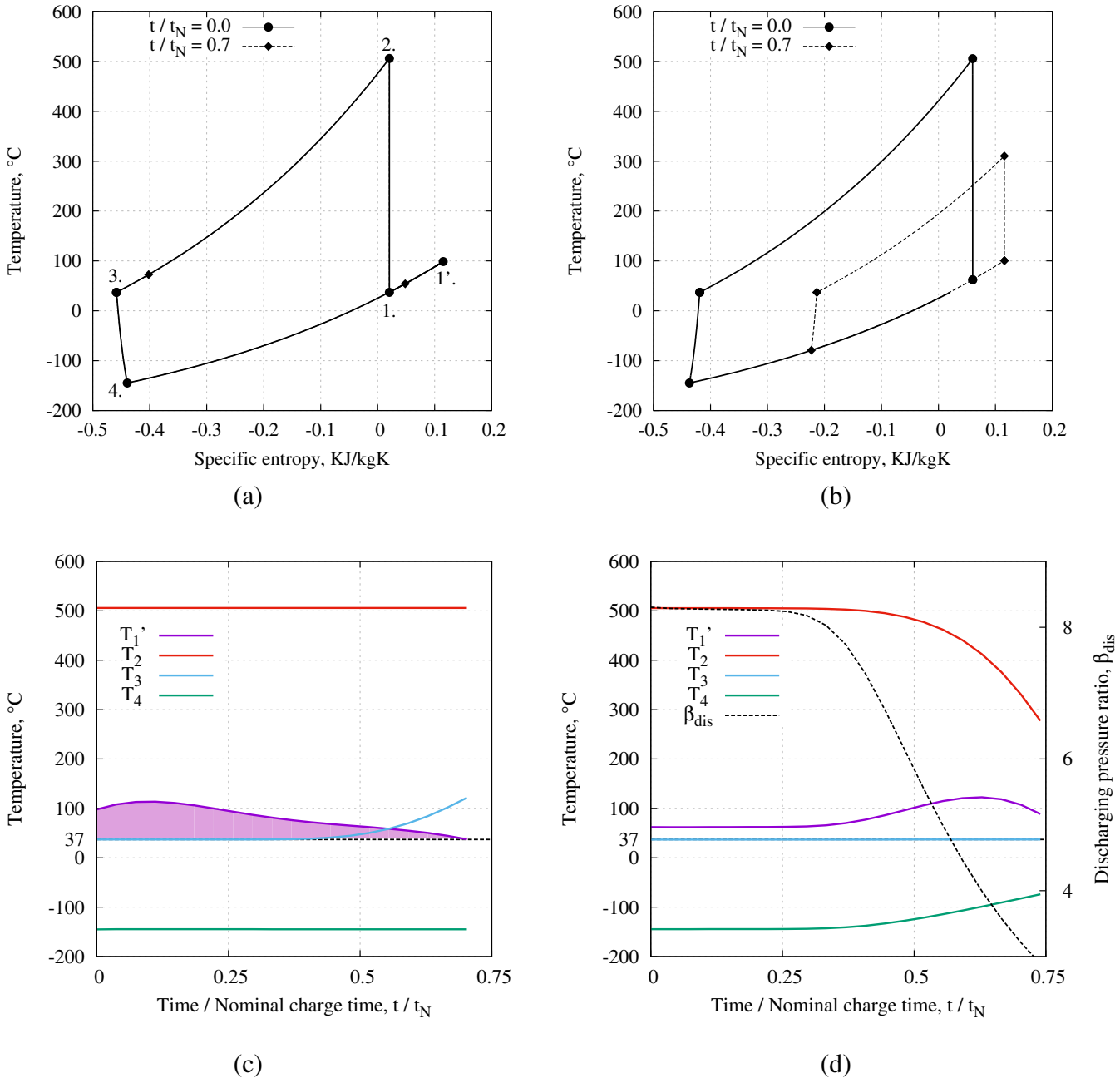

Figure 4.26: *T–s* diagrams and temperature traces for a PTES design with a cold store discharging temperature of T_1'. **(a)** *T–s* diagram during charge **(b)** *T–s* diagram during discharge **(c)** Reservoir inlet and exit temperatures during charge. Shaded area illustrates heat rejection that occurs **(d)** Reservoir inlet and exit temperatures during discharge

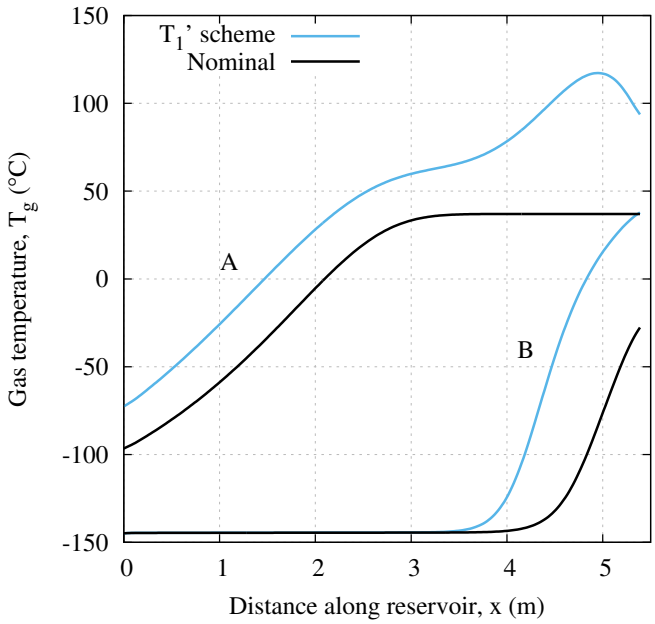

Figure 4.27: Thermal profiles in the cold store at (A) the end of discharging and (B) the end of charging. Profiles are shown for the nominal design and for a PTES design with a cold store discharging temperature of T_1'.

but this cycle does successfully avoid heat addition and achieves a round-trip efficiency of 78.4%. Furthermore, this approach does not require additional components (such as recuperators) or excessively high pressure ratios. However, the variable discharging pressure ratio has implications for the reciprocating devices and means the motor-generator may have to be variable speed.

A final consideration is that no heat is rejected during discharge. Therefore, to maintain cyclic operation all of the irreversibilities must be 'flushed' out of the system during charge. The *T*–*s* diagram indicates that most of the heat is rejected in HX1. It is possible to balance heat rejection more evenly between the two heat exchangers and also reduce the average temperature of heat rejection, by using a scheme where the discharging pressure ratio keeps $T_1 = T_3$. This may also reduce the maximum value of T_1'.

4.5.5 Liquid stores

Heat has to be added to the PTES system as a result of the thermal gradients in the packed beds. During charge and discharge the thermal fronts travel out of the reservoirs and heat rejection or addition is required to maintain cyclic operation. The preceding sections have discussed a number of options that avoid this problem. An alternative solution uses liquid stores rather than packed-bed thermal reservoirs.

Each liquid store comprises two tanks: one contains fluid at the discharged conditions and the other is for fluid at the charged conditions. Between the tanks is a heat exchanger that integrates the store with the heat pump/engine cycle, as illustrated in figure 4.28. As an example, consider the hot store during charge. Tank H3 is full of fluid at the discharged temperature T_3. Fluid leaves tank H3 and passes through the heat exchanger where it is heated to T_2 before entering tank H2. The reverse process occurs during discharge.

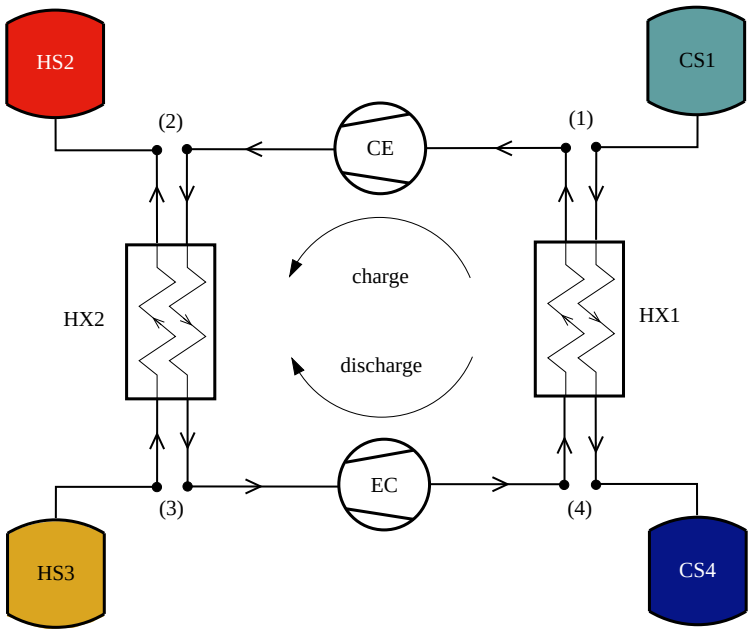

Figure 4.28: Schematic of an alternative PTES design utilising liquid during the charging phase.

The advantage of this method is that heat exchange always occurs between fixed temperatures. There are no thermal fronts so heat addition is not required (heat rejection will still occur, however). Furthermore, the thermal stores can be fully charged and discharged unlike the packed beds where the thermal front prevents this.

These systems require a liquid medium with suitable melting and boiling points since phase change should ideally be avoided. Potential candidates include water, molten salts and cryogens. The hot and cold stores would probably use different liquids. Although liquid based PTES systems have four storage vessels rather than two, they may not need to be pressurised (unless water is used at high temperatures) which would reduce the cost. Liquids such as water typically have higher specific heat capacities than rocks, but have smaller operating temperature ranges. Without detailed calculations it is difficult to determine how the energy density of liquid stores compare to the nominal PTES system. Further work is therefore required, although thermodynamic models of such systems have already indicated that the round-trip efficiency is heavily dependent upon heat exchanger efficiency [168].

4.6 Summary

In this chapter, a thermodynamic model of Pumped Thermal Energy Storage (PTES) systems has been developed, and the system's behaviour has been investigated in detail.

Reciprocating devices were characterised by simple loss factors such as the pressure loss factor f_p, the heat loss factor ν and the polytropic efficiency η. In section 4.2 the thermodynamic processes that governed availability losses were investigated which allowed estimates to be made. For instance, f_p is approximately 1% while ν is of the order of 2%. Simplified models of heat exchangers, electric heaters, pipes, valves and the buffer tank were then discussed. The estimated loss factors were only approximations, so the sensitivity of the system to each loss factor was studied. It was found that the round-trip efficiency decreased for around 2% for every 1% drop in η or ν. Pressure losses were less significant with each percentage decrease causing an 1% loss.

Parametric studies of geometric variables and operating variables were undertaken in section 4.4.2. Varying the geometric parameters illustrated the trade-off between thermal losses and pressure losses that was described in chapters 2 and 3. For instance, longer stores and smaller particles caused larger pressure losses and lower thermal losses. It was found that segmenting the cold store could increase the efficiency and that the effect was most significant when small particles were used. The parametric studies confirmed the simplified analysis of PTES systems described in section 1.5. One important parameter

is the utilisation factor Π which controls the trade-off between round-trip efficiency and the energy density. Increasing the charging pressure ratio, increasing T_1 and decreasing T_3 were all found to increase the round-trip efficiency. The discharging pressure ratio was found to have a significant effect on the round-trip efficiency, and primarily controlled the distribution of heat rejection between the two heat exchangers.

The objective of section 4.5 was to avoid the need for an electric heater, since the work input for the heater significantly reduces the round-trip efficiency. Several methods of operating the PTES system were considered and it was found that the thermodynamic round-trip efficiency could be increased from 72.6% to 78.4%. Further research is required in this area, since a large number of configurations exist.

Chapter 5

Thermo-economic optimisation

5.1 Introduction

Previous chapters have developed detailed thermodynamic models of packed-bed thermal reservoirs and Pumped Thermal Energy Storage (PTES) systems. These models include a large number of parameters that can make optimisation of the system by simple parameter variation a challenging task. Furthermore, optimisation of engineering systems typically requires consideration of several objectives: most commonly efficiency and cost. This chapter begins with a discussion of economic modelling of energy storage systems and a number of economic metrics are described. Most economic metrics are limited by uncertainty, and the approach of this chapter is to develop an economic model that is as simple as possible while still providing meaningful information.

The capital cost model of PTES systems is described in sections 5.2.1, 5.2.2 and 5.2.3 and is based on the material requirements of each component. The objective of this chapter is to compare PTES designs against one another, so the relative magnitude of the capital cost is of greater interest than its absolute magnitude.

Thermo-economic optimisation is carried out on packed-bed thermal reservoirs and on PTES systems. The optimisations investigate the benefit of various design features such as segmentation, radial-flow stores, and the avoidance of heat addition. In addition, the sensitivity of the optimal designs to the reciprocating device polytropic efficiency is investigated. Stochastic optimisation techniques are used as these are suitable for these types of problem, as described in section 5.3. Both the thermodynamic and economic models involve a number of simplifications and estimations and the outputs are therefore uncertain. Consequently, the uncertainties in the modelling must be taken into account when comparing the results with other technologies or when considering the values of efficiency and cost. By undertaking multi-objective optimisation it is possible to see the full range of optimal designs, i.e. designs that achieve high efficiency at high cost through to designs that achieve low costs at lower efficiencies. In this way, it is possible to compare one design to another and make informed judgements. As a result, the following optimisation studies are most appropriate for identifying promising designs.

Thermo-economic optimisation of Rankine-cycle based PTES systems has been carried out by Morandin et al. [88]. Optimisation of Joule-Brayton cycle based PTES systems

have been carried out by the Cambridge group and are presented in [84] and the results in this chapter are extensions of this work.

5.2 Economic modelling

Holistic optimisation of the PTES system should consider economic factors as well as technical issues. Economic factors are often incorporated into thermodynamic studies by a method known as 'thermo-economics', 'techno-economics', or, if the analysis is based on second-law considerations, 'exergo-economics'. The theory of exergo-economics was developed in the 1980s and early 1990s, and several introductory texts exist [169–171]. In 1994 an example problem (the 'CGAM' problem) was formulated to demonstrate a range of techniques [172–175]. The theory has since been widely applied to a number of energy systems [176] and several methodologies have been developed [177]. Exergo-economics considers not only the exergetic losses within components, but also the exergy that was required to produce those components and any fuel sources. Such analyses requires a set of equations to relate the flows of exergy between and within components. A further set of 'auxiliary equations' are also necessary to relate monetary costs to the exergetic flows. This approach requires the development of its own model rather than incorporating economic factors into an existing thermodynamic model.

These approaches consolidated several aims into a single objective. Reducing the dimensionality of the problem was advantageous as complex problems could be efficiently studied using the optimisation techniques and computing power that were available at the time. However, multi-objective optimisation theory was also being developed in the 1980s, and since then computational power has increased significantly. Multi-objective optimisation problems can now be easily tackled, and it is beneficial to consider technical and economic factors with separate objectives. Multi-objective optimisation theory is discussed in section 5.3.

The economics of energy storage is a complex field, riddled with uncertainty and speculation. A sophisticated economic model would take into account capital costs, operation and maintenance costs and future energy markets; electricity prices, subsidies, taxes and the influence of other technologies. Energy storage has several potential revenue streams, and

it is unclear how profitable these streams may be, how payments would be organised, and how the market would be regulated. The most commonly discussed revenue stream is arbitrage, which some authors believe could lead to 'self-cannibalisation' of its own market. The various economic benefits of storage are discussed in more detail in the chapter 1 and in [1,41]. Inclusion of these details would provide information about the feasibility and/or profitability of the system, and the design and mode of operation that would achieve this.

The inherent uncertainty of economic factors (and other externalities) suggests that any judgements about the profitability of an energy storage system are meaningless without undertaking comprehensive sensitivity analysis. The uncertainty and complexity can be reduced by developing simpler economic models although these may be unable to capture the true nature of the problem as well as still being quite uncertain.

It is not the aim of this thesis to evaluate how economically feasible a PTES system may be. Instead, economic factors are used to compare different designs and to evaluate which may be the most feasible design. Consequently, it is the relative magnitude of the economic factors that are of importance, rather than the absolute values themselves.

The simplest, and least uncertain, economic metric is the capital cost. Optimisation of the PTES system therefore involves minimisation of the capital cost and maximisation of the round-trip efficiency. A number of slightly more sophisticated economic metrics have been applied in the literature and are summarised below.

Net Present Value (NPV)

The Net Present Value (NPV) considers the capital cost and revenue streams from the system. Future revenue streams are discounted to the present value, thus giving an indication of whether investing the capital cost in the system would be more or less profitable than investing the money. An NPV greater than zero indicates a worthwhile investment. The simplest case to consider is the system earning revenue through arbitrage i.e. buying electricity at a low price, and selling it at a higher price. Rastler [41] and Strbac et al. [1] suggest that this is unlikely to be the most profitable scheme. However, its simplicity means it is

the most commonly discussed in the literature. The NPV is given by

$$\mathrm{NPV} = \sum_{i}^{N} \frac{\pi_i^{\mathrm{out}} W_i^{\mathrm{out}} - \pi_i^{\mathrm{in}} W_i^{\mathrm{in}}}{(1+r)^i} - C_{\mathrm{cap}} \tag{5.1}$$

Where i is the time period in consideration, r is the discount rate, and C_{cap} is the capital cost. Superscripts 'in' and 'out' indicate whether energy (or work) W is being bought or sold, respectively, and the price π at which the transaction occurs in that period. These parameters (which vary with time) are then summed over the period of operation; typically assumed to be around 20 years. Clearly this model introduces a great degree of uncertainty, requiring estimates of interest rates, capital costs, and how electricity prices will vary over the next 20 years at quite a fine resolution (e.g. on an hourly basis). An operational strategy is also required for the energy storage system – i.e. the conditions under which it will buy and sell energy – which also requires an understanding of the impact on this mode of operation on the system efficiency and level of storage.

The equation above can be simplified by assuming that the system operates by charging and discharging for regular periods, and that the efficiency is given by $\chi = W_{\mathrm{out}}/W_{\mathrm{in}}$. Thus,

$$\mathrm{NPV} = W^{\mathrm{in}} \left[\sum_{i}^{N} \frac{\chi \pi_i^{\mathrm{out}} - \pi_i^{\mathrm{in}}}{(1+r)^i} - \frac{C_{\mathrm{cap}}}{W^{\mathrm{in}}} \right] \tag{5.2}$$

For cyclic operation W_{in} is the same for every period, and no knowledge of π is required to see that maximisation of the NPV can be simply achieved by maximising the round-trip efficiency and minimising the capital cost. Therefore, it is clear that optimisation of this economic model is equivalent to the proposed optimisation scheme. The proposed approach has the additional benefit that electricity price markets do not have to be considered.

In the energy storage literature, DeForest et al. [178] used the NPV to compare the costs and operating behaviour of cold water thermal energy storage systems that were used for domestic cooling under a range of different economic and climatic conditions. Grunewald et al. [52] assessed several energy storage technologies by investigating the integration of storage into the grid. The economic benefit of CAES, compressed hydrogen, and flow batteries were compared as the proportion of renewables in the energy mix was varied. It was found that for low renewables penetration none of the storage systems were economically

viable. As the proportion of renewables was increased CAES was the first to become viable and were found to be more affordable than the other systems for all proportions of renewables. As the renewables proportion became very large, the NPV decreased: there was an abundance of excess renewable energy to be stored, but rarely an opportunity for storage to discharge to the grid.

Levelised cost of energy (LCOE)

The Levelised Cost of Energy (LCOE) is the total cost of the system throughout its lifetime (including construction, operation and maintenance) divided by its useful energy output. The costs are levelised to the current value using a discount rate r: the LCOE can be thought of as the Net Present Value of the unit cost of energy over the lifetime of the system [41].

Rastler [41] carried out a comparison of PHES, CAES and batteries using LCOE as economic metric, as did Schoenung and Hassenzahl [179]. When storage earned revenue from transmission and distribution grid support, and renewable integration/time shifting capabilities Rastler found that pumped hydro had the lowest LCOE followed by CAES, while batteries were more expensive.

Schoenung and Hassenzahl [179] considered three broad applications for energy storage: bulk storage, distributed generation and power quality. Different energy storage systems were placed in each category according to which application they were most suited. For bulk storage, Schoenung found similar results to Rastler, with CAES being the most affordable technology, closely followed by PHES, while batteries were more expensive. Both reports placed the LCOE for CAES and PHES in the range of 10–20 c/kWh (USD cents per kilowatt hour) while lead acid batteries were in the range of 40–60 c/kWh.

Life cycle analysis (LCA)

As the name suggests, life cycle analysis (LCA) or life cycle energy analysis (LCEA) is a method that takes into account the full life cycle of the system: from construction and operation, through to decommissioning. This can be evaluated in terms of economic costs, or of the energy that is required for each stage. It is also possible to incorporate externalities into

LCA and thereby give an indication of the wider impact of the system [180]. For instance, Denholm and Kulcinski [56] assigned an economic cost to the greenhouse gas emissions from different storage technologies. The analysis of pumped hydro, for example, includes emissions generated when constructing the dam, from clearing biomass and from the decay of biomass in the area that is flooded. Denholm investigated PHES, CAES and battery energy storage using LCEA, and the use of this technique provided a subtle comparison of the technologies: it was shown that batteries had much greater energy requirements for construction than PHES or CAES when normalised by the energy capacity since battery components are relatively complicated, and the energy storage media requires intensive mining and processing. On the other hand, CAES produced the most greenhouse gases throughout its lifetime, which is unsurprising given the required gas input. However, these results only occurred when the input energy to the three technologies came from renewables or nuclear. If the input energy was produced by a greenhouse-gas producing source such as coal, it was shown that CAES had lower greenhouse gas emissions than the other technologies.

Oro et al. [181] used LCA to compare three different thermal energy storage materials for applications in solar power plants. The materials considered were solid media (concrete), phase change materials and molten salts. The analysis also included the ecological impact and the effect on human health. These factors were combined into a single metric known as Eco-Indicator 99 (EI99) and the data was extracted from a dedicated database. For each of the stores it was found that the storage media contributed the most to the environmental impact. However, since the application is for solar power plants the stores were not pressurised and it is therefore unclear how significant the pressure vessel contribution would be. The study also found that concrete had the lowest environmental impact out of the three storage media. The disadvantage of such approaches is that it is somewhat arbitrary to assign an economic cost to external factors. Furthermore, this method generally depends on databases having reliably collected the required data.

Energy returned on energy invested (EROI)

The energy returned on energy invested (EROI) is defined as the ratio of the energy delivered by an energy system to the total energy required to produce the system over its entire

life-cycle. As a result, the EROI metric has similarities to Life Cycle Analysis and Net Energy Analysis. The EROI approach has been applied to energy storage systems by Barnhart et al. [182, 183] who defined another metric specifically for storage technologies: the 'energy stored on energy invested' (ESOI). The ESOI is the electrical energy stored over the lifetime of the storage divided by the electrical energy equivalent required to build the system.

Barnhart et al. calculated the ESOI and EROI for a number of storage technologies and renewable energy sources. Barnhart's results supports Denholm's LCA analysis which suggested that batteries are energetically expensive compared to bulk energy storage systems such as CAES and PHES. The analysis suggests that over their lifetime, batteries may only provide 5–30 times the amount of energy required to construct them, while bulk energy storage systems are of the order of 1000. The disadvantage of this approach is that it considers only the energetic cost rather than the full economic cost and involves many assumptions. Nevertheless, this methodology provides an interesting way to consider the energy system and how energy storage may best be integrated into it.

Evaluation of economic approaches

The range of economic approaches makes it difficult to compare technologies that are described in the literature. Even if the same economic metric is used, it is necessary to carefully consider the assumptions made, the factors that are included, and the data sources and values in order to fairly compare results. When a comparison is made using the same metric in the same piece of literature, it should be remembered that the quality of information and data available may vary substantially between technologies, especially if some systems are well established and others are only in the developmental stage.

The above discussion described a number of economic approaches that have been applied to energy storage systems. Despite the differences in methodologies and data, it is notable that most studies agreed that bulk storage systems such as PHES and CAES were less expensive and less energy intensive than battery systems. PTES potentially has similar economic characteristics to CAES because it uses similar components and is predicted to have similar technical performance.

5.2.1 Thermal reservoir costs

The capital cost of the thermal reservoirs is modelled by considering the material requirements of each component and is given by

$$C_{\text{bed}} = k_p V_p + k_i V_i + k_{\text{PV}} V_{\text{PV}} \left(P_0 + \Delta P + \rho_s g L \right) \tag{5.3}$$

where V refers to the volume of a material, and k is the material cost per unit volume. The subscripts p, i and PV refer to the packing material (magnetite), insulation, and pressure vessel, respectively. The pressure vessel cost is assumed to be proportional to the volume and the pressure difference across the walls, ΔP. The additional term P_0 allows unpressurised vessels to be modelled. The term $\rho_s g L$ takes into account the weight of the packing material, where ρ_s is the solid density, L is the height of the store, and $g = 9.81$ ms^{-2} is gravitational acceleration. The packing material will probably be supported by grids throughout the pressure vessel, to reduce the stress on the particles and the pressure vessel but such detail is not included in the present estimations.

The pressure vessel volume includes the volume required for the packing material, insulation, and end-caps that are similar to 'squashed' hemispheres. The volume of each end-cap is given by $a\pi D^3/12$ where a is taken as $1/2$ to reflect the fact that the dome ends are somewhat flatter than hemispheres ($a = 1$). For segmented stores, V_{PV} includes the additional volume which is required for bypass flow and inter-segment gaps as described in section 3.3.1. However, the extra costs of valves, sensing and control which are necessary in layered stores are not included. Values for k and its standard deviation are estimated using the CES Materials Selector database [131], and are shown in table 5.1. A value of k_{PV} was chosen following discussions with Isentropic Ltd [184].

Cost factors		Value	Standard deviation	Source
k_p	(£m^{-3})	500	100	[131]
k_i	(£m^{-3})	1400	500	[131]
k_{PV}	(£m^{-3}bar^{-1})	200	50	[184]
k_r	(£m^{-3}s)	8000	2000	(see table 5.3)

Table 5.1: Costs factors k used in the economic analysis

The cost of pressure vessels has also been estimated by Morandin et al. [88] who undertook

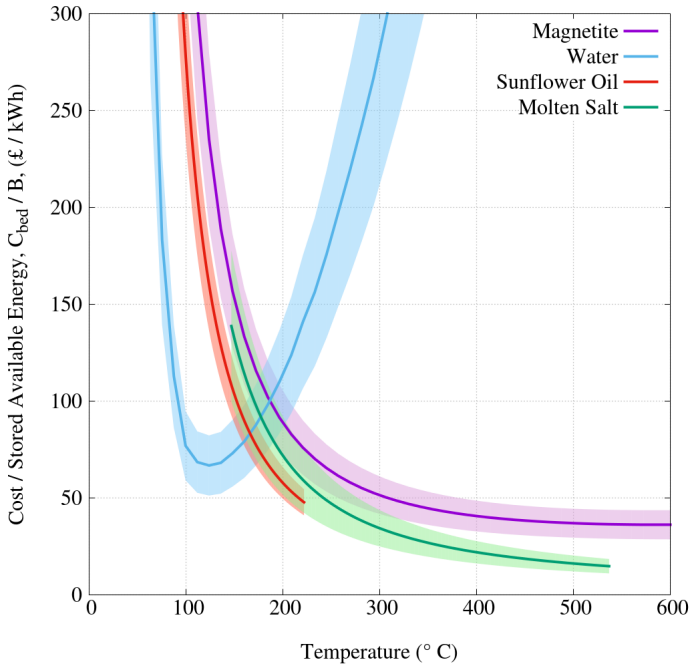

Figure 5.1: Variation in capital cost per stored available energy for a 16 MWh thermal reservoir using different storage materials. Costs factors and relevant material data are given in table 5.2. Shaded areas indicate the cost $\pm$ one standard deviation and represent the uncertainty of the cost factors

a thermo-economic optimisation of a Rankine-cycle based PTES system. Morandin fitted linear trends to data from vendors to suggest that the pressure vessel cost is

$$C_{\mathrm{PV}} = \mathcal{Z}\left[4500V_{\mathrm{PV}}^{0.6} + 10000\right] \tag{5.4}$$

where V is the pressure vessel volume and $\mathcal{Z} \approx 0.77$ is a factor that converts Morandin's cost (in US dollars in 2009) into January 2016 pounds sterling. The pressure vessels in Ref. [88] stored water at 10 bar. For an empty pressure vessel of volume 100 m^3 at 10 bar, equation 5.4 suggests a cost of £63 000 whereas the estimate using the above value of k_{PV} is £200 000. The difference emphasises the inherent uncertainty in these analyses.

Equation 5.3 has been used to calculate the cost of a 16 MWh thermal store for various storage materials, data for which are given in table 5.2. Figure 5.1 shows that increasing the storage temperature generally leads to a decrease in the cost per stored availability as the reservoir volume is reduced. For packed-beds, the pressure is increased in accordance

with $T_2/T_1 = \beta^{\phi_c}$ as if the heat transfer fluid is supplied by a compressor. As a result, as the pressure increases with temperature, and the value of C_{bed}/B reduces despite the increased pressure before plateauing. For liquid storage heat is transferred in a heat exchanger and the pressure thus remains at 1 bar. Consequently the cost drops continually as the temperature increases. These materials have a limited working temperature range: sunflower oil due to a maximum 'smoke temperature' [185]; and molten salts due to their freezing and evaporating points. Heat is also transferred to water in a heat exchanger, and the pressure is fixed at 1 bar until the water begins to boil at 100°C, at which point the pressure is set to the saturation pressure at that temperature. The large increase in pressure that is required to keep water in a liquid form is reflected in the steep increase in cost for temperatures above 100°C.

Material	ρ_s (kg m^{-3})	λ_s (W/kg K)	$\bar{c}_s$ (J/kg K)	Temperature range (°C)	Cost factor k (£m^{-3})	Standard deviation of k
Magnetite	5175	4.0	850	-200 – 800	500	100
Concrete	2300	-	920	-200 – 800	100	25
Sunflower oil	918	-	2400	177	550	100
Soybean oil	925	-	1900	191	410	100
Molten salt	1680	-	1560	112 – 459	1000	500
Glass foam	135	0.04	780	-	1200	200
Graphite foam	100	0.08	775	-	1800	500
Lightweight concrete	1100	0.20	950	-	50	10
Pressure vessel					200 (£m^{-3} bar^{-1})	50 (£m^{-3} bar^{-1})

Table 5.2: Material properties and cost factors k used in the economic analysis. Data comes from CES Edupack Materials Selector database [131]. Standard deviations have been estimated from the range of available data. The cost factor for the pressure vessel arose from discussions with Isentropic Ltd. Solid densities ρ_s, thermal conductivities λ_s and specific heat capacities are averages over the temperature range of operation.

Magnetite is a competitive option since it can be operated at high temperatures and thereby reach low values of cost per stored energy. Despite the high capital costs of molten salts, they are also a competitive option since the container does not need to be pressurised, although these estimates do not include the heat exchanger cost. For comparison, Strasser and Selvam [186] performed a cost analysis of concrete thermal storage in a solar farm. The storage had an extremely large capacity of 2165 MWh and Strasser obtained economic data from an EPRI study and by scaling certain parameters. The unpressurised concrete

storage operated at a temperature of 565°C and was found to have a cost of 30 USD $/kWh which converted to current units is 20 £/kWh. This price included a number of additional factors such as construction costs, tax and additional components. For just the storage media, insulation and tank Strasser's results suggested a cost of approximately 8 £/kWh. For a magnetite system of the equivalent size at the same temperature, the cost given by equation 5.3 is 36.6 $\pm$ 8 £/kWh, and this drops to 17.3 $\pm$ 4 £/kWh for an unpressurised vessel. This is a similar order of magnitude to Strasser's analysis and indicates that pressurising the storage adds significantly to the cost.

5.2.2 Reciprocating device costs

Isentropic Ltd. were developing bespoke compressors and expanders specifically for the PTES system, and estimating their cost is not straightforward. Correlations for turbomachinery have been presented frequently in the literature. These correlations tend to combine thermodynamic modelling with uncertain constants that are calculated by a regression through manufacturer's data [172, 187]. This approach has been widely used [172, 188–190], such as in Ref. [191] to evaluate the cost of an underwater compressed air energy storage system. However, the expressions are technically only applicable to turbomachinery. Furthermore, the data and regression analysis needs to have been obtained recently so that the resulting equation represents the current value of the components.

In the present study, reciprocating device cost is estimated in a similar way to the pressure vessel. Compressor–expander cost is likely to increase with the pressure ratio β, speed of rotation ω, swept volume V_s and mass flow rate $\dot{m}$. These factors are all related by equation 4.17. The capital cost is thus assumed to be proportional to the pressure ratio and volumetric flow rate $\dot{V} = \omega V_s$ as

$$C_r = k_r \beta \dot{V} \tag{5.5}$$

Where k_r is the cost factor. k_r is estimated by considering economic analyses of systems involving diesel generators. Although there are obviously some differences in design, diesel generators contain reciprocating components and can therefore provide a rough estimate of cost. There are a number of papers which present economic or thermo-economic studies of systems containing reciprocating devices or diesel engines, but meaningful data can only

be extracted from a subset of these. This data is shown in table 5.3.

The literature generally provided the diesel engine rated power, and either the cost of the engine or the cost per kilowatt of rated power, $C_r/\dot{W}$. Some sources also gave cylinder geometry making it possible to calculate k_r. The data in table 5.3 show that k_r is typically of the order of 10 000 £m^{-3}s. A representative value of $k_r = 8000$ £m^{-3}s has been chosen. Capital costs were calculated by inflating the cost to the current value (January 2016) for that currency, and then converting to pounds sterling using the current exchange rate. Further information about the data that was used is shown in table 5.4.

For a nominal design (see table 4.2) with $\omega = 1200\text{rpm} = 20\text{revs}^{-1}$, $\beta = 10$, and $V_s \approx 0.5\text{m}^3$, and using $k_r = 8000$ m^{-3}s gives a compressor cost of approximately £800 000.

	Power $\dot{W}$ (kW)	C_r (£$\times 10^3$)	N_{cyl}	β	V_s (m$^3 \times 10^{-3}$)	ω (rpm)	$C_r/\dot{W}$ (£kW^{-1})	$k_r = C_r/\beta\dot{V}$ (£m^{-3}s)
Bonnet et al. [192]	24	6.4	1	6.0	7.0	1000	271	9100
Herrera et al. [193]	44	8.4	4	17.0	3.9	1800	191	4200
Ehyaei et al. [194]	145	29.9	6	10.5	10.5	1800	206	9050
Acikkalp et al. [195]	5900	2200.0	-	-	-	-	371	-
Balli et al. [196]	6500	2340.0	18	≈30	580.0	750	360	10800
Abusoglu et al. [176]	28800	4000.0	18	-	-	-	139	-

Table 5.3: Data from the literature regarding diesel engine rated power, geometry, and capital costs. Further information about the literature sources is given in table 5.4.

	Notes
Bonnet et al. [192]	Investigates an Ericsson engine which uses reciprocating compressors and expanders. Compression occurs in two stages and there is a lack of data concerning the operating points of these two compressors. Expansion occurs in a single stage and data in table 5.3 is based on the expander which cost 7 200 euros in 2005.
Herrera et al. [193]	Diesel engine as part of a co-generation plant. Economic data originates in Herrera's PhD thesis (in Portuguese) and suggests a capital cost of USD$12 555.
Ehyaei et al. [194]	Internal combustion engine based on the Caterpillar G3306B engine for co-generation applications. Assumes cost of installation is 300 USD $/kW in 2012.
Acikkalp et al. [195]	Diesel engine for use in a tri-generation plant. Engine has a Purchasing Equipment Cost (PEC) of USD$3 280 000 in 2014.
Balli et al. [196]	Engine for use in a tri-generation plant, based on a Wartsilla 18V32GD diesel engine. Purchasing Equipment Cost is given as USD$3 250 000 in 2010. Engine geometry data in table 5.3 is from the Wartsila website [197].
Abusoglu et al. [176]	Data is for a diesel engine as part of a co-generation system. The diesel engine has a cost of USD$5 400 000 in 2009 and this data was provided by Sanko energy

Table 5.4: Further details about the literature sources for data on reciprocating diesel engines

5.2.3 PTES capital cost

Evaluation of the full PTES cost also requires estimation of the cost of heat exchangers, the motor-generator, pipework, valving and control systems, as well as construction costs. Thermo-economic optimisation of a Rankine-cycle based PTES system was undertaken in [88]. The costs for several components were estimated by fitting linear trends to data from vendors. The heat exchanger cost was given by

$$C_{\mathrm{HX}} = \mathcal{Z}\left[450 A_{\mathrm{HX}}^{0.82} + 5000\right] \tag{5.6}$$

where A_{HX} is the heat transfer area, and $\mathcal{Z} \approx 0.77$ is a factor that converts the cost (in US dollars in 2009) into January 2016 pounds sterling. The compact heat exchanger of surface type $8.0 - 3/8T$ described in section 4.3.1 has a geometry of $A_{\mathrm{HX}}/V = 587$ m^2 / m^3 [163]. Therefore, a heat exchanger of volume 1 m^3 would have a capital cost of $C_{\mathrm{HX}} =$ £68 000.

Ref. [88] proposed that the cost of a variable speed motor-generator would vary as

$$C_{\mathrm{mg}} = \mathcal{Z}\left[110P + 5000\right] \tag{5.7}$$

where P is the electric power (in kW). Therefore, a 2 MW system would have a capital cost of $C_{\mathrm{mg}} =$ £173 000.

The total capital cost is thus,

$$C_{\mathrm{cap}} = C_{\mathrm{bed}}^{\mathrm{hot}} + C_{\mathrm{bed}}^{\mathrm{cold}} + 2C_r + 2C_{\mathrm{HX}} + C_{\mathrm{mg}} \tag{5.8}$$

The expression for capital cost contains four rather uncertain cost factors k (not including the variables in the expressions of Ref. [88]). Table 5.1 shows these factors as derived from data in the literature. The standard deviation of the cost factors has also been estimated given the range of data found and assuming the costs follow a normal distribution.

The capital cost of the nominal 16 MW h, 2 MW PTES system of table 4.1 is estimated as £1.4 million, or 160 £/kWh. The distribution of cost between each component is given in table 5.5. The standard deviation is calculated using the values given in table 5.1 and is

		CE	EC	HS	CS	HX	MG	Total
C_{cap}	(£$\times$ 1000)	245	101	417	310	136	173	1380
$C_{\text{cap}}/W_{\text{dis}}$	(£/kWh)	28	12	48	36	16	20	160
standard deviation	(£/kWh)	7	3	10	6	-	-	14
$C_{\text{cap}}/\dot{W}_{\text{dis}}$	(£/kW)	170	70	290	215	94	120	958
standard deviation	(£/kW)	43	18	61	37	-	-	85

Table 5.5: Capital costs of each component in a nominal 16 MWh, 2MW PTES system described in table 4.1. Standard deviations are calculated assuming that the cost factors k are normally distributed with the values given in table 5.1. Key: CE/EC Reversible compressor-expander; HS/CS hot/cold store; HX heat exchangers; MG motor-generator.

roughly 14 £/kWh[1]. The standard deviation indicates the uncertainty in the cost factors but it does not reflect the uncertainty of the estimation method, which may be considerable and could vary by as much as a factor of two or three.

For comparison, table 5.6 gives the costs of several other prominent energy storage types. The data was obtained from Chen et al. [39] and adjusted to the current value. The present study suggests that PTES is significantly more expensive that PHES or CAES in terms of cost per work output, and has a value more comparable to lead-acid batteries. It is notable that PTES is an order of magnitude more expensive than other TES systems. PTES is comparable to PHES and CAES in terms of cost per power output, and is more expensive than most of the batteries by this metric.

The actual cost of PTES may be quite different to this value since optimisation has not been undertaken. In addition, these costs do not include the capital cost of control systems or construction costs. Morandin et al.'s [88] study of a 50 MW, 100 MWh PTES system suggested optimal designs would cost in the range of 210–290 £/kWh or 420–580 £/kW which is a similar order of magnitude to the estimates presented here. Alternatively Howes [5] suggested that Isentropic Ltd. could build a PTES system (including installation) for 10 £/kWh and 280 £/kW. Howes' estimation is significantly cheaper than the values suggested here, and seems to be optimistic. Nevertheless, it emphasises how uncertain even a rela-

[1]The overall standard deviation is found by assuming that each cost factor varies with a normal distribution such that $k_j \sim N\left(\mu_j, \sigma_j^2\right)$. Since the capital cost is given by a weighted sum of the cost factors such as $C = \sum_j k_j W_j$, then the capital cost also has a normal distribution given by $C \sim N\left(\sum_j \mu_j W_j, \sum_j \left(\sigma_j W_j\right)^2\right)$ from which the standard deviation is found.

System	Capital cost per work output (£/kWh)	Capital cost per power output (£/kW)
PHES	4 - 75	440 - 1500
CAES	1 - 40	300 - 600
Flywheel	700 - 4000	190 - 260
TES	20 - 50	-
Lead-acid	150 - 300	200 - 400
Li-ion	400 - 1800	900 - 3000
Super-capacitor	200 - 1500	75 - 200
PTES	150 - 200	850 - 1050

Table 5.6: Capital costs of several prominent energy storage systems, data originally from Chen [39] has been inflated and converted to current value of GBP (£). Capital costs for the nominal PTES design are shown. N.B. These do not represent the cost that the optimal design may be able to achieve.

tively simple measure such as the capital cost can be. As a result, the capital cost is used here to compare one PTES design with another, rather than making comparisons with other technologies.

Due to the uncertainty of the economic cost, a comprehensive sensitivity analysis should be carried out to explore the impact of each of the economic factors. Preliminary analysis suggests that the capital cost is dominated by the pressure vessel and the reciprocating devices. Without more detailed studies, it is unreliable to compare capital costs to other systems.

5.3 Multi-objective optimisation techniques

Optimisation can assist designers and engineers to find the best solution to a problem, by allowing them to maximise the potential of their work whilst minimising the expense. There are a wide range of optimisation algorithms each with its own strengths and weaknesses, and each suitable for certain types of problem.

The simplest technique is to differentiate the objective function (i.e. the function that is to be minimised or maximised) with respect to the parameters of interest. This method can be extended to constrained problems with the technique of Lagrange multipliers and Kuhn-Tucker multipliers. Iterative algorithms that search through potential solutions are

also popular, and are appropriate in certain circumstances. Common examples are the golden section method, method of steepest descent, the Newton-Rhapson method and the conjugate gradient method.

These techniques generally rely on the function being defined analytically and differentiable. Moreover, approaches such as the Newton-Rhapson method work most efficiently if the function is approximately quadratic, while other techniques may be computationally intensive, for instance, they may involve the inversion of matrices at each iteration.

5.3.1 Evolutionary Algorithms

The optimisation techniques mentioned above are limited to tackling certain types of problems. In practical scenarios, optimisation problems can become extremely complex for several reasons:

1. The objective function and its derivatives may not be obtainable analytically, for example, it may be the output of a complex computer model
2. The objective function may be a function of many design variables so that the search space is large and multi-dimensional
3. There may be several competing objectives. A common example in engineering problems is to maximise performance and minimise cost
4. The problem may be highly constrained, so that the search space is not only large and multi-dimensional, but also disjoint
5. The problem may be multi-modal, so that many local optima may exist that could easily trap an optimisation routine
6. The problem may be dynamic and the solutions may change with time

An appropriate approach to difficult optimisation problems such as these is to use a stochastic search method such as Monte Carlo sampling, which explores the design space in a random manner. This approach is suited to complex problems, since it can traverse the entire search space without the risk of becoming trapped in local optima. Monte Carlo

sampling can be improved if the random search is directed in some way, and there are several methods of doing this which are discussed below.

Simulated Annealing is inspired by the cooling of metal during which the structure formed is such that the energy of the configuration is minimised. The algorithm therefore seeks to minimise the internal energy of the system, that is, the objective function. Solutions are stochastically chosen and are accepted with a given probability. (The probability is one for solutions that are better than the previous solution, and less than one otherwise). Cooling is mimicked by reducing the probability of accepting worse solutions with time. Allowing worse solutions (with diminishing probabilities) prevents the algorithm becoming trapped in local minima.

Simulating the movements of large groups of organisms, such as schools of fish, or colonies of ants, led to the development of Particle Swarm Optimisation. Each particle in the swarm moves about the search space, and its direction and velocity is influenced by the movements and discoveries of other members of the swarm.

Tabu search [198, 199] uses a memory archiving scheme to store the most recently visited points and record them as *tabu*, thereby preventing them from being revisited for a certain period. Tabu search methods are well suited to highly constrained problems and make rapid initial progress.

Evolutionary algorithms are a popular branch of stochastic optimisation. These algorithms are inspired by the Darwinian theory of evolution, and aim to evolve solutions to problems [200]. This typically involves generating an initial population of solutions whose members breed and mutate, with only the 'fittest' members surviving. *Fitness* implies how good the member is in terms of the objective function, however, other factors can be incorporated, see the discussion on diversity below. Each activity (recombination, mutation, selection) is subject to much variation, depending on the exact implementation of the algorithm. This is a very broad field and many diverse approaches have been suggested; popular methods are genetic algorithms [201] and evolution strategies [202, 203].

One reason for the diversity, even within sub-disciplines, of optimisation algorithms is the "no free lunch" theorems [204] which imply that every optimisation algorithm performs equally well when its performance is averaged across all possible problems.

5.3.2 Multi-objective Optimisation and Pareto Fronts

A particularly relevant issue is how to handle problems in which multiple objectives require optimisation, especially when the improvement of one objective may come at the expense of another: that is, when trade-offs exist between the objectives. One solution to this is to combine each of the N objectives f_i into one composite objective, $\bar{f}$, by assigning a weight w_i to each objective depending on its perceived importance.

$$\bar{f} = \sum_{i=1}^{N} w_i f_i \tag{5.9}$$

$$1 = \sum_{i=1}^{N} w_i \tag{5.10}$$

This approach therefore allows the application of single-objective algorithms such as those discussed in section 5.3.1, however, it clearly has the disadvantage that the designer has to choose the weightings *prior* to running the optimisation leaving the results at risk of the designer's preconceptions. Ideally, the designer would like to be able to see the entire trade-off surface, in order to make a more informed decision.

Game theory and the Nash equilibrium provides the foundation for an alternative approach whereby each objective is treated as a 'player' in a game where every player aims to maximise their utility [205–207]. Every player seeks the strategy that maximises their pay-off given the strategy of every other player, where the strategy is the vector of decision variables. Whilst an advantage of this approach is its speed and the fact that weightings are not required, it also suffers from the fact that only one point on the trade-off surface is found. Game theoretic optimisation has been incorporated into algorithms which generate the full trade-off surfaces, however, as the game theoretic solution can be used to 'seed' an algorithm which generates the full trade-off front [208].

Algorithms which find points on the entire trade-off surface (also known as Pareto fronts) do so by the concept of dominance. Each of the solutions on the Pareto front is deemed as good as every other solution: one solution may be better in terms of the first objective function, but it will be worse in terms of the second. A Pareto front is therefore composed of solutions which are not dominated by any other solution. Formally, a solution $\mathbf{x}$ (where

x is the vector of design variables) is *dominated* by a solution **y** if **y** is at least as good in all objectives and is better in at least one:

$$f_i(\mathbf{y}) \leq f_i(\mathbf{x}) \quad \forall i = 1, N \quad \text{and} \quad f_i(\mathbf{y}) < f_i(\mathbf{x}) \quad \text{for some } i \tag{5.11}$$

where N is the number of objectives, and the optimiser is seeking to minimise the objectives.

A Pareto dominance based approach thus allows the designer to see the entire range of potential solutions without having to specify a weighting for each objective and can potentially suggest solutions that the designer would not have previously thought of or considered. This diversity in the solution space can also prevent 'inbreeding' – i.e. where the algorithm converges on a single, non-optimal point.

5.3.3 Diversity in Objective and Solution Spaces

There are many methods of achieving diversity which generally focus on diversity in the objective function space [209–211]. For example, the Non-dominated Sorting Genetic Algorithm (NSGA-II) [212] encourages diversity along the Pareto front by calculating a measure of distance between each member on the front known as the *crowding distance*. This measure of the density can be used to determine which solutions to keep and which to discard. In an alternative approach known as the Strength Pareto Evolutionary Algorithm (SPEA) [213] a distance metric is not required, and instead a ranking procedure based on the number of solutions that a given solution dominates is used. The fewer points a solution dominates, the more this solution is preferred since it is located in a less-explored area of the objective space. Comparisons of various algorithms (bearing in mind the 'no free lunch theorems') have determined that SPEA and NSGA-II generally show the best performance [212, 213], although SPEA has the disadvantage of greater computational complexity.

It is also important to maintain diversity in the design variable space. Members of a diverse population will generate equally diverse offspring therefore helping the design space to be more fully explored. The objectives of achieving convergence to a Pareto front and maximising diversity of the population may be at odds. The Genetic Diversity Evolutionary Algorithm (GDEA) [214] explores this conflict by making diversity an additional objective

in the problem.

5.4 Optimisation of packed-bed thermal reservoirs

5.4.1 Problem formulation

The multi-objective genetic algorithm (MOGA) is first applied to packed-bed thermal reservoirs. Thermal reservoirs can be integrated into a variety of storage systems including PTES, CAES, and LAES. While holistic optimisation should consider the full system and its requirements, an interesting preliminary study is to discover the optimum performance of packed beds.

Both hot and cold reservoirs are optimised independently. Furthermore, optimisations are carried out on unsegmented, segmented and radial-flow stores, which were introduced in chapter 3. Since the intended application of the packed beds is in bulk electricity storage, the internal energy storage capacity and nominal charging time of the stores is held constant. For consistency, the reservoirs have the same energy capacity as the nominal PTES design, see table 3.1. The nominal charging time is 8 hours, and the maximum energy capacities of the hot and cold store are 26.5 MWh (95.3 GJ) and 10.7 MWh (38.5 GJ), respectively.

The objective functions of the thermo-economic optimisation are the round-trip efficiency and the capital cost per unit returned available energy. For the thermal stores, the round-trip efficiency is defined as in equation 2.44, as the ratio between the recovered available energy flux, and the net available energy flux during charge

$$\chi = \frac{B_{\mathrm{out}}}{B_{\mathrm{in}}} \tag{5.12}$$

The capital cost per unit returned available energy is given by

$$\hat{C}_E^{\mathrm{res}} = \frac{C_{\mathrm{bed}}}{B_{\mathrm{out}}} \tag{5.13}$$

Where C_{bed} is the capital cost of the packed bed as defined in equation 5.3. The MOGA is

a minimisation routine so that the objective functions are expressed as

$$f_1 = 1 - \chi \tag{5.14}$$

$$f_2 = \hat{C}_E^{\text{res}} \tag{5.15}$$

The design variables of interest are the aspect ratio L/D, the particle diameter d_p, the exit temperature fractions which indicate the end of charge or discharge θ_c and θ_d, the charging and discharging temperatures T_1 and T_2, the number of segments N_{seg} and the temperature thresholds which switch segments on and off θ_l and θ_h. The nominal values of these parameters, and the lower and upper bounds are shown in tables 5.7 and 5.8 for hot and cold stores respectively.

The operating temperatures are design variables, and the reservoir volume is calculated to keep the energy capacity of the stores E_{res} constant. For instance, for a hot store the volume is given approximately by

$$V_{\text{pack}} = \frac{E_{\text{res}}}{\rho_s(1-\varepsilon)\bar{c}_s\,(T_1 - T_2)} \tag{5.16}$$

(A more exact value would integrate over the temperatures to take into account the varying specific heat capacity c_s). In addition, the nominal charging time t_N (equation 2.5) is held constant which determines the mass flow rate:

$$\dot{m} = \frac{\rho_s(1-\varepsilon)V_{\text{pack}}\bar{c}_s}{c_{p,g}t_N} \tag{5.17}$$

Constraints are placed on the temperatures so that $T_1 > T_2 + 50$ for a hot store and $T_1 < T_2 - 50$ for a cold store. The constraint is imposed such that the temperatures must be at least 50°C apart (an infinitesimal difference would be the most efficient, but would require an infinitely large store which is clearly not practicable).

As well as the objective functions, a number of other metrics are of interest:

- The charging duration Δt_{chg} and storage duration Δt_{store}.
- The volume of the packing media V_{pack}
- The mass flow rate, $\dot{m}$

	L/D	d_p (mm)	θ_c (%)	θ_d (%)	T_1 (°C)	T_2 (°C)	N_{seg}	θ_l (%)	θ_h (%)
Nominal	1.0	20.0	25.0	25.0	505.0	37.0	1	1.0	99.0
Lower bound	0.5*	1.5	5.0	5.0	37.0	37.0	1	1.0	95.0
Upper bound	2.0	20.0	50.0	50.0	600.0	600.0	32	5.0	99.0

Table 5.7: Lower and upper bounds for parameters used in optimisation of hot stores. For radial stores and unsegmented stores θ_l and θ_h are not variables and $N_{\text{seg}} = 1$. * for radial stores the lower bound of L/D is 0.1.

	L/D	d_p (mm)	θ_c (%)	θ_d (%)	T_1 (°C)	T_2 (°C)	N_{seg}	θ_l (%)	θ_h (%)
Nominal	1.0	20.0	25.0	25.0	-150.0	37.0	1	1.0	99.0
Lower bound	0.5*	1.5	5.0	5.0	-170.0	-170.0	1	1.0	95.0
Upper bound	2.0	20.0	50.0	50.0	37.0	37.0	32	5.0	99.0

Table 5.8: Lower and upper bounds for parameters used in optimisation of cold stores. For radial stores and unsegmented stores θ_l and θ_h are not variables and $N_{\text{seg}} = 1$. * for radial stores the lower bound of L/D is 0.1.

- The returned available energy B_{out}
- The average power output $P_{\text{ave}} = B_{\text{out}}/\Delta t_{\text{chg}}$
- The energy density $\rho_E = B_{\text{out}}/V_{\text{pack}}$
- The power density $\rho_P = P_{\text{ave}}/V_{\text{pack}}$
- The capital cost of the packed bed C_{bed}
- The capital cost per unit average power output $\hat{C}_P^{\text{res}} = C_{\text{bed}}/P_{\text{ave}}$

5.4.2 Results

Thermo-economic optimisation results for hot and cold stores are presented below. Pareto fronts for cold and hot thermal stores are shown in figures 5.2(a) and 5.2(c), respectively. The Pareto front visualises the optimisation results by plotting one objective function against the other. The Pareto front effectively displays the trade-off between efficiency and capital cost: each point on the Pareto front is better than any other point in at least one objective. For instance, on figure 5.2(a), the point marked C1 is cheaper than C2, although C2 is more efficient than C1.

The design variables, and several other metrics are tabulated in tables 5.9 and 5.10 for

selected optimal points (as indicated on the Pareto fronts). A comprehensive understanding of the optimal designs is best achieved by studying the full range of designs along the Pareto front. For brevity, two points are selected from each Pareto front with the aim of being representative of the type of designs that occur at each end of the trade-off surface.

A thermo-economic optimisation with fixed operating temperatures was also carried out, using the same objective functions and thermodynamic model. Results are presented in [80] and are not replicated here as the results of both optimisations followed the same trends. The main differences were that when the temperatures were fixed, the optimal stores were found to be less efficient than when the temperatures could vary. For instance, the most efficient hot and cold stores were 99.7% and 96.8% respectively, compared to 98.7% and 94.2%. This is not unduly surprising, but indicates the importance of operating temperatures on the design. It also indicates that optimising a full PTES system cannot be achieved by optimising individual components independently.

Pareto front behaviour

The Pareto fronts for hot and cold stores show the expected trade-off between capital cost and efficiency: high efficiency stores have high costs. The Pareto front of the cold store is particularly flat at high efficiencies meaning that it is possible to significantly reduce the capital cost without unduly compromising the efficiency. However, the efficiency drops very suddenly once the cheapest designs are sought. The best compromise exists around the 'knee' of the curve where the gradient of the trade-off surface changes most rapidly. Table 5.11 below indicates the likely performance of points in this region for hot and cold segmented stores. Comparing these results with the performance of other established technologies in table 5.6 on page 197 suggests that packed-bed thermal reservoirs are slightly more expensive per work output than other bulk technologies such as PHES and CAES. Thermal storage systems that utilise packed-beds will be more expensive than the indicated values, as this study does not include the cost of the rest of the storage system. However, these estimates are very approximate and the true values could vary significantly. These results indicate that hot stores are more efficient and cost effective than cold stores, which are unlikely to be used unless the full energy storage system specifically requires it.

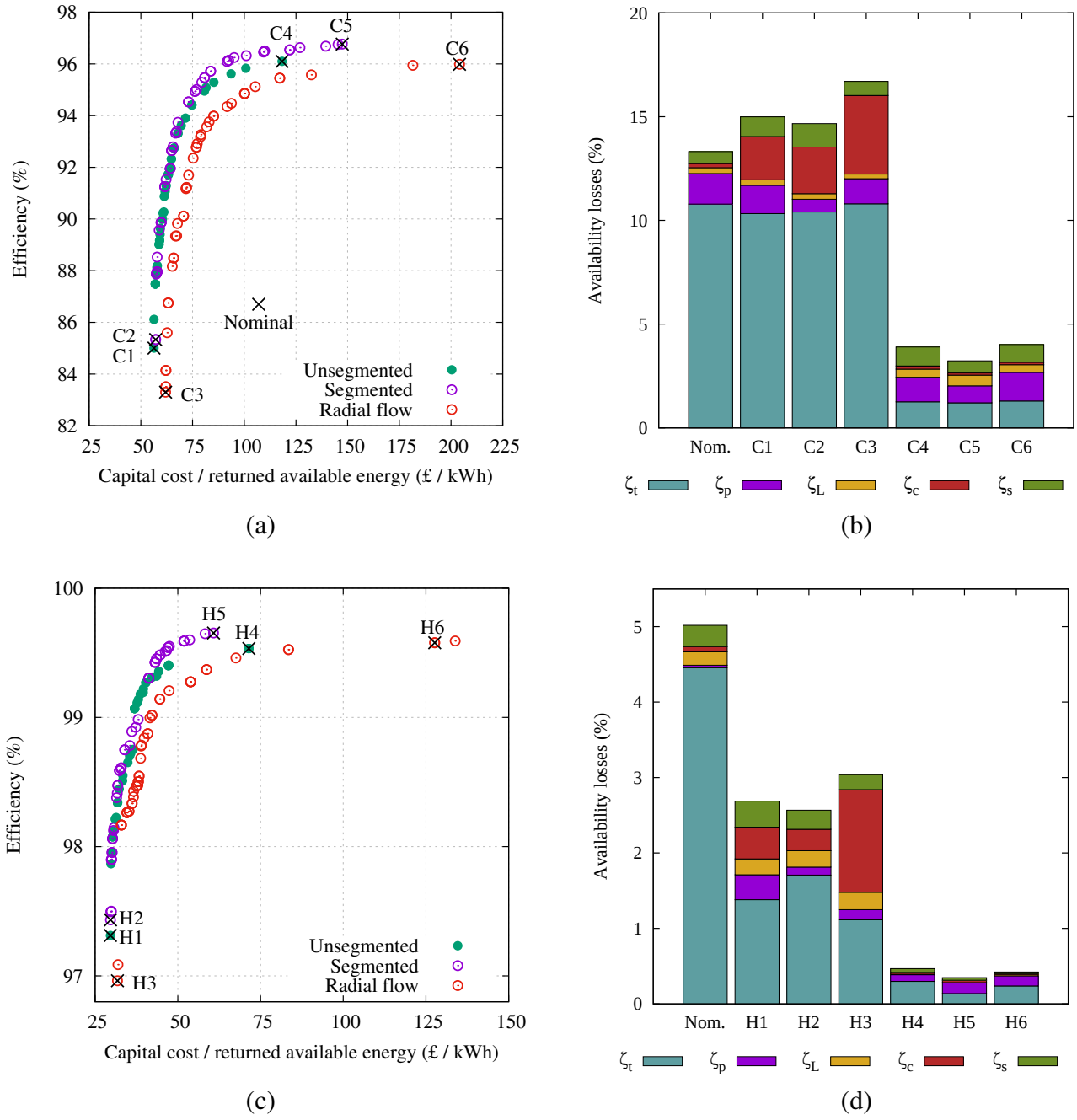

Figure 5.2: Optimisation results for cold and hot packed-bed thermal reservoirs. **(a)** Cold store Pareto fronts **(b)** Cold store distribution of availability losses for the selected points in figure (a) **(c)** Hot store Pareto fronts **(d)** Hot store distribution of availability losses for the selected points in figure (c)

		Nom.	C1	C2^s	C3^r	C4	C5^s	C6^r
L/D		1.00	0.50	0.51	0.43	0.51	0.51	0.45
d_p	(mm)	20.0	6.0	5.6	5.9	7.5	8.1	10.7
θ_c	(%)	25.0	50.0	44.0	47.0	17.0	24.0	8.5
θ_d	(%)	25.0	50.0	49.0	50.0	9.7	18.1	17.5
T_1	(°C)	-150.0	-170.0	-170.0	-170.0	-169.7	-167.7	-165.5
T_2	(°C)	37.0	15.0	17.6	-5.1	-76.9	-114.1	-104.9
N_{seg}		1	1	9	-	1	14	-
θ_l	(%)	-	-	3.2	-	-	3.9	-
θ_h	(%)	-	-	98.7	-	-	98.5	-
Δt_{chg}	(h)	5.5	7.3	7.2	7.3	4.5	6.2	4.1
Δt_{store}	(h)	6.5	6.5	4.7	4.8	4.7	5.8	7.9
$\dot{m}$	(kg/s)	13.7	13.9	13.7	15.6	27.7	47.9	42.4
V_{pack}	(m^3)	127.1	139.4	136.8	162.5	342.9	667.5	564.8
B_{out}	(MWh)	3.0	5.4	5.3	5.9	6.1	10.2	6.4
P_{ave}	(MW)	0.55	0.74	0.74	0.81	1.36	1.66	1.53
ρ_E	(kWh m^{-3})	23.5	38.7	39.0	36.3	17.7	15.3	11.2
ρ_P	(kW m^{-3})	4.3	5.3	5.4	5.0	4.0	2.5	2.7
C_{cap}	(£$\times$1000)	320.0	304	305	365	717	1510	1300
$\hat{C}_P^{\text{res}}$	(£/ kW)	586	409	414	452	529	909	845
χ	(%)	86.7	85	85.3	83.3	96.1	96.8	96.0
$\hat{C}_E^{\text{res}}$	(£/ kWh)	107	56.4	57.2	62.0	118.3	147.4	204.1

Table 5.9: Design variables and results for selected points from the optimisation of a cold store. Points correspond to those in figure 5.2(a). Note that those marked with a ^{s} are segmented beds and those with ^{r} are radial-flow stores. The first data block provides the design variables for these points. The second and third data block gives some other useful information, while the final data block provides the objective functions (efficiency and cost per unit returned energy).

General trends in decision variables

Reductions in $\hat{C}_E^{\text{res}}$ are achieved by either reducing the capital cost or increasing the available energy that is returned during discharge. The capital cost is generally minimised by reducing the pressure vessel volume. This is achieved by the charging temperature T_1 converging to its extreme limit (maximum for hot stores and minimum for cold stores) which also increases the efficiency. Conversely, T_2 varies along the Pareto front as the least expensive designs have a large $\Delta T = |T_1 - T_2|$ whereas a small ΔT maximises the efficiency, as in section 3.2.2. However, it should be noted that operating temperatures may in fact be

		Nom.	H1	H2^s	H3^r	H4	H5^s	H6^r
L/D		1.00	0.85	0.93	1.07	0.50	0.51	1.90
d_p	(mm)	20.0	2.9	4.1	2.5	8.0	4.0	1.7
θ_c	(%)	25.0	0.50	0.50	0.50	7.0	12.0	33.8
θ_d	(%)	25.0	0.15	0.35	0.39	17.3	10.9	38.3
T_1	(°C)	505.0	600.0	600.0	600.0	595.0	600.0	600.0
T_2	(°C)	37.0	110.3	133.4	112.4	308.8	350.7	516.2
$\mathrm{N_{seg}}$		1	1	4	-	1	15	-
θ_l	(%)	-	-	2.6	-	-	1.2	-
θ_h	(%)	-	-	98.2	-	-	97.7	-
Δt_{chg}	(h)	5.5	7.9	7.9	8.0	4.3	5.8	6.6
$\Delta t_{\mathrm{store}}$	(h)	6.5	4.1	4.1	4.0	7.7	6.2	5.4
$\dot{m}$	(kg/s)	13.7	13.0	13.1	13.3	22.2	25.5	76.3
V_{pack}	($\mathrm{m^3}$)	75.5	66.5	66.9	66.9	104.4	117.5	329.0
B_{out}	(MWh)	7.1	12.6	12.7	12.8	8.3	11.5	14.0
P_{ave}	(MW)	1.31	1.60	1.61	1.60	1.92	1.97	2.1
ρ_E	($\mathrm{kWh\ m^{-3}}$)	94.6	190.0	190.6	190.9	79.4	97.7	42.5
ρ_P	($\mathrm{kW\ m^{-3}}$)	17.4	24.1	24.2	24.0	18.4	16.8	6.4
C_{cap}	(£$\times$1000)	422	374	378	405	592	698	1784
$\hat{C}_P^{\mathrm{res}}$	(£/ kW)	322.3	233.5	233.9	252.9	308.3	353.7	844.9
χ	(%)	95.0	97.3	97.4	97.0	99.5	99.7	99.6
$\hat{C}_E^{\mathrm{res}}$	(£/ kWh)	59.1	29.6	29.6	31.8	74.5	60.8	127.7

Table 5.10: Design variables and results for selected points from the optimisation of a hot store. Points correspond to those in figure 5.2(c). Note that those marked with a ^{s} are segmented beds and those with ^{r} are radial-flow stores. The first data block provides the design variables for these points. The second and third data block gives some other useful information, while the final data block provides the objective functions (efficiency and cost per unit returned energy).

constrained by the whole system design.

The trade-off between efficiency and cost may be illustrated by considering the shape of the thermal fronts that are formed. Choosing values of decision variables that lead to steep thermal fronts leads to lower efficiencies due to larger thermal and conductive losses. On the other hand, steeper fronts travel further along the packed bed by the end of the charging phase and therefore increase the returned available energy.

As a result, the position of a point on the Pareto front is primarily controlled by the charging duration, which is determined by the gas exit temperature fractions θ_c and θ_d. As discussed in chapter 3 longer charging times lead to steeper thermal fronts. The optimal particle size

	χ (%)	$\hat{C}_E^{\text{res}}$ (£/kWh)	$\hat{C}_P^{\text{res}}$ (£/kW)
Hot store	99.5	35–50	400–500
Cold store	95.5	60–90	250–350

Table 5.11: Typical efficiencies and capital costs of optimal packed-bed thermal reservoirs

depends on the charging periods. When a steep front is formed, smaller particles increase the heat transfer area and reduce the thermal losses. As a result, lower cost stores tend to use smaller particles.

Available energy loss mechanisms for the selected points are illustrated in histograms in figures 5.2(b) and 5.2(d). The most efficient points (C4–C6 and H4–H6) have designs where thermal losses are approximately equal to pressure losses which is a result of the optimiser finding a trade-off between these two conflicting loss mechanisms. On the other hand, thermal losses dominate in the high energy density designs as a result of the steep thermal fronts. The steep fronts (and small particles) in designs C1–C3 and H1–H3 also lead to large conductive losses during operating and storage.

Benefit of segmentation

Inspection of the Pareto fronts suggests that segmented thermal stores out-perform unsegmented stores. As expected, segmentation provides the greatest improvement to cold stores. For example, the highest efficiency unsegmented cold store is 96.2% whilst the best segmented store is 96.8%. At a fixed efficiency, cold segmented stores offer a significant saving. For example, the unsegmented store C4 has $\hat{C}_E^{\text{res}} = 118$ £/ kWh but a corresponding segmented point costs around 93 £/ kWh which is roughly 20% cheaper. However, this does not include the cost of control systems or valving, so this saving represents the amount of money that is available to be spent on additional equipment before segmented stores stop being economically competitive with unsegmented stores. (Note, that this study does in fact include a simple economic penalty for segmentation; bypass flow requires extra volume resulting in larger containment vessels and higher pressure vessel costs.) The optimiser finds value in layering hot stores, but the benefit is quite small as pressure losses are low.

The reduced pressure losses in segmented stores typically lead to larger aspect ratios (par-

ticularly in the most efficient hot stores) and smaller particles. Consequently, the thermal fronts are steeper, and the utilisation of the reservoirs increases.

θ_h and θ_l affect the truncation of the thermal front that occurs when segments are activated and de-activated as discussed in section 3.3.2. Front truncation leads to thermal losses that are most significant at the trailing edge during discharge. The optimiser therefore converges towards the upper limit of θ_h in cold stores and the lower limit of θ_l in hot stores.

Optimisation of radial-flow stores

Radial-flow stores are outperformed by segmented and unsegmented axial-flow packed beds. Although radial-flow stores can achieve similar efficiencies to the axial-flow stores, it is always more expensive to do so. These high costs stem from the additional space that is required for the inner and outer plena. A good example is to compare H1 (unsegmented) and H3 (radial-flow). These points have similar operating temperatures, require similar volumes of packing material and achieve similar efficiencies and available energy outputs. However, the extra volume required for the inner and outer plena leads to a pressure vessel that is 6% larger than the unsegmented store which increases $\hat{C}_E^{\mathrm{res}}$.

The optimisation was carried out with the assumption that the radius of the inner plenum should be 20% of the packing radius. The outer plenum has an equal area to the inner plenum. Reducing the size of the inner plenum would reduce the required volume and therefore the cost. However, detailed studies are necessary to determine how small the inner plenum may be and to realise the full implications of this design feature. The potential improvements in radial-store performance could be checked by undertaking an optimisation with $R_i/R_o = 0$.

Economic considerations

A breakdown of the capital cost between the various components for selected points is given in figure 5.3. Both the capital cost C_{cap} and the capital cost per unit returned available energy $\hat{C}_E^{\mathrm{res}}$ are shown. Error bars are plotted to indicate the uncertainty in the cost factors and show the total cost plus or minus one standard deviation, which is calculated as described in a footnote on page 196. A cursory glance at the figures suggests that the

uncertainty is quite high. Furthermore, the uncertainty is likely to be higher than the error bars indicate, as they do not reflect the uncertainty in the estimation method. The capital cost is therefore best used to compare one design against another rather than determining the feasibility of packed-bed thermal reservoirs.

The cost of the steel containment vessel dominates the capital cost. There is also a large difference in cost between the most efficient designs and the least efficient designs. This is primarily due to the variation in volume due to the variable operating temperatures. For instance, points C4–C6 have more than double the packing volume of points C1–C3. This leads to much larger reservoirs with larger insulation and containment requirements. Hot stores are more expensive (despite their lower volumes) due to the higher pressure of operation. Radial stores are typically more expensive due to the larger volumes that are required as a result of the inner and outer plena. H6 (radial) has a much higher capital cost C_{cap} as a result of a small difference between T_1 and T_2.

The results above are consistent with the theory and parametric studies of packed beds presented in chapters 2 and 3. The optimisation algorithm is nevertheless a useful tool as it identifies the surface of optimal points which would have been difficult to achieve using only the knowledge developed in the opening chapters.

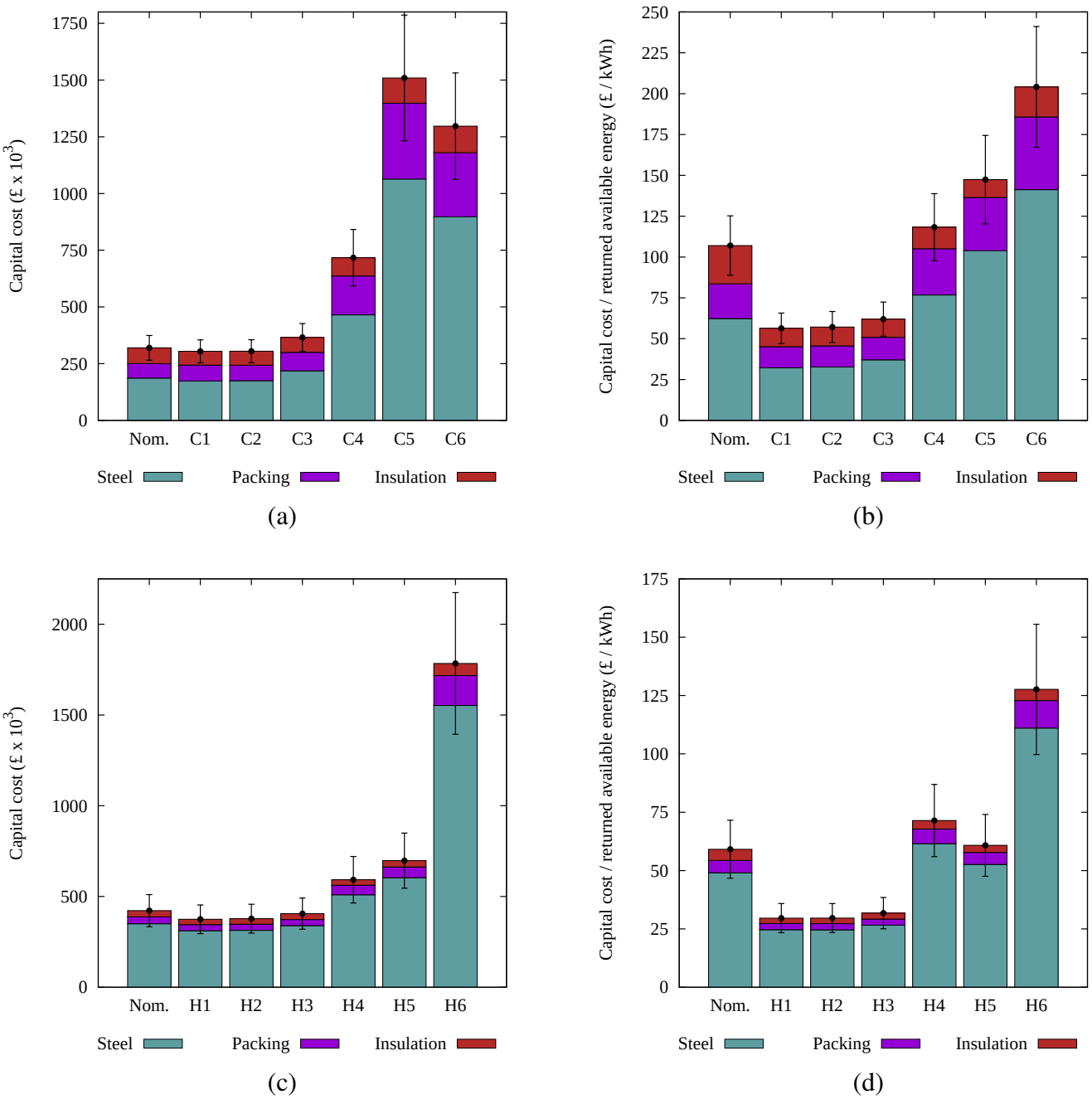

Figure 5.3: Distribution of capital costs in optimal cold and hot stores. Indicated points are shown on figure 5.2. **(a)** Capital costs (cold) **(b)** Capital costs normalised by the returned available energy (cold) **(c)** Capital costs (hot) **(d)** Capital costs normalised by the returned available energy (hot)

5.5 Optimisation of PTES systems

The optimisation method has been applied to several complete PTES systems. Optimisation is first carried out on the nominal PTES design described in section 5.5.1, before also considering systems with layered stores, and with lower values of reciprocating device polytropic efficiency. In addition, constraints on the highest temperature T_2 are relaxed so that systems more similar to the SAIPEM design can be considered. A PTES design that does not require an electric heater, as described in section 4.5, is also investigated.

Each optimisation study has the same decision variables, objective functions and constraints. The decision variables of interest are the aspect ratio L/D, particle diameter d_p, and number of segments N_{seg} of both reservoirs, as well as the charging and discharging pressure ratios β_{chg} and β_{dis}, the utilisation Π, and the discharged reservoir temperatures, T_1 and T_3. The nominal values, as well as upper and lower bounds are given in table 5.12. This table also illustrates the constraints that are placed on temperatures T_2 and T_4.

	L/D	d_p (mm)	N_{seg}	$\beta_{\text{chg,dis}}$	T_1 (°C)	T_2 (°C)	T_3 (°C)	T_4 (°C)	Π
Nominal	1.0	20.0	1	10.0	37.0	505.0	37.0	-150.0	0.75
Lower bound	0.5	2.0	1	5.0	37.0	$T_3 + 50$	37.0	-160.0	0.10
Upper bound	2.0	20.0	32	15.0	600.0	600.0	600.0	$T_1 - 50$	0.99

Table 5.12: Lower and upper bounds for parameters used in optimisation of PTES systems. For unsegmented stores $N_{\text{seg}} = 1$, and in all cases $\theta_l = 1\%$ and $\theta_h = 99\%$. Note that T_2 and T_4 are not decision variables, but are constrained as indicated.

The objective functions are the thermodynamic round-trip efficiency χ and the capital cost per unit net work during discharge $\hat{C}_E$. To recap, the thermodynamic efficiency does not include mechanical or electrical losses, and is given by the net work during discharge divided by the net work input during charge. There are a number of other metrics of interest and including:

- The charging duration Δt_{chg}
- The mass flow rate $\dot{m}$
- The work ratio R, defined as the ratio of compression to expansion work during charge. For simplicity, and to allow comparison with the use of the work ratio in section 1.5.2, the work ratio is calculated as $R = T_2/T_3$

- The average power output $\dot{W}_{\mathrm{ave}} = W_{\mathrm{dis}}^{\mathrm{net}}/\Delta t_{\mathrm{chg}}$
- The energy density $\rho_E = W_{\mathrm{dis}}^{\mathrm{net}}/(V_{\mathrm{CR}} + V_{\mathrm{HR}})$, where $V_{\mathrm{CR,HR}}$ are the volumes of packing material in the cold and hot reservoirs, respectively
- The average power density $\rho_P = \dot{W}_{\mathrm{dis}}/V_{\mathrm{cyl}}$ where V_{cyl} is the total volume of the largest compression–expansion device
- The capital cost per unit power $\hat{C}_P = C_{\mathrm{cap}}/\dot{W}_{\mathrm{ave}}$

Two previous optimisation studies of PTES systems have been undertaken by the author and are presented in [81, 84]. Ref. [84] was a thermodynamic optimisation with three objective functions: the round-trip efficiency, the energy density, and the power density. This initial study did not consider layered stores or include conductive losses, leakage losses or storage periods. This investigation found that there was no trade-off between power density and efficiency: designs that increased one objective would increase the other. A trade-off did occur between efficiency and energy density and the compromise between the two objectives was mainly controlled by the utilisation.

In Ref. [81] conduction, leakage, and storage losses were included, and segmented reservoirs were allowed. The objective functions were round-trip efficiency and capital cost per unit work output. The paper carried out three optimisations with different values of k_r to investigate what impact the economic factors may have on the optimal designs. It was found that while k_r significantly affected the capital cost, it had little influence over the designs that the optimisation routine converged on. This suggests that the PTES design may be robust to variations in component costs, and that these factors have little impact on the final design. Further sensitivity analysis is ideally required.

5.5.1 Optimisation of normal PTES configurations

The 'normal' PTES configuration is investigated in this section, and results are presented in figure 5.4. Data for several key points are tabulated in table 5.13 and loss distributions are shown in figure 5.6. The 'Normal' design configuration is that which has been discussed throughout this report and is based on the Isentropic Ltd. scheme. Details of the nominal design are given in tables 3.1 and 4.1. In this optimisation the number of segments N_{seg} is

a decision variable, but the temperatures at which segments are turned on and off are fixed to $\theta_l = 1\%$ and $\theta_h = 99\%$. PTES systems with unsegmented stores are also optimised for comparison. The impact of the compression-expression polytropic efficiency is investigated by optimising a system with $\eta = 90\%$ as well as the nominal value of $\eta = 98\%$.

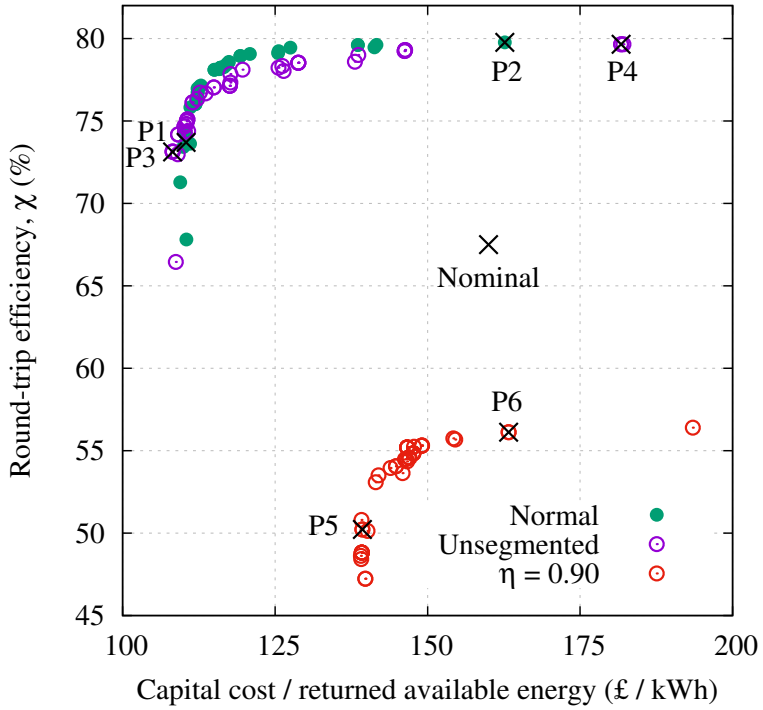

Figure 5.4: Pareto fronts of the optimised results of PTES systems with the basic configuration. 'Normal' refers to a system with the design variables shown in table 5.12; 'Unsegmented' has the same design variables although the thermal stores are constrained to have a single segment;'$\eta = 0.90$' indicates the polytropic efficiency that the compression–expansion system used.

		Nom.	P1	P2	P3	P4	P5	P6
Hot L/D		1.00	0.95	0.99	0.88	0.71	0.61	1.08
Hot d_p	(mm)	20.00	2.71	2.11	4.05	3.22	2.65	3.44
Hot N_{seg}		1	4	8	1	1	5	7
Cold L/D		7.00	0.53	0.51	0.51	0.51	0.50	0.52
Cold d_p	(mm)	20.00	4.39	3.16	4.80	4.83	4.80	4.05
Cold N_{seg}		1	14	29	1	1	10	3
β_{chg}		10.00	9.57	9.98	9.25	9.75	8.44	10.90
β_{dis}		10.00	7.28	9.89	7.73	9.20	5.95	6.97
Π		0.75	0.86	0.55	0.86	0.49	0.89	0.72
T_1	(°C)	37.0	77.4	72.9	84.3	75.7	70.1	35.0
T_2	(°C)	505.9	591.9	595.2	597.3	594.3	596.0	599.1
T_3	(°C)	37.0	37.6	35.4	39.9	36.3	35.3	36.2
T_4	(°C)	-145.1	-142.7	-145.6	-140.0	-144.1	-127.8	-140.0
$\dot{m}$	(kg/s)	13.7	11.5	11.3	11.5	11.4	10.6	9.9
R		2.51	2.78	2.81	2.78	2.80	2.82	2.82
$W_{\text{dis}}^{\text{net}}$	(MWh)	8.64	10.79	7.41	10.78	6.51	7.64	6.94
Δt_{chg}	(h)	6.01	6.88	4.42	6.92	3.88	7.15	5.77
$\dot{W}_{\text{ave}}$	(MW)	1.44	1.57	1.68	1.56	1.68	1.07	1.20
C_{cap}	(£$\times$ 1000)	1382	1191	1205	1166	1184	1065	1133
ρ_E	(kWh m^{-3})	43.78	62.26	41.28	65.44	39.38	48.24	46.94
ρ_P	(MW m^{-3})	2.94	3.76	4.10	3.71	4.08	2.85	3.31
$\hat{C}_{\text{P}}$	(£/ kW)	960	759	717	747	705	995	944
$\hat{C}_{\text{E}}$	(£/ kWh)	160	110	163	108	182	139	163
χ	(%)	67.48	73.70	79.77	73.12	79.65	50.22	56.12

Table 5.13: Design variables and results of PTES optimal points P1–P6 (see figure 5.4). Objective functions (efficiency and capital cost per work output) are shown in the final two rows..

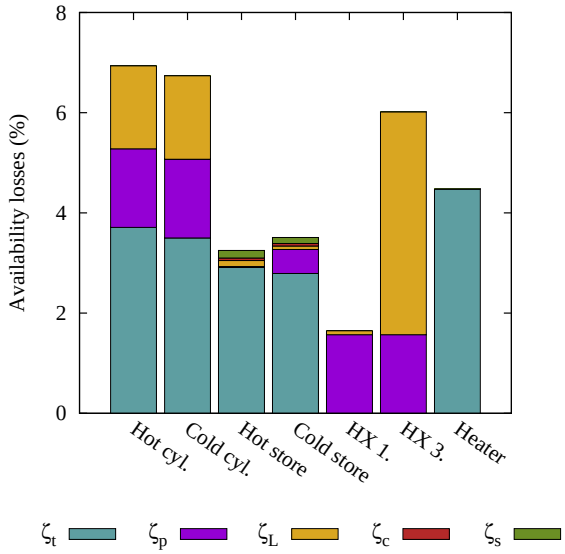

Figure 5.5: Distribution of availability losses in the nominal PTES design.

Optimal design characteristics

Comparing the optimal design results with the nominal design indicates that the improvement in round-trip efficiency is mainly due to a reduction in the packed bed losses, which cause a corresponding reduction in heat rejection. The reciprocating device losses do not change significantly which may be an artefact of the simplified modelling of the compression–expansion system. For instance, the polytropic efficiency is likely to be a function of the operating conditions which would cause greater variation in the reciprocating device losses.

Like the optimisation of the thermal stores, the cycle period (or utilisation Π) has the greatest influence over a design's position on the Pareto front. High utilisations correspond to low efficiencies but large work outputs and therefore low $\hat{C}_E$. The operating pressures and temperatures have a smaller impact and the cheapest designs typically have slightly lower pressure ratios and higher values of T_1. Lower pressure ratios reduce the cost of the compressor, expander and hot store. The higher value of T_1 then maintains T_2 at close to its maximum value of 600°C.

Operational parameters therefore have a significant influence, and this may have important consequences for off-design behaviour. For instance, the electrical grid may require PTES to operate flexibly, with irregular charge durations or power requirements. Further research into realistic load cycles is required to quantify this effect.

Benefits of segmented packed beds

For costs in the range of 115–150 £/kWh the calculations predict that segmentation increases the efficiency by around 1%. Moreover, segmented systems are able to achieve high efficiencies at lower costs than unsegmented systems. This may be illustrated by considering systems with an efficiency of 79% in which case segmented systems cost around 125 £/kWh and unsegmented systems cost around 140 £/kWh, saving 11%. (This margin will decrease once the cost for the valves and control systems required for segmentation have been included). Layering the stores typically leads to longer reservoirs and smaller particles, which is consistent with the packed bed optimisation results in section 5.4.

Influence of the polytropic efficiency

The round-trip efficiency is sensitive to the polytropic efficiency, with the results suggesting that reducing η from 0.98 to 0.90 reduces the maximum achievable efficiency from 79.8% to 56.1%. Reducing the polytropic efficiency increases the availability losses in the reciprocating devices from approximately 6% to 15%. In addition, heat exchanger losses increase (particularly during discharge). The optimal designs of the $\eta = 0.90$ case are reasonably similar to the segmented results. The main difference is that the discharging pressure ratios are typically lower in order to reduce heat rejection.

The capital costs are quite similar to those of the $\eta = 0.98$ designs, since the systems have similar designs. However, the capital cost per unit returned work is larger due to the low round-trip efficiency which reduces the work output. This effect is most significant for the lowest efficiency designs. For instance, the cheapest $\eta = 0.90$ design (P5) is approximately 21% more expensive than a cheap segmented design (P1).

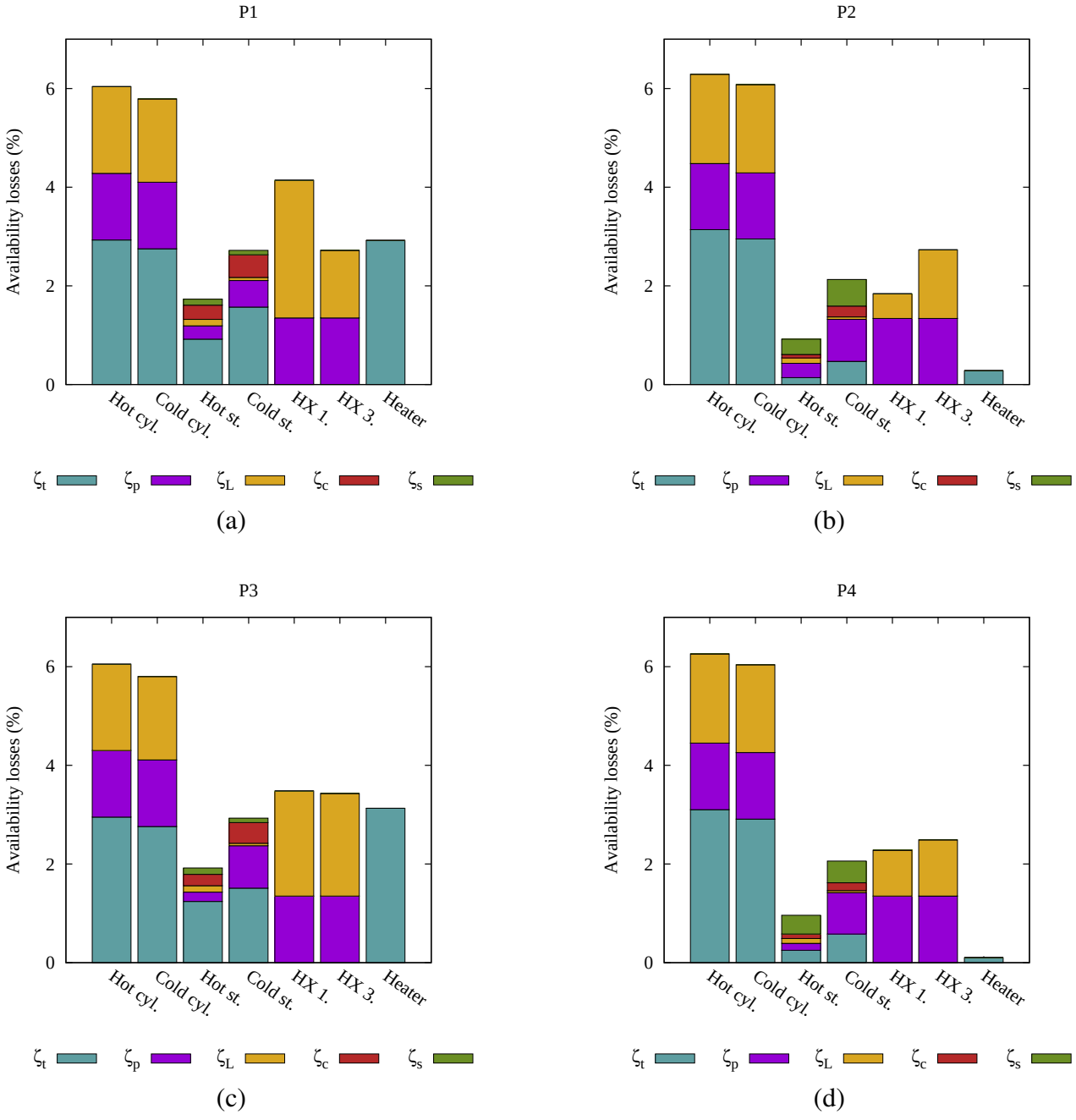

Figure 5.6: Distribution of availability losses in optimal PTES designs for points P1 – P4 which are illustrated on figure 5.4. The optimisation was carried out on a PTES system with the basic configuration. **(a)** P1 **(b)** P2 **(c)** P3 **(d)** P4

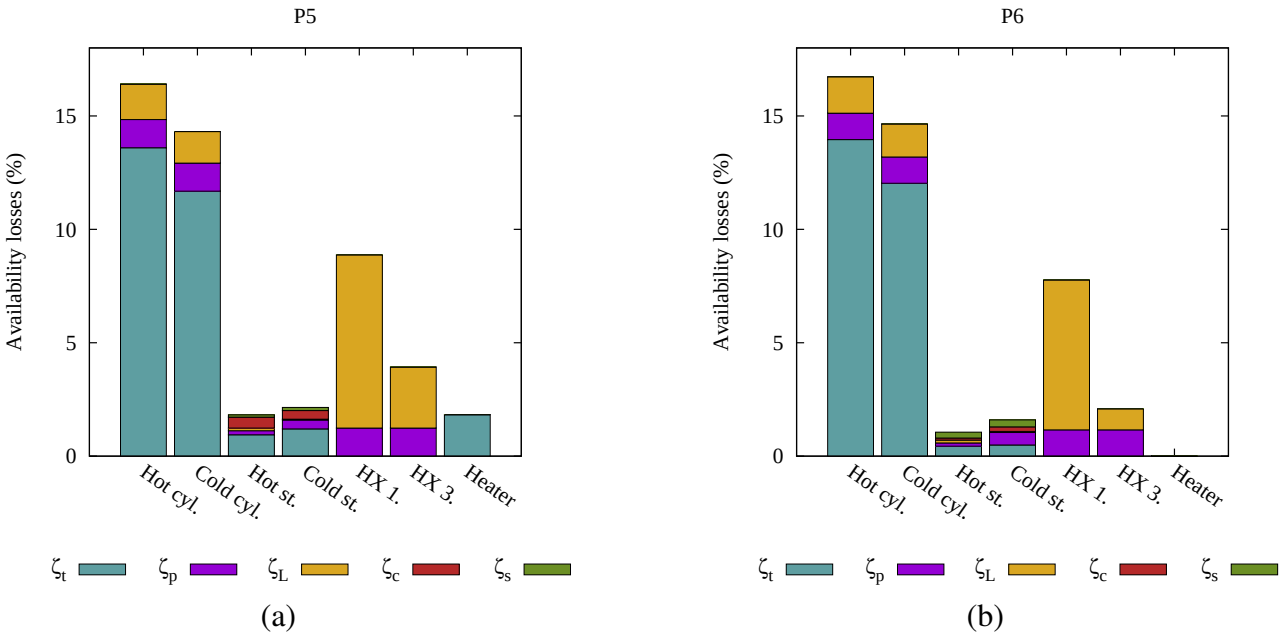

Figure 5.7: Distribution of availability losses in optimal PTES designs for points P5 and P6 which are illustrated on figure 5.4. This optimisation was carried out on a PTES system with the basic configuration, but with the compressor–expander polytropic efficiency set to $\eta = 0.90$. **(a)** P5 **(b)** P6

Economic considerations

Figure 5.8 illustrates the distribution of costs between each component for the points P1–P10. Reciprocating devices are generally around a quarter of the total cost per unit work output, while the reservoirs are around half. The hot store is more expensive than the cold store due to higher pressures. Hot cylinders are more expensive than the cold cylinders since they work at lower densities and thus have larger volumes.

Error bars are shown on the cost distributions and indicate the total cost plus or minus one standard deviation which is around $\pm$10–20% for most designs. The cheapest designs are approximately 100 £/kWh while the most efficient designs are around 175 £/kWh. The cost of additional components such as the electrical heater, pipes/valves, control systems or land costs is not included and it should be emphasised that these estimates are very approximate. However, these results do provide an indication of the minimum capital cost.

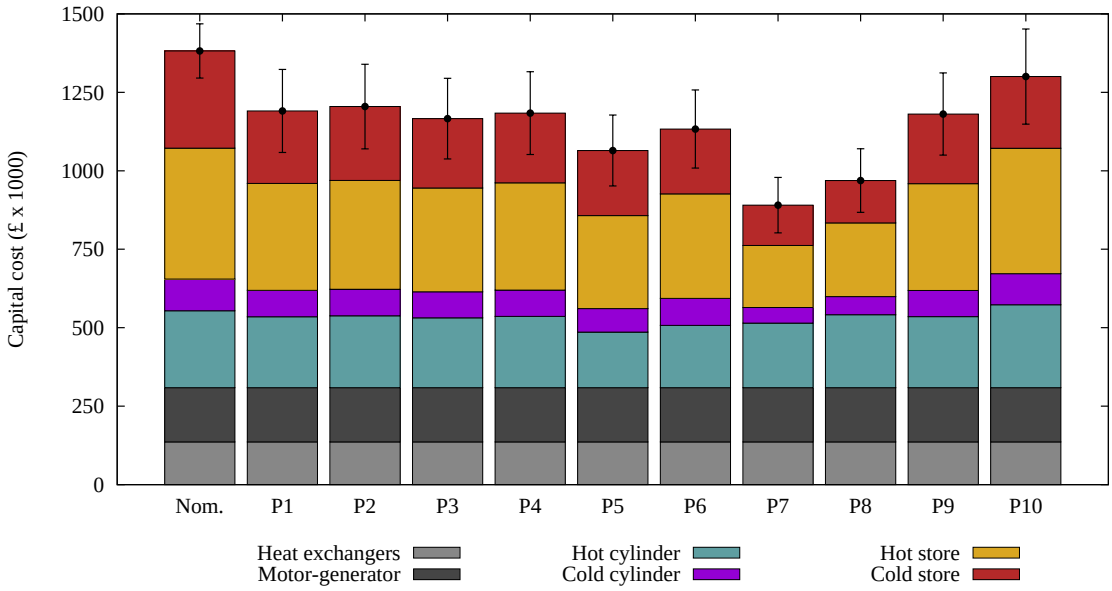

(a)

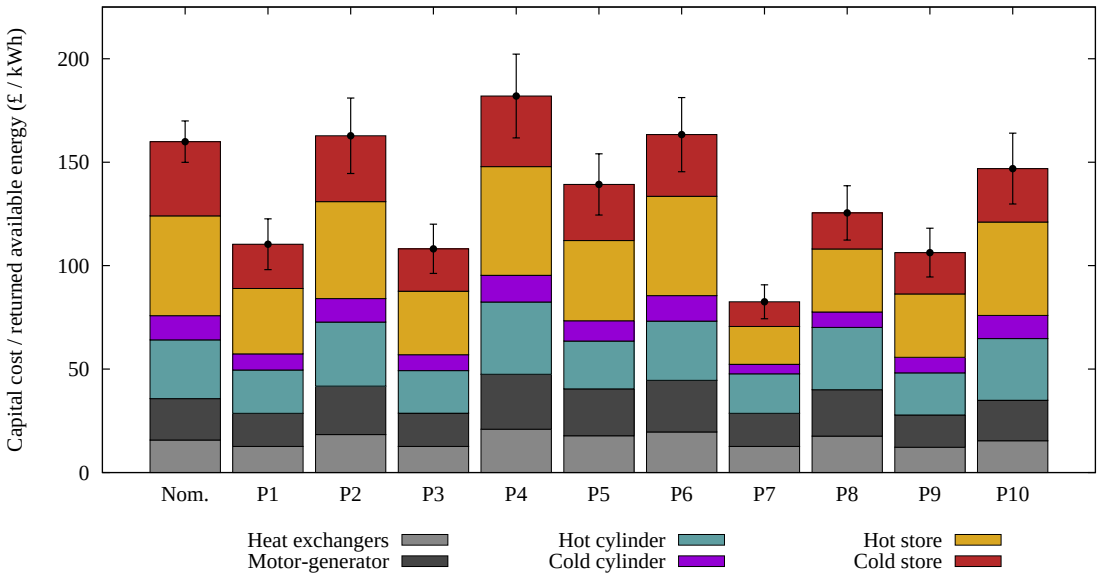

(b)

Figure 5.8: Distribution of capital costs amongst the system components for optimal PTES systems. **(a)** Capital costs **(b)** Capital costs normalised per unit returned available energy

5.5.2 Optimisation of alternative PTES configurations

Optimisations have been carried out on two alternative PTES configurations, and Pareto fronts are presented in figure 5.9. The first alternative relaxes the top temperature constraint, and T_2 can increase up to 1100°C. This option investigates systems similar to the Saipem design which uses a top temperature of $T_2 = 1200$°C, small pressure ratios of $\beta = 4$, and results in high work ratios (see section 1.5.3).

The second alternative design avoids electric heat addition as discussed in section 4.5 but is otherwise similar to the nominal design. The configuration that is optimised has a variable temperature T_1' which is greater than T_1. During charge, heat is continually rejected at the exit of the cold store between T_1' and T_1. As the cold thermal front emerges from the reservoir T_1' decreases, but does not drop below T_1. During discharge, the pressure ratio is varied and HX1 is bypassed to ensure that $T_1' > T_1$. A more detailed explanation is given in section 4.5.

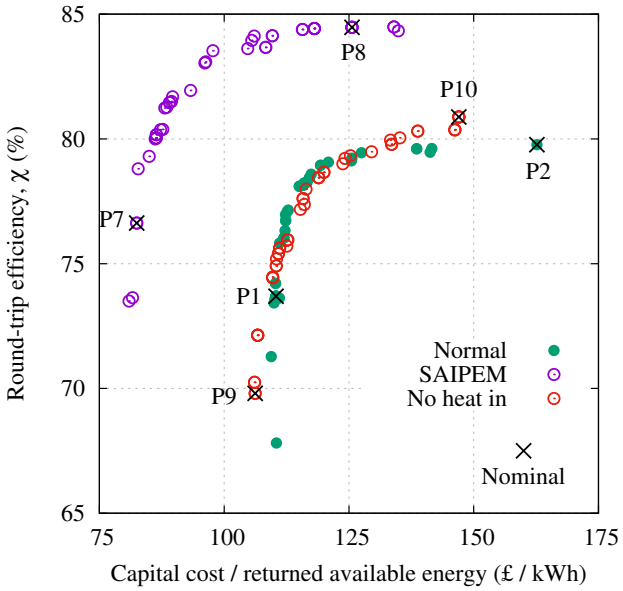

Figure 5.9: Pareto fronts of the optimised results of PTES systems with alternative configurations. 'Normal' refers to a system with the design variables shown in table 5.12; 'SAIPEM' is a scheme similar to that proposed by Desrues [91] and the constraint on top temperature is set to 1100°C rather than 600°C; 'No heat in' is a configuration that avoids heat addition as discussed in section 4.5.

		Nom.	P7	P8	P9	P10
Hot L/D		1.00	0.93	1.15	1.00	0.83
Hot d_p	(mm)	20.00	2.69	2.00	3.99	2.04
Hot N_{seg}		1	7	13	6	2
Cold L/D		7.00	0.53	0.53	0.52	0.51
Cold d_p	(mm)	20.00	2.48	2.53	2.69	4.23
Cold N_{seg}		1	24	29	3	1
β_{chg}		10.00	11.30	13.95	9.73	12.97
β_{dis}		10.00	10.49	13.93	7.07	9.26
Π		0.75	0.80	0.52	0.96	0.65
T_1	(°C)	37.0	241.9	189.2	77.3	36.3
T_2	(°C)	505.9	1085.1	1053.7	597.7	589.6
T_3	(°C)	37.0	42.7	43.3	36.1	37.6
T_4	(°C)	-145.1	-148.7	-158.2	-144.1	-157.0
$\dot{m}$	(kg/s)	13.7	5.9	5.8	11.3	10.7
R		2.51	4.30	4.19	2.82	2.78
$W_{\text{dis}}^{\text{net}}$	(MWh)	8.64	10.80	7.71	11.12	8.84
Δt_{chg}	(h)	6.01	6.69	4.35	7.64	5.22
$\dot{W}_{\text{ave}}$	(MW)	1.44	1.61	1.77	1.45	1.69
C_{cap}	(£$\times$ 1000)	1382	891	969	1181	1300
ρ_E	(kWh m^{-3})	43.78	130.47	91.15	67.70	54.11
ρ_P	(MW m^{-3})	2.94	7.24	7.77	3.56	4.16
$\hat{C}_{\text{P}}$	(£/ kW)	960	553	547	814	769
$\hat{C}_{\text{E}}$	(£/ kWh)	160	83	126	106	147
χ	(%)	67.48	76.63	84.47	69.80	80.88

Table 5.14: Design variables and results of PTES optimal points P7–P10 (see figure 5.9). Objective functions (efficiency and capital cost per work output) are shown in the final two rows.

Optimisation of the Saipem design

This optimisation converges on solutions which maximise the temperature T_2 to 1100°C. These designs have large values of T_1 ($\sim$200°C rather than 40°C) and larger pressure ratios (11–14 rather than 10) which is somewhat different to the original Saipem design of Ref. [90]. These differences increase the maximum efficiency from 79.8% to 84.5% as well as reducing the capital cost. For instance, higher temperatures lead to smaller thermal stores, which reduces the cost despite the increase in pressure, as can be seen on the cost distributions in figure 5.8. The cost reductions are significant: the most efficient Saipem design (P8) is roughly 30% cheaper than the most efficient segmented design (P2). At a

fixed efficiency of 80% the Saipem scheme is almost half the cost of a segmented system. However, this may be a result of the simplified economic models which are independent of temperature. The high temperatures are in fact likely to increase the component costs significantly.

The benefit of increasing T_2 as much as possible is clear but further work is required to determine the maximum operating temperatures for the storage media and other components, as well as the economic implications.

The distribution of availability losses (figure 5.10) reveals more information about how these designs achieve high efficiencies. The largest gains occur in the reciprocating devices. The analysis of PTES systems in section 1.5 suggested that the efficiency could be increased by maximising the work ratio $R = T_1/T_4 = T_2/T_3$ – i.e. maximising T_1 and T_2 and minimising T_3 and T_4. The optimal temperatures for the Saipem design achieve this: the work ratio of P8 is 4.2 compared to 2.8 for P2. As a result, each reciprocating device availability loss is around 4% for P8 compared to 6% for P2.

These optimal operational temperatures increase packed bed losses. Thermal losses in the hot store are slightly larger in P8 than P2 as a result of the increased temperature difference. The high temperatures also lead to large conductive and leakage losses, particularly during the storage phase. On the other hand, pressure losses decrease slightly due to reduced mass flow rates.

The benefit of avoiding heat addition

The optimal designs of normal PTES configurations have low levels of heat addition. For instance, heat addition losses in P2 are 0.28% suggesting there is limited scope to increase the efficiency by avoiding heat addition. However, the No Heat Addition Configuration (NHAC) achieves a higher maximum efficiency (80.9%) than the normal design (79.8%), and has comparable performance along the entire Pareto front, as shown in figure 5.9. The expression for $\hat{C}_E$ does not include the cost of the electric heater, meaning that the NHAC is slightly more attractive than the Pareto fronts would suggest. On the other hand, NHACs require a variable discharging pressure ratio e.g. $5.8 < \beta_{\text{dis}} < 9.9$ for P10 which may compromise off-design performance of the reciprocating devices. However, this may be

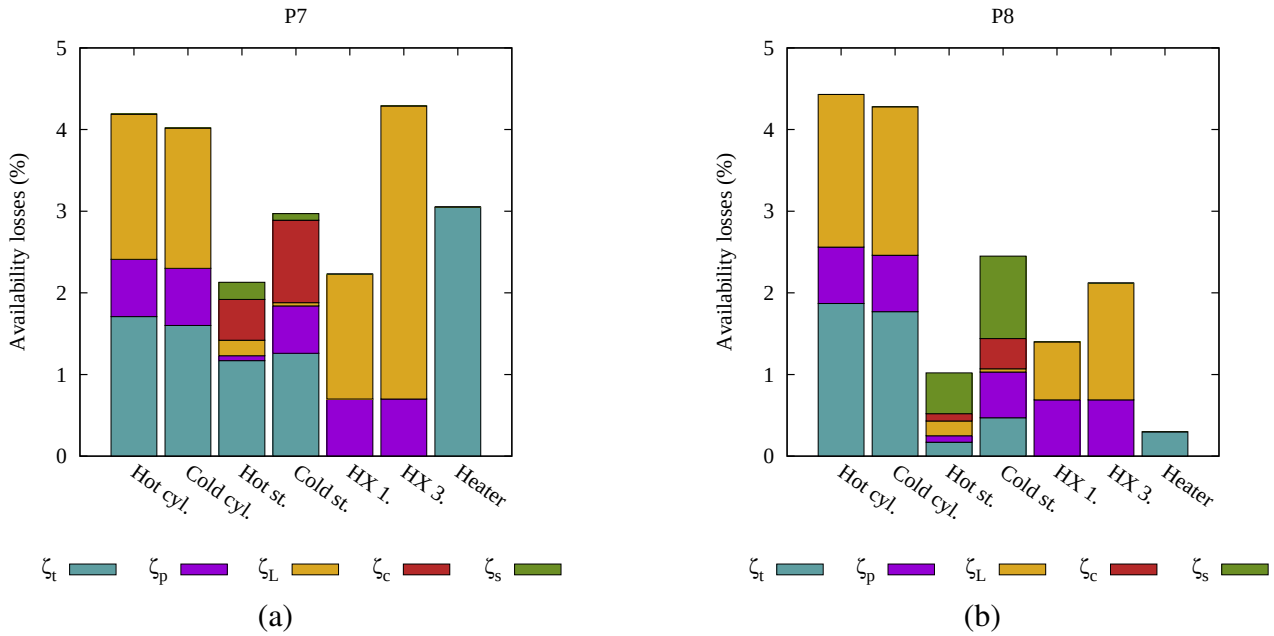

Figure 5.10: Distribution of availability losses in optimal PTES designs for points P7 and P8 which are illustrated on figure 5.9. This optimisation was carried out on a PTES system with the 'SAIPEM' configuration, in that temperature T_2 was constrained to 1100°C rather than 600°C. **(a)** P7 **(b)** P8

outweighed by better power variation.

Availability losses in the cold store of design P9 are large compared to other optimal designs. Section 4.5 described how irregularly shaped thermal fronts were formed in the cold reservoir of the NHAC, as illustrated in figure 4.27. When the cold store is not segmented, the irregular section of the front is contained in the top of the store - i.e. at the 'warm' end. However, point P9 has three segments, and as segments at the 'warm' end are deactivated during discharge irregular front shapes penetrate further towards the 'cold' end and take up a larger proportion of the reservoir. Consequently, thermal and conductive losses are significantly higher than comparative designs such as P1. The cold store in the most efficient NHAC design P10 has only one segment and avoids these high losses.

These optimisation results indicate that the NHAC could achieve high efficiencies without the expense of segmenting the cold packed bed or installing an electric heater. Further work is necessary to quantify the magnitude of this saving and to investigate the off-design behaviour of the reciprocating devices.

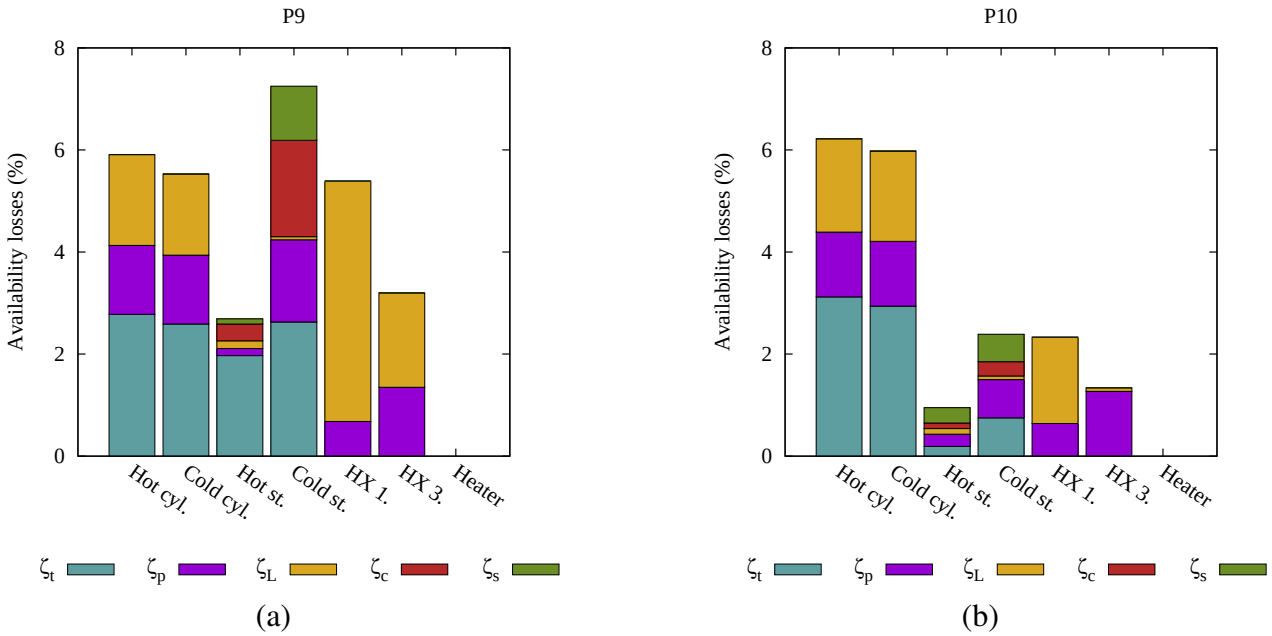

Figure 5.11: Distribution of availability losses in optimal PTES designs for points P9 and P10 which are illustrated on figure 5.9. This optimisation was carried out on a PTES system where heat addition was avoided as described in section 4.5. **(a)** P9 **(b)** P10

5.6 Summary

In this chapter, optimisation studies were carried out on the thermal energy storage systems that have been described throughout this thesis: packed-bed thermal reservoirs and Pumped Thermal Energy Storage. The optimisations considered technical and economic metrics separately. This chapter began by describing a number of economic metrics and their application to energy storage systems. A simple model of capital cost was developed for packed beds and PTES systems and was found to be quite uncertain. As a result, it is most appropriate to use the capital cost to compare different designs. This provides an insight into which designs may be the most economically feasible, but does not provide a reliable indication of how feasible the system is.

Multi-objective optimisation is a useful tool for identifying promising designs and it allows the full trade-off between optimal designs to be examined. However, due to uncertainties in the thermodynamic and economic modelling quantitative results should be viewed

cautiously.

Multi-objective optimisation was first applied to hot and cold packed-bed thermal reservoirs. The observed behaviour was consistent with the parametric studies of chapter 3. The cycle period was the main factor that controlled the trade-off between efficiency and energy density. Segmented thermal stores were found to outperform unsegmented stores, particularly in cold packed beds. Radial-flow packed beds had a similar performance to axial-flow stores but were typically more expensive due to larger volume requirements.

PTES systems were optimised in section 5.5 by maximising efficiency and minimising the capital cost per work output. Again, the cycle frequency was found to be the main parameter that controlled the trade off between efficiency and cost. By segmenting the thermal stores, the round-trip efficiency could be increased by around 1%. PTES performance was very sensitive to the polytropic efficiency of the reciprocating devices: reducing η by 8% led to a 23% drop in round-trip efficiency. Further research on reciprocating devices is required in order to analyse and maximise their performance. If these devices can be designed to achieve high polytropic efficiencies, then the optimisation suggested that thermodynamic round-trip efficiencies of around 80% may be achievable. Including mechanical and electrical efficiencies of 80% [84], suggests that PTES systems could achieve efficiencies of up to 64%.

Two variants on the standard PTES design were optimised. A Saipem-like scheme where the maximum hot store charging temperature was increased to 1100°C reached round-trip efficiencies of up to 85%. The optimisation results therefore suggest that there is a significant benefit to this type of design. However, further work is required to establish the impact of high temperatures on the components, as well as including temperature dependence in the economic models. An alternative configuration which avoided heat addition was also optimised and achieved efficiencies of up to 81%. This configuration has the benefit of not requiring an electric heater to be installed, although it does require flexible operation of the reciprocating devices. Further research is require to determine how off-design performance of the compressors and expanders may affect the PTES performance.

Chapter 6

Conclusions and future work

Energy storage solutions

Chapter 1 introduced energy storage technologies and described how they could be used to improve the electrical grid and the integration of greater proportions of renewables. This project set out to investigate a novel energy storage system known as Pumped Thermal Energy Storage (PTES). The ultimate objective of the project was to develop a detailed thermo-economic model of the PTES system, and to use optimisation techniques to determine the best designs.

Modelling of thermal stores

PTES systems are comprised of a number of components, the most important of which are the thermal stores and the compression-expansion system. Chapter 2 concentrated on the thermodynamic modelling of the packed-bed thermal stores. Heat transfer processes were described in detail, and a one-dimensional system of energy equations was developed. An efficient numerical scheme was described, and it was verified against the analytical solution of the equations and against a less efficient numerical scheme.

The packed-bed thermodynamic model captured the most influential heat transfer processes and provided the necessary starting point to investigate their behaviour. However, future work could relax some of the assumptions. For instance, the stores could be modelled using two-dimensional energy equations which would allow the impact of radial variations in temperature and velocity to be studied. In particular, the packing density of particles decreases near the walls, creating by-pass flows due to the reduced frictional resistance. It would be interesting to study the influence of this on the behaviour of the store, particularly with regard to heat leakage losses.

Improvements to thermal store modelling by CFD and experiments

More detailed studies of packed beds could be performed using Computational Fluid Dynamics (CFD) analysis. CFD has been used to study packed beds, such as in [215, 216] which presented analysis of the flow distributions and heat transfer coefficient. Extending this work to consider second-law factors would provide a more detailed understanding of

the loss coefficients. The model described in chapter 2 assumed that heat transfer characteristics are represented by an average equivalent diameter. It may be possible to use CFD to investigate particles that are non-spherical, have a range of shapes and sizes and are not uniformly distributed.

Experimental studies of packed beds would also be a beneficial area for further research. Experimental studies could provide data to validate the existing numerical models (or CFD schemes). In particular, values of the effective conductivity and heat transfer coefficient are quite uncertain, and experiments could provide correlations or estimates that are specific to the applications of interest. Furthermore, experiments could be used to investigate thermal store behaviour from a more practical perspective.

Investigations have concentrated on the thermodynamics of the problem. However, further work is required to establish the mechanical properties of storage material. For instance, it is necessary to understand the conditions under which particles may be crushed, fuse together, or otherwise be damaged.

Improvements to packed bed understanding and design

The thermodynamic model developed in chapter 2 provided a way of rapidly studying a wide range of packed bed behaviour. A detailed account was provided in chapter 3 which illustrated the impact of a number of design variables on the performance of the store. Studying the packed beds from a second-law perspective with the use of loss coefficients revealed areas where the thermal store behaviour could be improved. These investigations resulted in a set of design guidelines for packed beds which include:

- Hot stores should have higher aspect ratios and lower particle diameters than cold stores due to lower pressure losses.
- Larger volumes reduce heat leakage and lead to lower optimal aspect ratios.
- The charging period is the main factor that controls the trade off between efficiency and energy density, with low utilisations providing the highest efficiency.
- The efficiency can be increased by increasing the charging temperature of the hot store and decreasing that of the cold store.

- The energy density can be maximised by increasing the difference between charging and discharging temperature, although this reduces the efficiency.
- Using a packing material with a low fractional change in specific heat capacity reduces the thermal losses.

As a result of these investigations, two innovative design solutions were investigated in more detail. In section 3.3, segmentation of the packed beds was introduced. It was found that segmentation reduced pressure losses. As a result, smaller particles could be used and led to the formation of steeper thermal fronts which increases the efficiency and the energy density. Further work on layered stores should concentrate on the heat transfer that occurs between successive segments. In addition, it would be beneficial to understand in more detail the process by which the segments are switched on or off and the impact of gas travelling where it is not intended to (for instance, through inactive segments). Furthermore, understanding the space requirements of the control system would improve estimates of the energy density of segmented stores.

The second innovative design feature that was investigated was radial-flow packed beds. The thermodynamic model was designed to be comparable to the axial-flow packed bed model. Comparison of dimensionally similar radial-flow and axial-flow packed beds indicated that radial-flow packed beds typically had lower pressure losses. However, these stores also had steeper thermal fronts which led to larger thermal and conductive losses. Further work could investigate whether decreasing the particle size along the radius of the bed would improve performance, as suggested by [158].

Modelling of reciprocating devices

Having established the fundamental characteristics of packed-bed thermal reservoirs, a thermodynamic model of the PTES system was developed in chapter 4. Simplified models of the reciprocating compressors and expanders were first developed. Performance was characterised in terms of average loss factors: pressure loss factors, heat leakage factors, and polytropic efficiencies, and the likely magnitude of these factors was investigated. Further work is required to model reciprocating devices in comparable detail to the packed beds. Currently, experimental work is being carried out at Imperial College, London, and

CFD analysis is being undertaken at Cambridge University. This work is focussing on gas springs, which are similar to reciprocating compressors except that there is no through flow of gas. The CFD analysis at Cambridge has modelled gas springs with a baffle near top dead centre in order to represent the valves and the associated pressure loss. This work provides the necessary background for developing models of reciprocating devices.

Understanding PTES behaviour

In chapter 4 the influence of a number of design variables on PTES behaviour was investigated using parametric studies. This provided an understanding of the importance of certain variables, and how they may affect the optimum design. These investigations add to the packed bed design guidelines. In particular, the cycle period was found to control the trade-off between efficiency and energy density. The polytropic efficiency also had a significant impact on the round-trip efficiency as a result of there being four compression or expansion processes. The round-trip efficiency can be improved by increasing the charging pressure ratio and the temperature T_1 and by reducing temperature T_3. The discharging pressure ratio controlled the distribution of heat rejection between the two heat exchangers.

Avoiding the electric heater

The nominal design required a heat input due to the behaviour of thermal fronts in the packed beds, which is costly and inefficient. Several configurations that avoided the heater were investigated in section 4.5. An effective method involved varying the discharging pressure ratio, and bypassing HX1 during discharge. As a result, during charge gas always leaves the cold store at a temperature greater than the design temperature T_1, so that heat is rejected rather than added. The potential success of this scheme depends on the off-design performance of the reciprocating devices and emphasises the need for further research in this area.

Other methods for avoiding heat addition were discussed. For instance, recuperation or the use of liquid stores also provide promising alternatives. Liquid store PTES is currently being investigated at Cambridge University, and results have so far indicated the need for high heat exchanger effectiveness, and the importance of the temperature limits of the liquid

storage media. Another avenue for further research is to consider the integration of PTES into other industrial systems. Waste heat from industrial applications could be used as a heat input to the PTES system. Furthermore, the heat that is rejected by PTES could be used in waste heat applications such as domestic heating. Such arrangements may place additional constraints or requirements upon the system, and future work could investigate the impact and potential benefits.

Irregular load cycles

Once a PTES system is integrated into the electrical grid it may not necessarily charge and discharge with regular periods, as has been assumed in this report. Chapter 4 emphasised the importance of the cycle period on the round-trip efficiency, and the load cycle is likely to be equally influential. Furthermore, PTES performance depends on the historical operation: previous load cycles will affect the thermal front shape and thereby impact on future performance.

Load cycles may be affected by a number of factors such as instantaneous electricity demand and generation, the position of the storage on the grid, and the current state of charge of the storage (and of other storage systems). Network analysis tools have been developed by other research groups in order to analyse the behaviour of storage on the grid. These models typically assume very simple characteristics and efficiency and 'self-discharge' typically have fixed values. This project has shown that PTES efficiency depends on many factors, such as the state of charge, the position and shape of the thermal fronts, the power input or output to the system, and historical operation.

There are several options for future research on the impact on load cycles. For instance, research could focus on the influence of irregular load cycles on PTES behaviour. The existing model could be executed using a large number of typical load cycles. This would provide information about how a given load input may affect future performance. Alternatively, the storage characteristics in network analysis models could be improved by integrating the PTES model. This would suggest how PTES would behave in the electrical grid and how it may best be operated. Furthermore, a range of scenarios could be investigated, with different types of generation, or different objectives.

Such investigations have been initiated in a collaboration between Durham University and Cambridge University. It was found that integrating the PTES model and network analysis model was not straightforward. For instance, the network analysis tool solved a set of linear equations in a dedicated software package, whereas the PTES model is coded in Fortran and solves a set of differential equations. One option that is being investigated is to reduce the complexity of the PTES model by representing its behaviour with regression equations which could be generated from the existing model and should capture the main behaviour. However, whether these equations are able to represent the complexity of the thermal fronts and the dependency on historical behaviour remains to be seen.

Application of thermo-economic optimisation techniques

Having developed a model of the PTES system and investigated its behaviour, chapter 5 undertook thermo-economic optimisation of a number of systems that had been introduced throughout this thesis. Since the 'best' design may not be the one with the best technical characteristics, it is important to consider other objectives such as the cost. Thermo-economic optimisation was therefore an suitable method to study a range of optimal designs.

Chapter 5 described several economic metrics and their application to energy storage technologies. It was recognised that economic metrics could be uncertain and difficult to quantify. Of the available economic metrics capital cost was the most straightforward and least uncertain to model and a simplified economic model of the PTES capital cost was developed. The objective was to keep the model relatively simple whilst capturing the key parameters that would impact the economic cost. Despite this, the absolute values of PTES capital cost are likely to be inaccurate and it was most appropriate to use the capital cost as a metric to compare different PTES designs.

Optimisation of packed-bed thermal reservoirs

Multi-objective optimisation was first applied to hot and cold packed-bed thermal reservoirs. A thermo-economic optimisation of the efficiency and energy density provided an insight into optimal packed bed designs. The observed behaviour was consistent with the

parametric studies of chapter 3. Segmented thermal stores were found to outperform unsegmented stores, particularly in cold packed beds. Radial-flow packed beds had a similar performance to axial-flow stores but were typically more expensive due to larger volume requirements. Further research into radial-flow stores should investigate the volume requirements of the inner and outer plena, as these empty spaces are the main factor that increases the cost.

Optimisation of PTES

PTES systems were optimised in section 5.5 by maximising efficiency and minimising the capital cost per work output. Cycle frequency was found to be the main parameter that controlled the trade-off between efficiency and cost. By segmenting the thermal stores, the round-trip efficiency could be increased by around 1%. PTES performance was very sensitive to the polytropic efficiency of the reciprocating devices: reducing the polytropic efficiency by 8% led to a 23% drop in round-trip efficiency. If the reciprocating devices can be designed to achieve high polytropic efficiencies, then the optimisation suggested that it may be possible to achieve thermodynamic round-trip efficiencies of around 80%. Including mechanical and electrical losses, which may have an efficiency of 80% [84], suggests that PTES systems could achieve efficiencies of up to 64%. However, if a less optimistic polytropic efficiency of 90% was used for the compressor and expander, PTES had a maximum thermodyanmic round-trip efficiency of 56% - corresponding to an electricity-to-electricity round-trip efficiency of 45%.

Two variants on the standard PTES design were optimised. A Saipem-like scheme where the maximum hot store charging temperature was increased to 1100°C reached round-trip efficiencies of up to 85%. However, further work should determine the maximum operating temperatures of the components and how this may affect the cost. An alternative configuration which avoided heat addition was also optimised and achieved efficiencies of up to 81%. This configuration has the benefit of not requiring an electric heater to be installed, although it does require flexible operation of the reciprocating devices.

Improving economic models

Improved estimates of capital cost could be made by collaboration with an energy economist or commercial partner. In addition, more complex economic models that incorporate a range of revenue streams could be developed. This type of investigation could feasibly occur as part of a network analysis model. However, comprehensive sensitivity analysis is required in order to quantify the uncertainty of the results.

Improving thermo-economic optimisation techniques

Thermo-economic optimisation has shown itself to be a useful tool to compare different systems, whether they are packed beds or the PTES scheme. As a result, further research could compare different energy storage types using this methodology. It would be important to develop comparable technical and economic models in order to provide useful information.

One limitation of the optimisation algorithm was that it was time consuming to obtain results. For instance, the optimum designs typically had small particle diameters which required the model to take very small grid- and time-steps. The model was executed several hundred or even thousand times before the results converged. As a result, it may be beneficial to investigate alternative optimisation routines or approaches. A promising option is known as 'multi-fidelity' optimisation. In this approach, a number of models of the system exist, with varying degrees of complexity. Undertaking the optimisation on the simplest model would quickly provide information about regions where the optimal solutions may exist. The search space is then constrained to this region and a more complex (higher fidelity) model is optimised. For this approach to be successful, the low fidelity models need to be able to capture the main characteristics of the problem. Low fidelity models could be obtained either from simplified analysis such as that in section 1.5 or by developing regression equations.

Main conclusions:

1. Energy storage (along with interconnection and demand-side response) will have an integral role in future energy systems. Storage provides value in a number of ways, such as through arbitrage, easing grid congestion or upgrade deferrals. However, current regulations and uncertainty about future electricity markets has prevented investment.

2. Thermodynamic models of packed-bed thermal stores have been developed and have provided a set of design guidelines, which are summarised on page 230.

3. Optimisation studies suggest that packed-bed thermal reservoirs can effectively store thermal energy. Hot stores can achieve round-trip efficiencies of 99.6% and energy densities of 190 kWh m^{-3}. Cold stores can achieve round-trip efficiencies of 96.5% and energy densities of 38 kWh m^{-3}. However, there is some uncertainty to these values and experimental studies are required.

4. A number of variants of a storage scheme known as Pumped Thermal Energy Storage (PTES) exist. The behaviour of a variant based on the Joule cycle which employs packed-bed thermal reservoirs has been investigated and design guidelines developed, as summarised on page 232.

5. Under the assumptions made thermo-economic optimisation suggested that PTES could achieve thermodynamic round-trip efficiencies of up to 79.8%. Once mechanical and electrical inefficiencies are included the efficiency is 64%.

6. The PTES system is very sensitive to the polytropic efficiency of the compressors and expanders. A 1% decrease in polytropic efficiency reduces the thermodynamic round-trip efficiency by 2%.

7. Several innovative design features were investigated and found that:

   (a) Segmentation of the packed beds could improve the performance of the thermal stores by reducing pressure losses and enabling smaller particles to be used. When included in PTES systems, segmentation increased the round-trip efficiency by 1% at a fixed cost, or could reduce costs by 10% at fixed efficiency.

(b) Radial-flow packed beds were effective energy stores and are comparable to axial flow stores. The mass flow rate decreases with radius, leading to lower pressure losses. However, radial flow stores are expensive due to large volume requirements.

(c) Heat addition to PTES systems can be avoided by controlling the discharging pressure ratio and the thermal front in the cold store. This removes the need for an electric heater, but requires flexible operation of the compressors and expanders.

Promising areas for future research:

1. Detailed modelling (including CFD) and experimental investigations on the thermal stores
2. Modelling of the reciprocating devices, particularly off-design behaviour
3. Investigations into the impact of realistic load cycles on PTES behaviour and its integration into electrical networks
4. More reliable modelling and sensitivity analysis of PTES economics.

Nomenclature

Abbreviations

CAES	Compressed Air Energy Storage
CE	Reversible compressor/expander (hot cylinders)
EC	Reversible expander/compressor (cold cylinders)
HS, CS	Hot/cold store
HX	Heat exchanger
MOGA	Multi-objective Genetic Algorithm
PCM	Phase Change Materials
PHES	Pumped Hydroelectric Energy Storage
PTES	Pumped Thermal Energy Storage
TES	Thermal Energy Storage

Greek symbols

α	Packed bed diffusivity, see equation 2.21 (m^2 / s)
β	Compression or expansion pressure ratio
β	Non-dimensional availability
β	Packed bed heat leakage time constant (s^{-1})
Γ	Dimensionless packed bed charge period, t_c/τ
γ	Ratio of specific heat capacities
Δ	A difference
δ	An infinitesimal difference
ϵ	Heat exchanger effectiveness
ε	Clearance (dead) volume ratio of reciprocating devices, see equation 4.19
ε	Emissivity
ε	Packed bed void fraction
ζ	Loss coefficient, see section 2.5 (%)
η	Non-dimensional time in the Schumann equations, see equation 2.27
η	Polytropic efficiency of reciprocating devices
η_s	Isentropic efficiency of reciprocating devices
η_v	Reciprocating device volumetric efficiency
θ	Dimensionless temperature
Λ	Dimensionless packed bed length L/ℓ
λ	Thermal front length (m)

ν	Kinematic viscosity (m^2 / s)
$\nu_{c,d}$	Compression or expansion heat leakage factor, see section 4.2
ξ	Non-dimensional length in the Schumann equations, see equation 2.27
ξ	Specific exergy (J / kg)
$\phi_{c,d}$	Compression or expansion polytropic exponent, see section 4.2
Π	Dimensionless cycle period (or utilisation) $\Pi = t_c/t_N = \Gamma/\Lambda$
ρ	Density (kg / m^3)
ρ_E	Energy density (kWh / m^3)
ρ_P	Power density (kW / m^3)
σ	Stefan-Boltzmann constant (W / m^2·K^4)
τ	Compression or expansion temperature ratio
τ	Packed bed time scale, see equation 2.20 (s)
τ_L	Heat leakage time constant, see section 2.5.4 (s)
χ	Round-trip efficiency (%)
ω	Reciprocating device angular velocity (rad / s)

Roman symbols

A	Packed bed area (m^2)
B	Availability (J)
b	Specific availability (J / kg)
Bi	Biot number
$\mathcal{C}$	Unsteady gas terms, see equation 2.23 (K / m)
C	Capital cost (£)
c	Specific heat capacity (J / kg·K)
$\hat{C}_E$	Capital cost per work output (£/kWh)
C_f	Friction coefficient, see equation 2.54
$\hat{C}_P$	Capital cost per power output (£/kW)
D	Diameter of the packed bed (m)
d_p	Particle diameter (m)
e	Specific internal energy (J / kg)
$\Delta E_{\max}$	Maximum energy capacity of a packed bed or PTES system (MW h)
F	View factor
f_p	Pressure loss factor, see section 4.2

G	Mass flow rate per unit area (kg / m^2·s)
g	Acceleration due to gravity (m / s^2)
Gr	Grashoff number
h	Heat transfer coefficient (W / m^2·K)
h	Specific enthalpy (J / kg)
k	Conductivity (W / m·K)
k	Cost factors, see section 5.2.2
k_{eff}	Effective conductivity of the packed bed (W / m·K)
ℓ	Packed bed length scale, see equation 2.19 (m)
L	Length of the packed bed (m)
$\dot{m}$	Mass flow rate (kg / s)
M	Mass (kg)
N_{cyl}	Number of cylinders in the reciprocating devices
N_{seg}	Number of segments in a packed bed
Nu	Nusselt number
p	Pressure (bar)
Pr	Prandtl number
Q	Heat transfer (J)
R	Specific gas constant (J / kg·K)
R	Work ratio = $T_1/T_4 = T_2/T_3$
r	Radius of the packed bed (m)
Re	Reynolds number
$r_{i,o}$	Inner or outer radius in radial-flow stores (m)
r_v	Reciprocating device volumetric compression ratio
s	Specific entropy (J/ kg·K)
$\dot{S}_{\mathrm{irr}}$	Rate of irreversible entropy generation (W / K)
St	Stanton number $\mathrm{St} = h/Gc_p$
S_v	Particle surface-area-to-volume ratio, $S_v = 6/d_p$, (m^{-1})
T	Temperature (K)
t	Thickness (m)
t	Time (s)
t_{chg}	Charging duration (s)

t_N	Nominal charging time of the packed bed, see equation 2.5 (s)
U	Overall heat transfer coefficient (W / m^2·K)
u	Gas velocity (m /s)
u_i	Interstitial gas velocity = u_s/ε (m /s)
u_s	Superficial gas velocity = $\dot{m}/\rho_g A$ (m /s)
V	Volume (m^3)
V_f	Velocity of the thermal front, see equation 2.3 (m / s)
V_s	Reciprocating device swept volume
W	Work (J)
$\dot{W}_{\max}$	Maximum power capacity of a PTES system (MW)

Subscripts

0	Ambient conditions
chg, dis	Charging, discharging conditions
c	Availability losses due to conduction
c, e	Compression, expansion
c, h	Cold, hot reservoir
L	Availability losses due to heat leakage
p	Availability losses due to pressure drops
s, g	Solid, gas
t	Availability losses due to convective heat transfer
x	Availability losses or temperatures due to exit flow from a packed bed
1, 2	Charging, discharging conditions

Bibliography

[1] G. Strbac, M. Aunedi, D. Pudjianto, P. Djapic, F. Teng, A. Sturt, D. Jackravut, R. Sansom, V. Yufit, and N. Brandon, "Strategic Assessment of the Role and Value of Energy Storage Systems in the UK Low Carbon Energy Future Report for," *Carbon Trust*, no. June, pp. 1–99, 2012.

[2] G. Zanganeh, A. Pedretti, S. Zavattoni, M. Barbato, and A. Steinfeld, "Packed-bed thermal storage for concentrated solar power - Pilot-scale demonstration and industrial-scale design," *Solar Energy*, vol. 86, pp. 3084–3098, Oct. 2012.

[3] R. Anderson, L. Bates, E. Johnson, and J. F. Morris, "Packed bed thermal energy storage: A simplified experimentally validated model," *Journal of Energy Storage*, vol. 4, pp. 14–23, 2015.

[4] W. van Antwerpen, C. G. du Toit, and P. G. Rousseau, "A review of correlations to model the packing structure and effective conductivity in packed beds of mono-sized spherical particles," *Nuclear Engineering and Design*, vol. 240, pp. 1803–1818, 2010.

[5] J. Howes, "Concept and Development of a Pumped Heat Electricity Storage Device," *Proceedings of the IEEE*, vol. 100, pp. 493–503, Feb. 2012.

[6] A. Kornhauser and J. Smith Jr., "Effects of heat transfer on gas spring performance," *Journal of Energy Resources Technology, Transactions of the ASME*, vol. 115, no. 1, pp. 70–75, 1993. cited By 0.

[7] K. Lee, "A simplistic model of cyclic heat transfer phenomena in closed spaces," *Proceedings of the intersociety energy conversation engineering conference, US*, vol. 2, 1983.

[8] B. Lawton, "Effect of compression and expansion on instantaneous heat transfer in reciprocating internal combustion engines," *Proceedings of the Institution of Mechanical Engineers, Part A: Journal of Power and Process Engineering*, vol. 201, no. 3, pp. 175–186, 1987.

[9] P. Tans and R. Keeling, "Trends in Atmospheric CO2 at Mauna Loa, Hawaii (Earth System Research Labatory, National Oceanic and Atmospheric Administration and

Scripps Institution of Oceanography, La Jolla, California, 2013)," Available at http://www.esrl.noaa.gov/gmd/ccgg/trends/.

[10] S. Solomon, *Climate Change 2007: The Physical Science Basis*. Working Group I Contribution to the 4th Assessment Report of the Intergovernmental Panel on Climate Change, 2007.

[11] The Royal Society, *Climate change: a summary of the science*, 2010.

[12] N. C. Stenseth, A. Mysterud, G. Ottersen, J. W. Hurrell, K.-S. Chan, and M. Lima, "Ecological effects of climate fluctuations," *Science (New York, N.Y.)*, vol. 297, pp. 1292–6, Aug. 2002.

[13] T. Wheeler and J. von Braun, "Climate change impacts on global food security," *Science (New York, N.Y.)*, vol. 341, pp. 508–13, Aug. 2013.

[14] T. Oki and S. Kanae, "Global Hydrological Cycles and World Water Resources," *Science*, vol. 313, no. 5790, pp. 1068–1072, 2006.

[15] Department of Energy and Climate Change, *Digest of United Kingdom Energy Statistics 2015*, 2015. Available at https://www.gov.uk/government/statistics/digest-of-united-kingdom-energy-statistics-dukes-2015-printed-version (accessed 23/02/2016).

[16] Department of Energy and Climate Change, *UK Renewable Energy Roadmap Update 2012*, 2012. Available at https://www.gov.uk/government/publications/uk-renewable-energy-roadmap-update.

[17] Department of Energy and Climate Change, *Energy trends: renewables*, 2016. Available at https://www.gov.uk/government/statistics/energy-trends-section-6-renewables (accessed 23/02/2016).

[18] Department of Energy and Climate Change, *Renewable energy planning database monthly extract*, 2016. Available at https://www.gov.uk/government/publications/renewable-energy-planning-database-monthly-extract (accessed 23/02/2016).

[19] Renewable Energy Foundation, *UK Renewable Electricity Target Tracker*, 2016. Available at http://www.ref.org.uk/planning/index.php (accessed 23/02/2016).

[20] renewable UK, *UK Wind Energy Database (UKWED)*, 2016. Available at http://www.renewableuk.com/en/renewable-energy/wind-energy/uk-wind-energy-database/uk-wind-energy-database-ukwed.cfm (accessed 23/02/2016).

[21] United Nations, *Kyoto Protocol to the United Nations Framework Convention on Climate Change*, 1998. Available at http://unfccc.int/kyoto_protocol/items/2830.php.

[22] United Nations, *Doha amendment to the Kyoto Protocol Article 1: Amendment* , 2012. Available at http://unfccc.int/kyoto_protocol/doha_amendment/items/7362.php.

[23] *Climate Change Act 2008*, 2008. Available at http://www.legislation.gov.uk/ukpga/2008/27/contents.

[24] Department of Energy and Climate Change, *2014 UK greenhouse gas emissions, final figures*, 2015. Available at https://www.gov.uk/government/statistics/final-uk-greenhouse-gas-emissions-national-statistics-1990-2014 (accessed 30/05/2016).

[25] European Commission, *Renewable Energy Progress Report*. Available at http://ec.europa.eu/energy/renewables/reports/reports_en.htm.

[26] Department of Energy and Climate Change, *Digest of United Kingdom Energy Statistics 2013*, 2013. Available at https://www.gov.uk/government/uploads/system/uploads/attachment_data/file/225067/DUKES_2013_published_version.pdf.

[27] Y.-H. P. Zhang, "Next generation biorefineries will solve the food, biofuels, and environmental trilemma in the energy-food-water nexus," *Energy Science & Engineering*, Apr. 2013.

[28] D. Mackay, *Sustainable Energy - without the hot air*. UIT Cambridge Ltd., 2009.

[29] D. Abbott, "Is Nuclear Power Globally Scalable?," *Proceedings of the IEEE*, vol. 99, no. 10, 2011.

[30] D. Abbott, "Keeping the Energy Debate Clean: How Do We Supply the World's Energy Needs?," *Proceedings of the IEEE*, vol. 98, pp. 42–66, Jan. 2010.

[31] M. Z. Jacobson, "Review of solutions to global warming, air pollution, and energy security," *Energy & Environmental Science*, vol. 2, no. 2, p. 148, 2009.

[32] M. Z. Jacobson and M. A. Delucchi, "Providing all global energy with wind, water, and solar power, Part I: Technologies, energy resources, quantities and areas of infrastructure, and materials," *Energy Policy*, vol. 39, pp. 1154–1169, Mar. 2011.

[33] C. W. Forsberg, "Sustainability by combining nuclear, fossil, and renewable energy sources," *Progress in Nuclear Energy*, vol. 51, pp. 192–200, Jan. 2009.

[34] R. Shinnar and F. Citro, "Energy. A road map to U.S. decarbonization.," *Science (New York, N.Y.)*, vol. 313, pp. 1243–4, Sept. 2006.

[35] A. V. Thoms, "Rocks of ages: propagation of hot-rock cookery in western North America," *Journal of Archaeological Science*, vol. 36, pp. 573–591, Mar. 2009.

[36] P. R. Lewis and G. D. B. Jones, "Roman Gold-Mining in North-West Spain," *The Journal of Roman Studies*, vol. 60, pp. 169–185, 1970.

[37] J. N. Baker and A. Collinson, "Electrical energy storage at the turn of the Millennium," *Power Engineering Journal*, pp. 107–112, June 1999.

[38] S. van der Linden, "Bulk energy storage potential in the USA, current developments and future prospects," *Energy*, vol. 31, pp. 3446–3457, Dec. 2006.

[39] H. Chen, T. N. Cong, W. Yang, C. Tan, Y. Li, and Y. Ding, "Progress in electrical energy storage system: A critical review," *Progress in Natural Science*, vol. 19, pp. 291–312, Mar. 2009.

[40] R. M. Dell and D. A. J. Rand, "Energy storage - a key technology for global energy sustainability," *Journal of Power Sources*, vol. 100, pp. 2–17, 2001.

[41] D. Rastler, *Electricity Energy Storage Technology Options: A White Paper Primer on Applications, Costs, and Benefits*. Electric Power Research Institute, 2010.

[42] National Infrastructure Commission, *Smart Power*, 2016. Available from https://gov.uk/government/publications/smart-power-a-national-infrastructure-commission-report, accessed 20/04/2016.

[43] Energy Storage Research Network, *UK Budget finds £50 million for storage - news article*, 2016. Available from energysuperstore.org/esrn/latest-news/uk-budget-finds-50-million-for-storage/, accessed 20/04/2016.

[44] L. Smith, "UK National Grid status - uses data from the Balancing Mechanism Reporting System," Available at http://www.gridwatch.templar.co.uk. Accessed 05/02/2016.

[45] C. L. Archer and M. Z. Jacobson, "Supplying baseload power and reducing transmission requirements by interconnecting wind farms," *Journal of Applied Meteorology and Climatology*, vol. 46, no. 11, pp. 1701–1717, 2007.

[46] J. P. Palutikof, H. F. Cook, and T. D. Davies, "Effects of geographical dispersion on wind turbine performance in England: A simulation," *Atmospheric Environment Part A, General Topics*, vol. 24, no. 1, pp. 213–227, 1990.

[47] M. a. Delucchi and M. Z. Jacobson, "Providing all global energy with wind, water, and solar power, Part II: Reliability, system and transmission costs, and policies," *Energy Policy*, vol. 39, pp. 1170–1190, mar 2011.

[48] EirGrid Group, *Irish wind farm and demand data*. Data from http://www.eirgrid.com/operations/systemperformancedata/ accessed 21/10/2014. This site no longer seems to be accessible, be data can be gathered from http://www.smartgriddashboard.eirgrid.com/#all/wind accessed 05/02/2016.

[49] Energinet.dk, "Danish wind farm and demand data," Available at http://www.energinet.dk/EN/El/Engrosmarked/Udtraek-af-markedsdata/

Sider/default.aspx. Accessed 05/02/2016.

[50] M. Carbajales-Dale, C. J. Barnhart, and S. M. Benson, "Can we afford storage ? A dynamic net energy analysis of renewable electricity generation supported by energy storage," *Energy & Environmental Science*, vol. 7, no. 5, pp. 1538–1544, 2014.

[51] M. Carbajales-Dale, C. J. Barnhart, and S. M. Benson, "Can we afford storage ? A dynamic net energy analysis of renewable electricity generation supported by energy storage - Supporting Information," *Energy & Environmental Science*, vol. 7, no. 5, pp. 1538–1544, 2014.

[52] P. Grünewald, T. Cockerill, M. Contestabile, and P. Pearson, "The role of large scale storage in a GB low carbon energy future: Issues and policy challenges," *Energy Policy*, vol. 39, pp. 4807–4815, Sept. 2011.

[53] H. Safaei and D. W. Keith, "How much bulk energy storage is needed to decarbonize electricity?," *Energy & Environmental Science*, vol. 8, no. 12, pp. 3409–3417, 2015.

[54] A. Evans, V. Strezov, and T. J. Evans, "Assessment of utility energy storage options for increased renewable energy penetration," *Renewable and Sustainable Energy Reviews*, vol. 16, pp. 4141–4147, Aug. 2012.

[55] *First Hydro Analysts Conference*, 2005. Available at http://www.iprplc-gdfsuez.com/~/media/Files/I/IPR-Plc/Attachments/presentations-pdfs/2005/hydrosite05.pdf. Accessed May 2016.

[56] P. Denholm and G. L. Kulcinski, "Life cycle energy requirements and greenhouse gas emissions from large scale energy storage systems," *Energy Conversion and Management*, vol. 45, pp. 2153–2172, Aug. 2004.

[57] W. F. Pickard, "The History, Present State, and Future Prospects of Underground Pumped Hydro for Massive Energy Storage," *Proceedings of the IEEE*, vol. 100, pp. 473–483, Feb. 2012.

[58] N. Uddin, "Geotechnical Issues in the Creation of Underground Reservoirs for Massive Energy Storage," *Proceedings of the IEEE*, vol. 100, pp. 484–492, Feb. 2012.

[59] X. Luo, J. Wang, M. Dooner, and J. Clarke, "Overview of current development in electrical energy storage technologies and the application potential in power system operation q," *Applied Energy*, vol. 137, pp. 511–536, 2015.

[60] A. J. White, "Loss analysis of thermal reservoirs for electrical energy storage schemes," *Applied Energy*, vol. 88, pp. 4150–4159, Nov. 2011.

[61] G. Grazzini and A. Milazzo, "A Thermodynamic Analysis of Multistage Adiabatic CAES," *Proceedings of the IEEE*, vol. 100, pp. 461–472, Feb. 2012.

[62] C. Bullough, C. Gatzen, C. Jakiel, M. Koller, A. Nowi, and S. Zunft, "Advanced Adiabatic Compressed Air Energy Storage for the Integration of Wind Energy," pp. 22–25, November 2004.

[63] W. F. Pickard, N. J. Hansing, and A. Q. Shen, "Can large-scale advanced-adiabatic compressed air energy storage be justified economically in an age of sustainable energy?," *Journal of Renewable and Sustainable Energy*, vol. 1, no. 3, 2009.

[64] A. Cavallo, "Controllable and affordable utility-scale electricity from intermittent wind resources and compressed air energy storage (CAES)," *Energy*, vol. 32, pp. 120–127, Feb. 2007.

[65] M. Medrano, A. Gil, I. Martorell, X. Potau, and L. F. Cabeza, "State of the art on high-temperature thermal energy storage for power generation. Part 2 - Case studies," *Renewable and Sustainable Energy Reviews*, vol. 14, pp. 56–72, Jan. 2010.

[66] R. Muthusivagami, R. Velraj, and R. Sethumadhavan, "Solar cookers with and without thermal storage - A review," *Renewable and Sustainable Energy Reviews*, vol. 14, pp. 691–701, Feb. 2010.

[67] A. V. Novo, J. R. Bayon, D. Castro-Fresno, and J. Rodriguez-Hernandez, "Review of seasonal heat storage in large basins: Water tanks and gravelwater pits," *Applied Energy*, vol. 87, pp. 390–397, Feb. 2010.

[68] A. Sharma, V. Tyagi, C. Chen, and D. Buddhi, "Review on thermal energy storage with phase change materials and applications," *Renewable and Sustainable Energy Reviews*, vol. 13, pp. 318–345, Feb. 2009.

[69] Y. Li, H. Chen, and Y. Ding, "Fundamentals and applications of cryogen as a thermal energy carrier: A critical assessment," *International Journal of Thermal Sciences*, vol. 49, pp. 941–949, jun 2010.

[70] D. Fernandes, F. Pitié, G. Cáceres, and J. Baeyens, "Thermal energy storage: How previous findings determine current research priorities," *Energy*, vol. 39, pp. 246–257, Mar. 2012.

[71] J. Baker, "New technology and possible advances in energy storage," *Energy Policy*, vol. 36, pp. 4368–4373, Dec. 2008.

[72] I. Dincer, "Thermal energy storage systems as a key technology in energy conservation," *International Journal of Energy Research*, vol. 26, pp. 567–588, June 2002.

[73] A. Gil, M. Medrano, I. Martorell, A. Lázaro, P. Dolado, B. Zalba, and L. F. Cabeza, "State of the art on high temperature thermal energy storage for power generation. Part 1 - Concepts, materials and modellization," *Renewable and Sustainable Energy Reviews*, vol. 14, pp. 31–55, Jan. 2010.

[74] R. Daschner, S. Binder, and M. Mocker, "Pebble bed regenerator and storage system for high temperature use," *Applied Energy*, vol. 109, pp. 394–401, Sept. 2013.

[75] G. Zanganeh, M. Commerford, A. Haselbacher, A. Pedretti, and A. Steinfeld, "Stabilization of the outflow temperature of a packed-bed thermal energy storage by combining rocks with phase change materials," *Applied Thermal Engineering*, vol. 70, pp. 316–320, sep 2014.

[76] G. Zanganeh, R. Khanna, C. Walser, a. Pedretti, a. Haselbacher, and a. Steinfeld, "Experimental and numerical investigation of combined sensiblelatent heat for thermal energy storage at 575C and above," *Solar Energy*, vol. 114, pp. 77–90, 2015.

[77] D. Okello, C. W. Foong, O. J. Nydal, and E. J. K. Banda, "An experimental investigation on the combined use of phase change material and rock particles for high temperature (˜350 C) heat storage," *Energy Conversion and Management*, vol. 79, pp. 1–8, 2014.

[78] D. Crandall and E. Thacher, "Segmented thermal storage," *Solar Energy*, vol. 77, pp. 435–440, Oct. 2004.

[79] J. MacNaghten, J. S. Howes, and R. G. Hunt, "Improved heat storage apparatus," no. EP/2689207/2011, 2011.

[80] A. J. White, J. D. McTigue, and C. N. Markides, "Analysis and optimisation of segmented packed-bed thermal reservoirs for electricity storage applications," 2016. Manuscript in preparation.

[81] J. McTigue and A. J. White, "Segmented packed beds for improved thermal energy storage performance," *IET Renewable Power Generation*, 2016. Submitted to journal.

[82] I. H. Bell, J. Wronski, S. Quoilin, and V. Lemort, "Pure and pseudo-pure fluid thermophysical property evaluation and the open-source thermophysical property library coolprop," *Industrial & Engineering Chemistry Research*, vol. 53, no. 6, pp. 2498–2508, 2014.

[83] A. White, G. Parks, and C. N. Markides, "Thermodynamic analysis of pumped thermal electricity storage," *Applied Thermal Engineering*, vol. 53, pp. 291–298, May 2013.

[84] J. D. McTigue, A. J. White, and C. N. Markides, "Parametric studies and optimisation of pumped thermal electricity storage," *Applied Energy*, vol. 137, pp. 800–811, Sept. 2015.

[85] A. Thess, "Thermodynamic Efficiency of Pumped Heat Electricity Storage," *Physical Review Letters*, vol. 111, no. 11, p. 110602, 2013.

[86] F. Ni and H. S. Caram, "Analysis of pumped heat electricity storage process using exponential matrix solutions," *Applied Thermal Engineering*, vol. 84, pp. 34–44, 2015.

[87] M. Mercangöz, J. Hemrle, L. Kaufmann, A. ZGraggen, and C. Ohler, "Electrothermal energy storage with transcritical CO2 cycles," *Energy*, vol. 45, pp. 407–415, sep 2012.

[88] M. Morandin, M. Mercangöz, J. Hemrle, F. Maréchal, and D. Favrat, "Thermoeconomic design optimization of a thermo-electric energy storage system based on transcritical CO2 cycles," *Energy*, vol. 58, pp. 571–587, 2013.

[89] W. Steinmann, "The CHEST (Compressed Heat Energy STorage) concept for facility scale thermo mechanical energy storage," *Energy*, vol. 69, pp. 543–552, 2014.

[90] T. Desrues, J. Ruer, P. Marty, and J. Fourmigué, "A thermal energy storage process for large scale electric applications," *Applied Thermal Engineering*, vol. 30, pp. 425–432, Apr. 2010.

[91] T. Desrues, *Stockage massif d'électricité sous forme thermique*. PhD thesis, Université de Grenoble, 2011.

[92] E. M. Smith, "Storage of electrical energy using supercritical liquid air," *ARCHIVE: Proceedings of the Institution of Mechanical Engineers 1847-1982 (vols 1-196)*, vol. 191, pp. 289–298, jun 1977.

[93] H. Chen, Y. Ding, T. Peters, and F. Berger, "A method of storing energy and a cryogenic energy storage system," no. WO 2007/096656 A1, 2007.

[94] B. Ameel, C. T'Joen, K. De Kerpel, P. De Jaeger, H. Huisseune, M. Van Belleghem, and M. De Paepe, "Thermodynamic analysis of energy storage with a liquid air Rankine cycle," *Applied Thermal Engineering*, vol. 52, no. 1, pp. 130–140, 2013.

[95] R. Morgan, S. Nelmes, E. Gibson, and G. Brett, "Liquid air energy storage Analysis and first results from a pilot scale demonstration plant," *Applied Energy*, vol. 137, pp. 845–853, jan 2015.

[96] A. Stamatiou, A. Ammann, L. J. Fischer, D. Gwerder, and J. Worlitschek, "Combined Storage of Heat , Cold and Electricity," *GREENSTOCK 2015 – The 13th International Conference on Energy Storage*, vol. 69, no. 12, pp. 777–779, 2015.

[97] A. White, J. McTigue, and C. Markides, "Wave propagation and thermodynamic losses in packed-bed thermal reservoirs for energy storage," *Applied Energy*, vol. 130, pp. 648–657, 2014.

[98] F. Marguerre, "Ueber ein neues verfahren zur aufspeicherung elektrischer energie," *Mitteilungen der Vereinigung der Elektrizitätswerke*, vol. 354, pp. 27–35, 1924. (in German).

[99] F. Marguerre, "Das thermodynamische speicherverfahren von marguerre," *Escher-Wyss Mitteilungen*, vol. 6, pp. 67–76, 1933. (in German).

[100] F. Marguerre, "Thermodynamic energy storage method," 1934. US patent number 1,979,393.

[101] F. Marguerre, "Thermodynamic energy storage," 1936. US patent number 2,065,974.

[102] B. Atlantique, "Heat accumulation - for balancing off-peak and peak demands in a thermal power producing unit (in french)," 1972. FR/2098833.

[103] R. P. Cahn, "Thermal energy storage by means of reversible heat pumping," 1978. US patent number 4,089,744.

[104] R. P. Cahn and E. W. Nicholson, "Thermal energy storage by means of reversible heat pumping utilizing industrial waste heat," 1978. US patent number 4,110,987.

[105] J. Guo, L. Cai, J. Chen, and Y. Zhou, "Performance optimization and comparison of pumped thermal and pumped cryogenic electricity storage systems," *Energy*, vol. 106, pp. 260–269, 2016.

[106] Y. M. Kim, D. G. Shin, S. Y. Lee, and D. Favrat, "Isothermal transcritical CO2 cycles with TES (thermal energy storage) for electricity storage," *Energy*, vol. 49, no. 1, pp. 484–501, 2013.

[107] J. Ruer, "Installation and methods for storing and recovering electrical energy," 2008. WO/2008/148962 A2.

[108] J. MacNaghten and J. S. Howes, "Energy Storage," no. WO2009044139 A2, 2009.

[109] B. Weissenbach, "Thermal energy storage device," 1979. EP/0003980 A1.

[110] R. Kurz and K. Brun, "Efficiency definition and load management for reciprocating and centrifugal compressors," in *ASME Turbo Expo GT2007-27081*, 2007.

[111] M. Morandin, F. Maréchal, M. Mercangöz, and F. Buchter, "Conceptual design of a thermo-electrical energy storage system based on heat integration of thermodynamic cycles Part A: Methodology and base case," *Energy*, vol. 45, pp. 375–385, sep 2012.

[112] A. Willmot, *Dynamics of Regenerative Heat Transfer*. Taylor & Francis, 2002.

[113] K. Ismail and R. Stuginsky, "A parametric study on possible fixed bed models for pcm and sensible heat storage," *Applied Thermal Engineering*, vol. 19, pp. 757–788, 1999.

[114] D. E. Beasley and J. A. Clark, "Transient response of a packed bed for thermal energy storage," *International Journal of Heat and Mass Transfer*, vol. 21, no. 9, pp. 1659–1669, 1984.

[115] R. F. Benenati and C. B. Brosilow, "Void Fraction Distribution in Beds of Spheres," *A.I.CH.E Journal*, vol. 8, no. 3, pp. 359–361, 1962.

[116] A. Meier, C. Winkler, and D. Wuillemin, "Experiment for modeling high temperature rock bed storage," vol. 24, pp. 255–264, 1991.

[117] D. Vortmeyer and R. Schaefer, "Equivalence of one- and two-phase models for heat transfer processes in packed beds: one dimensional theory," *Chemical Engineering Science*, vol. 29, no. 2, pp. 485–491, 1974.

[118] T. Schumann, "Heat transfer: A liquid flowing through a porous prism," *Journal of the Franklin Institute*, vol. 208, pp. 405–416, Sept. 1929.

[119] A. Anzelius, "Heating by means of percolating media," *Journal of Mechanical Design*, vol. 6, pp. 291–294, 1926.

[120] N. Wakao, S. Kaguei, and T. Funazkri, "Effect of fluid dispersion coefficients on particle-to-fluid heat transfer coefficients in packed beds," *Chemical Engineering Science*, vol. 34, pp. 325–336, 1979.

[121] J. D. Anderson, *Computational Fluid Dynamics: the basics with applications*. McGraw-Hill, Inc, 1995.

[122] R. G. Holdich, *Fundamentals of particle technology*. Midland Information Technology and Publishing, 2002.

[123] S. Yagi and D. Kunii, "Studies on Effective Thermal Conductivities in Packed Beds," no. 20, pp. 373–381, 1957.

[124] A. R. Balakrishnan and D. C. T. Pei, "Heat Transfer in Gas-Solid Packed Bed Systems. 1. A Critical Review," *Industrial & Engineering Chemistry Process Design and Development*, vol. 18, no. 1, pp. 30–40, 1979.

[125] J. Lis and P. O. Kellard, "Measurements of the thermal conductivity of thin films of magnetite," *British Journal of Applied Physics*, vol. 1, 1968.

[126] G. A. Slack, "Thermal Conductivity of MgO, Al2O3, MgAl2O3, and Fe3O4 Crystals from 3K to 300K," *Physical Review*, vol. 126, no. 2, 1962.

[127] J. Mølgaard, "Thermal Conductivity of Magnetite and Hematite," *Journal of Applied Physics*, vol. 42, no. 9, p. 3644, 1971.

[128] R. G. Deissler and C. S. Eian, "Investigation of effective thermal conductivities of powders," *National Advisory Committee for Aeronautics*, 1952.

[129] D. Kunii and J. M. Smith, "Heat Transfer Characteristics of Porous Rocks," *American Institute of Chemical Engineers*, vol. 6, no. 1, pp. 71–78, 1960.

[130] V.Prasad, N. Kladias, A.Bandyopadhaya, and Q.Yian, "Evaluation of correlations for stagnant thermal conductivity of liquid-saturated porous beds of spheres," *International heat and mass transfer*, vol. 32, no. 9, pp. 1793–1796, 1989.

[131] Granta Design Ltd., *CES Materials Selector Edupack*, 2015. Available from http://www.grantadesign.com/education/edupack. Accessed 05/11/2015.

[132] O. Laguerre, S. B. Amara, and D. Flick, "Heat transfer between wall and packed bed crossed by low velocity airflow," *Applied Thermal Engineering*, vol. 26, pp. 1951–1960, Nov. 2006.

[133] S. Yagi and N. Wakao, "Heat and Mass Transfer from Wall to Fluid in Packed Beds," *A.I.CH.E Journal*, vol. 5, no. 1, pp. 79–85, 1959.

[134] C. Li and B. Finlayson, "Heat transfer in packed beds - a re-evaluation," *Chemical Engineering Science*, vol. 32, pp. 1055–1066, 1977.

[135] J. Beek, "Design of packed catalytic reactors," *Advances in Chemical Engineering*, vol. 3, pp. 203 – 271, 1962.

[136] G. F. Froment, "Fixed Bed Catalytic Reactors - Current Design Status," *Industrial & Engineering Chemistry*, vol. 59, no. 2, pp. 18–27, 1967.

[137] F. Incropera and D. DeWitt, *Fundamentals of Heat and Mass Transfer*. John Wiley, 2007.

[138] C. Popiel, J. Wojtkowiak, and K. Bober, "Laminar free convective heat transfer from isothermal vertical slender cylinder," *Experimental Thermal and Fluid Science*, vol. 32, pp. 607–613, Nov. 2007.

[139] S. W. Churchill and H. H. S. Chu, "Correlating equations for laminar and turbulent free convection from a vertical plate," *International Journal of Heat and Mass Transfer*, vol. 18, no. 11, pp. 1323–1329, 1975.

[140] Y. Ammar, S. Joyce, R. Norman, Y. Wang, and A. P. Roskilly, "Low grade thermal energy sources and uses from the process industry in the UK," *Applied Energy*, vol. 89, pp. 3–20, Jan. 2012.

[141] C. Chan, J. Ling-Chin, and a.P. Roskilly, "A review of chemical heat pumps, thermodynamic cycles and thermal energy storage technologies for low grade heat utilisation," *Applied Thermal Engineering*, vol. 50, pp. 1257–1273, Jan. 2013.

[142] H.-G. Fassbinder, "Regenerator," 1996. US Patent 5,577,553.

[143] A. Emmel, D. Stevanovic, and H. Fassbinder, "Process for operating a regenerator and regenerator," 1999. EP 0 908 682 A2.

[144] W. L. Vargas and J. J. Mccarthy, "Stress effects on the conductivity of particulate beds," *Chemical Engineering Science*, vol. 57, pp. 3119–3131, 2002.

[145] V. Dreißigacker, S. Zunft, and H. Müller-Steinhagen, "A thermo-mechanical model of packed-bed storage and experimental validation," *Applied Energy*, May 2013.

[146] "NIST-JANEF Thermochemical Tables," Available at http://kinetics.nist.gov/janef/ (accesssed November 2015).

[147] E. F. Westrum, "Magnetite Heat capacity and thermodynamic properties from 5 to 350 K ," pp. 543–557, 1969.

[148] Y. S. Touloukian and C. Y. Ho, *Thermophysical Properties of Matter Volume 2, Thermal conductivity of non-metallic solids*. Plenum Press, New York, 1972.

[149] R. M. Dickinson, C. A. Cruickshank, and S. J. Harrison, "Charge and discharge strategies for a multi-tank thermal energy storage," *Applied Energy*, vol. 109, pp. 366–373, Sept. 2013.

[150] D. S. Miller, *Internal Flow Systems*. BHRA, 2nd edition ed., 1990.

[151] A. L. Lopez de Ramos and F. F. Pironti, "Effective Thermal Conductivity in a Packed-Bed Radial-Flow Reactor," *AIChE Journal*, vol. 33, no. 10, pp. 1747–1750, 1987.

[152] J. Fuentes, F. F. Pironti, and A. L. Lopez de Ramos, "Effective Thermal Conductivity in a Radial-Flow Packed-Bed Reactor," *International Journal of Thermophysics*, vol. 19, no. 3, pp. 781–792, 1998.

[153] a. a. Kareeri, H. D. Zughbi, and H. H. Al-Ali, "Simulation of Flow Distribution in Radial Flow Reactors," *Industrial & Engineering Chemistry Research*, vol. 45, pp. 2862–2874, 2006.

[154] P. J. Heggs, D. I. Ellis, and M. S. Ismail, "The modelling of fluid-flow distributions in annular packed beds," *Gas Separation and Purification*, vol. 8, no. 4, pp. 257–264, 1994.

[155] P. J. Heggs, D. I. Ellis, and M. S. Ismail, "Prediction of flow distributions and pressure changes in multi-layered annular packed beds," *Gas Separation and Purification*, vol. 9, no. 4, pp. 243–252, 1995.

[156] V. Hlavacek and M. Kubicek, "Modelling of chemical reactors - XXV Cylindrical and spherical reactor with radial flow," *Chemical Engineering Science*, vol. 27, no. 2, pp. 177–186, 1972.

[157] J. Votruba and V. Hlaváček, "An experimental study of radial heat transfer in catalytic radial-flow reactors," *The Chemical Engineering Journal*, vol. 4, no. 1, pp. 91–95, 1972.

[158] L. Bradley, "Regenerative stove," 1942. US Patent 2,272,108.

[159] A. Emmel and D. Stevanovic, "Method for converting thermal energy into mechanical work," 2015. US 2004/0088980 A1.

[160] A. White, "Thermodynamic analysis of the reverse Joule-Brayton cycle heat pump for domestic heating," *Applied Energy*, vol. 86, pp. 2443–2450, Nov. 2009.

[161] R. Mathie, C. N. Markides, and A. J. White, "A Framework for the Analysis of Thermal Losses in Reciprocating Compressors and Expanders," *Heat Transfer Engineering*, vol. 35, pp. 1435–1449, Apr. 2014.

[162] R. K. Shah and S. P. Dušan, *Fundamentals of heat exchanger design*. John Wiley & Sons, Inc., 2003.

[163] W. Kays and A. London, *Compact heat exchangers*. McGraw-Hill, 1984.

[164] B. S. Massey, *Mechanics of fluids*. Chapman & Hall, 1989.

[165] F. M. White, *Fluid mechanics*. McGraw-Hill, 1994.

[166] R. W. Moss, A. P. Roskilly, and S. K. Nanda, "Reciprocating Joule-cycle engine for domestic CHP systems," *Applied Energy*, vol. 80, pp. 169–185, 2005.

[167] H.-J. Huff and R. Radermacher, "CO2 Compressor- Expander Analysis," 2003. Report ARTI-21CR/611-10060-01.

[168] P. Farres-Antunez and A. J. White, "Optimisation of heat exchangers operating with real fluids for thermo-mechanical energy storage," in *Offshore Energy and Storage Conference, Malta*, 2016.

[169] G. Wall, "Thermoeconomic optimization of a heat pump system," *Energy*, vol. 11, no. 10, pp. 957–967, 1986.

[170] M. A. Lozano and A. Valero, "Theory of the Exergetic Cost," *Energy*, vol. 18, no. 9, pp. 939–960, 1993.

[171] R. F. Boehm, ed., *Developments in the Design of Thermal Systems*. Cambridge University Press, 1997.

[172] A. Valero, M. a. Lozano, L. Serra, G. Tsatsaronis, J. Pisa, C. Frangopoulos, and M. R. von Spakovsky, "CGAM problem: Definition and conventional solution," *Energy*, vol. 19, pp. 279–286, Mar. 1994.

[173] A. Valero, M. A. Lozano, L. Serra, and C. Torres, "Application of the exergetic cost theory to the CGAM problem," *Energy*, vol. 19, no. 3, pp. 365–381, 1994.

[174] G. Tsatsaronis and J. Pisa, "Exergoeconomic evaluation and optimization of energy systems - application to the CGAM problem," *Energy*, vol. 19, no. 3, pp. 287–321, 1994.

[175] M. R. V. Spakovsky, "Application of engineering functional analysis to the analysis and optimization of the CGAM Problem," *1Energy*, vol. 19, no. 3, pp. 343–364, 1994.

[176] A. Abusoglu and M. Kanoglu, "Exergoeconomic analysis and optimization of combined heat and power production: A review," *Renewable and Sustainable Energy Reviews*, vol. 13, pp. 2295–2308, Dec. 2009.

[177] M. a. Rosen, "A Concise Review of Exergy-Based Economic Methods," *Int. Conf. on Energy & Environment*, p. 9, 2008.

[178] N. DeForest, G. Mendes, M. Stadler, W. Feng, J. Lai, and C. Marnay, "Optimal deployment of thermal energy storage under diverse economic and climate conditions," *Applied Energy*, vol. 119, pp. 488–496, Apr. 2014.

[179] S. M. Schoenung and W. V. Hassenzahl, "Long- vs . Short-Term Energy Storage Technologies Analysis A Life-Cycle Cost Study A Study for the DOE Energy Storage Systems Program," tech. rep., Sandia Report SAND2003-2783, 2003.

[180] R. Sioshansi, P. Denholm, T. Jenkin, and J. Weiss, "Estimating the value of electricity storage in PJM: Arbitrage and some welfare effects," *Energy Economics*, vol. 31, pp. 269–277, Mar. 2009.

[181] E. Oró, A. Gil, A. D. Gracia, D. Boer, and L. F. Cabeza, "Comparative life cycle assessment of thermal energy storage systems for solar power plants," *Renewable Energy*, vol. 44, pp. 166–173, 2012.

[182] C. J. Barnhart, M. Dale, A. R. Brandt, and S. M. Benson, "The energetic implications of curtailing versus storing solar- and wind-generated electricity," *Energy & Environmental Science*, vol. 6, no. 10, p. 2804, 2013.

[183] C. J. Barnhart and S. M. Benson, "On the importance of reducing the energetic and material demands of electrical energy storage," *Energy & Environmental Science*, vol. 6, no. 4, p. 1083, 2013.

[184] J. MacNaghten, "Commercial potential of different thermal storage technologies under development globally," in *UK Thermal Energy Storage Conference, 2016*, 2016.

[185] A. Mawire, "Performance of Sunflower Oil as a sensible heat storage medium for domestic applications," *Journal of Energy Storage*, vol. 5, pp. 1–9, 2016.

[186] M. N. Strasser and R. P. Selvam, "A cost and performance comparison of packed bed and structured thermocline thermal energy storage systems," *Solar Energy*, vol. 108, pp. 390–402, 2014.

[187] R. M. Kavanagh and G. T. Parks, "A Systematic Comparison and Multi-Objective Optimization of Humid Power CyclesPart II: Economics," *Journal of Engineering for Gas Turbines and Power*, vol. 131, no. 4, p. 041702, 2009.

[188] A. Traverso, A. F. Massardo, and G. Lagorio, "WIDGET-TEMP: A novel web-based approach for thermoeconomic analysis and optimization of conventional and innovative cycles," in *Proceedings of ASME-IGTI Turbo Expo*, (Vienna), pp. 1–9, 2004.

[189] A. Agazzani and A. F. Massardo, "A tool for thermoeconomic analysis and optimization of gas, steam, and combined plants," *Journal of Engineering for Gas Turbines and Power*, vol. 119, pp. 885–892, 1997.

[190] C. A. Frangopoulos, "Optimal synthesis and operation of thermal systems by the thermoeconomic functional approach," *Journal of Engineering for Gas Turbines and Power*, vol. 114, pp. 707–714, 1992.

[191] B. C. Cheung, R. Carriveau, and D. S. Ting, "Multi-objective optimization of an underwater compressed air energy storage system using genetic algorithm," *Energy*, vol. 74, pp. 396–404, 2014.

[192] S. Bonnet, M. Alaphilippe, and P. Stouffs, "Energy, exergy and cost analysis of a micro-cogeneration system based on an Ericsson engine," *International Journal of Thermal Sciences*, vol. 44, pp. 1161–1168, dec 2005.

[193] M. D. M. Herrera, F. R. P. Arrieta, and J. R. Sodré, "Thermoeconomic assessment of an absorption refrigeration and hydrogen-fueled diesel power generator cogeneration system," *International Journal of Hydrogen Energy*, vol. 39, no. 9, pp. 4590–4599, 2014.

[194] M. Ehyaei, P. Ahmadi, F. Atabi, M. Heibati, and M. Khorshidvand, "Feasibility study of applying internal combustion engines in residential buildings by exergy, economic and environmental analysis," *Energy and Buildings*, vol. 55, pp. 405–413, 2012.

[195] E. Açkkalp, H. Aras, and A. Hepbasli, "Advanced exergoeconomic analysis of a trigeneration system using a diesel-gas engine," *Applied Thermal Engineering*, vol. 67, pp. 388–395, jun 2014.

[196] O. Balli, H. Aras, and A. Hepbasli, "Thermodynamic and thermoeconomic analyses of a trigeneration (TRIGEN) system with a gas-diesel engine: Part II - An application," *Energy Conversion and Management*, vol. 51, no. 11, pp. 2260–2271, 2010.

[197] *Wartsila Diesel Engine 32*, 2016. Available at http://www.wartsila.com/products/marine-oil-gas/engines-generating-sets/diesel-engines/wartsila-32. Accessed Jan. 2016.

[198] R. M. Kavanagh and G. T. Parks, "A Systematic Comparison and Multi-Objective Optimization of Humid Power Cycles - Part I: Thermodynamics," *Journal of Engineering for Gas Turbines and Power*, vol. 131, no. 4, p. 041701, 2009.

[199] D. Jaeggi, G. Parks, T. Kipouros, and P. Clarkson, "A Multi-objective Tabu Search Algorithm for Constrained Optimisation Problems," *The Third International Conference of Evolutionary Multi-Criterion Optimisation*, 2005.

[200] J. Knowles, D. Corne, and K. Deb, *Multiobjective Problem Solving from Nature*. Springer, 2008.

[201] D. E. Goldberg, *Genetic Algorithms in Search, Optimisation and Machine Learning*. Boston, MA, USA: Addison-Wesley Longman Publishing Co., Inc., 1st ed., 1989.

[202] H.-P. Schwefel and G. Rudolph, "Contemporary evolution strategies," in *Advances in Artificial Life* (F. Morn, A. Moreno, J. Merelo, and P. Chacn, eds.), vol. 929 of *Lecture Notes in Computer Science*, pp. 891–907, Springer Berlin Heidelberg, 1995.

[203] H.-G. Beyer and H.-P. Schwefel, "Evolution strategies," *Natural Computing*, vol. 1, pp. 3–52, 2002.

[204] D. Wolpert and W. Macready, "No free lunch theorems for optimization," *IEEE Transactions on Evolutionary Computation*, vol. 1, pp. 67–82, Apr. 1997.

[205] J. Periaux, H. Chen, B. Mantel, M. Sefrioui, and H. Sui, "Combining game theory and genetic algorithms with application to DDM-nozzle optimization problems," *Finite Elements in Analysis and Design*, vol. 37, pp. 417–429, May 2001.

[206] M. Sefrioui and J. Periaux, "Nash genetic algorithms: examples and applications," in *Evolutionary Computation, 2000. Proceedings of the 2000 Congress on*, vol. 1, pp. 509–516 vol.1, 2000.

[207] R. Meng, Y. Ye, and N. gang Xie, "Multi-objective optimization design methods based on game theory," in *Intelligent Control and Automation (WCICA), 2010 8th World Congress on*, pp. 2220–2227, 2010.

[208] D. Lee, L. F. Gonzalez, J. Periaux, K. Srinivas, and E. Onate, "Hybrid-Game Strategies for multi-objective design optimization in engineering," *Computers & Fluids*, vol. 47, pp. 189–204, Aug. 2011.

[209] A. Konak, D. W. Coit, and A. E. Smith, "Multi-objective optimization using genetic algorithms: A tutorial," *Reliability Engineering & System Safety*, vol. 91, pp. 992–1007, Sept. 2006.

[210] E. Zitzler, K. Deb, and L. Thiele, "Comparison of multiobjective evolutionary algorithms: empirical results.," *Evolutionary computation*, vol. 8, pp. 173–95, Jan. 2000.

[211] C. A. C. Coello, "An Updated Survey of GA-Based Multiobjective Optimization Techniques," *ACM Computing Surveys*, vol. 32, June.

[212] K. Deb, A. Pratap, S. Agarwal, and T. Meyarivan, "A Fast and Elitist Multiobjective Genetic Algorithm: NSGA-II," *IEEE Transactions on Evolutionary Computation*, vol. 6, no. 2, pp. 182–197, 2002.

[213] E. Zitzler and L. Thiele, "Multiobjective Evolutionary Algorithms: A Comparative Case Study and the Strength Pareto Approach," *IEEE Transations on Evolutionary Computation*, vol. 3, no. 4, pp. 257–271, 1999.

[214] A. Toffolo, V. Venezia, and E. Benini, "Genetic Diversity as an Objective in Multi-Objective Evolutionary Algorithms," *Evolutionary computation*, vol. 11, no. 2, pp. 151–167, 2003.

[215] P. R. Gunjal, V. V. Ranade, and R. V. Chaudhari, "Computational study of a single-phase flow in packed beds of spheres," *AIChE Journal*, vol. 51, pp. 365–378, feb 2005.

[216] A. Guardo, M. Coussirat, F. Recasens, M. Larrayoz, and X. Escaler, "CFD study on particle-to-fluid heat transfer in fixed bed reactors: Convective heat transfer at low and high pressure," *Chemical Engineering Science*, vol. 61, pp. 4341–4353, jul 2006.

Appendix A

Estimation of thermal front lengths

A.1 Front lengths in axial-flow thermal stores

In section 2.5.1 thermal losses ζ_t in the packed-bed thermal reservoirs were discussed. It was noted that the specific heat capacity of solid c_s varies with temperature. The speed of the thermal front depends inversely on c_s, and consequently the shape of the thermal front changes. Numerical results demonstrated that variable c_s leads to slightly increased thermal losses, and claimed that this was the result of the thermal front length changing. A simple model is now developed to demonstrate this behaviour.

The thermal loss was shown in section 2.5.1 to be approximately

$$\zeta_t \approx \frac{T_0}{\beta t_{\text{chg}}} \left(\frac{\Delta T^2}{T_1 T_2} \right) \ell \int_0^{t_{\text{chg}}} \frac{1}{\lambda} dt \tag{A.1}$$

where λ is the front length and is a function of time t. In order for changing front lengths to cause larger losses than the average front length $\bar{\lambda}$ then it should be the case that

$$\int_0^{t_{\text{chg}}} \frac{1}{\lambda(t)} dt > \frac{t_{\text{chg}}}{\bar{\lambda}} \tag{A.2}$$

If $\lambda(t)$ is a function that varies linearly with time some thought leads to the conclusion that this expression is true. This may be demonstrated for the case where variable c_s causes the front lengths to fluctuate. Expressions are developed for the left and right hand side of equation A.2 and these terms are referred to as 'wave-speed coefficients'.

Figure A.1 illustrates idealised thermal fronts at the beginning and end of a charging phase during cyclic operation of a hot store. The thermal fronts are assumed to have a linear shape. The hot store is charged at temperature T_1 and discharged at temperature T_2. The cycle period is given by $\Pi = t_c/t_N$ where t_c is the charging duration, and t_N is the nominal time for a wave at temperature T_1 to travel the length of the store, where

$$t_N = \frac{\rho_s c_{s1} A L (1 - \varepsilon)}{\dot{m} c_p} \tag{A.3}$$

(c.f equation 2.5). c_{s1} is the solid heat capacity at temperature T_1. At the beginning of charge, the front length is $\lambda_1 = L - V_{f2} t_c$ where V_{f2} is the speed of the thermal front at T_2

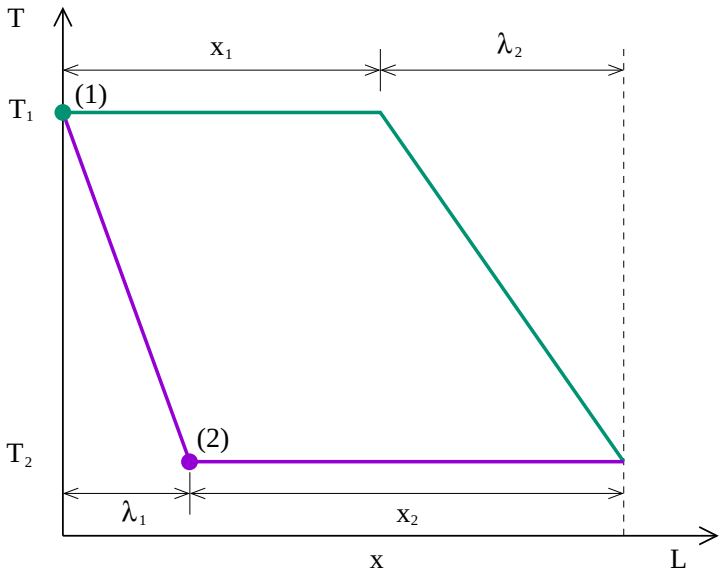

Figure A.1: Idealised thermal fronts at the end of charge (1 – green) and the start of charge (2 – purple). c_s is assumed to vary with temperature leading to the front changing shape. Charge and discharge periods are estimated by assuming the period ends when the leading edge of the front reaches the exit.

– i.e. $V_{f2}t_c$ is the distance point (2) on figure A.1 travels during charge. Rearranging gives

$$\lambda_1 = L\left(1 - \Pi\frac{c_{s1}}{c_{s2}}\right) \tag{A.4}$$

A similar expression can be found for the front length at the end of charge, λ_2. The average front length is then given by

$$\bar{\lambda} = 1/2(\lambda_1 + \lambda_2) = L\left[1 - \frac{\Pi}{2}\left(\frac{c_{s1} + c_{s2}}{c_{s2}}\right)\right] \tag{A.5}$$

The wave-speed coefficient for constant front length (L.H.S of equation A.2) is then

$$\frac{t_c}{\bar{\lambda}} = \frac{\Pi}{V_f}\left[1 - \frac{\Pi}{2}\left(\frac{c_{s1} + c_{s2}}{c_{s2}}\right)\right]^{-1} \tag{A.6}$$

An expression now needs to be developed for the variable front length $\lambda(t)$. The change in

front length $\delta\lambda$ is found by noting that in time δt point (1) will have moved a distance

$$\delta x_1 = \frac{\dot{m} c_p}{(1-\varepsilon)\rho A c_{s1}} \delta t \tag{A.7}$$

A similar expression is found for δx_2. The change in front length is then $\delta\lambda = \delta x_2 - \delta x_1$

$$\delta\lambda = \frac{\dot{m} c_p}{(1-\varepsilon)\rho_s A} \left(\frac{1}{c_{s2}} - \frac{1}{c_{s1}} \right) \delta t \tag{A.8}$$

The front length therefore varies linearly and can be written as

$$\lambda = \lambda_1 + \frac{d\lambda}{dt} t \tag{A.9}$$

$$\lambda = \left(1 - \Pi \frac{c_{s1}}{c_{s2}} \right) L + \frac{t}{t_N} \left(\frac{c_{s1} - c_{s2}}{c_{s2}} \right) L \tag{A.10}$$

An expression for the wave-speed coefficient for fluctuating front lengths is then given by

$$\int_0^{t_{\text{chg}}} \frac{1}{\lambda(t)} dt = \frac{1}{V_f} \left(\frac{c_{s2}}{c_{s1} - c_{s2}} \right) \ln \left[1 - \Pi \left(\frac{c_{s1} - c_{s2}}{\Pi c_{s1} - c_{s2}} \right) \right] \tag{A.11}$$

The two wave-speed coefficients are plotted on figure A.2 for a range of charging periods Π. It is clear that the fluctuating wave-speed coefficient is always slightly larger than when the average thermal front length is used. As a result, this analysis demonstrates the fact that variations in c_s with temperature lead to slightly larger thermal losses.

A.2 Front lengths in radial-flow thermal stores

Front lengths in radial-flow thermal stores can be estimated in a similar way to those in axial-flow stores. Figure A.3 illustrates linear thermal fronts in a radial-flow store. As described in section 3.4 the mass flow rate per unit area decreases along the radius. Consequently the thermal wave speed is inversely proportional to the radius (equation 3.18), thereby leading the thermal front to steepen up during charge.

The nominal charging time of an axial-flow store with outer radius r_o and inner radius r_i is

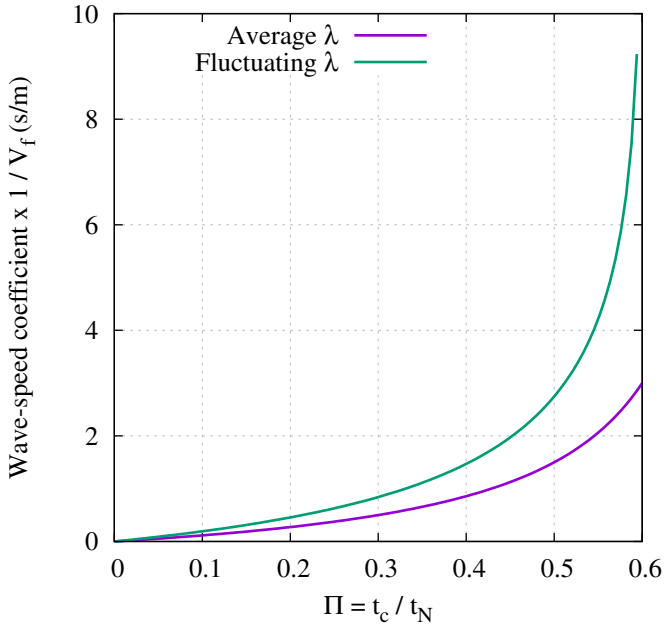

Figure A.2: Wave speed coefficients calculated with either the average thermal front length or a fluctuating thermal front length. Compare with equations A.2, A.6 and A.11

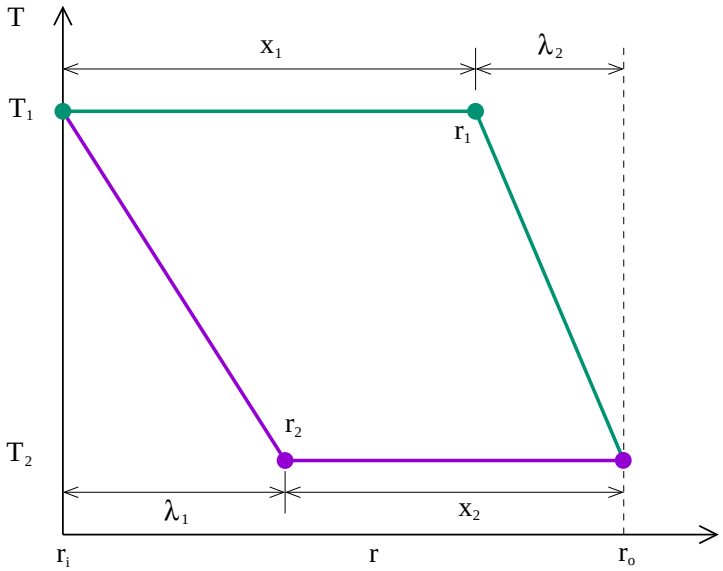

Figure A.3: Idealised thermal fronts in a radial-flow thermal store at the end of charge (green) and the start of charge (purple). c_s is assumed to be constant but the varying mass flow rate per unit area changes the front shape. Charge and discharge periods are estimated by assuming the period ends when the leading edge of the front reaches the exit.

given by

$$t_N = \frac{\rho_s \bar{c}_s (1-\varepsilon)}{2 G_i r_i c_p} \left(r_o^2 - r_i^2\right) \tag{A.12}$$

where it is assumed that the specific heat capacity is a constant. The thermal fronts are assumed to have a linear shape and to just reach the ends of the reservoir at the end of charge and discharge. By inspection of figure A.3 the charging time t_c may be written as

$$\Pi = \frac{t_c}{t_N} = \frac{r_1^2 - r_i^2}{r_o^2 - r_i^2} = \frac{r_o^2 - r_2^2}{r_o^2 - r_i^2} \tag{A.13}$$

Furthermore the front lengths λ_1 and λ_2 are given by

$$\lambda_1 = r_o - r_i - x_2 = r_2 - r_i \tag{A.14}$$

$$\lambda_2 = r_o - r_i - x_2 = r_o - r_1 \tag{A.15}$$

By substituting the utilisation Π into these expressions, normalising by the flow length $r_o - r_i$ and writing $\rho = r_i / r_o$ the fractional front lengths are given by

$$\frac{\lambda_1}{r_o - r_i} = \frac{\rho}{1-\rho} \left\{ \frac{1}{\rho} \left[1 - \Pi \left(1 - \rho^2\right)\right]^{1/2} - 1 \right\} \tag{A.16}$$

$$\frac{\lambda_2}{r_o - r_i} = \frac{1}{1-\rho} \left\{ 1 - \rho \left[1 + \Pi \frac{1-\rho^2}{\rho^2}\right]^{1/2} \right\} \tag{A.17}$$

Figure A.4 compares the radial-flow front lengths to the fractional front length in axial reservoirs (which is given by $\lambda_x / L = 1 - \Pi$ when c_s is constant). As expected $\lambda_1 > \lambda_2$. However, the axial front length lies between these values, and this is supported by the numerical results in figure 3.19. The figure also illustrates the average radial front length which is less than the axial front length for $\Pi < 0.5$. (For larger values of Π this model becomes increasingly inaccurate since the thermal fronts protrude further from the store).

These results have particular significance for the thermal loss. An approximate expression for the thermal loss was derived in equation 2.50 as

$$\zeta_t \approx \frac{T_0}{\beta} \left(\frac{\Delta T^2}{T_1 T_2} \right) \frac{\bar{\ell}}{\lambda} \tag{A.18}$$

This expression also applies to radial-flow stores if the length scale $\bar{\ell}$ is calculated at the

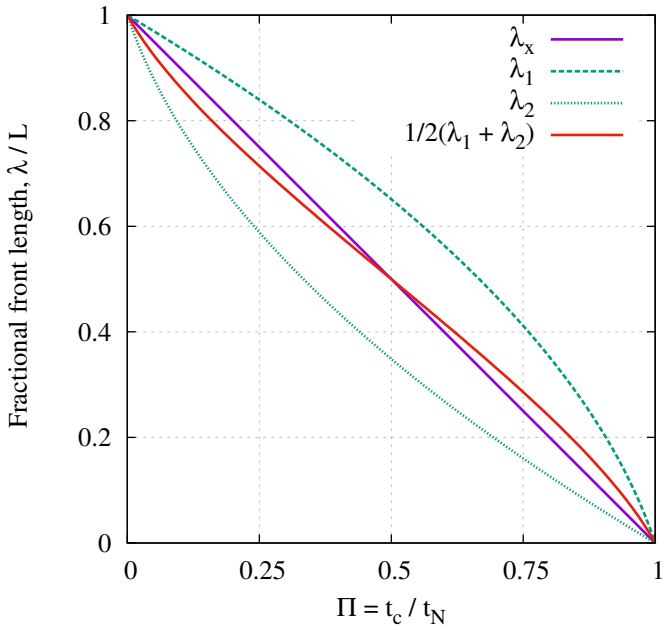

Figure A.4: Fractional front lengths calculated for axial-flow stores λ_x and radial-flow stores λ_1 and λ_2, see equation A.17.

average radius $\bar{r} = 1/2(r_i + r_o)$. The above analysis has shown that the front length may be replaced by $\lambda = Lf(\Pi)$, where L is the length of the flow path ($r_o - r_i$ for radial-flow stores) and $f(\Pi)$ is a function of the utilisation. The thermal loss coefficient is then

$$\zeta_t \approx \frac{T_0}{\beta}\left(\frac{\Delta T^2}{T_1 T_2}\right)\frac{\bar{\ell}}{Lf(\Pi)} \tag{A.19}$$

Axial-flow and radial-flow stores are approximately equivalent if they have the same dimensionless length $\Lambda = L/\ell = (r_o - r_i)/\bar{\ell}$. For such reservoirs, the store with the smallest value of $f(\Pi)$ will generate the largest thermal loss. Therefore, these results suggest that thermal losses are larger in radial-flow stores than in the equivalent axial-flow store, particularly at low utilisations. In addition, the fluctuation of the radial front length between λ_1 and λ_2 will lead to greater losses, as described in the previous section. However, the variable c_s will counteract these fluctuations to some extent, and the effect may not be as large as anticipated.